<u>OXIDATION OF LEAD SULPHIDE</u>

Peter John SLEEMAN

A thesis presented for the Research Degree of

DOCTOR OF PHILOSOPHY

of the

COUNCIL FOR NATIONAL ACADEMIC AWARDS

LONDON

John Graymore Chemistry Laboratories,
School of Environmental Sciences,
Plymouth Polytechnic,
PLYMOUTH PL4 8AA,
Devon

July 1976

ABSTRACT

Previous research on the precipitation and oxidation of lead sulphide has been reviewed especially in relation to thermodynamic and kinetic studies.

Samples of lead sulphide have been precipitated from aqueous solutions of lead salts under varying conditions of pH, concentration, temperature and time of ageing. The precipitates were examined by optical and electron microscopy, X-ray diffraction and gas sorption analysis. Their crystallinity, particle size and phase composition have been correlated with the conditions of precipitation.

The oxidation of selected samples of precipitated and commercial lead sulphide was investigated by thermal analysis and the above techniques. The phase composition of the oxidation products were studied under varying conditions of temperature, gas flow rate and oxygen content of air. For the low temperature oxidation ($\sim 500^{\circ}$C) the thickness of the lead sulphate product layer was estimated and attempts made to correlate this value with the kinetics of the oxidation. The stability of lead sulphate at high temperature ($\sim 900^{\circ}$C) has been investigated. Sintering behaviour of the products in relation to their incomplete desulphurization was examined.

Oxidation studies on lead sulphide were extended to lead-zinc ores with respect to the effect of moisture content and bentonite on sintering. This investigation was carried out on a sinter pallet using 22 kg mixes at ISP Research Department of Imperial Smelting Processes Limited, Avonmouth.

The possible formation of lead sulphite as an intermediate in the low temperature oxidation of lead sulphide was investigated by studying the thermal stability of the sulphide under various gaseous atmospheres. These studies were extended to zinc sulphite in relation to previous studies on the oxidation of zinc sulphide.

These researches form a part of a wider study in the oxidation of sulphides during shipment, storage and processing.

ACKNOWLEDGEMENTS

CONTENTS

CHAPTER 1

INTRODUCTION AND REVIEW

1.1 INTRODUCTION

In the earth's crust lead is estimated to be present to the extent
of $1.6 \times 10^{-3}\%$ by weight and in sea-water at a concentration of 0.004
grams per ton.   Very small quantities of native lead occur as a
mixture of the four isotopes:- $^{204}Pb(1.48\%)$, $^{206}Pb(23.6\%)$, ^{207}Pb
(22.6%), and $^{208}Pb(52.3\%)$.   The lead isotopes are the end products of
three series of naturally-occurring radioactive elements, i.e. the
uranium series yields ^{206}Pb, the thorium series yields ^{207}Pb and the
actinium series yields ^{208}Pb.   Seventeen other isotopes, all of which
are radioactive are recognized.

The majority of lead used today is obtained by smelting the
natural sulphide of lead, galena.

1.1.1 The Mineral Galena

The mineral galena is the principal ore of lead.   It occurs most
frequently associated with the zinc ore, sphalerite; the lead-zinc ores
often contain recoverable amounts of copper, silver, antimony and
bismuth.   In general, the lead-zinc minerals were deposited by hot
ascending mineralizing solutions with moderate conditions of
temperature and pressure.   However, some of the largest ore bodies
were formed under high temperature and pressure conditions, e.g.
Broken Hill, Sullivan and Bawdwin Mines.

The Broken Hill Mines of New South Wales, Australia are
located in a shear zone traversing sedimentary, igneous and
metamorphic rocks.   The ores contain 9-14% Zn and 12-16% Pb with
3-12 oz Ag per ton.   In British Columbia the Sullivan mines produce
ore containing ∼13% Zn and 11% Pb.   The Bawdwin mines of Burma
are located in a zone of crushed, faulted rocks of rhyolite and rhyolite
tuffs and yield ∼24% Pb and 15% Zn, being amongst the richest in the
world.

The mineralization solutions may also traverse limestone structures, which they can easily replace, following the bedding planes to form horizontal or low dipping ore bodies, such as the Flats which formerly yielded large quantities of galena in Derbyshire.

Galena smelting operations flourished in Great Britain in the seventeenth century especially in Derbyshire and Wales and from there spread to the colonies as ores were discovered.

1.1.2 Metallurgy and Recovery of Lead

The metallurgy and recovery of lead is complex, not because the reduction of galena is difficult, but due to the separation of other metals commonly associated with galena.

A considerable number of the associated metals can be removed from the lead ore by a series of selective flotation processes, resulting in lead concentrates with an average lead content of 50%, although pure lead concentrates will analyse up to 80% lead.

In the process of smelting lead ore in a blast furnace, the sulphur must be largely removed prior to introduction in the blast furnace, to prevent the formation of undue quantities of matte and control the formation of sulphide crusts.

The preliminary sulphur removal in modern plants is carried out by sintering the lead ore with slag-forming reagents on a continuous travelling-grate sinter machine.

The sinter process serves a two-fold purpose, namely, desulphurization and the production of a material with suitable physical characteristics for introduction to the blast furnace.

The principal chemical reactions involved in the industrial sinter process are:-

$$2PbS + 3O_2 \longrightarrow 2PbO + 2SO_2$$
$$PbS + 2PbO \longrightarrow 3Pb + SO_2$$
$$PbS + O_2 \longrightarrow PbSO_4$$
$$\text{and} \quad 2PbO + SiO_2 \longrightarrow Pb_2SiO_4$$
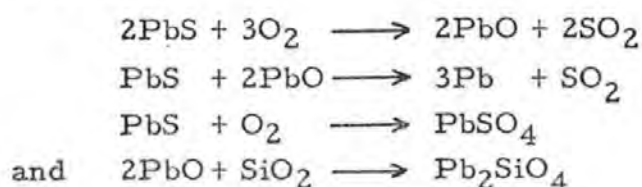
The blast furnace essentially consists of a rectangular refractory brick and water-jacketed column mounted above a crucible fitted with tuyères along the lower sides for introduction of the air blast.

Air is introduced under pressure through the tuyères causing

the coke in the charge to burn and provide heat for smelting, as well as for the formation of carbon monoxide to reduce the lead oxide to lead. The gangue material consisting of silica, lime, and iron oxide combines with the zinc oxide and alumina, if present, to form slag, while the reduced lead collects such valuable metals as copper, silver, gold and antimony.

Some sulphur, usually less than 2%, is always left in the sinter and will combine with copper and arsenic to form a matte and speiss respectively.

The principal reactions taking place in the blast furnace are:

$$2PbO + C \longrightarrow 2Pb + CO_2$$
$$PbO + CO \longrightarrow Pb + CO_2$$
$$CO_2 + C \longrightarrow 2CO$$

and $Pb_2SiO_4 + CaO + FeO \longrightarrow 2PbO + CaO.FeO.SiO_2$ (slag)
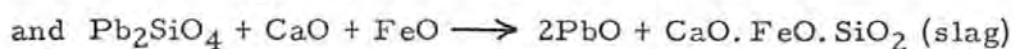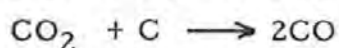
The lead bullion probably contains several valuable metals, as mentioned above; to extract these further refining steps are necessary.

Copper is removed by simply cooling the bullion as it comes from the blast furnace to about 350°C, at which temperature the copper compounds become insoluble and separate out as a dross, leaving a copper-lead eutectic containing only traces of copper.

The lead may be further refined directly by electrolysis by the Betts process, or by a continuing series of pyrometallurgical methods. In electrolytic refining, the electrolyte is lead fluorosilicate; the anode is the impure lead bullion and the cathode is a thin sheet of pure lead. On passing an electric current through the cell, lead is deposited on the cathode and the impurities associated with the lead bullion, having a lower solution potential than lead, remain undissolved on the anode, forming a slime. The slime is removed and treated for the recovery of the valuable metals.

In pyrometallurgical refining, the lead bullion after copper recovery is treated for the removal of arsenic, antimony and tin. This can be achieved by two methods, namely, "softening" and the Harris process. In the Harris process, liquid lead bullion just above its melting point is pumped through molten sodium hydroxide. Arsenic, antimony and tin are removed from the lead and may be recovered separately from the caustic mix by leaching.

In the "softening" process, molten lead bullion at about 750°C is blown through with air and the metals alloyed with lead are converted to their oxides together with some lead and slagged off.

Other processes, such as the Parkes process, are used to remove silver and gold from the lead bullion. The Pattinson process for removal of silver and gold is not now in commercial usage, but CSIRO are currently working on a modern equivalent fractional crystallization process.

1.1.3   Synthesis of Lead Sulphide

Lead sulphide may be prepared by numerous wet processes, from lead salts and both organic and inorganic sulphur compounds. It may also be prepared directly from lead and sulphur, by stirring sulphur into molten lead. Good crystals of lead sulphide are produced by heating mixtures of lead oxide, ammonium chloride and sulphur, or lead oxide with excess potassium thiocyanate, and by heating lead silicate in sulphur vapour.

A comprehensive review of the methods used for the preparation of lead sulphide is given in Mellor.[1]

1.1.4   Properties of Lead Sulphide

Lead sulphide crystallizes in the sodium chloride face-centred cubic structure, with the Pb-S distance 2.97 Å and is the only stable sulphide of lead. Lead sulphide is a p-type semiconductor when sulphur-rich and an n-type when lead-rich. Thus, crystalline lead sulphide was used in early radio receivers as the radio detector.

Table 1.1a summarizes the properties of lead sulphide.

According to the differences in electronegativity values for lead (1.8) and sulphur (2.5), lead sulphide has a 12% ionic character. On the same scale, NaCl has 67% and CsF 93% ionic character.

1.1.5   The Oxides of Lead

Lead (II) oxide exists in two crystal forms; yellow massicot is orthorhombic and stable above 488°C and the red, tetrahedral form, litharge, is stable at room temperature. In wet processes for the preparation of lead oxide the yellow form is obtained first, which then undergoes a transformation to the red form. This transformation is very sensitive to impurities and the presence of elements such as

Table 1.1a   Properties of Lead Sulphide

Molecular Weight	239.25
Density	7.5 g cm^{-3}
Colour	Black
Melting point	1114°C
Crystal structure	Face-centred cubic
Solubility product	3.4×10^{-28}, 18°C

Solubility of lead sulphide in solutions of varying pH levels against temperature

pH	25°C	100°C	200°C	400°C	600°C
3	2.30×10^{-7} M	2.38×10^{-6}	1.58×10^{-5}	1.42×10^{-4}	4.73×10^{-4}
7	3.28×10^{-11}	6.36×10^{-10}	8.56×10^{-9}	1.82×10^{-9}	1.15×10^{-6}
11	2.34×10^{-13}	7.85×10^{-12}	4.06×10^{-10}	5.31×10^{-8}	7.5×10^{-7}

Si, Ge, P, As, Sb, Mo, W in concentrations as low as 10 ppm prevent the transformation.

In tetragonal lead oxide, each lead atom has four oxygens as near neighbours, all lying to one side, and all the oxygen atoms lie between every other pair of lead layers, see Figure 1.
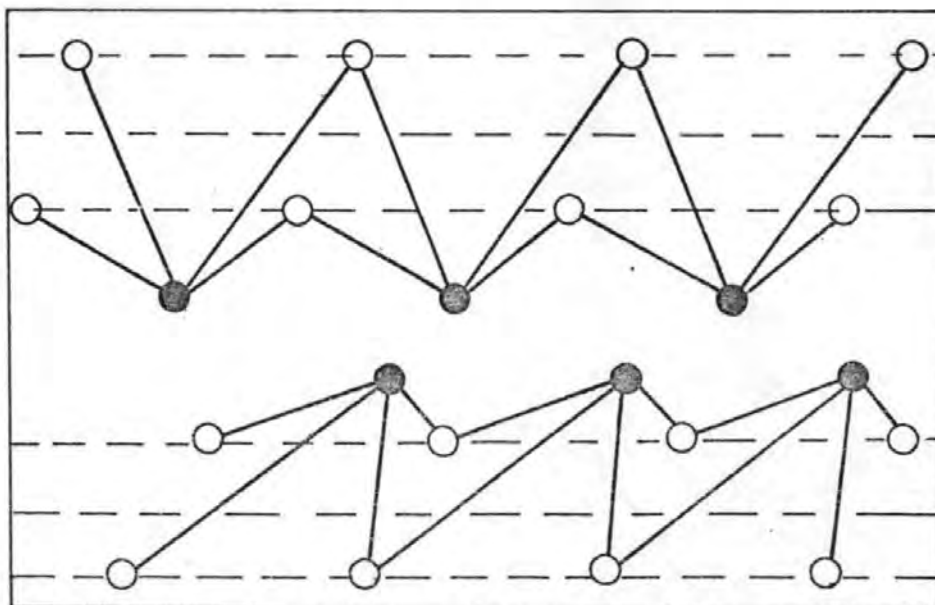
Figure 1   Tetrahedral lead (II) oxide

The layering in orthorhombic lead oxide is a slightly puckered version of the tetragonal form where four equal Pb-O bonds (2.30 $\overset{o}{A}$) replace the two short (2.21 $\overset{o}{A}$) and two long (2.49 $\overset{o}{A}$) Pb-O bonds. This close similarity presumably allows small quantities of impurities to stabilize the yellow orthorhombic form at room temperature.

Red lead or minim (Pb_3O_4) can be formed by heating lead oxide and lead dioxide at about $250^{\circ}C$. It has a structure which consists of chains of $Pb^{4+}O_6$ octahedra joined by opposite edges; the chains are linked by Pb^{2+} ions co-ordinated to three oxygen atoms pyramidally, see Figure 2.
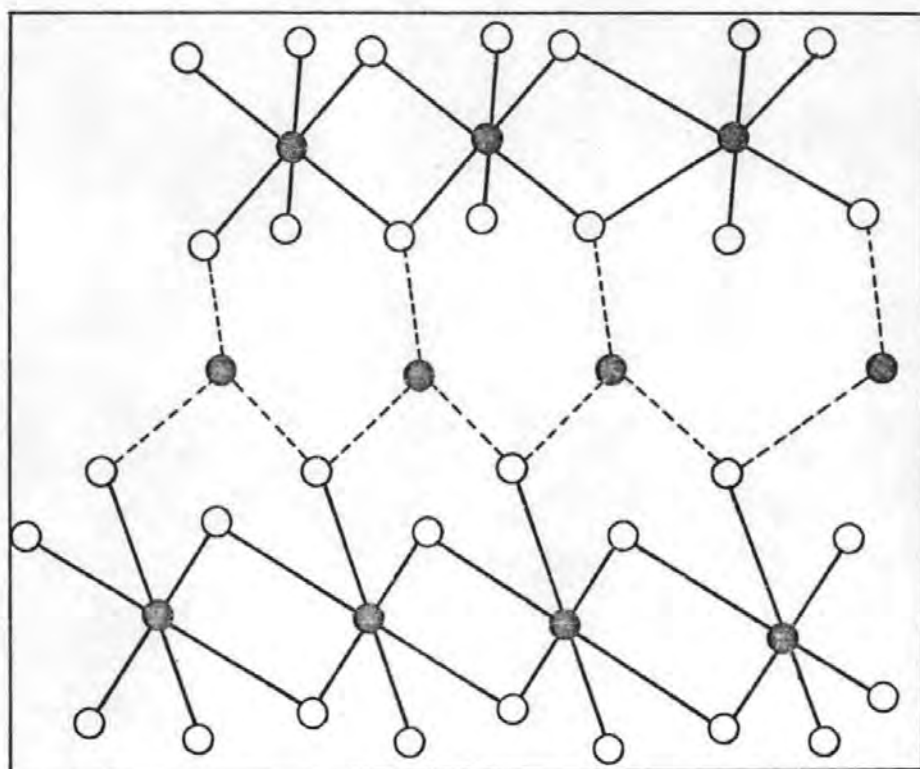
Figure 2   Structure of Pb_3O_4

On heating, Pb_3O_4 decomposes to lead oxide and oxygen (oxygen partial pressure of about 0.2 atm at $550^{\circ}C$).

Lead (IV) oxide (PbO_2) is formed in nature as the somewhat rare mineral plattnerite with the rutile structure, but another orthorhombic form is known and is usually referred to as $\alpha-PbO_2$. It is difficult to obtain in the perfectly anhydrous state as the

temperature for complete drying initiates the release of oxygen to form PbO and Pb_3O_4. On heating, it decomposes to lead oxide and oxygen (partial pressure of oxygen reaches 1 atm at 344°C).

D T A studies of the decomposition of lead oxide, together with X-ray analysis have shown two further oxide phases:-

$$PbO_2 \xrightarrow{\sim 280^{\circ}C} \alpha\text{-}PbO_x \qquad x = \sim 1.66$$

$$\alpha\text{-}PbO_x \xrightarrow{\sim 375^{\circ}C} \beta\text{-}PbO_y \qquad y = \sim 1.5$$

$$\beta\text{-}PbO_y \xrightarrow{>375^{\circ}C} Pb_3O_4$$
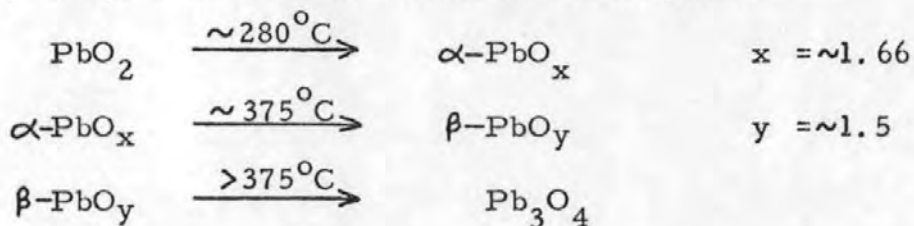
A monoclinic structure is proposed for the $\alpha\text{-}PbO_{1.66}$ which is probably the Pb_7O_{11} and Pb_5O_8 of earlier workers. The $\beta\text{-}PbO_{1.5}$ is orthorhombic with composition Pb_2O_3.

The suboxide of lead, Pb_2O, has been reported by a few workers, but there is considerable doubt over its existence.

1.2   A REVIEW OF THE OXIDATION OF LEAD SULPHIDE

The system lead sulphide/air was considered by Wittung[2] from a theoretical aspect by giving a quantitative description of the equilibrium reactions occurring in the roasting process (627-927°C) under varying conditions, e.g. reaction temperature, molar ratio of lead sulphide/air, and heat change when the reactions occur in a hypothetical reactor.

The model considered, consisted of $PbS(s)$, $O_2(g)$ and $N_2(g)$ being brought into the hypothetical reactor at 25°C, heated to the reaction temperature, T°C, allowed to react and form a large number of different products.   The reaction is summarized in the form:-

$$n^*_{PbS} \cdot PbS + n^*_{O_2} \cdot O_2 + 3.729\, n^*_{O_2} \cdot N_2 \longrightarrow n_1 A_1$$
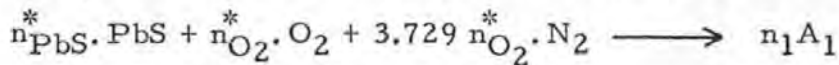
where n_1 =   the number of moles of substance in the equilibrium mixture

n^* =   the number of moles of substance in the initial mixture

A_1 refers to all substances which were assumed to be formed in the equilibrium mixture.

In order to carry out the complex calculation a computer programme "SOLGAS"[3] was used.

From primary calculations using logarithmic diagrams (Sillen, Rengen[4]) it was found that lead sulphite is unstable, and lead dioxide is only stable when $P_{O_2} > 10^4$ atm.   Consequently, neither lead sulphite or lead dioxide will be formed when lead sulphide and air react under normal conditions.

In the following cases, $n^*_{PbS} = 10.$

FROM 627-727°C

For $n^*_{O_2} \leqslant 17.5$ the following reaction will occur:-

$$2PbS(s) + 3.5\, O_2(g) \rightleftharpoons PbSO_4 \cdot PbO(s) + SO_2(g) \quad\text{------------ (1)}$$
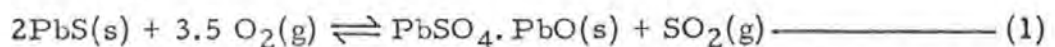
when all the sulphur from the lead sulphide is oxidized ($n^*_{O_2} = 17.5$), the $PbSO_4 \cdot PbO$ will be converted to $PbSO_4$ via

$$PbSO_4 \cdot PbO(s) + 0.5\, O_2(g) + SO_2(g) \rightleftharpoons 2PbSO_4(s) \quad\text{------------ (2)}$$
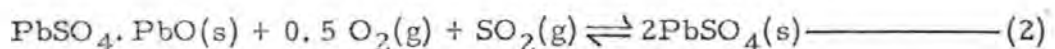
FROM 752-802°C

All three basic sulphates appear, $PbSO_4 \cdot PbO$ via reaction (1), $PbSO_4 \cdot 2PbO$ and $PbSO_4 \cdot 4PbO$ according to the following reactions:-

$$3PbS(s) + 5 O_2(g) \rightleftharpoons PbSO_4 \cdot 2PbO(s) + 2SO_2(g) \text{—————(3)}$$

$$5PbS(s) + 8 O_2(g) \rightleftharpoons PbSO_4 \cdot 4PbO(s) + 4SO_2(g) \text{—————(4)}$$
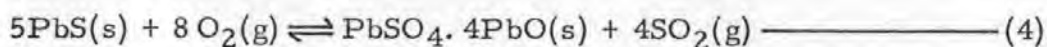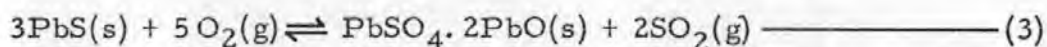
When $n_{O_2}^*$ is increased the basic sulphates react according to the reactions:-

$$3(PbSO_4 \cdot 4PbO)(s) + 2SO_2(g) + O_2(g) \rightleftharpoons 5(PbSO_4 \cdot 2PbO)(s)\text{————(5)}$$

$$2(PbSO_4 \cdot 2PbO)(s) + SO_2(g) + 0.5 O_2(g) \rightleftharpoons 3(PbSO_4 \cdot PbO)(s)\text{————(6)}$$
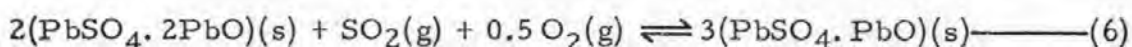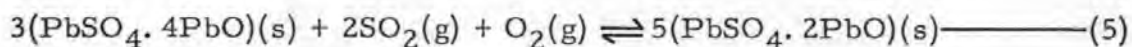
and finally to $PbSO_4$, via reaction (2).

FROM 827-927°C

Metallic lead is the product primarily formed.

$$PbS(s) + O_2(g) \rightleftharpoons Pb(l) + SO_2(g)\text{——————(7)}$$
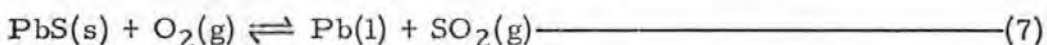
For oxygen $n_{O_2}^* = 10$ (PbS $n_{PbS}^* = 10$) all the sulphur from the lead sulphide is converted to SO_2, and metallic lead remains the only condensed phase. For higher values of $n_{O_2}^*$, lead will react according to the equation:-

$$5Pb(l) + SO_2(g) + 3 O_2(g) \rightleftharpoons PbSO_4 \cdot 4PbO \text{——————(8)}$$
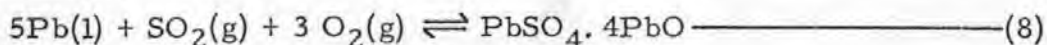
Further additions of oxygen will cause reactions (5), (6), (2) to occur.

Thus it appears possible to produce metallic lead directly from lead sulphide in a reactor at a temperature $>852°C$, if the ratios $n_{O_2}^* / n_{PbS}^* = 1$, via reaction (7) and such a process has been demonstrated in the pilot plant scale by Fuller[5].

Yazawa & Gubcova[6] carried out thermodynamical calculations on the Pb-S-O system and presented the results in isothermal reaction diagrams (680, 900, 1100°C) where $\log P_{S_2}$ and $\log P_{O_2}$ were the axes.

At 680°C (Figure 3) the final roast products under normal roasting conditions, where the gaseous phase contains several percent SO_2 and O_2, seems to be $PbSO_4$. The diagram also suggests that the oxidation product co-existing with lead sulphide under normal roasting conditions is $PbSO_4$ or $PbSO_4 \cdot PbO$, and not PbO.

At 900°C (Figure 4) the "roast reaction" begins with lead sulphide reacting with $PbSO_4$ or oxide to form a more stable phase i. e.

Figure 3. Isothermal reaction diagram at 680°C
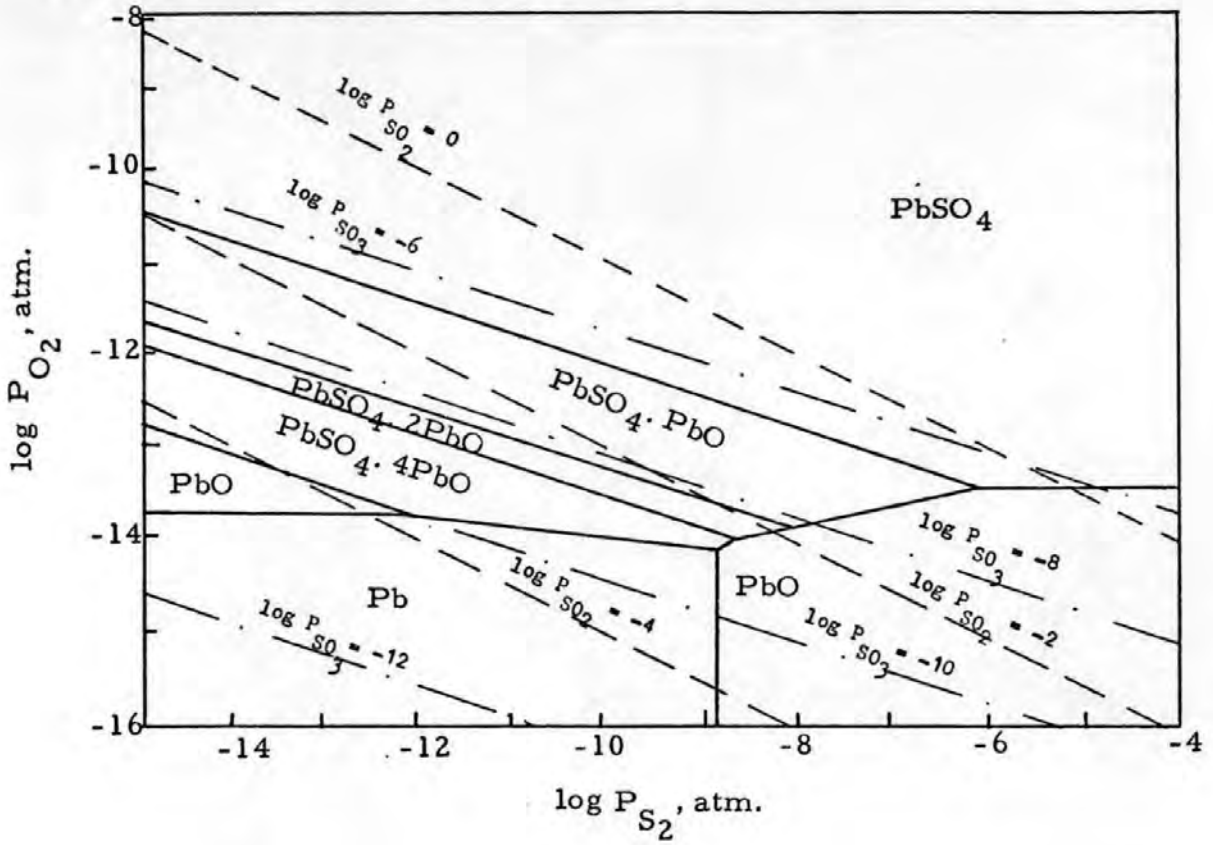
Figure 4. Isothermal reaction diagram at 900°C

$$PbS + PbSO_4 \longrightarrow 2Pb + 2SO_2$$
$$\text{or } PbS + 2PbO \longrightarrow 3Pb + SO_2$$
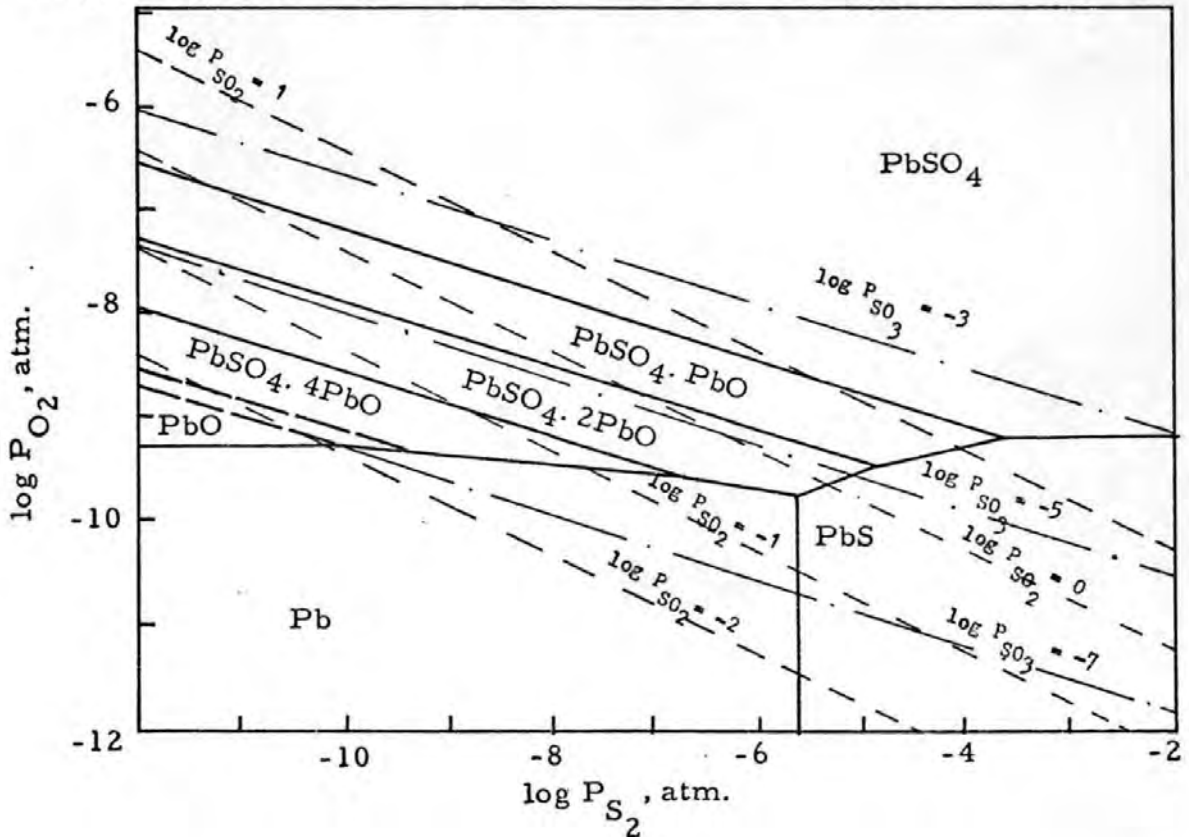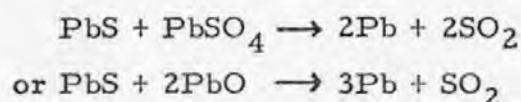
At $1100^{\circ}C$ (Figure 5) all but $PbSO_4$ are in the molten state, the relationship between the condensed phase and SO_2 pressure suggests the roast reaction will proceed readily, resulting in metallic lead.

The reaction $PbS + O_2 \longrightarrow Pb + SO_2$ may also be considered with the conditions for direct production of lead being approximated by the line $\log P_{SO_2} = 0$ (Figure 5).

Thermodynamic calculations performed by Polyvannyi et al[7] show that the following reactions can occur during the sintering of galena in air at $450-1150^{\circ}C$:-

$$2PbS + 3\,O_2 \rightleftharpoons 2PbO + 2SO_2$$
$$PbS + 2\,O_2 = PbSO_4$$
$$PbS + O_2 = Pb + SO_2$$

and the reactions:-

$$PbS + PbSO_4 = 2Pb + 2SO_2$$
$$PbS + 2PbO = 3Pb + SO_2$$
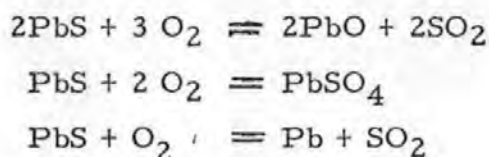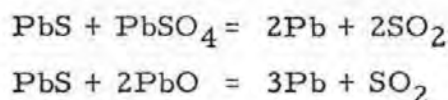
may occur above $800^{\circ}C$ and $1050^{\circ}C$ respectively.

A review of the physico-chemical principles involved in lead sulphide roasting are given by Melin & Winterhager[8] and includes equilibrium phase diagrams showing that $PbSO_4$ is the stable oxidation product with P_{O_2} between 0.01-0.1 atm up to $900^{\circ}C$, above this temperature the basic sulphates are stable until $\sim 1150^{\circ}C$ when PbO becomes the stable phase.

The products formed on roasting lead sulphide between 400 and $1250^{\circ}C$ according to Kellogg & Basu[9] and Lander[10] are lead sulphate, mono-basic lead sulphate, dibasic lead sulphate, tetra-basic lead sulphate, lead oxide (two crystal forms) and metallic lead. The reactions forming these products may be divided into two distinct categories, namely, oxidation and reduction reactions.

Oxidation reactions:-

$$4PbS + 7\,O_2 \rightleftharpoons 2(PbSO_4 \cdot PbO) + 2SO_2 \quad\text{———————}(9)$$
$$\text{or } \quad 3PbS + 5\,O_2 \rightleftharpoons PbSO_4 \cdot 2PbO + 2SO_2 \quad\text{—————}(10)$$
$$\text{or } \quad 5PbS + 8\,O_2 \rightleftharpoons PbSO_4 \cdot 4PbO + 4SO_2 \quad\text{—————}(11)$$
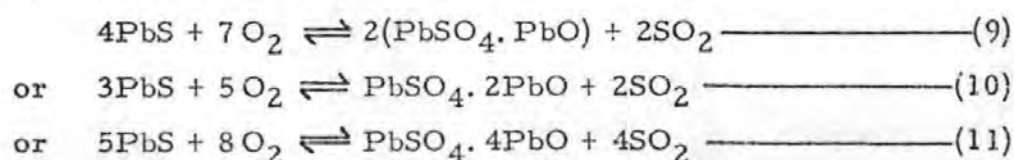
Figure 5. Isothermal reaction diagram at 1100°C
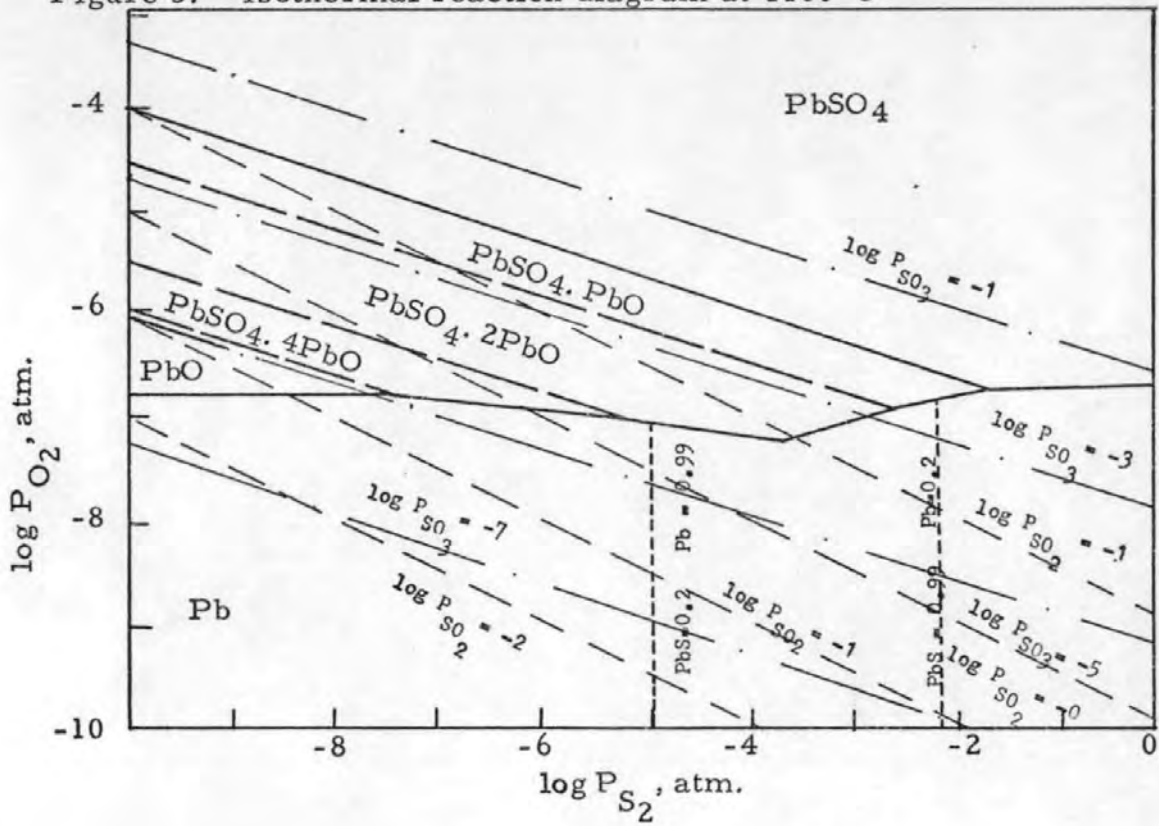
Figure 6. Curve relating the vapour pressure of lead sulphide to temperature

or $\quad PbS + 2O_2 \rightleftharpoons PbSO_4$ —————————————(12)
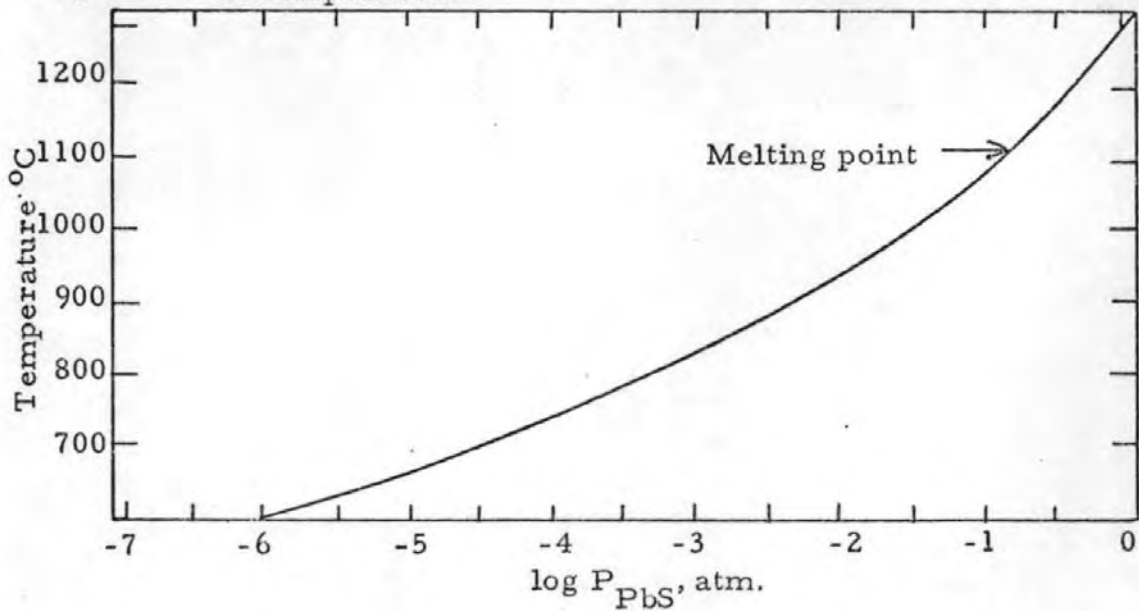
Sulphation of the above products with SO_2 may also occur

e. g. $\quad 2(PbSO_4 . PbO) + 2SO_2 + O_2 = 4PbSO_4$ —————(13)
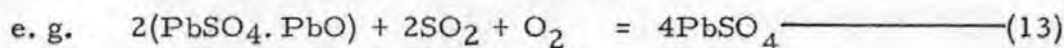
Reduction reactions may occur with the oxidation products being reduced by lead sulphide vapour to lead or lead oxide.

e. g. $\quad 3PbS + PbSO_4 . 4PbO = 8Pb + 4SO_2$ —————————(14)

or $\quad PbS + 3(PbSO_4 . 4PbO) = 16PbO + 4SO_2$ —————(15)

or $\quad PbS + 2PbO \qquad = 3Pb + SO_2$ —————————(16)
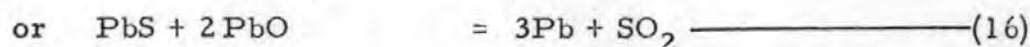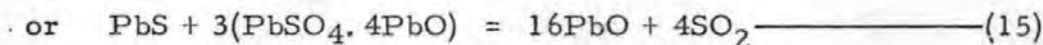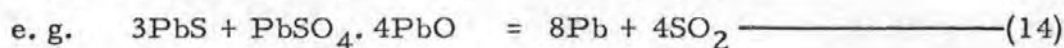
i. e. the lead is being formed by reduction of the basic sulphate directly (14), or step-wise (15, 16).

The reduction reactions depend upon the lead sulphide vapour being present. Figure 6 shows the volatility of lead sulphide against temperature.

Equilibrium diagrams for the oxidation and reduction reactions have been calculated from published data (Table 1.2a) by Kellogg & Basu[9]; Kirkwood & Nutting[11]; Kubaschewski & Evans[12] and Tuffley & Russell[13, 14].

Table 1.2a

Substance	$\Delta H_f^o \quad kJmol^{-1}$	$\Delta G_f^o \quad kJmol^{-1}$	$S^o \quad JK^{-1}mol^{-1}$
PbO (yellow)	217. 11	188. 57	71. 5
PbS	93. 89	92. 84	93. 1
$PbSO_4$	918. 58	812. 69	151. 4
Pb (liquid)	3. 88	2. 18	70. 5
SO_2 (gas)	296. 71	299. 98	247. 8
$PbSO_4 . PbO$	1153. 15	1019. 28	224. 9
$PbSO_4 . 2PbO$*	1358. 57	1200. 90	312. 3
$PbSO_4 . 2PbO$*	1357. 60	1201. 74	318. 5
$PbSO_4 . 4PbO$*	1814. 32	1595. 81	442. 9
$PbSO_4 . 4PbO$*	1815. 57	1594. 76	435. 3

Table 1.2a gives thermodynamic data for the reactants and products involved in the oxidation of lead sulphide. The thermodynamic values given for the compounds marked * were calculated from different reactions. The phase diagrams for the oxidation and reduction

reactions at 600, 800, 900, 1100 and 1200°C are reproduced in (Figures 7 to 17). These diagrams being essentially horizontal sections of three dimensional diagrams where the temperature is plotted on the vertical axis. (Figure 17) represents the vertical section of the three dimensional diagram at constant oxygen partial pressure (0.21 atm.).

From (Figure 17) the following conclusions were drawn:-

(a) $PbSO_4.4PbO$ is unstable above 940°C

(b) $PbSO_4.2PbO$ is unstable below 620°C

(c)   Stable regions depend upon the partial pressures of oxygen and sulphur dioxide, and temperature.

(d)   The lead sulphide vapour pressure curve (Figure 6) limits the scope of the reduction reactions.

Roasting experiments were performed by Tuffley & Russell[13] on lead sulphide prepared from high purity lead and excess sulphur at 450°C in an evacuated pyrex capsule. From the results it was concluded that:-

(a)   825°C is the lowest temperature at which metallic lead was detected.

(c)   Samples roasted at 800°C; after 5 min. the intensity of the $PbSO_4.PbO$ X-ray diffraction lines equalled those of the $PbSO_4.4PbO$, but after 30 min. the intensity of the $PbSO_4.PbO$ had increased, whereas those of $PbSO_4.4PbO$ had decreased and after 60 min. had disappeared.

(c)   No evidence of $PbSO_4.2PbO$ was found which confirms the phase diagram (Figure 17) findings that $PbSO_4.2PbO$ decomposes below 620°C.

i.e. $3(PbSO_4.2PbO) \xrightarrow{<620°C} 2PbSO_4.PbO + PbSO_4.4PbO$

Since $PbSO_4.4PbO$ is unstable above 940°C (Figure 17), the X-ray lines for the $PbSO_4.4PbO$ present after roasting at 1000°C and 1100°C are accounted for by the decomposition of $PbSO_4.2PbO$ below 620°C. At 800°C after 5 min. the products identified were $PbSO_4.PbO$ and $PbSO_4.4PbO$, and it is assumed that $PbSO_4.2PbO$ was also present. Thus the reactions concerned would be:-

$$4PbS + 7O_2 = 2(PbSO_4.PbO) + 2SO_2$$
$$3PbS + 5O_2 = PbSO_4.2PbO + 2SO_2$$
$$5PbS + 8O_2 = PbSO_4.4PbO + 4SO_2$$
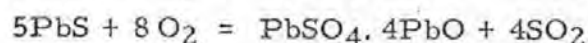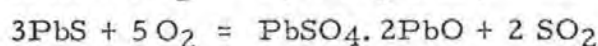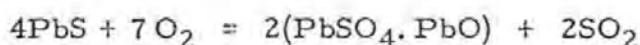
Figure 7. Equilibrium diagram for oxidation reactions at 600°C
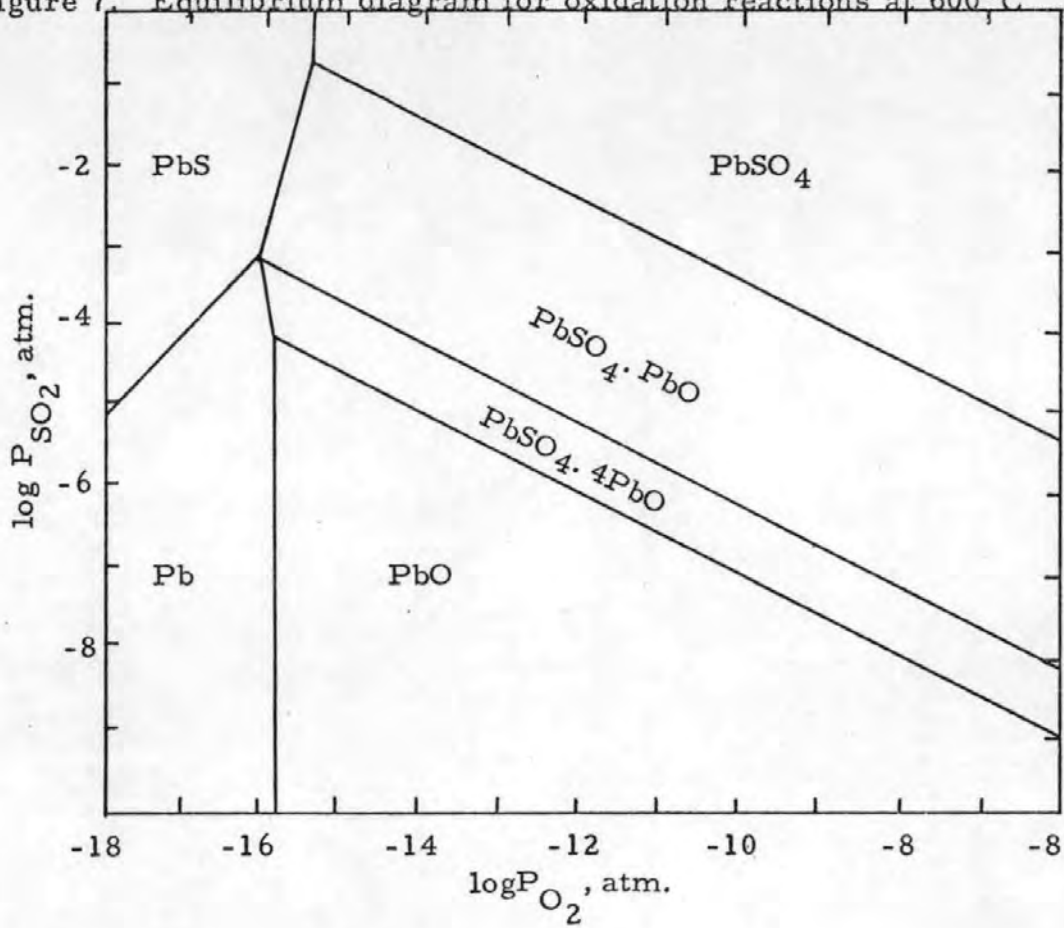
Figure 8. Equilibrium diagram for reduction reactions at 600°C
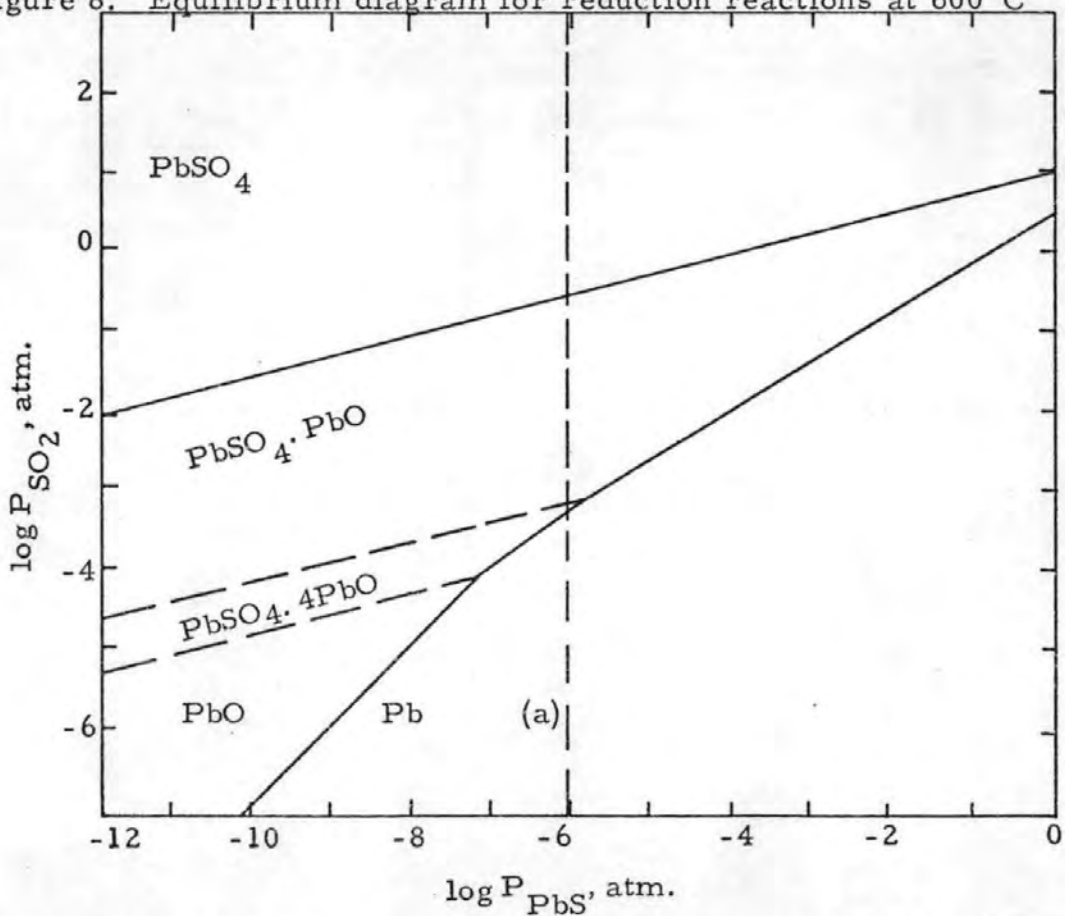
The dotted line (a) represents the maximum vapour pressure of PbS at 600°C.

Figure 9. Equilibrium diagram for oxidation reactions at 800°C
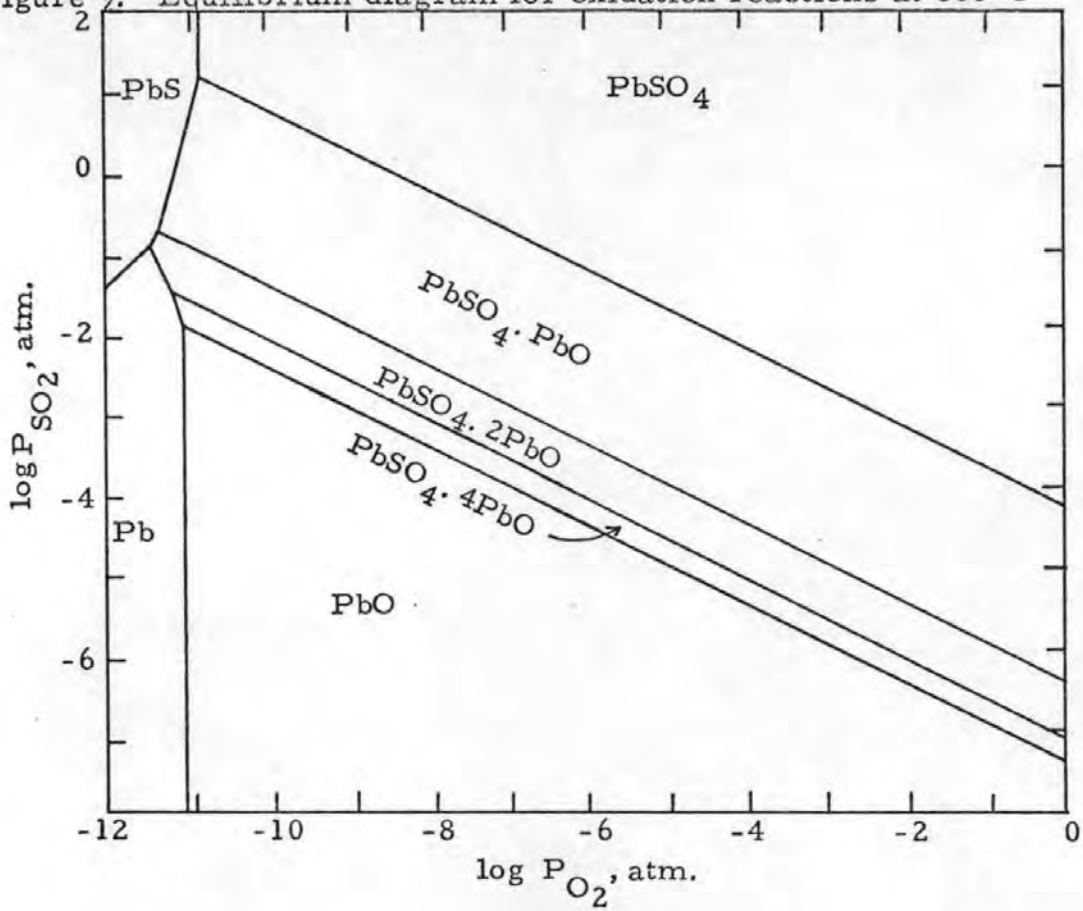
Figure 10. Equilibrium diagram for reduction reactions at 800°C
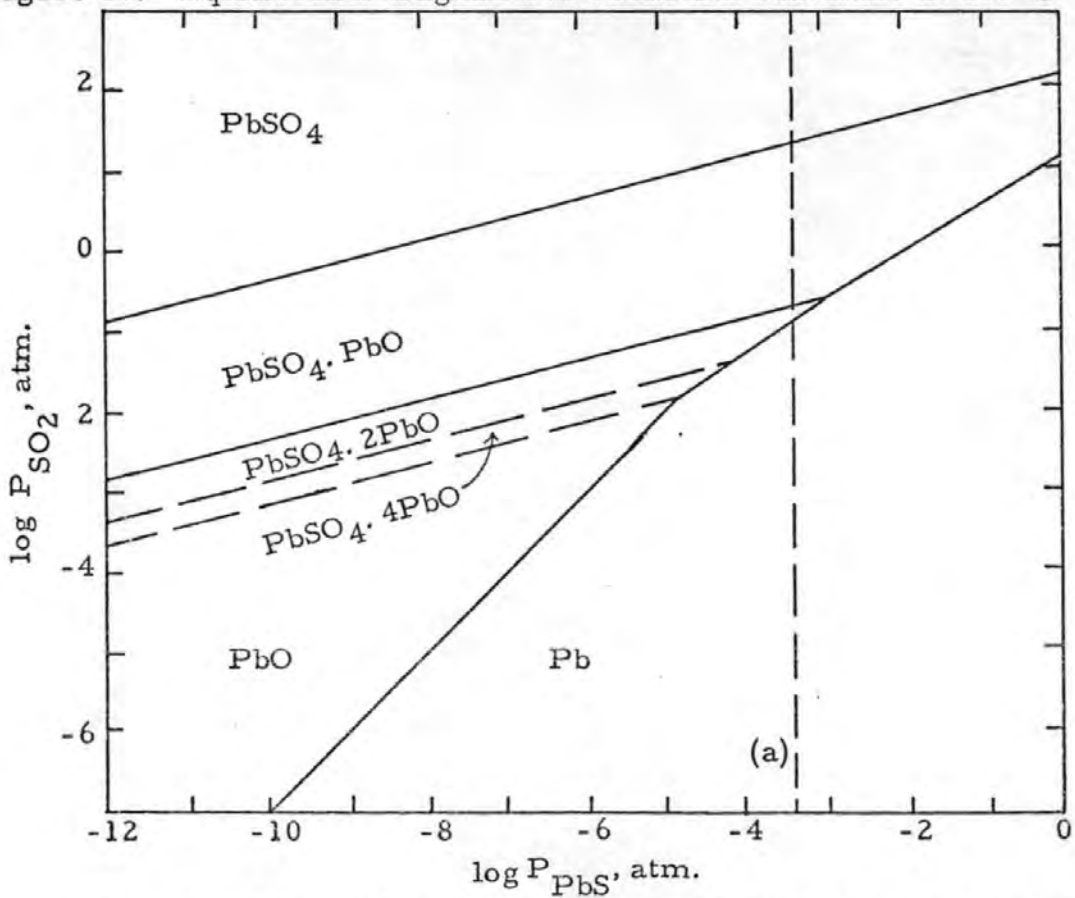
The dotted line (a) represents the maximum vapour pressure of PbS at 800°C.

Figure 11. Equilibrium diagram for oxidation reactions at 900°C
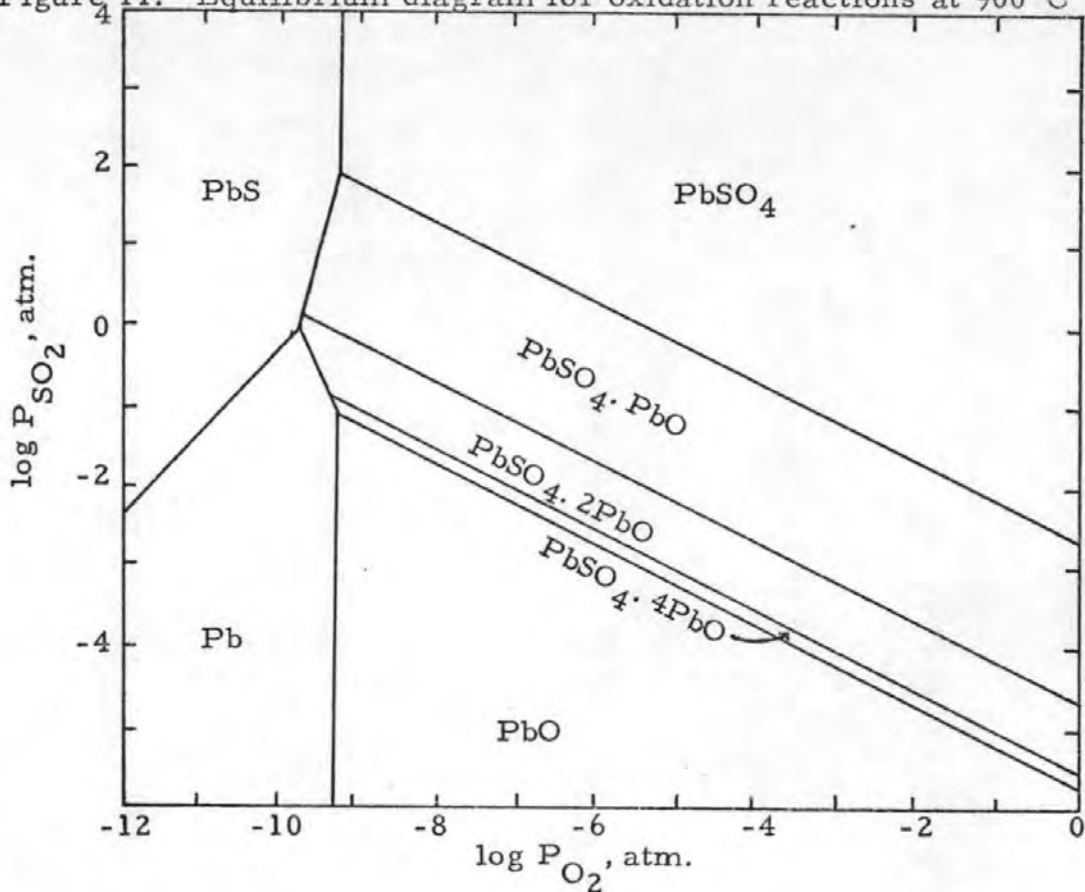
Figure 12. Equilibrium diagram for reduction reactions at 900°C
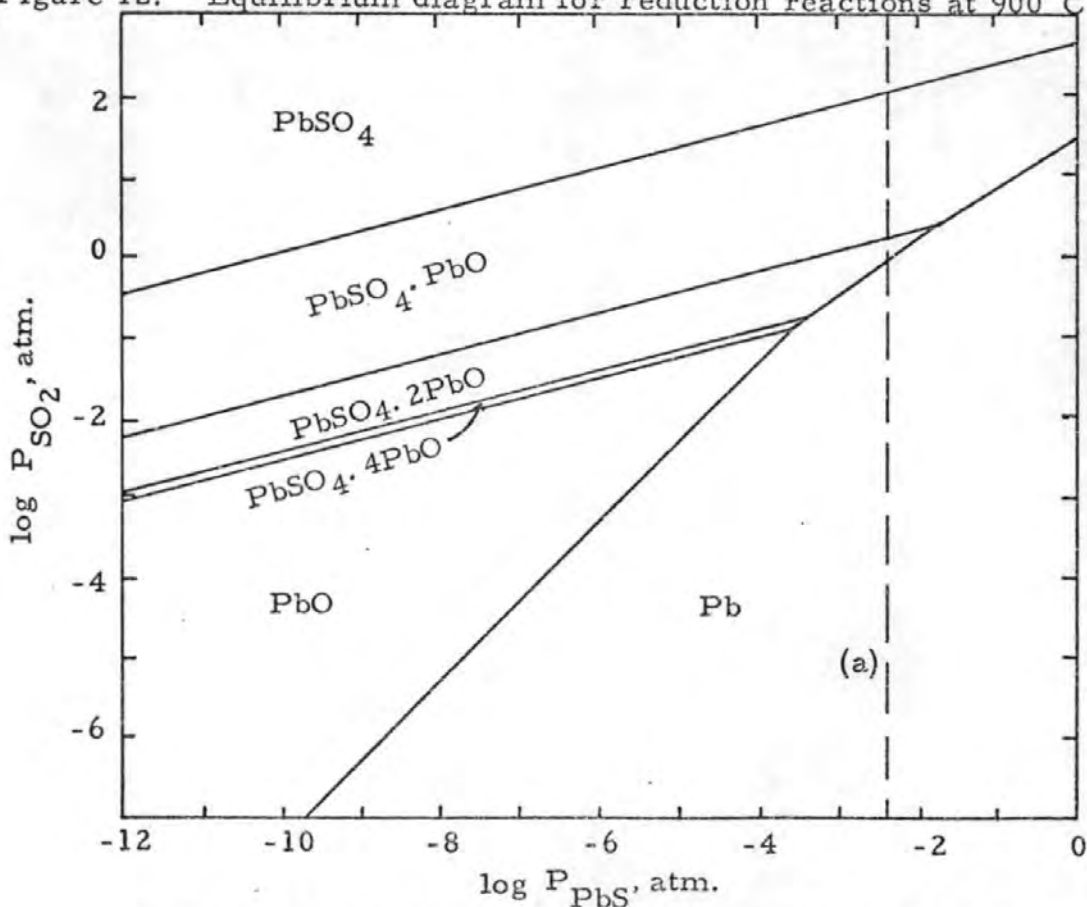
The dotted line (a) represents the maximum vapour pressure of PbS at 900°C

- 17 -

Figure 13. Equilibrium diagram for oxidation reactions at 1100°C
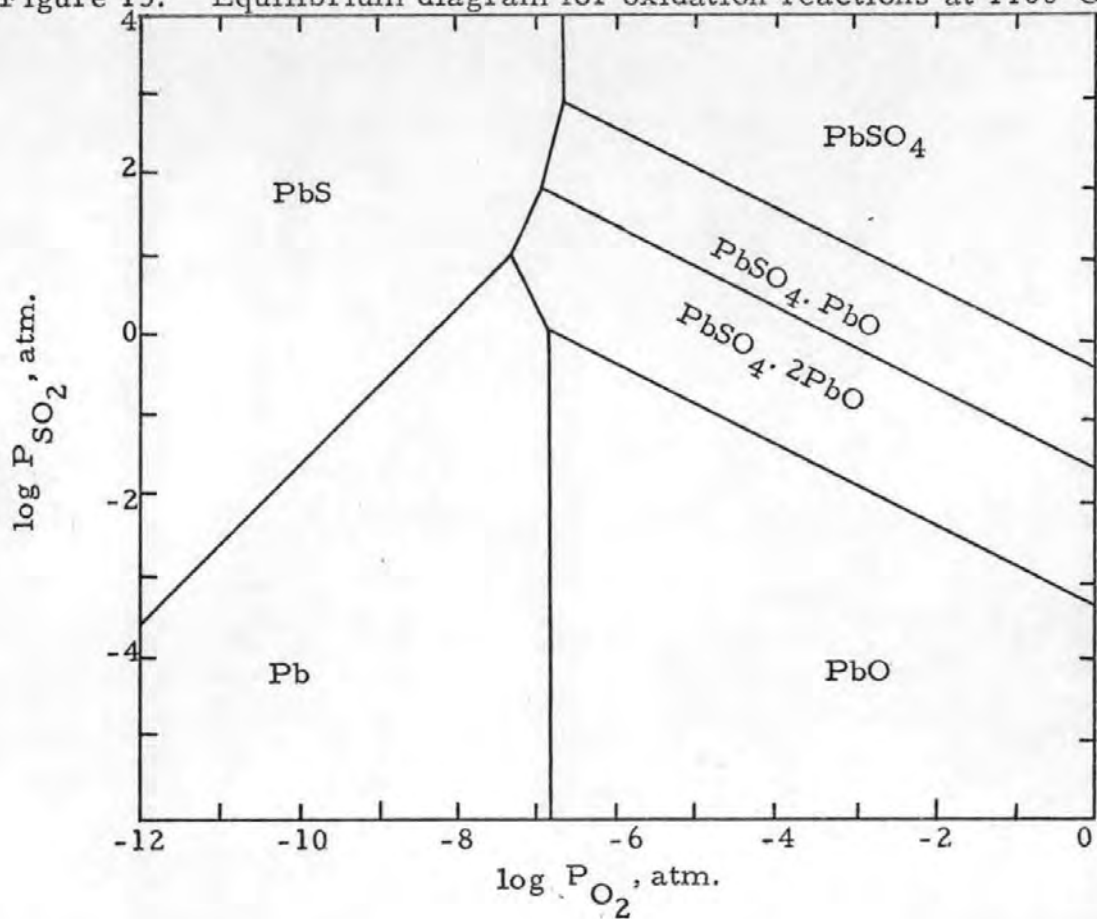
Figure 14. Equilibrium diagram for reduction reactions at 1100°C
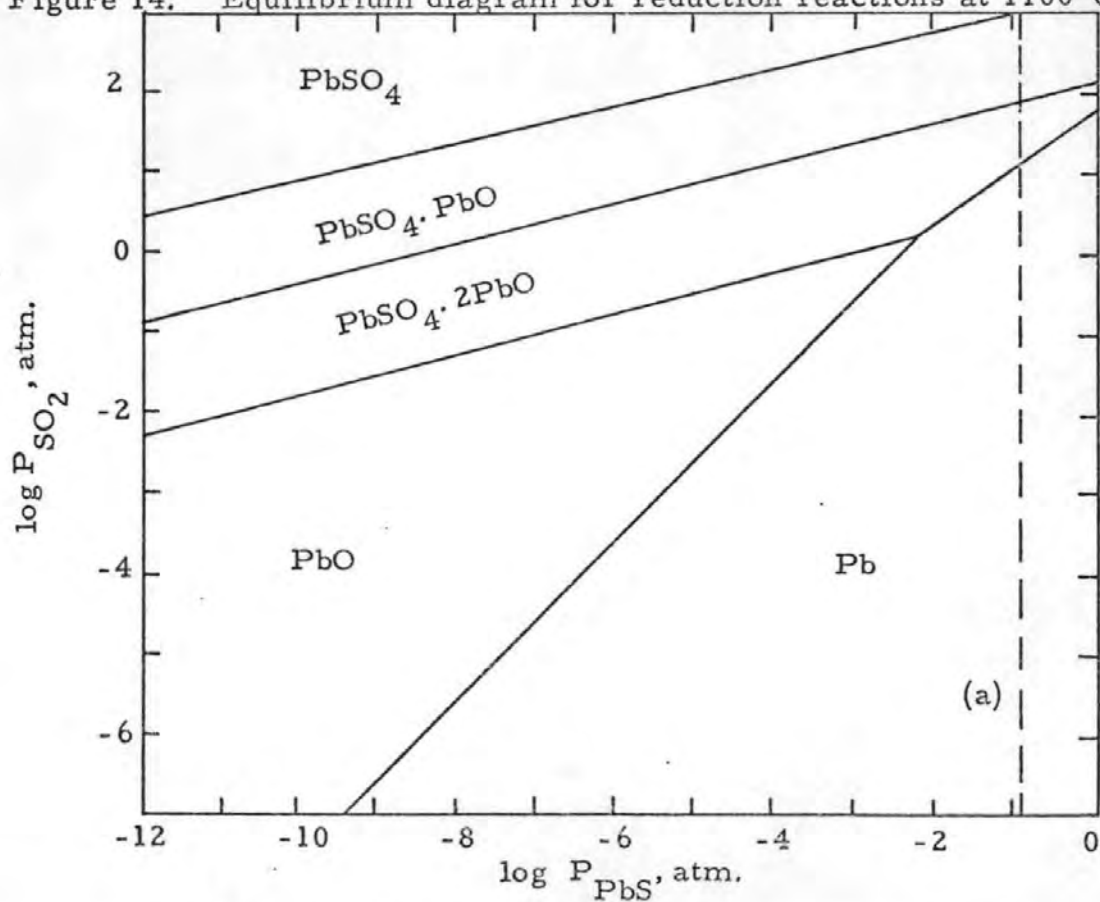
The dotted line (a) represents the maximum vapour pressure of PbS at 1100°C.

Figure 15.   Equilibrium diagram for oxidation reactions at 1200°C
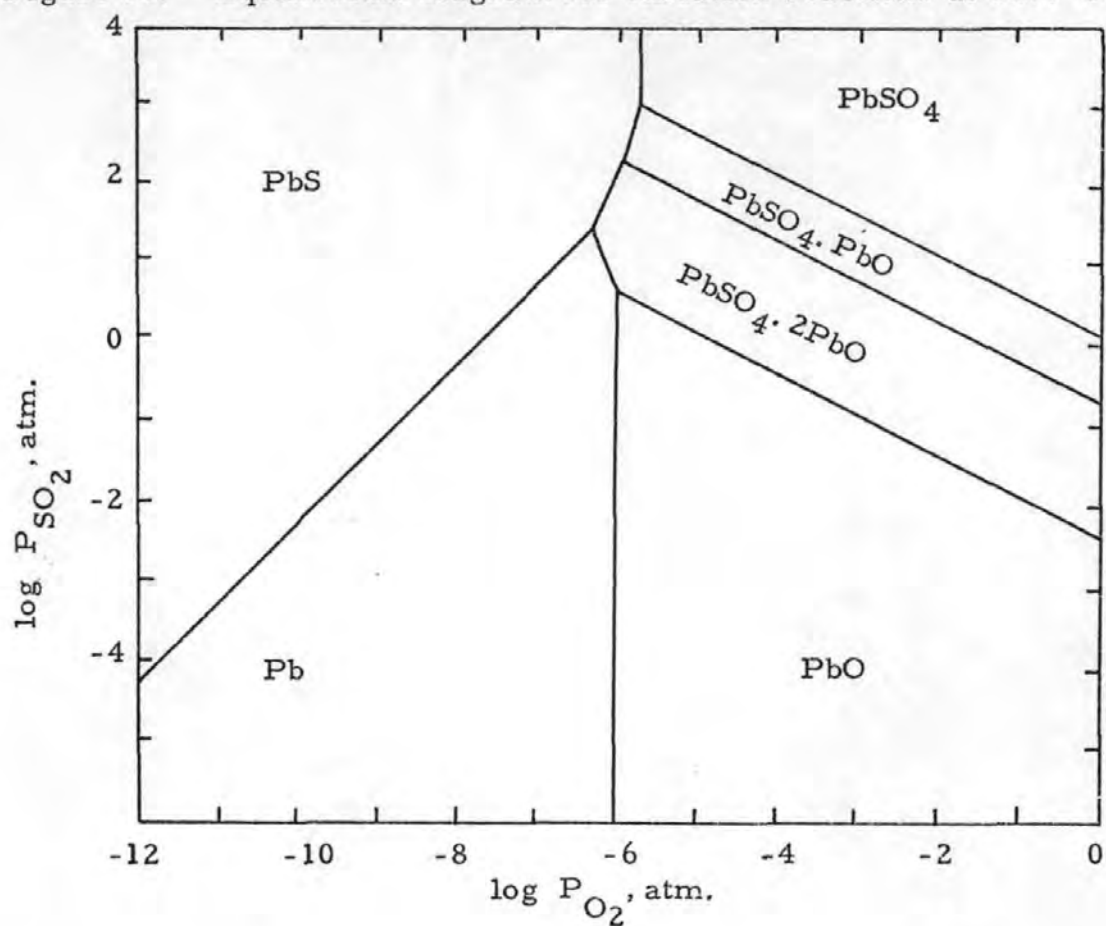
Figure 16.   Equilibrium diagram for reduction reactions at 1200°C
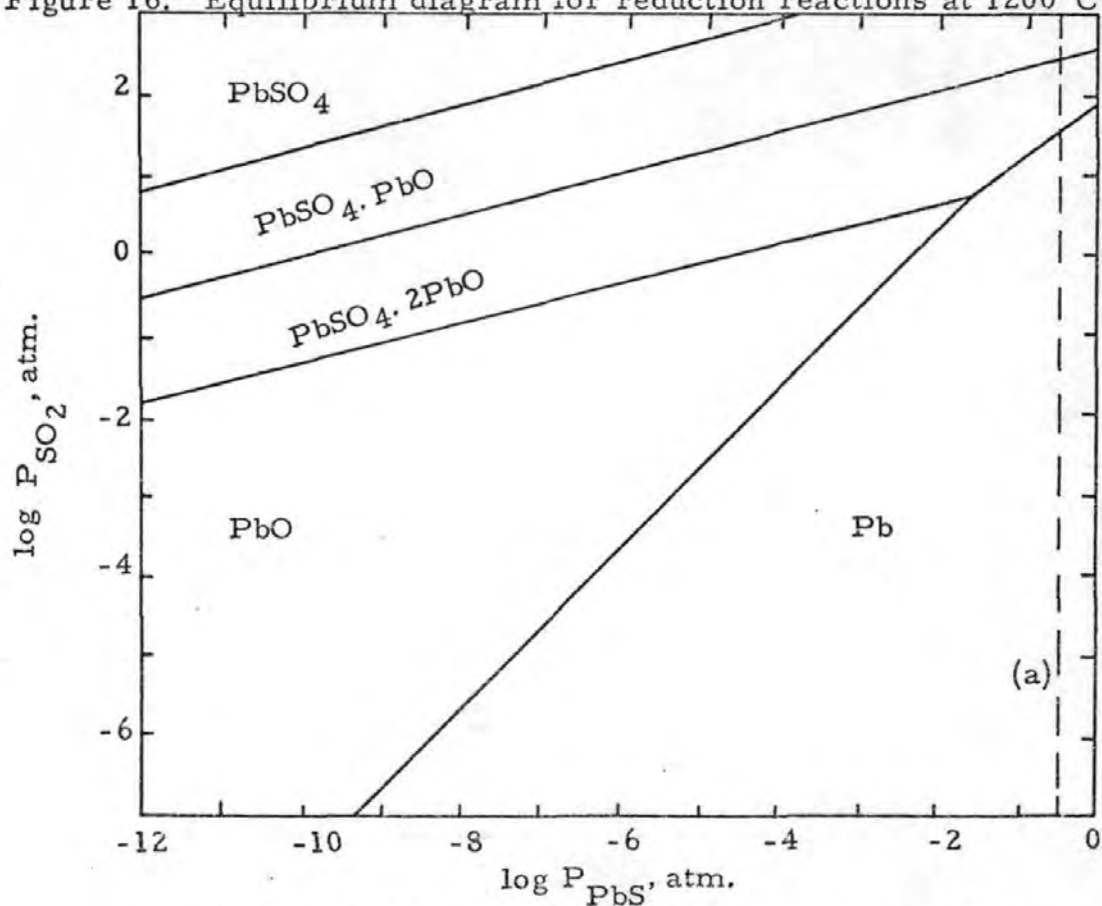
The dotted line (a) represents the maximum vapour pressure of PbS at 1200°C
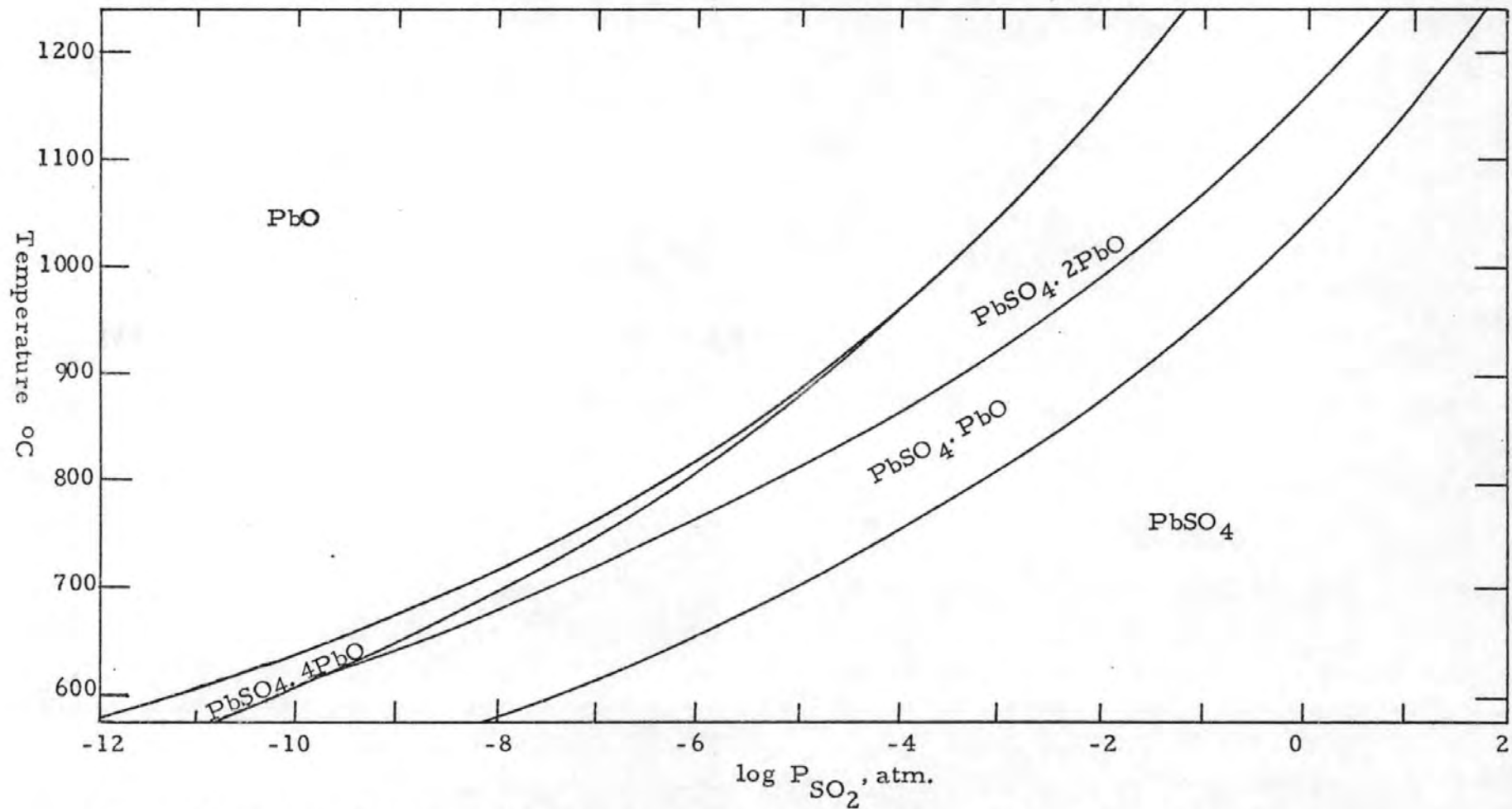
Figure 17.   Vertical section of 0.21 atm. oxygen partial pressure of the three-dimensional equilibrium diagram for oxidation reactions

with the following sulphation reactions also occurring:-

$$3(PbSO_4.4PbO) + O_2 + 2SO_2 = 5(PbSO_4.2PbO)$$

$$4(PbSO_4.2PbO) + O_2 + 2SO_2 = 6(PbSO_4.PbO)$$
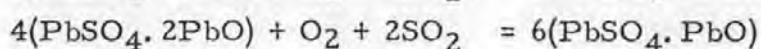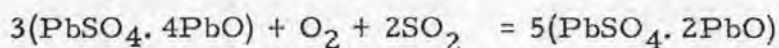
At 1100°C both oxidation and reduction reactions would occur simultaneously with lead sulphide vapour involved thus:-

$$3PbS(vap) + 2(PbSO_4.PbO) = 7Pb + 5SO_2$$

$$or \quad 2PbS(vap) + PbSO_4.2PbO = 5Pb + 3SO_2$$
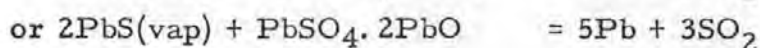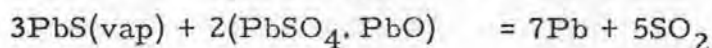
Lead sulphate is the highest oxidation product, the free energy of the reduction reaction to $PbSO_4.PbO$ becomes negative at 490°C; direct reduction to other compounds is not thermodynamically feasible until 700°C (Figures 10, 14).

Another experiment performed by Tuffley & Russell[13] at 800°C between lead sulphate and lead sulphide vapour in a nitrogen atmosphere produced metallic lead; the reaction mechanism put forward is:-

$$PbS(vap) + 7PbSO_4 = 4(PbSO_4.PbO) + 4SO_2$$

$$PbS(vap) + 10(PbSO_4.PbO) = 7(PbSO_4.2PbO) + 4SO_2$$

$$2PbS(vap) + PbSO_4.2PbO = 5Pb + 3SO_2$$
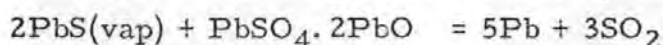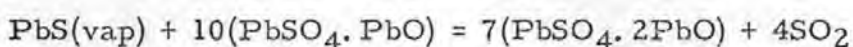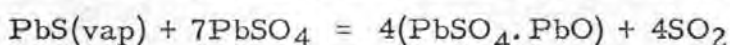
Tuffley & Russell[13] conclude that a necessary condition for lead formation, when lead sulphide is roasted in air, is that the partial pressure of lead sulphide must be sufficient to allow the reaction to proceed in contact with gases containing up to 0.21 atm sulphur dioxide; 825°C is the minimum temperature at which these conditions are fulfilled. This is in close agreement with the theoretical findings of Wittung[2], in that, 850°C is the minimum temperature for lead formation.

Gray et al[15] studied the kinetics of sulphation of single crystals (3-4 mm) of lead sulphide between 696-800°C in known composition gas atmospheres using a thermobalance technique. An equation was derived on the basis that diffusion through the product layer was the major rate-controlling step. Thus the rate of sulphation was linearly related to the log of the sulphur trioxide partial pressure. Gold marker experiments showed that the sulphate layer grows outwards by ion diffusion.

Vander Poorten & Meunier[16] found $PbSO_4.PbO$ is produced on heating 44-74 μm lead sulphide in air on a thermobalance between 550-650°C, with the reaction proceeding according to the equation:-

$4PbS + 7 O_2 = 2(PbSO_4 \cdot PbO) + 2SO_2$ and following a parabolic rate law being almost complete at $650^{\circ}C$. The kinetics of the oxidation are due to the diffusion of oxygen and sulphurdioxide through the oxidized layer. Between $700-750^{\circ}C$ the reaction goes further and follows a linear rate law for the first 20 min, the kinetics probably depending upon sulphation at lower temperatures, primarily forming $PbSO_4 \cdot PbO$ and PbO. After 25 min, the only reaction product is $PbSO_4 \cdot PbO$ with little diffusion through the oxidized layer, and recrystallization of $PbSO_4 \cdot PbO$ occurring. After 90 min at $700^{\circ}C$, $PbSO_4$ appears for the first time, forming on the lead sulphide underneath the $PbSO_4 \cdot PbO$ by a secondary reaction with SO_2 according to the equation:-

$$2(PbSO_4 \cdot PbO) + 2SO_2 + O_2 = 4PbSO_4$$
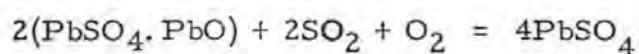
From $815-860^{\circ}C$ the main reaction is direct oxidation of lead sulphide to lead

i.e. $\quad PbS + O_2 \longrightarrow Pb + SO_2$
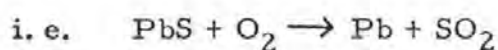
At $860^{\circ}C$ this direct oxidation follows a linear rate law virtually to completion. When the reaction was quenched at $860^{\circ}C$, lead and very small quantities of $PbSO_4 \cdot PbO$ and PbO were found. The resulting lead may be further oxidized to PbO at $860^{\circ}C$, following a linear rate law.

Culver et al[17] obtained similar weight-time curves for the $PbSO_4 \cdot PbO$ formation, and for the formation of lead and lead oxide.

Oxidation of $<74\ \mu m$ galena in air $(3.841h^{-1})$ was carried out by Margulis & Ponomarev[18]. In contrast to Tuffley & Russell[13], and Vander Poorten & Meunier[16], they found that between $600-650^{\circ}C$ lead sulphate is produced, at $680^{\circ}C$ $PbSO_4 \cdot PbO$, and by $750^{\circ}C$ mainly $PbSO_4 \cdot PbO$ and $PbSO_4 \cdot 2PbO$ with a little $PbSO_4$, at $830^{\circ}C$ a basic sulphate-lead oxide eutectic melt; at $900^{\circ}C$ after 10 min lead, a little lead oxide and basic sulphate, whilst after 60 min substantially lead oxide.

Ponomarev & Polyvannyi[19] oxidized $62-74\ \mu m$ galena in air $(10\ 1h^{-1})$ and found $PbSO_4$ and PbO (or $PbSO_4$ and $PbSO_4 \cdot PbO$) at $400^{\circ}C$, and traces of lead at $550^{\circ}C$ resulting from a reaction between lead sulphide and its oxidation products. The amount of lead reached a maximum after 5 min between $700-850^{\circ}C$ and was then oxidized to lead oxide.

Under similar conditions (air flow 27 1h[-1]) Chizhikov et al[20] found lead formation maximized at 800°C.   Further studies on the oxidation of galena (< 74 μm) in air (6 1h[-1]) at 550-800°C were reported by Polyvannyi[21].

Ponomarev & Polyvannyi[19] calculated the degree of desulphurization as a percentage (proportion of lead sulphide converted to sulphur free products) of 62-74 μm galena oxidized in air (10 1h[-1]) from 400-1000°C.   The "percentages" for various reaction times and temperatures are given in Table 1.2b.

Table 1.2b

Time min	400°C	550°C	700°C	850°C	900°C	1000°C
5	-	-	25.90	79.20	93.70	99.00
10	-	-	29.00	88.70	95.90	99.80
15	0.96	6.30	36.70	89.80	97.00	100.00
30	1.20	9.05	40.70	92.10	-	-
60	1.45	10.09	41.30	96.70	-	-

Table 1.2b gives the percentage desulphurization for various reaction times and temperatures for 62-74 μm galena oxidized in air flowing at 10 1h[-1].   Similar studies have been made by Margulis & Ponomarev[22].

According to Ponomarev & Polyvannyi[19] the rate of oxidation of 62-74 μm galena in air (10 1h[-1]) at 400°C is low.   At 550°C the rate-time curve has a maximum after 2 min, then remains constant, with the maximum oxidation rate occurring at 700°C (greatest weight gain). As the temperature rises, the rate of initial oxidation increases.   A relationship between temperature and oxidation rate was derived:-

$$\log \; r_{max} = A - \frac{B}{T}$$ from 400-700°C   where A = 4.22, B = 2240 K,

and from 700-1000°C, A = 2.65, B = 728 K.   The activation energies in the studies were 46.67 and 13.93 k J mol^{-1} respectively; below 700°C the rate determining step is chemisorption, and above 700°C is diffusion of oxygen.

Further experiments on the oxidation rate performed by Polyvannyi[21] between 550-850°C, and Culver et al[17] obtained rate constants for the oxidation of powdered galena from 767-912°C.

Ponomarev & Polyvannyi[19] reports on the course of oxidation of powdered galena in air with continually rising temperature (420-1050°C).

1.2.1 Dependence upon Oxygen Concentration
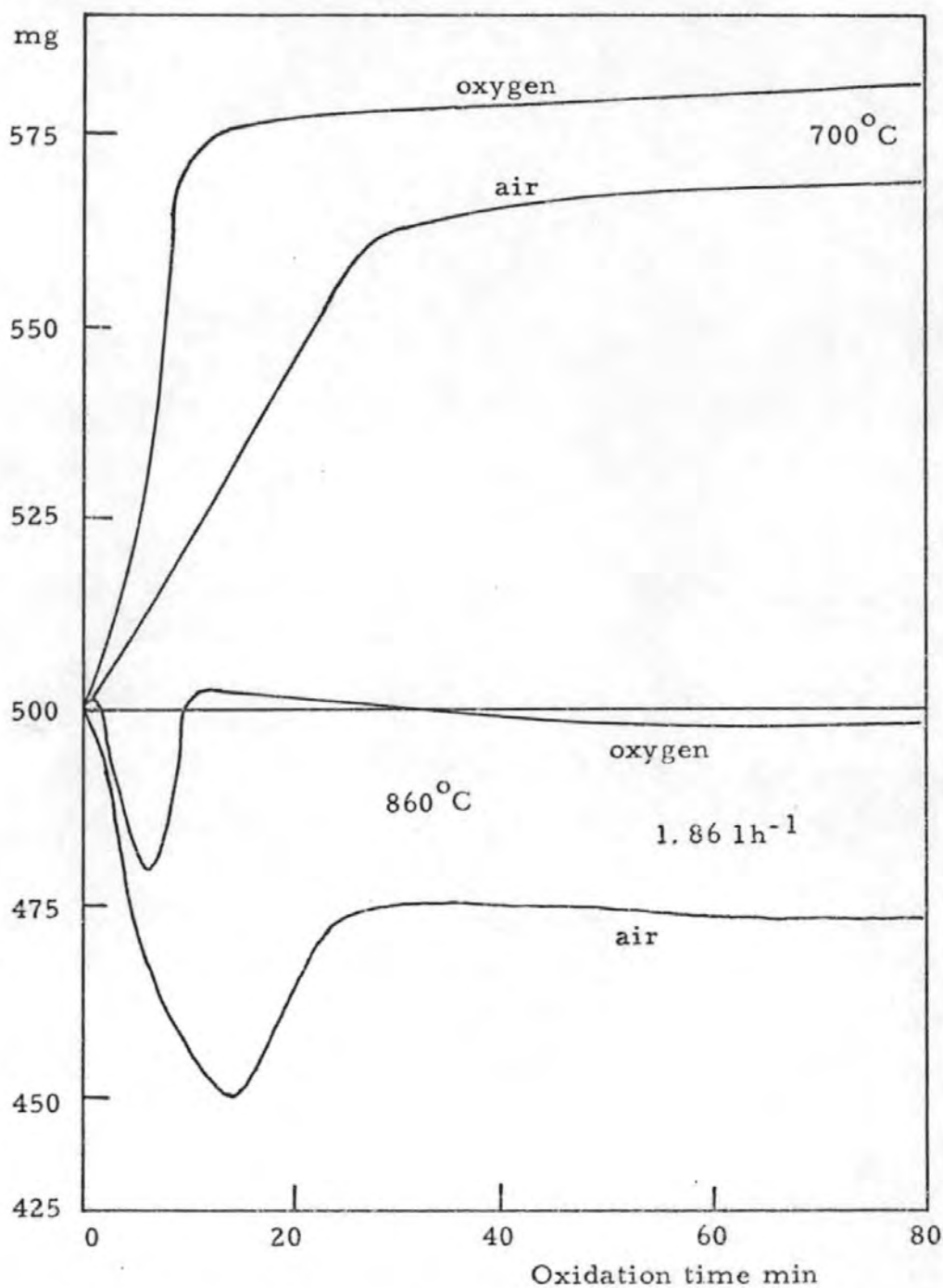
Figure 18   Isothermal curves for the oxidation of 74 µm PbS in air and oxygen

Figure 18 shows the thermogravimetric curves for the oxidation of 44-74 µm lead sulphide in air and oxygen (1.86 1h⁻¹). They show that at both 700 and 860°C increasing the oxygen partial pressure

increases the rate of sulphation. Analysis shows that with pure oxygen, the percentage of lead sulphate produced is considerably increased, but $PbSO_4.PbO$ remains the main oxidation product. After 90 min at 860°C the oxidation to metallic lead and lead oxide is more rapid in oxygen than air, according to Vander Poorten & Meunier[23].

With 74 μm galena in a gas flow of 6 1h^{-1} the following results were obtained by Polyvannyi[21].

Table 1.2c

Oxygen %	21	30	50	100
550°C 60 min	12.76	13.85	19.45	23.04
700°C 5 min	35.47	42.42	50.00	54.74
850°C 5 min	50.78	58.44	66.20	71.65

Table 1.2c shows the variation in percentage lead oxide formed against oxygen concentration.

Polyvannyi[21] inferred that increasing the oxygen concentration raised the reaction rate at all temperatures. Between 550 and 700°C both the formation of oxide and sulphate increases with increasing oxygen concentration. At 850°C the lead sulphate produced begins to react with the remaining lead sulphide giving lead. Metallic lead was found between 700-850°C, and at a given temperature the amount decreases as the oxygen concentration is increased. Polyvannyi[21] gives the full details of the proportions of lead sulphate, lead oxide and lead in oxidations using 21, 30, 50 and 100% oxygen at 550, 700 and 850°C from 5 to 60 min.

Kinetic experiments performed by Polyvannyi et al[24] in a flow reactor with galena and oxygen enriched air containing 21, 25, 29, 35 and 95% oxygen at a series of temperatures show the reaction rates at a maximum between 600-800°C. The results obtained confirm the earlier findings of Ponomarev & Polyvannyi[19], in that, above 700-800°C there is a 4-fold decrease in activation energy as the rate controlling process changes from chemisorption to diffusion control. Polyvannyi et al[24] conclude by pointing out that it would be advantageous in an

industrial process to use 29% oxygen-enriched air. Polyvannyi[21] also investigated the degree of desulphurization of 74 μm lead sulphide with oxygen content at a flow of 6 $1h^{-1}$. Table 1.2d summarizes the results at 700°C.

Table 1.2d

Reaction time min \ Oxygen %	21	30	50	100
5	25.40	37.00	40.20	43.00
15	36.25	45.50	52.70	56.10

Table 1.2d gives the variation in percentage desulphurization with oxygen concentration and reaction time at 700°C.

Increasing the oxygen concentration, in general, results in an increase in desulphurization, and oxidation rate. At 550°C increasing the oxygen concentration leads to only a small increase in desulphurization and oxidation rate. At 700°C it is far more noticeable, but the increase in desulphurization by raising the oxygen content from 21 to 30% is greater than raising it from 50 to 100%. The reaction order with reference to oxygen is virtually zero at temperatures < 700°C.

Chizhikov et al[20] found at higher oxygen concentrations lead oxide, with the quantities of lead sulphate and lead in many cases reaching a maximum at 800-900°C, with the phases being subsequently, wholly or partly consumed by the reactions:-

$$PbSO_4 + PbS = 2Pb + 2SO_2$$
$$or \quad 2Pb + O_2 = 2PbO$$
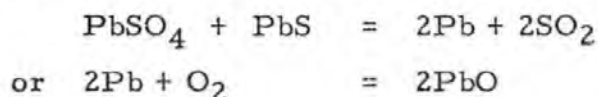
Table 1.2e shows the products obtained with 74 μm galena in a stream of pure oxygen after 15 min and 1 h at 550, 700 and 850°C. A more comprehensive table is given by Polyvannyi[21].

Table 1.2e

	Unreacted PbS	% PbSO$_4$	% PbO	% Pb	% Desulphurization
550°C 15 min	75.30	12.30	13.20	-	14.00
60 min	58.15	18.85	23.04	1.20	25.10
700°C					
15 min	31.80	14.84	54.74	1.44	56.10
60 min	20.21	12.82	64.15	1.00	66.09
850°C					
15 min	3.30	4.35	89.21	2.38	92.45
60 min	1.06	1.44	96.63	-	97.10

Table 1.2e gives the percentages of unreacted lead sulphide and proportions of lead sulphate, lead oxide and lead produced at a series of reaction temperatures after 15 and 60 min in pure oxygen.

1.2.2   Dependence upon Gas Velocity

A thermogravimetric study by Vander Poorten & Meunier[23] using 44-74 µm galena with two different gas flows (0.22, 1.86 1h^{-1}) found at 700°C both the oxidation rate to PbSO$_4$.PbO and the quantity of PbSO$_4$.PbO produced decreased with decreasing gas velocity, see Figure 19.   In the second period of oxidation, the rate is dependent upon the diffusion of gases through the PbSO$_4$.PbO layer and the gas velocity no longer affects the reaction rate.   At 860°C the rate of reduction of lead sulphide to lead is lowered with decreasing gas velocity.   As the lead is formed it is oxidized to lead oxide, leading to the weight gain (A) Figure 19.
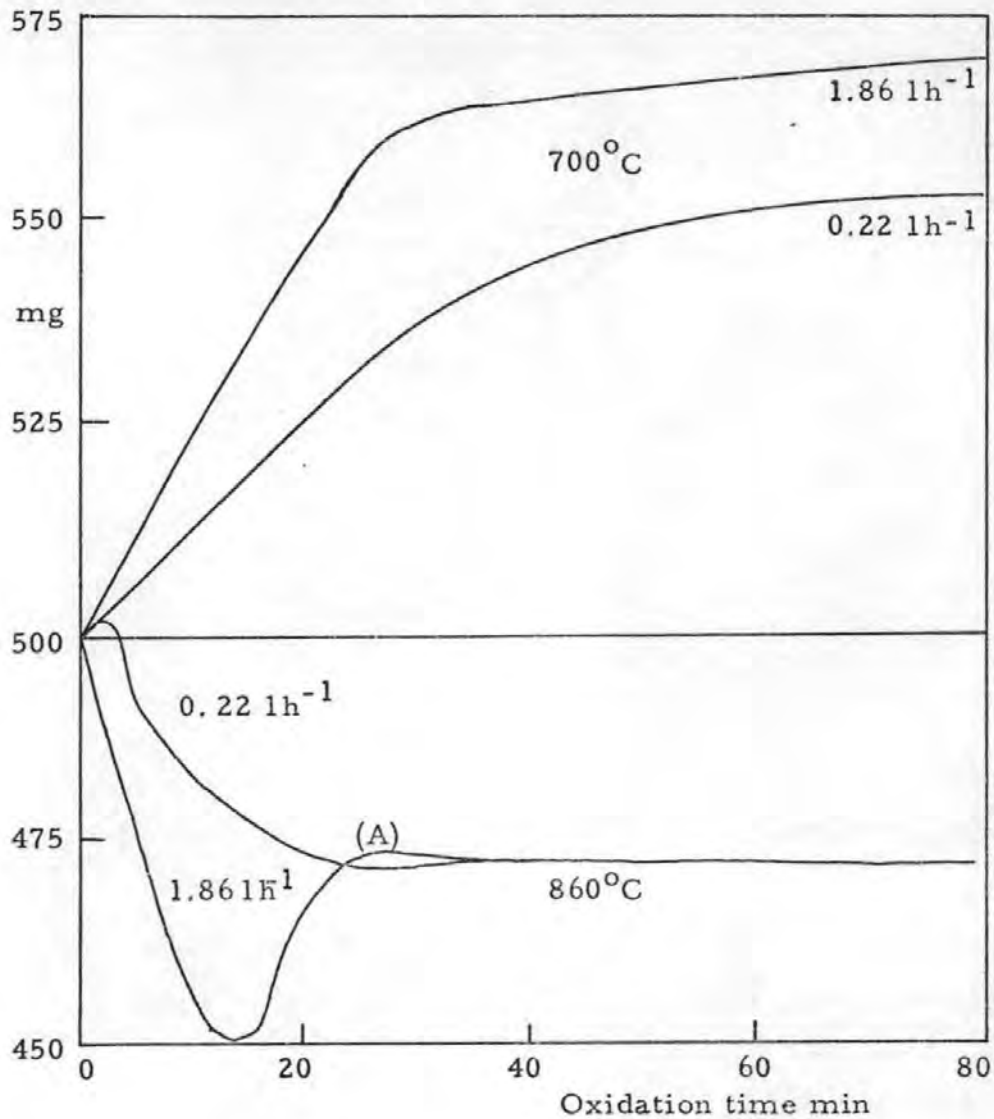
Figure 19   Isothermal curves for the oxidation of PbS in air
flowing at 0.22 and 1.86 $1h^{-1}$

According to Ponomarev & Polyvannyi[19], gas velocities from
1.5 to 10 $1h^{-1}$ have no effect on the oxidation rate of 62-74 μm galena
at 400-550°C.

The relation log r_{max} = A - $\frac{B}{T}$ between temperature and
maximum rate of oxidation, yields activation energies of 48.59, 48.40
and 46.67 kJ mol^{-1} in the temperature range 400-700°C with gas
velocities of 1.5, 3.5 and 10 $1h^{-1}$; (A = 3.08, 3.66 and 4.22; B = 2540,
2530 and 2240 K) respectively.   This constant value for the activation
energy shows that within this temperature range the reaction mechanism
is independent of gas velocity.   Above 700°C the reaction does not solely
depend on gas velocity but also on the diffusion of oxygen, although the

higher the gas velocity the greater the oxidation rate and degree of desulphurization.

The difference in the assertions of Vander Poorten & Meunier[23] over the lack of dependence of the oxidation rate on the gas velocity in the diffusion region may be due to the different gas velocities used.

Oxidation rate-time curves for 700-900°C with three different gas velocities are given in the original[19]. With the higher gas velocities, lead oxide increases above all other phases. In the oxidation of 62-74 μm with air flowing at 1.5, 3.5 and 10 $1h^{-1}$, the percentage lead sulphide converted to lead oxide at 700 and 850°C in 15 and 60 min is given in the following Table 1.2f.

Table 1.2f

Gas velocity $1h^{-1}$ Temp Time	1.5	3.5	10
700°C 15 min	20.00	27.20	34.69
60 min	25.68	32.00	41.00
850°C			
15 min	23.98	59.62	82.65
60 min	50.52	86.19	95.50

Table 1.2f shows the percentage lead sulphide converted to lead oxide at 700 and 850°C after 15 and 60 min.

The amount of lead sulphate only marginally increases with increasing gas velocity, whilst the quantity of lead declines with increasing gas velocity.

Very similar rate/time curves were achieved when the air passed through or over the sample. At 400°C the reaction rates were the same. At higher temperatures especially above 700°C, Ponomarev & Polyvannyi[19], found the maximum rate of oxidation was lower, desulphurization slower, and the quantities of oxidation products smaller, when the air passed over the sample.

The use of sintered pastilles of lead sulphide in air (1.86 $1h^{-1}$) results in the reaction to $PbSO_4$. PbO on the surface, and lead sulphate inside. At 780°C the remaining lead sulphide and sulphate react to give lead and sulphur dioxide. The lead layer prevents direct oxidation

of lead sulphide to lead oxide with oxygen according to Vander Poorten & Meunier[25]. Lead oxide is unstable in the presence of lead sulphide yielding lead and sulphur dioxide. Thus the presence of lead sulphide stabilizes the lead against oxidation of oxygen, and only when all the lead sulphide is converted to lead does lead oxide appear on the surface of the molten lead.

Spasov et al[26] investigated the oxidation of briquettes of lead sulphide in air (30 lh^{-1}) employing a thermal balance, and found between 300-650°C the briquettes weight increased due to preferential formation of sulphates. Above 390°C desulphurization begins, and above 650°C increases very rapidly with temperature. The activation energy was calculated from the desulphurization curves on the basis of the relation derived by Spasov & Machov[27],

$$Q = k (t^2 - \frac{t^2}{2u})$$

where Q = desulphurization in time t

u = time for complete oxidation of the briquette

k = rate constant for the process

which gave a value of 44.92 kJ mol^{-1}. The composition of a new phase $PbSO_4.PbO$ was established, and concluded to be a product of the reaction of lead oxide and lead sulphate.

Tuffley & Russell[13, 14] oxidized synthetic galena ($\sim$ 6mm) in air (9 lh^{-1}) and found the oxidation products $PbSO_4.PbO$ and $PbSO_4.4PbO$ at temperatures from 600-1000°C. Lead oxide was only found at 600°C; at 700°C it disappeared. Lead sulphate was not observed at any temperature. The fact that Tuffley & Russell[13, 14] in contrast to Vander Poorten & Meunier[23] found no lead sulphate, may be due to the higher rate of air flow, and removal of the sulphur dioxide formed before sulphation could occur.

1.2.3   The Effect of Particle Size

Vander Poorten & Meunier[23] studied the oxidation lead sulphide of three different particle sizes (44-74 μm, 74-297 μm, 297-840 μm) in air (1.86 lh^{-1}) and found increasing the particle size decreases the initial quantity of $PbSO_4.PbO$ formed at 700°C. Thus the reaction rate is a function of accessible surface. In the second period of the

oxidation, the rate is dependent on diffusion, but independent of particle size.

Ponomarev & Polyvannyi[19] oxidized lead sulphide of three different size ranges (62-74 μm, 143-147 μm, 250-500 μm) in air flowing at 10 lh^{-1}.

The following Table 1.2g shows the values for A and B and the activation energy in two temperature ranges with three particle size ranges. They used the formula $\log r_{max} = A_{(1)} - \frac{B}{T}_{(1)}$ to find the maximum rate, and concluded that the small variation in activation energy, Q, within each temperature range proved that the oxidation mechanism is independent of the particle size. The smaller the particles the greater was the quantity of oxidation product, especially lead oxide.

This is confirmed by Saito[28] and Friedrich[29].

Table 1.2g

	400°C - 700°C				700°C - 1000°C		
	62-74 μm	143-147 μm	250-500 μm		62-74 μm	143-147 μm	250-500 μm
A_1	4.22	3.35	3.18	A_2	2.65	2.60	2.64
B_1	2440 K	2650	2775	B_2	728 K	800	888
Q_1	46.67 $kJ\,mol^{-1}$	50.64	52.99	Q_2	13.92 $kJ\,mol^{-1}$	15.31	16.98

Table 1.2g shows the variation of constants A and B and activation energy Q with particle size in the temperature ranges 400-700°C and 700-1000°C.

1.2.4 Comparisons of Natural and Synthetic Galena

Vander Poorten & Meunier[23] compared the oxidation of synthetic and natural galena (44-74 μm), and found at 700°C natural galena sulphated considerably more slowly and less completely than the synthetic material. By ~770°C the oxidation rates are similar, and at 860°C the two reactions proceed at the same rate.

The oxidation of 52-74 μm natural, crystalline synthetic, and amorphous synthetic galena with air (10 lh^{-1}), after 15 min at 700°C gave the following percentage conversions of lead sulphide to lead oxide 34.7, 35.0, 52.8% respectively. At 800°C, the comparable figures

are 82.6, 85.3, 94.9%. Thus, the reaction rates are similar in the first two cases, but the amorphous galena reacts appreciably faster at any given temperature according to Polyvannyi[30].

1.2.5 The Effect of Sulphur Dioxide on Oxidation

In further studies Polyvannyi[31] oxidized < 74 μm galena in air (6 lh^{-1}) between 550-850°C with sulphur dioxide concentrations of 4-100%. With only 4-8% sulphur dioxide the oxidation rate is reduced by 12%, and with 100% the oxidation practically ceased. Between 550-700°C the effect of sulphur dioxide addition is most marked. This is explained by the fact that sulphur dioxide is more easily adsorbed onto the lead sulphide than oxygen, and thus crowds the active sites. At higher temperatures the adsorption decreases, and the effect of sulphur dioxide is less. The higher concentrations of sulphur dioxide lead to a greater proportion of lead sulphide being converted to lead sulphate especially between 550-700°C.

Table 1.2h

Sulphur dioxide percentage	0	4	8	12	20	50
% Lead Sulphate	15.72	16.95	17.95	20.47	21.05	23.43
% Desulphurization	41.87	42.95	40.20	39.20	37.40	33.50

Table 1.2h shows the percentage lead sulphate formed, and desulphurization with various concentrations of sulphur dioxide at 700°C after 60 min.

Later work by Gaivoronskii & Polyvannyi[32] using sulphur dioxide concentrations from 2-100% in air (6 lh^{-1}) at temperatures from 500-1000°C found similar trends, i.e. gaseous products containing > 10% sulphur dioxide slowed down the process. An equation was derived relating the rate of oxidation with air/sulphur dioxide ratio and temperature; and it was concluded that the roasting of lead sulphide ores would proceed without appreciable accumulation of sulphate if the sulphur dioxide is < 10%.

Further results on the oxidation of galena in a mixture of 95% air, 5% sulphur dioxide are given by Saito[33].

Statements on the relationship between the oxidation products and sulphur dioxide content of the air at various temperatures are given

by Trifonov[34].

Culver et al[17] oxidized 350-420 μm galena in a stream of O_2-N_2-SO_2 gas mixtures flowing at 36-60 1h^{-1}. At 673-787°C with 5% oxygen and 1% sulphur dioxide the only product is lead sulphate, agreeing with the phase diagram (Figure 10). The lead sulphate formation follows a parabolic rate law, $w^2 = Kt + c$

where w = weight increase in time t

t = time in min.

K and c are constants

Using an O_2-N_2-SO_2 gas mixture with 0.003% sulphur dioxide at 780°C, $PbSO_4.PbO$ is formed, and the rate constants are - with 5% oxygen, 5.7×10^2; 10% oxygen, 3.0×10^2; 20% oxygen, 2.35×10^2; 50% oxygen 5.7×10^1 kg^{2}m^{-4} min^{-1}. Thus the oxidation rate is inversely proportional to the oxygen partial pressure. At >50% oxygen practically no reaction takes place.

Vander Poorten & Meunier[23] report that the oxidation of galena in air in a closed space favours the formation of lead sulphate when sulphur dioxide is added.

Further information on the stability of lead sulphate in higher sulphur dioxide concentrations is given by Kirkwood & Nutting[35], and by Collett-Descostils[36].

Paduchev et al[37] studied the reaction between sulphur dioxide and lead sulphide containing ^{35}S at 650 and 700°C. In a stream of sulphur dioxide, the radioactivity gain of the sulphur dioxide was slight. In a closed system the sulphur dioxide became appreciably radioactive, with the radioactivity of the lead sulphide being reduced. The results were interpreted on the assumption that lead oxide is formed in the initial stage by the reaction of lead sulphide and sulphur dioxide, and the lead oxide reacts with the sulphur dioxide to form lead sulphite which disproportionated to give lead sulphate and lead sulphide.

1.2.6 Low Temperature Oxidation in Dry Air

Lead sulphide prepared from hydrogen sulphide and lead acetate solutions contain excess lead and free sulphur according to Reuter & Stein[38], and is more easily oxidized than the lead sulphide prepared by the decomposition of lead thiourea in alkaline solution, which

contain excess sulphur. The lead sulphide, with excess sulphur, increased in weight by 0.36% at 100°C in 3 months, whereas the lead sulphide with excess lead increased by 15% at 100°C in 24 days. Similar differences are noticeable at 200°C. At 400°C both are rapidly converted to lead sulphate.

Hillenbrand[39] investigated the reaction of lead sulphide with oxygen, and noted a reaction at room temperature. Measurements made above 100°C found that the reaction rate was directly proportional to the surface area of lead sulphide, oxygen pressure and inversely proportional to the lead sulphate product layer for oxygen concentrations < 0.4 mole per mole of lead sulphide.

Oxidation of lead sulphide in air between 200-350°C was studied by Kirkwood & Nutting[40] by using electron diffraction of thick films and galena surfaces. Between 200-300°C the film is composed of very small crystallites of lead sulphate initially, this being followed by the formation of oxide in the form of needles; after a time, $PbSO_4 \cdot 4PbO$ is obtained. The proposed mechanism is that after the continuous film is formed, lead ions diffuse to the surface leading to the formation of lead oxide, and sulphur accumulates in the kernel. The sulphur pressure increases and erupts through the film of oxide permitting the formation of basic sulphate.

Hagihana[41] found 170°C to be the temperature where lead sulphate first appeared on the surface of a single crystal. At 250°C, the lead sulphate formation was rapid and after ~1 h yellow lead oxide is produced in increasing quantities. After 8h at 250°C, $PbSO_4 \cdot 4PbO$ is formed. This data agrees with the results obtained by Kirkwood & Nutting[40].

At low pressures (10^{-2} - 10^{-3} mm. Hg(1.3-.13 Pa)) and between 100-300°C $PbSO_4$ is formed, and at 350°C mainly Pb_2O. Probes heated to 500°C produced Pb_2O and lead oxide, it was assumed that under these conditions Pb_2O is converted to lead sulphate in the lack of oxygen, Hagihana[42].

At 0.2 mm. Hg(26Pa) oxygen pressure, lead sulphide is converted to lead oxide (5-40%) with the release of sulphur dioxide at 550-600°C according to Sosonovskii et al[43].

1.2.7 The Effect of Moisture on Low Temperature Oxidation

The action of moist air on lead sulphide with excess lead at $20^\circ C$ results not only in lead oxide and sulphur as with dry air, but also basic lead thiosulphate ($PbS_2O_3 \cdot PbO \cdot x H_2O$) from a secondary reaction according to Reuter & Stein[38]. Similarly Mellgren[44] describes the formation of basic thiosulphate and thiosulphate as oxidation products of the surface of galena in moist air, Leja et al[45] also found lead thiosulphate resulting from atmospheric conditions.

Percy[46] in 1870 reported the action of oxygen on moist lead sulphide at between $50-150^\circ C$; at $125^\circ C$ sulphur dioxide was detected by smell. Between $100-400^\circ C$ moist lead sulphide is oxidized to lead sulphate, at lower temperatures basic thiosulphate is produced first, but later decomposes to lead sulphate, Reuter & Stein[38].

Eadington & Prosser[47] investigated the surface oxidation of lead sulphide and found the principal oxidation product depends upon the time over which oxidation has occurred. Up to 12 h. basic lead thiosulphate is predominant with lead sulphate not appearing in significant quantities until after 4h; with increasing time lead sulphate becomes the more predominant species.

Further experiments performed by Eadington & Prosser[48] on the oxidation of precipitated lead sulphide ($15.7 \, m^2 g^{-1}$) by oxygen in water at low temperatures found the products dependent upon pH, and time of exposure. At pH 1.5 lead thiosulphate is unstable and the major product is sulphur; at pH 7.0 the major product is lead sulphate after 12 h. and at pH 9.0 is lead thiosulphate. They[48] conclude by saying that at all pH levels no detectable quantities of lead sulphate appeared until at least 5 h. oxidation.

Myuller et al[49] oxidized precipitated films of lead sulphide in air, and found washing in water leads to lead hydroxide by hydrolysis; drying at $145^\circ C$ produced lead oxide.

1.2.8 D T A Studies

Kurian & Tamhankar[50] made thermodynamic and kinetic investigations (using differential thermal analysis), of some metal sulphides, including lead sulphide.

Finely divided samples of sulphides were roasted under

controlled conditions in a recording differential thermal analyser
(Delta therm DTA equipment).

DTA thermogram of Lead Sulphide in Static Air
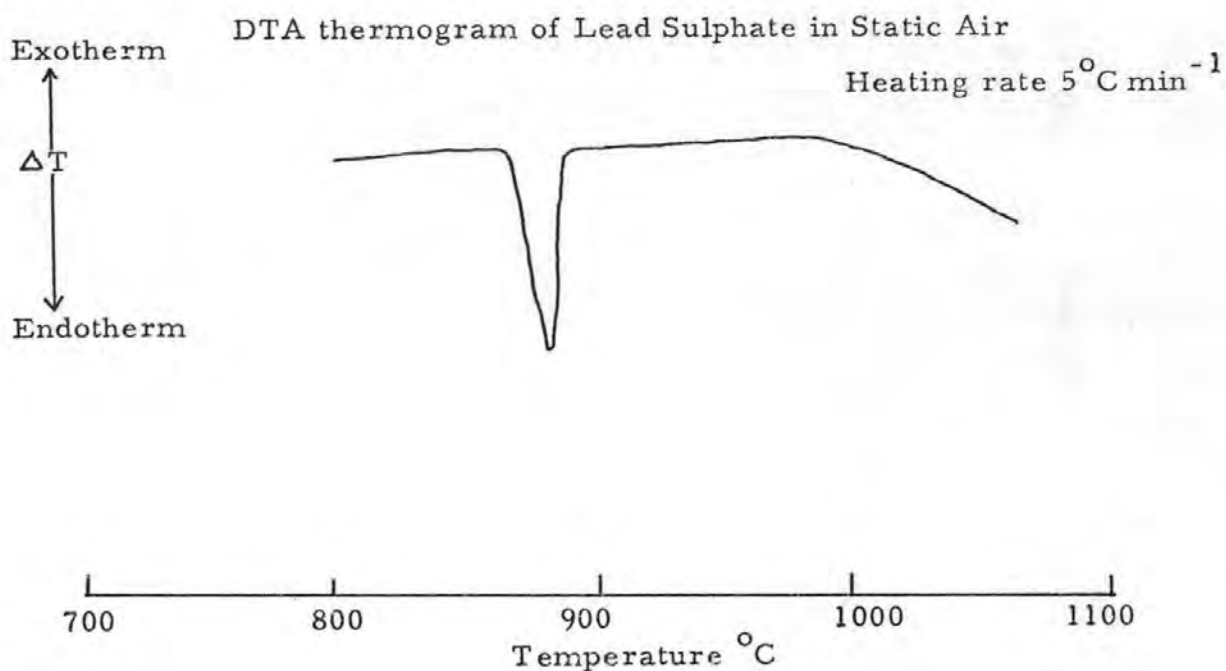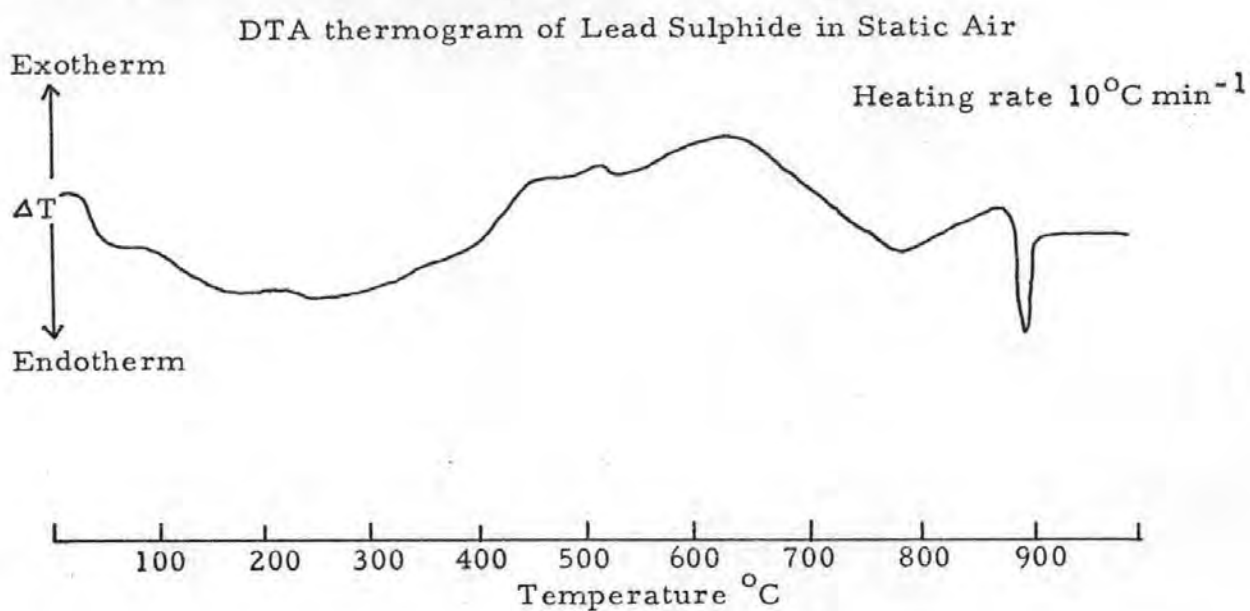
Figure 20 illustrates the DTA thermograms obtained for lead
sulphide and lead sulphate.

Lead sulphide undergoes a sluggish endothermic transition in
the range 60-360°C with maxima at 150°C and 250°C in static air.
This was followed by an exothermic transition in the range 360-725°C
with a maximum at 640°C. A further sharp endothermic transition in
the range 870-890°C occurred.

Lead sulphate displays a prominent endothermic transition in

the range 867-895°C, and another at 980-1010°C, see Figure 20; (980-1010°C transition not illustrated).

The sulphation process is invariably an exothermic reaction, hence the major exotherm in the range 360-725°C. An attempt was made to calculate the kinetics and thermodynamics of some of the transformations, giving an activation energy of 50.18 kJ mol^{-1} for the reaction $PbS + 2O_2 = PbSO_4$.

Dimitrov et al[51] determined the characteristic temperatures of several sulphides, by measuring their D.T.A. thermogram. They list three temperatures for each -

T_1 = beginning of the oxidation process

T_2 = temperature of vigorous reaction

T_3 = temperature at which the oxidation nearly goes to completion.

For lead sulphide, T_1 = 740°C, T_2 = 760°C and T_3 = 780°C.

1.2.9 Summary

Summarizing the main points of the previous work on the oxidation of lead sulphide: at low temperatures Reuter & Stein[38], Mellgren[44] and Leja[45] all report basic lead thiosulphate as the main oxidation product in moist air at room temperature. Eadington & Prosser[47] also found basic lead thiosulphate as the main oxidation product up to 12 h., for longer oxidation periods lead sulphate becomes the predominant species. Further investigations[48] conclude the oxidation product is dependent upon pH, as well as time of exposure.

Kirkwood & Nutting[40] and Hagihara[41] investigated the oxidation of thin films and single crystals respectively and reports that lead sulphate is first formed between 170-200°C and that this is followed by the formation of lead oxide at 250-300°C and $PbSO_4$. 4PbO after a time.

At higher temperatures from the phase diagrams for the oxidation and reduction reactions it is found that $PbSO_4$. 4PbO is unstable above 940°C and $PbSO_4$. 2PbO is unstable below 620°C. Tuffley & Russell[13, 14] conclude a necessary condition for lead formation is the partial pressure of lead sulphide being sufficient to allow the reduction reactions to proceed in contact with gases containing up to 0.21 atm. sulphur dioxide; 825°C is the minimum temperature at which these

conditions occur.

Vander Poorten & Meunier[23] found $PbSO_4.PbO$ to be the main oxidation product between 550-650°C; on roasting at 700°C for 25 min it was the only reaction product and only after 90 min was lead sulphate detected. Culver[17] obtained similar results. In contrast, Margulis & Ponomarev[22] found lead sulphate to be produced between 600-650°C and $PbSO_4.PbO$ was not detected until 680°C. Similar results were obtained by Ponomarev & Polyvannyi[19] in that, lead sulphate was detected first, at 400°C.

Studies on the effect of sulphur dioxide on the oxidation rates and products performed by a number of workers[31, 32] show that low concentrations of sulphur dioxide (4-8%) can reduce the oxidation rates by 10-20%. Higher percentages lead to greater proportions of sulphide being converted to sulphate.

Vander Poorten & Meunier[23] and Polyvannyi[21] agree that between 550-850°C increasing the oxygen concentration raises the rate of sulphation. Kinetic experiments performed by Polyvannyi[21] show the oxidation rate increasing with higher oxygen concentrations and overall results in an increase in desulphurization, 29% oxygen enrichment being optimum.

Ponomarev & Polyvannyi[19] inferred the gas velocity has no effect on the oxidation rate between 400-550°C. At 700°C and above Vander Poorten & Meunier[23], and Ponomarev & Polyvannyi[19] found the oxidation rate increased with higher gas velocities, even though the reaction rate is diffusion controlled above 700°C.

Both Vander Poorten & Meunier[23] and Polyvannyi[21] concluded that the particle size only affects the initial oxidation rate. Above 700°C the oxidation rate becomes independent of particle size. When comparing oxidation rates of natural and synthetic galena (44-74 μm) they[23, 21] found similar trends, i.e. the synthetic reacted more rapidly than the natural.

In practice reactions of solids which are thermodynamically feasible are often kinetically unfavourable due to sintering of reactants and products. Thus, reactivity with gases may be considered reduced at certain temperatures by the sintered material impeding the ingress of the reacting gases or the escape of gaseous products, to or from

the reaction zones or interfaces.   A short survey of the phenomenon
of sintering is now presented with particular reference to temperature
conditions in relation to the physical properties of solids generally.

1.3   SINTERING OF SOLIDS

The phenomenon of adhesion of powder particles which occurs at elevated temperatures is known as sintering.   The term is broadly used, but always involves a reduction in the specific surface of a solid.

There are two types of system that may undergo sintering, namely:-

(a)   homogeneous systems consisting of a single component or components which give a continuous series of solid solutions.

(b)   heterogeneous systems consisting of multicomponent systems.

In the homogeneous sintering of a powder distinctions may be made between three overlapping stages of sintering.   Stage one is characterized by the formation and growth of bonds, i.e. the contact areas between adjacent powder particles.   The growth of these contact areas takes place during the early stages of sintering, and manifests itself by improving the cohesion of the compact.   Stage two is where the material is densified and the pore volume reduced.   In stage three the larger pores remaining within the grains grow at the expense of the smaller pores and similarly the larger grains grow at the expense of the smaller ones, but the overall density remains practically constant.

Figure 21 shows the general effect of sintering on the various physical properties, e.g. porosity, density etc.
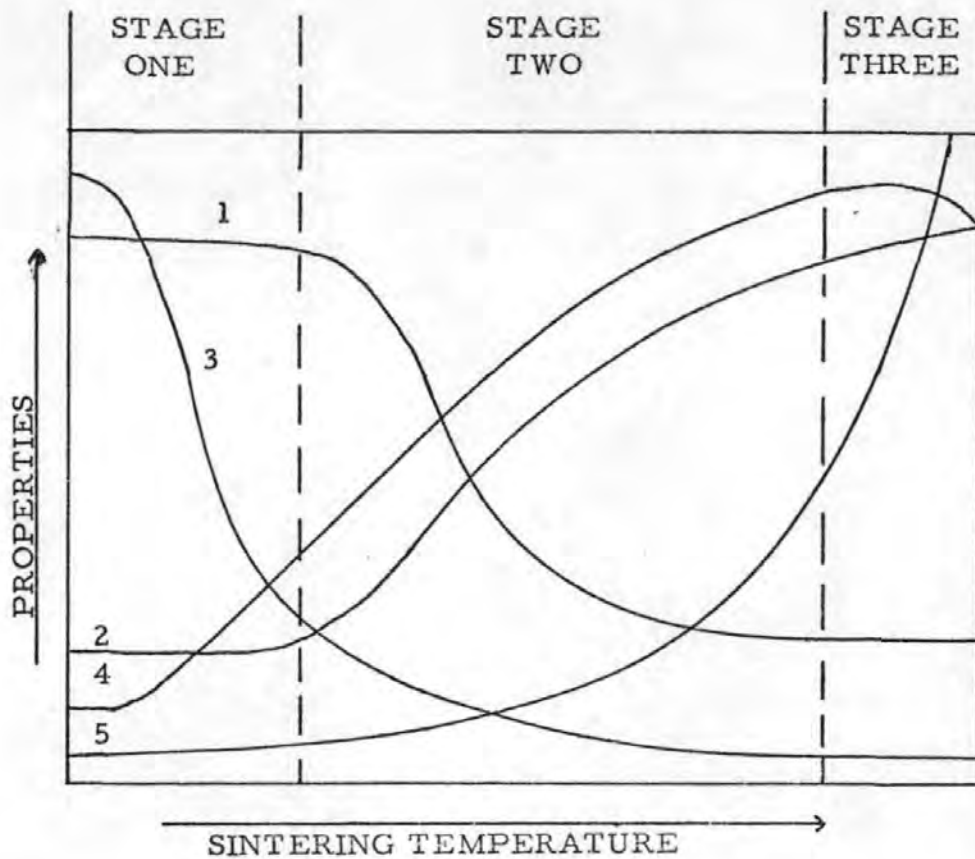
Figure 21   1.   Porosity
             2.   Density
             3.   Electrical resistivity (ionic solids)
             4.   Strength
             5.   Grain Size

In order to analyse the sintering process one must determine what the driving force for the mass transfer is, and also which kind of transportation processes determine the kinetics of sintering.   The free energy of a given amount of a single phase substance will be at a minimum when the substance exists as a perfect single crystal.   Thus the driving force for sintering is the decrease of surface free energy which occurs as the surface area of polycrystalline aggregates is reduced.   Simultaneously, the crystallites will grow in order to decrease the interfacial energy of the grain boundaries.   If no molten phase appears during the sintering process, then compaction occurs through mass transport in the solid phase and grain growth occurs by a rearrangement of lattice atoms at the moving grain boundaries.   Well-known examples of this type of sintering are the production of sintered iron, tungsten and oxide ceramics.

In the porous media, several modes of transport are available. So long as the pores are connected with one another and change only in shape during the first stages of sintering, then evaporation-condensation within the pores as well as surface diffusion are possible. In the advanced stages of sintering, when the pores are closed, the process continues via crystal lattice diffusion, grain boundary diffusion and diffusion along dislocations. In these latter stages, the pores become filled. This can occur only as a result of mass transfer to the pores from a source on an inner or outer surface. If only volume diffusion is considered, then this means that the interstitial atoms diffuse into the pores or that vacancies diffuse away from the pores, either from or to the outer surface, or from or to low or high angle grain boundaries and dislocations.

If we consider a model in which spherical particles of equal radius are placed in a close-packed array, we can distinguish the three stages of sintering in the sense of limiting cases.
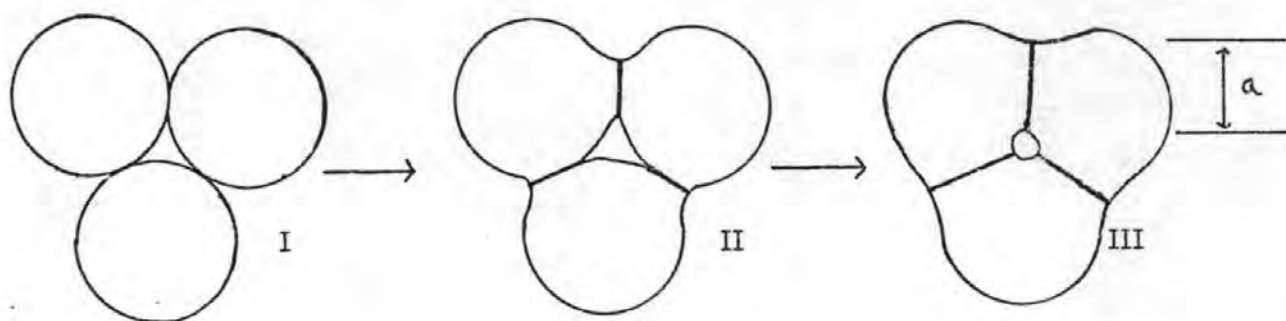
Figure 22

Stage one, the porosity remains constant, but the pores assume a shape that has the minimum surface area, that is, they take on a circular cross-section as shown in Figure 22. This sintering of the particles may occur by any of the previously mentioned transport paths. Depending on which transport path predominates, quite different rate laws for the growth of the contact surface between spheres will result. If "a" is the width of the contact area, then the rate law over a certain time interval will be of the form $x = k t^n$, where $n < 1$.

In the second stage of sintering, matter is transported from grain boundaries and surfaces to the pores.
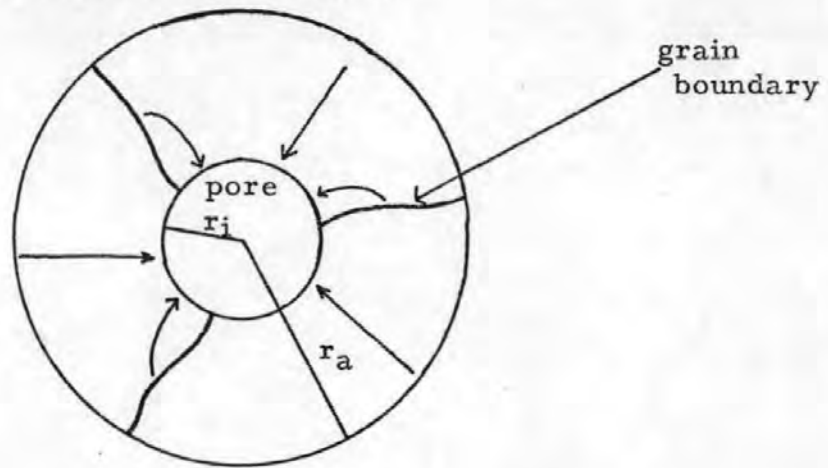
Figure 23

Figure 23 illustrates a case where the porosity is limited and the pores are already closed. As the curvature of the inner and outer surfaces of the material are different, a chemical potential difference exists, which is derived from the surface free energy, from the Gibbs-Thomson equation under the assumption that $r_a \gg r_i$

$$\text{then} \quad \Delta \mu_a = 2 \, \gamma_o \, V_m \left(\frac{1}{r_i} - \frac{1}{r_a} \right) \approx \frac{2 \, \gamma_o \, V_m}{r_i}$$

where

μ_a = chemical potential

γ_o = surface free energy

V_m = volume of particle

r_i = radius of pore

r_a = radius of sphere of material

This resultant potential gradient gives rise to a mass transfer towards the pore. Both grain boundary, and volume diffusion can occur.

In stage two it is assumed that all pores are intersected by grain boundaries. However, not all pores are like this, and Figure 24 shows the distribution of pores found in the third stage of sintering.
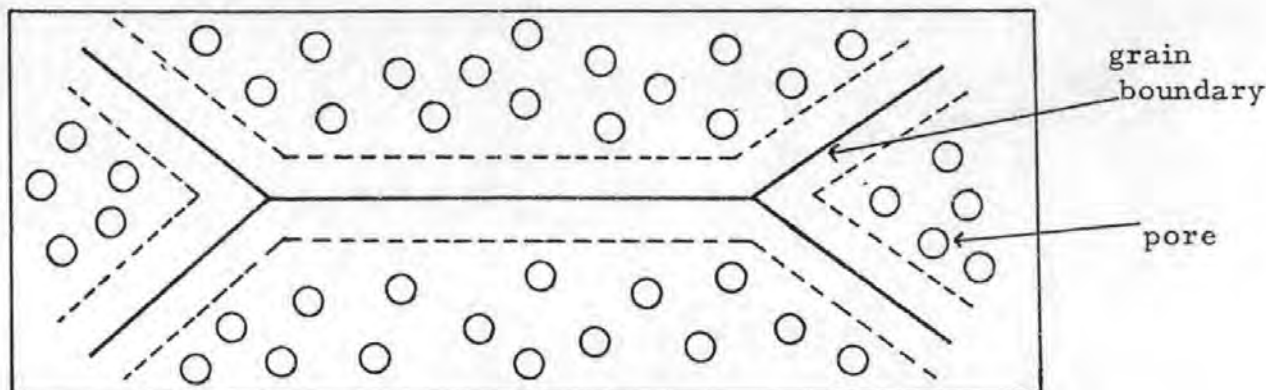
Figure 24

In this stage, the pores are found within the crystallites. From Figure 24 it can be seen that the grain boundaries act as vacancy sinks (or as sources of atoms or ions), since the pores have completely disappeared from the immediate vicinity of the grain boundaries. Observations show that the larger pores, within the crystallites, grow at the expense of the smaller pores because of the difference in chemical potentials in the vicinity of the large and small pores. This leads to a sort of "Ostwald ripening" of the pores. A similar argument is put forward for the growth of grains which occurs in the later stage of sintering. Both these processes have little effect upon the overall density of the compact.

The mechanisms for sintering have been developed by many workers, including Hüttig[52], Kingery & Berg[53], Coble[54], Kuczynski[55] and White[56]. Hüttig[52] concluded that sintering caused by surface diffusion became appreciable above $\sim \frac{1}{3}$ the melting point (K) and was considerably accelerated by lattice diffusion becoming prominent above $\sim \frac{1}{2}$ the melting point; known as the Tammann temperature. Further researchers found that generally ionic solids sintered readily above about half of the melting point, but less ionic type solids required a higher temperature for sintering.

Kuczynski[55] was the first to give quantitative evidence of volume diffusion by comparing the observed time-dependence of neck growth with the time-dependence predicted for viscous flow evaporation-condensation, volume diffusion and surface diffusion. He showed that in each case, the sintering time, t, to produce a neck of radius, x, should be given by the expression:

$$\left(\frac{x}{a}\right)^n = \frac{A\,(T)\,t}{a^m}$$

where A (T) = a function of only temperature

a = radius of particle

n = 2; m = 1   for viscous flow

n = 3; m = 2   for evaporation condensation

n = 5; m = 3   for volume diffusion

n = 7; m = 4   for surface diffusion

n = 6; m = 6   for grain boundary growth

Kuczynski's[55] model assumed that the vacancy sinks were confined to the particle surfaces and could only account for densification as long as the pores remained interconnected.   Kingery & Berg[53] showed that the observed rates of sintering were too rapid to be accounted for by neck growth due to volume diffusion and proposed a model where the grain boundary existing between two particles is considered to act as the vacancy sink.   The mass transfer would then pass from the vacancy sinks to the neck surface, as indicated by the arrows in Figure 25, and by spreading out of material at the neck causes the particles to coalesce.
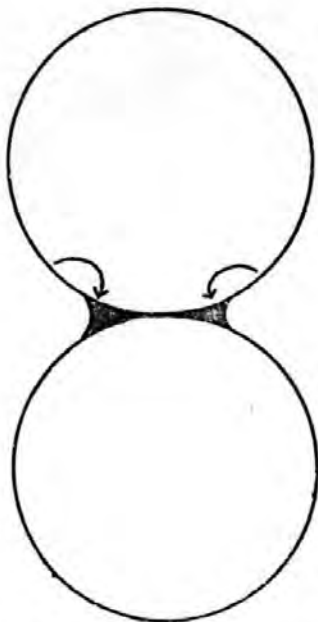
Figure 25

Kuczynski model for initial
sintering
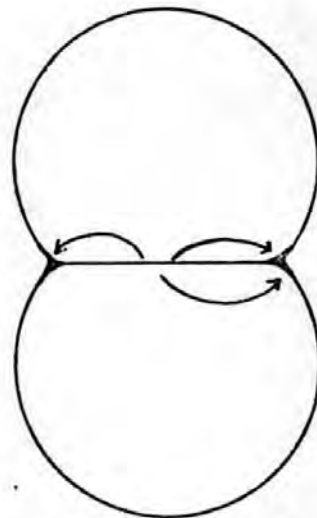
Kingery & Berg model for vacancies
eliminated at grain boundaries

Since the oxidation of lead sulphide was expected to depend significantly on surface area, basic oxidation studies in the present research were made on synthetic lead sulphide samples of widely different particle size, precipitated from solutions at various pH levels and electrolyte concentrations.

Precipitation may begin with the formation of embryos, or nucleation on impurity particles (seeds) from supersaturated solutions. The nuclei grow and form visible crystallites.   According to Strickland-Constable[57] the growth process is sometimes accompanied by the formation of new (secondary) nuclei, so that crystallites of two or more size groups may be present.   The crystallites formed may coagulate or form a stable suspension.   When the crystallites or the coagulated clusters become larger they tend to sediment; this is usually the last step of the process.

1.4.1   Supersaturation

Precipitation will not occur unless the solution is supersaturated. A saturated solution may become supersaturated by temperature fluctuation or by fractionation through evaporation of the solvent.

With the classical treatment of precipitation one considers three processes:- nucleation, growth and ageing.

1.4.2   Nucleation

At a stage after supersaturation has occurred, small crystallites are formed.   Because small crystallites have a greater equilibrium concentration than larger ones they may redissolve.   Thus a critical size of crystallite has to be surpassed before precipitation can begin. This critical size is attained by either homogeneous nucleation or heterogeneous nucleation.

Homogeneous nucleation

In a supersaturated solution there are numbers of sub-critical associates of crystal-like structure which are in equilibrium with the solution and are known as embryos.   A fraction of these embryos may attain the critical size for crystallite formation by thermal fluctuation. When this happens the embryos will associate and grow, forming the new phase.

Heterogeneous nucleation

It is quite possible for one cubic centimetre of filtered solution to contain many hundred minute foreign bodies.   These minute particles may act as heterogeneous nuclei for the initiation of precipitation. Initially the supersaturated solute is adsorbed on the surface of the

foreign particles, the layer formed may be larger than the critical size for precipitation and thus crystallites will grow and the new phase is formed.

Kahlweit[58] considered precipitation to be a continuous race between the size of the nuclei and that of the crystallites of the precipitate.   A coherent treatment of the course of precipitation may then be given, where the steady state nucleation theory as well as the theory of ageing at low supersaturations appear as limiting cases.

1.4.3   Suspension Stability

Crystallites in a suspension act on one another by electrostatic and dispersion forces.   If the crystallites have an appreciable charge (sulphides have a negative charge) of the same sign, they will rarely collide and if they do they will probably part again.   Overbeek[59], Tezak et al[60] and Kratohvil et al[61] showed that if the charges were small the crystallites collide more readily and stick together because of the short-range dispersion forces.   Substances which neutralize the charges on the crystallites, by forming an electrical double layer such as oppositely charged ions may induce coagulation.   Conversely, other substances such as specifically adsorbed ions or ions with high charge, stabilize a suspension.

1.4.4   Kinetics of Crystal Growth

The rate of crystal growth may be controlled by a number of factors:- (a) diffusion in the surrounding liquid, (b) convection in the liquid, (c) molecular processes at the surface, such as adsorption and surface diffusion.

(a)   Diffusion-controlled growth follows Fick's   diffusion law:-

The concentration gradient in the solution at the surface of a sphere of radius r is $\frac{(c-s)}{r}$ and $\frac{dr}{dt} = \frac{D v (c-s)}{r}$

where $\frac{dr}{dt}$ = velocity of growth

D   = diffusion coefficient

v   = molar volume of precipitating substance

c   = concentration of solute in the supersaturated solution

s   = solubility

The main features of diffusion control is that the rate is proportional to the effective concentration (c - s), and is inversely proportional to the sphere radius (small particles grow faster than larger ones).

(b)   Convection-controlled growth entails the transport of matter to the surface of the growing particle.

(c)   Influences of molecular processes such as surface diffusion and adsorption may be very marked on the absolute rate of growth, but can probably be represented by a constant factor in the above expression.

1.4.5   Growth at the Crystal face

Growth may follow one of two paths depending on concentration. On the crystal face, very small surface embryos are unstable and dissolve at the expense of larger surface nuclei which grow. At low supersaturations the surface nucleation is slow, and thus crystal growth is slow, but rapid enough to spread over the crystal face before the next surface nucleus is formed. This process is known as mono-nuclear formation. At higher concentrations there will be many more nuclei present and thus several nuclei may be present on the crystal face simultaneously. Thus each layer is formed by several nuclei and is known as poly-nuclear formation.

1.4.6   The Ageing Process

The free energy of a precipitate is proportional to the interfacial area; to stabilize a system this energy must be as small as possible. This decrease in interfacial area is known as ageing.

There are various modes in which a precipitate can age:

(a)   recrystallization of primary particles

(b)   transformation of a crystal from a metastable modification into a stable modification by dissolution and re-precipitation

(c)   aggregation of primary particles followed by sintering

(d)   Ostwald ripening - which probably always occurs with a new precipitate.

1.4.7   Ostwald Ripening

As smaller crystallites have a higher Gibbs free energy per

molecular unit than larger crystallites (due to the larger interface per molecular unit), the solubility of small crystallites is greater than the solubility of a large crystallite. If a solution is in contact with three crystallite sizes and is in equilibrium with the middle size, the small crystallites will find the solution undersaturated and dissolve, whilst the larger crystallites find it supersaturated and grow. It follows that a solution cannot be in equilibrium with a precipitate consisting of crystallites of two or more sizes (Todes[63], Lifshitz et al[64], Klein et al[65], Kahlweit[66]).

When a solution is left with a polydisperse precipitate, the concentration will sooner or later reach a value of between the solubilities of the largest and smallest crystallites, and remain in this interval while the small crystallites dissolve and the larger ones grow, until ultimately one large crystal remains.

1.4.8 Precipitation of Sulphides

With hydrogen sulphide

In 1908 Knox[67] found that an aqueous solution of hydrogen sulphide ionizes as a very weak acid.

In a saturated solution of hydrogen sulphide the following equilibria are present:-

$$H_2S \rightleftharpoons H^+ + HS^-$$
$$HS^- \rightleftharpoons H^+ + S^{2-}$$
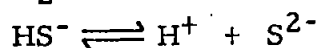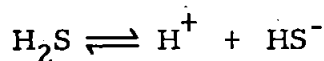
and $$K_1 = \frac{[H^+][HS^-]}{[H_2S]} = 9.1 \times 10^{-8} \quad \text{———————(1)}$$

$$K_2 = \frac{[H^+][S^{2-}]}{[HS^-]} = 1.2 \times 10^{-15} \quad \text{———————(2)}$$

The very small value of K_2 indicates that secondary dissociation and consequently $[S^{2-}]$ is exceedingly small. It therefore follows that only the primary ionization is of importance, and $[H^+]$ and $[HS^-]$ are practically equal in value.

The saturated solution of hydrogen sulphide at 25°C and one atmosphere pressure, is approximately 0.1M and has a pH of ~4.1.

By substituting $[H^+] = [HS^-]$ and $[H_2S] = 0.1$ in equation 1 we find

$$[H^+] = [HS^-] = \sqrt{9.1 \times 10^{-8} \times 10^{-1}} = 9.5 \times 10^{-5}$$

Thus the $[H^+]$ in saturated hydrogen sulphide water $= 9.5 \times 10^{-5} M$
$\equiv$ pH 4.002 (Measured value pH $= 4.1$).

As both equilibrium equations must be satisfied simultaneously, by substituting the values of $[H^+]$ and $[HS^-]$ in equation 2 we find:

$$\frac{9.5 \times 10^{-5} [S^{2-}]}{9.5 \times 10^{-5}} = 1.2 \times 10^{-15}$$

i.e. $[S^{2-}] = 1.2 \times 10^{-15}$ which is the value for K_2.

Now if we multiply equations 1 and 2 together, we obtain

$$\frac{[H^+]^2 [S^{2-}]}{[H_2 S]} = 1.1 \times 10^{-22}$$

$[H_2 S] = 0.1$ in saturated hydrogen sulphide water

$$\therefore \quad [S^{2-}] = \frac{1.1 \times 10^{-22} \times 10^{-1}}{[H^+]^2} \quad\quad\quad\quad\quad\quad (3)$$

$$[S^{2-}] = \frac{1.1 \times 10^{-23}}{[H^+]^2}$$

Thus the concentration of the sulphide ion is inversely proportional to the square of the hydrogen ion concentration. Thus by varying the pH of a solution, the $[S^{2-}]$ may be controlled; in this way separations of metallic sulphides may be effected.

With sodium sulphide

In aqueous solution sodium sulphide will be almost entirely hydrolysed, and can be represented:

$$Na_2 S + H_2 O \rightleftharpoons 2Na^+ + 2OH^- + H_2 S$$
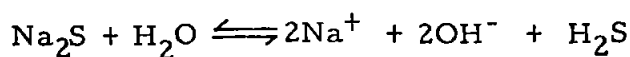
The week acid hydrogen sulphide will then dissociate as described earlier giving

$$[S^{2-}] = \frac{K_1 K_2 [H_2 S]}{[H^+]^2}$$

Table 1.4a

	pH	$[S^{2-}]$
Saturated hydrogen sulphide soln.	4.1	1×10^{-14}
1M HNO_3 + $H_2 S$ soln.	0	1×10^{-23}
1M $Na_2 S$ soln.	13.9	8.9×10^{-2}

Table 1.4a shows the variation of solution pH and $[S^{2-}]$

The table shows that in an acid solution the sulphide ion concentration is of the order of 10^{-23} mol l^{-1} whereas in 1 molar sodium sulphide solution, pH 13.9 it is of the order 10^{-1} mol l^{-1}. Despite the very low sulphide ion concentration in acid solution, there is still sufficient to precipitate lead sulphide, due to the low solubility product.

Consider the precipitation of lead sulphide from 1 M lead nitrate in the presence of 1M nitric acid (conditions analogous to those found at the end of precipitation) with hydrogen sulphide.

Solubility product for lead sulphide, S_{PbS} = 4 x 10^{-28}, 1M nitric acid has a pH = 0 $\therefore$ $[H^{+}]$ = 1

$$[Pb^{2+}] = \frac{S_{PbS}}{S^{2-}}$$

$$[S^{2-}] = \frac{1.1 \times 10^{-22} \times 10^{-1}}{(1)^2} \quad \text{from equation 3}$$

$$[Pb^{2+}] = \frac{4 \times 10^{-28} \times 1}{1.1 \times 10^{-22} \times 10^{-1}} = 3.64 \times 10^{-5}$$

$$[Pb^{2+}] = 3.64 \times 10^{-5} \text{ M}$$

Thus precipitation will continue until the lead ion concentration is reduced to 3.64 x 10^{-5} M, i.e. 7.5 mg of lead will remain unprecipitated per litre.

In the presence of 0.1 M nitric acid, the lead ion concentration would be reduced to 3.64 x 10^{-7}M, before precipitation stops.

With sodium sulphide of pH 13.9, the sulphide ion concentration = 8.9 x 10^{-2} from Table 1.4a

The $[Pb^{2+}] = \frac{4 \times 10^{-28}}{8.9 \times 10^{-2}} = 4.5 \times 10^{-27}$

Thus precipitation will continue virtually to completion.

1.5   PRODUCTION OF SINTER FOR THE BLAST FURNACE

The sinter process serves a two-fold purpose, namely desulphurization and production of a material with suitable physical characteristics for introduction to the blast furnace.   The term sintering, in this context, is defined as the simultaneous desulphurization and agglomeration of zinc and lead-bearing material to produce a burden suitable for the blast furnace, and a gas suitable for the production of sulphuric acid.

In the sintering process a hot zone moves progressively through the sinter bed from bottom to top, the temperature of the solids being raised to a level at which sintering of the loose agglomerate into a strong coherent porous mass occurs.   The quality of the sinter produced may be judged by measuring its "hardness", which is defined as the ability to withstand plant handling.   The handling treatment at Avonmouth seems to be best reflected by measuring the "hardness" in a rotating tumbler.   In the test employed a 25 Kg sample of sinter sized -50mm + 12mm is rotated in a drum 406 mm long and 406mm in diameter fitted with a 50 mm lifter for 93 s. in which time the drum has completed 84 revolutions.   The percentage of sinter remaining on a $\frac{1}{2}$" screen is quoted as the rattle index.   For the testing of laboratory sinters a small-scale tumbler is used, which has been calibrated against the plant tumbler.

The sinter process may be conveniently divided into four stages, namely:-

1.   conditioning of the raw material
2.   mixing the feed for the sinter machine
3.   sintering of this mix
4.   separation of sintered material into "product" and "returns".

The raw concentrate imported is the product of concentration processes such as froth flotation, e.g. Broken Hill zinc concentrate on typical analysis contains 52.7% Zn, 1.0% Pb, 10.0% Fe, 32.2% S etc., whereas Broken Hill lead concentrate analyses to 3.5% Zn, 75.5% Pb, 2.5% FeO, 15.5% S etc.

A good sintering mix for combined Zn-Pb smelting may consist 40% Zn, 20% Pb, 7.5% Fe, 7.5% SiO_2, 5% CaO and 2-4% moisture with

5% fresh sulphur as fuel, and small proportions of other gangue-forming materials such as magnesia and alumina. Thus to achieve this desired analysis, mixtures of the fresh concentrates and sinter returns are mathematically formulated. In formulating the mix, allowances are made for the loss of the more volatile components during sintering, such as lead and lead oxide.

During sintering the feed becomes fritted together and is discharged from the machine largely in the lump form. This is screened on a bar screen, the undersize provides "returns" and the oversize the "product" for the blast furnace. The sinter quality is judged by the sulphur content (ideally <1%) and the rattle index (ideally >85).

During the course of experimental work on the preparation of sinters, it became evident that the quality of the sinter was affected by variations in its chemical composition. Harris et al [68] studied the effects of variation of lead, lime, silica, iron, alumina and magnesia on the quality of the sinter.

The optimum fuel content in lead-zinc sinter production is approximately 5% new sulphur in the mix, as determined by Woods & Harris [69]. The sintering was performed on the laboratory updraught pallet, the technique is described in Chapter 6.

1.5.1   Effect of Lead, Lime and Silica on Sinter Quality

Sinter studies were carried out varying the lime and silica with lead levels of 20 and 30% in the mix, with iron held at 7.5%. The results concluded that the total sulphur content of the 30% lead sinters was higher than at the 20% level. The total sulphur content increased with both lime and silica additions. There was no difference in the rattle index attributable to the change in lead level. The effect of increasing the silica level was to increase the rattle index linearly at both lead levels. The rattle index also increased with lime content at the lower lead level, the relationship being quadratic and tending to flatten at the higher lime levels. At the higher lead level lime has little effect.

1.5.2   Effect of Iron on Sinter Quality

The experiments were performed using zinc concentrates with

a low iron content.   Iron additions were made in the form of iron
sulphate (essentially FeS) in one case and in the form of iron oxide
(essentially Fe_2O_3) in the other.   The lead lime and silica levels were
held at 15, 8 and 5.5% respectively.

From the results it was clear that the rattle index of the sinter
decreased with increasing iron content, but the effect was more marked
when the iron was introduced in the form of iron oxide.   No effect of
iron was found on either the total sulphur content or on the sulphate
content of the sinter.   This was in accordance with neither ferric
sulphate or ferrous sulphate being stable at the sintering temperature.

1.5.3   Effect of Magnesia on Sinter Quality

Magnesia is normally a minor constituent of sinter and has a
typical level of about 0.5%.   Previous work had shown that small
variations in magnesia content could have an effect on sinter strength.
Harris[70] investigated the effect of magnesia on sintering mixes with a
low gangue content (8.5% Fe, 3.8% CaO, 2.5% SiO_2) and a high gangue
content (7.0% Fe, 7.5% CaO; 5.0% SiO_2), with lead held at 20% and
zinc lying between 40-44%.   He concluded that increasing the magnesia
content from 0.7% to 2.3% was associated with a mean reduction in
rattle index of 20 points at the low gangue level and a 10 point reduction
at the higher level.

1.5.4   Effect of alumina on sinter quality

Alumina, like magnesia, is a relatively minor component of
zinc-lead sinters, with a typical level of 0.5%.   It had been found that
sinters with the highest rattle index were made at the higher alumina
levels using ball-clay (impure alumina silicate).   Also, sinters with
low rattle indices have been made at the higher alumina levels using
alumina (Al_2O_3).   The effect on the rattle index was clearly
attributable to the form in which the alumina was added.   The probable
reason for high rattle indices when using ball-clay is that the ball-clay
is more easily assimilated into glassy material which binds the sinter
together.

From experiments performed along similar lines to that of the
magnesia, with high and low gangue sinters it was concluded that
increasing the alumina from 0.5 to 2.3% was associated with a mean
reduction of rattle index of 6.5 points with the lower gangue, but no such
effect with the higher gangue sinters.

1.6 AIMS OF THE RESEARCH

The research comprises a physicochemical study of the roasting and sintering processes for lead sulphide. Conditions under which the sulphide is oxidized to oxide, basic sulphate and sulphate are to be studied to determine the relative effect of time of heating and composition of the surrounding atmosphere. To elucidate the mechanisms and kinetics of the oxidation process, information is also required about the surface area, crystallinity and crystallite sizes of the materials and the influence of any impurities.

The results of previous researchers, especially at lower temperatures, on the oxidation of lead sulphide are not consistent with one another. Thus, according to some workers[22, 19] the initial oxidation product is lead sulphate followed by monobasic lead sulphate. However, other workers[23, 17] report the formation of basic sulphate initially and lead sulphate later.

Accordingly, oxidation studies on lead sulphide are to be undertaken to provide further information which might also resolve the above inconsistency. Since the reactivity of the material is governed by its particle size, more active samples of lead sulphide are to be prepared by precipitation from aqueous solution. Therefore, the precipitation conditions, e.g. pH, temperature, concentration of reagents and time of ageing will be adjusted to obtain lead sulphide with suitable variations in crystallinity and crystallite size, as previously carried out with zinc sulphide[85].

From the early stages of the present research it was observed that lead sulphate is produced at a lower temperature than that reported by other investigators. Previous work had shown that calcium sulphite is an intermediate in the oxidation of calcium sulphide to sulphate. Thus, in the present research the thermal stability of lead and zinc sulphites are to be investigated.

Oxidation studies will be further extended to the industrial processing of lead-zinc ores. Hence, the effects of moisture and bentonite on the sintering of the lead-zinc mixes are to be studied at Imperial Smelting Processes Limited, Avonmouth, the industrial sponsors of the project.

CHAPTER 2

EXPERIMENTAL TECHNIQUES

2.1 THERMAL ANALYSIS

Thermal analysis may be defined as those techniques in which some physical parameter of a system is determined as a function of temperature. The two thermo-analytical techniques used in the study of the oxidation of lead sulphide and thermal decomposition of related sulphides were thermogravimetry, TG, and differential thermal analysis, DTA.

2.1.1 Thermogravimetry

Thermogravimetry is an analytical technique where the change in mass of a sample is recorded as a function of temperature or time. Thermogravimetry may be performed in one of three modes, namely:-

(a) isothermal or static where the sample mass is recorded as a function of time at a constant temperature

(b) quasi-static where the sample is heated to a constant mass at each of a series of temperatures

(c) dynamic where the sample is heated at a linear rate.

The resulting mass change versus temperature or time curve can provide information concerning the thermal stability of a compound, e.g. dehydration (of salts), decomposition, dissociation, disproportionation, oxidation etc.

Isothermal thermogravimetry has been widely used to study the kinetics of thermal decompositions. The basis for the calculation of kinetic data from isothermal thermograms is the general equation:-

$$- \frac{dX}{dt} = k X^n \text{————————(1)}$$

where X = sample mass

n = order of reaction

k = rate constant

The temperature dependence of the rate constant, k, is given by the Arrhenius equation:-

$$k = A e^{-E/RT} \text{————————(2)}$$

where   A = pre-exponential factor

     E = activation energy

From 1 and 2

$$- \frac{dX}{dt} = A e^{-E/RT} \cdot X^n$$

For a decomposition Newkirk[72] obtained rate constants from thermograms by taking a series of temperatures T_1, T_2, T_3 etc., corresponding to the amount of sample remaining $(a - x_1)$, $(a - x_2)$, $(a - x_3)$ etc. The reaction rates were obtained by taking tangents to the curve $(dx/dt)_1$, $(dx/dt)_2$, $(dx/dt)_3$ etc. If the decomposition is first order (i.e. n = 1 in equation 1) then the logarithm of the reaction constant, k, $(dx/dt = k (a - x))$ when plotted against $1/T$ should yield a straight line.

Coats & Redfern[73] derived an expression where the activation energy could be found from dynamic thermograms which has the advantage that only one sample is needed. From the thermogram, the fraction of sample decomposed, α, is measured; by using the expression:-

$$\log \left[\frac{1 - (1 - \alpha)^{n-1}}{T^2 (1 - n)} \right] = \log \frac{AR}{aE} \left[1 - \frac{2RT}{E} \right] - \frac{E}{2.303\,RT}$$

and plotting $\quad \log \left[\dfrac{1 - (1 - \alpha)^n}{T^2 (1 - n)} \right] \quad$ against $\quad \dfrac{1}{T}$

or where n = 1, $\quad \log \left[\dfrac{- \ln (1 - \alpha)}{T^2} \right] \quad$ against $\quad \dfrac{1}{T}$

should result in a straight line of slope $\dfrac{-E}{2.303\,RT}$ for the correct value of n. The limitation of this method is that the order of the reaction, n, must be known.

2.1.2   Differential Thermal Analysis

A typical differential thermal analysis, DTA, apparatus is illustrated schematically in Figure 26. The apparatus consists of a furnace (A), furnace temperature controller (B), microvolt D C amplifier (C), differential temperature detector (D), sample holder (E), and chart recorder (F).
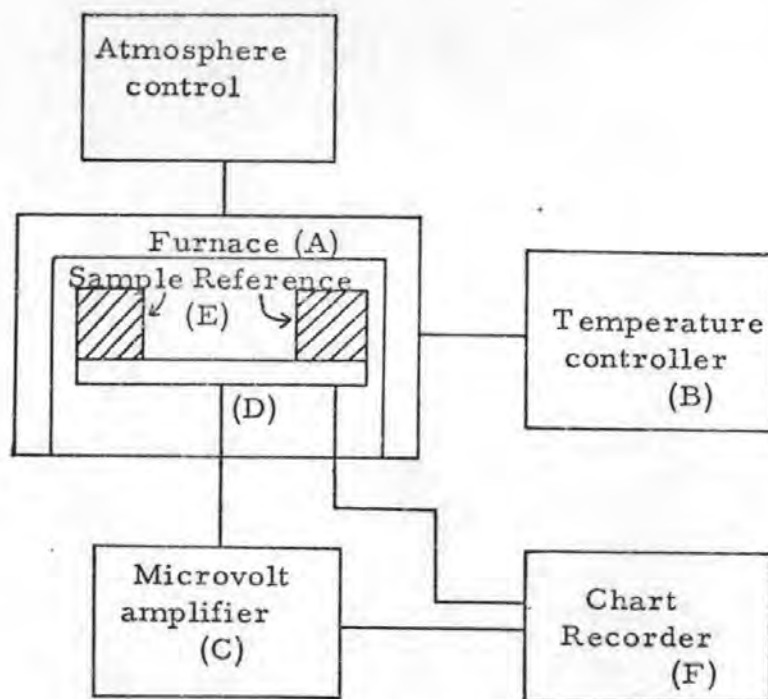
Figure 26   Schematic diagram of a typical DTA apparatus

Differential thermal analysis is a thermal technique where the temperature of the sample is compared with the temperature of a thermally inert material (reference).   The difference in temperature is recorded as the sample and reference are heated or cooled at a uniform rate.   Temperature changes in the sample are caused by exothermic or endothermic enthalpic transitions or reactions, such as those arising from phase changes, fusion, crystalline structure inversions, dehydrations, dissociation or decomposition reactions and oxidation and reduction reactions.   Any temperature difference between sample and reference is monitored by two thermocouples differentially coupled.

The output trace is a record of temperature difference between sample and reference against the temperature of the reference.

The number, shape and position of the various endothermic and exothermic peaks with reference to the temperature may be used as a means of qualitative identification of the substance under investigation. The area under the peak is proportional to the heat change involved and may be used for quantitative determinations of heats of reaction, after suitable calibration.

The heat of transition (or reaction) may be expressed very simply:- $\Delta H.m = KA$

where ΔH = heat of transition

        m = mass of reactive sample

        K = calibration coefficient

        A = curve peak area

The calibration coefficient is related to the geometry and thermal conductivity of the sample holder and is usually determined by calibration with compounds of known heats of transition. As the calibration coefficient depends on the temperature and atmosphere present, a series of substances of known heats of transition at a range of temperatures must be used and a calibration graph plotted.

2.1.3   The Massflow Thermal Balance

The equipment employed to study the oxidation of lead sulphide and the thermal decomposition of related sulphites was a Stanton-Redcroft Massflow Thermobalance Model MF-H5.

Plate 1 shows the apparatus used together with the sulphur dioxide determination equipment.

The balance chamber was a 10-gauge copper tube 178 mm diameter, silver brazed and epoxy-resin coated with doors 10 mm thick sealed with"O" rings. A water-cooled silicone "O" ring seals the mullite reaction tube to the chamber. There are four gas entry or outlet ports, two to the reaction tube and two to the main balance chamber, all fitted with valves.

The thermobalance design incorporates two beams, one inside the chamber and the other outside, the two being coupled by a magnetic link. Changes in weight occurring on the inner beam are transferred to the outer beam, detected electronically and indicated by an arm with a full-beam deflection of 20 mg and sensitivity of 0.2mg.

Automatic electric weight loading increases the range of the instrument to the equivalent of ten full beam deflections of gain or loss without a decrease in sensitivity. This enables weight gains or losses of up to 200 mg to be followed.

During operation the balance automatically arrests and releases itself every 5 min to check that it is not sticking and to improve the sensitivity with very small weight changes.
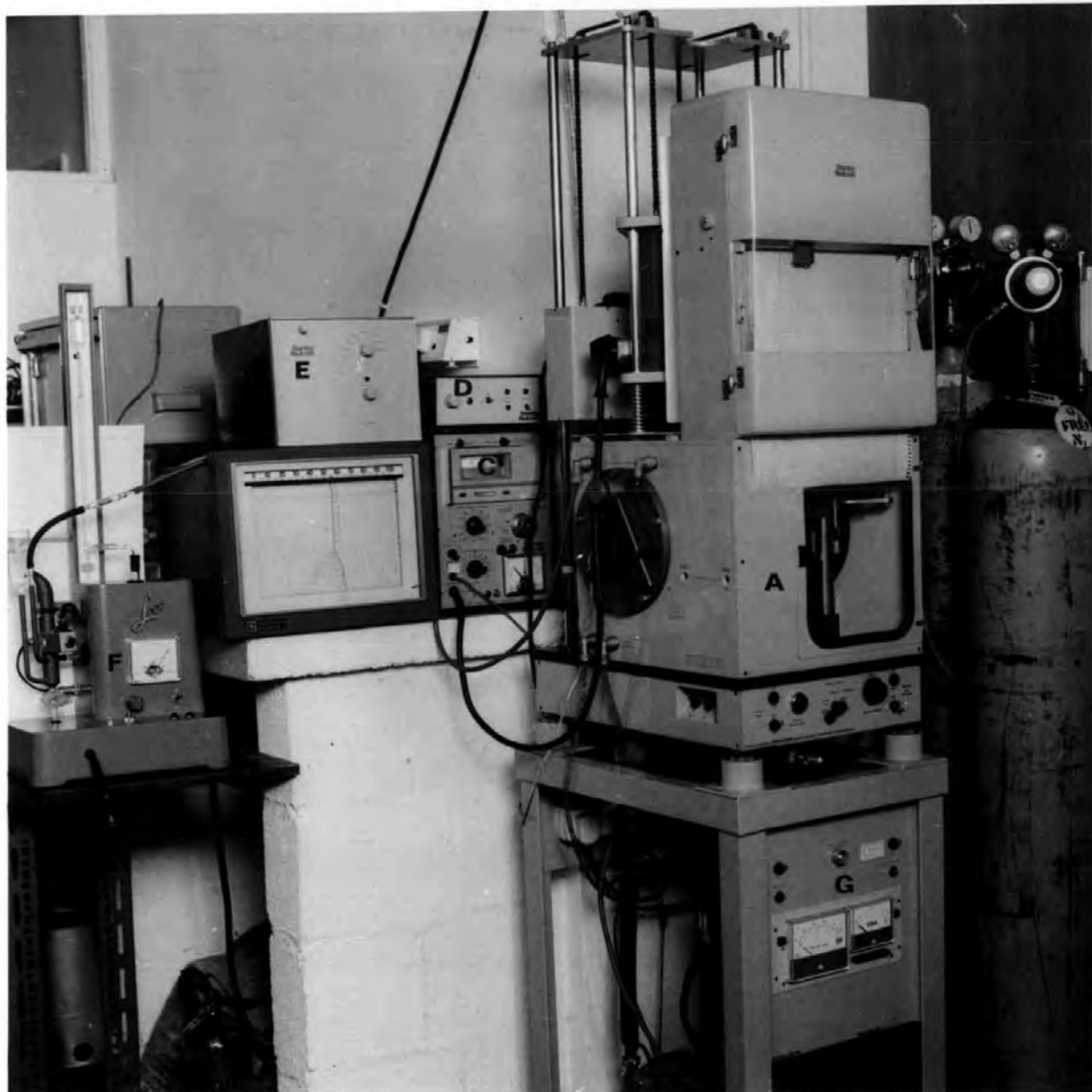
Plate 1   Stanton-Redcroft Massflow balance with ancillary equipment

When the thermobalance is used with the DTA attachment, the sample holder consists of an alumina block 20 mm diameter and 13 mm in depth with two wells each 6.5 mm diameter and 10 mm in depth to take the crucibles. The alumina head is coupled to the internal balance by alumina and silica rods joined by an aluminium chuck (Figure 27). When the DTA attachment is not utilized, the head may be replaced with an alumina pedestal on which crucibles can be placed for thermogravimetric work.

With the DTA attachment, the sample is heated along side a thermally-inert reference material (α-alumina). Two Pt/13% Rh. Pt thermocouples are employed to detect the temperature difference between sample and reference. The signal from the thermocouples is passed from the alumina head down the inside of the alumina and silica rods to the outside by 0.025 mm compensated platinum wires, which have a very small damping effect on the balance. Further compensated leads are employed to connect the signal with the DC amplifier and constant-reference-temperature ice-bath. The DC amplifier has seven pre-set ranges from 20-1000 μV; normally the 100 μV sensitivity setting is used. A single channel Leeds Northrup Speedomax W chart recorder is used with a switching unit enabling the differential output to be recorded for 4 min 55 s and then the temperature recorded for 5 s.

Two matched (0.8g) platinum crucibles with dimples are used to contain the sample and reference material. The crucibles are placed in the 6.5 mm wells of the alumina head with the thermocouples sitting in the dimples and are thus surrounded by the sample. This leads to high sensitivity for the differential thermal output. Silica crucibles were also employed, but these are limited in temperature range due to reaction with alumina above $1000^{\circ}C$.

With the four gas entry and exit points as shown in Figure 27, it is possible to keep a nitrogen atmosphere in the balance chamber and pass air containing corrosive gases over the sample. By means of the vacuum attachment, the system can be easily flushed out and known atmospheres introduced. The air and gases used were all obtained from pressurized cylinders having pressure and flow
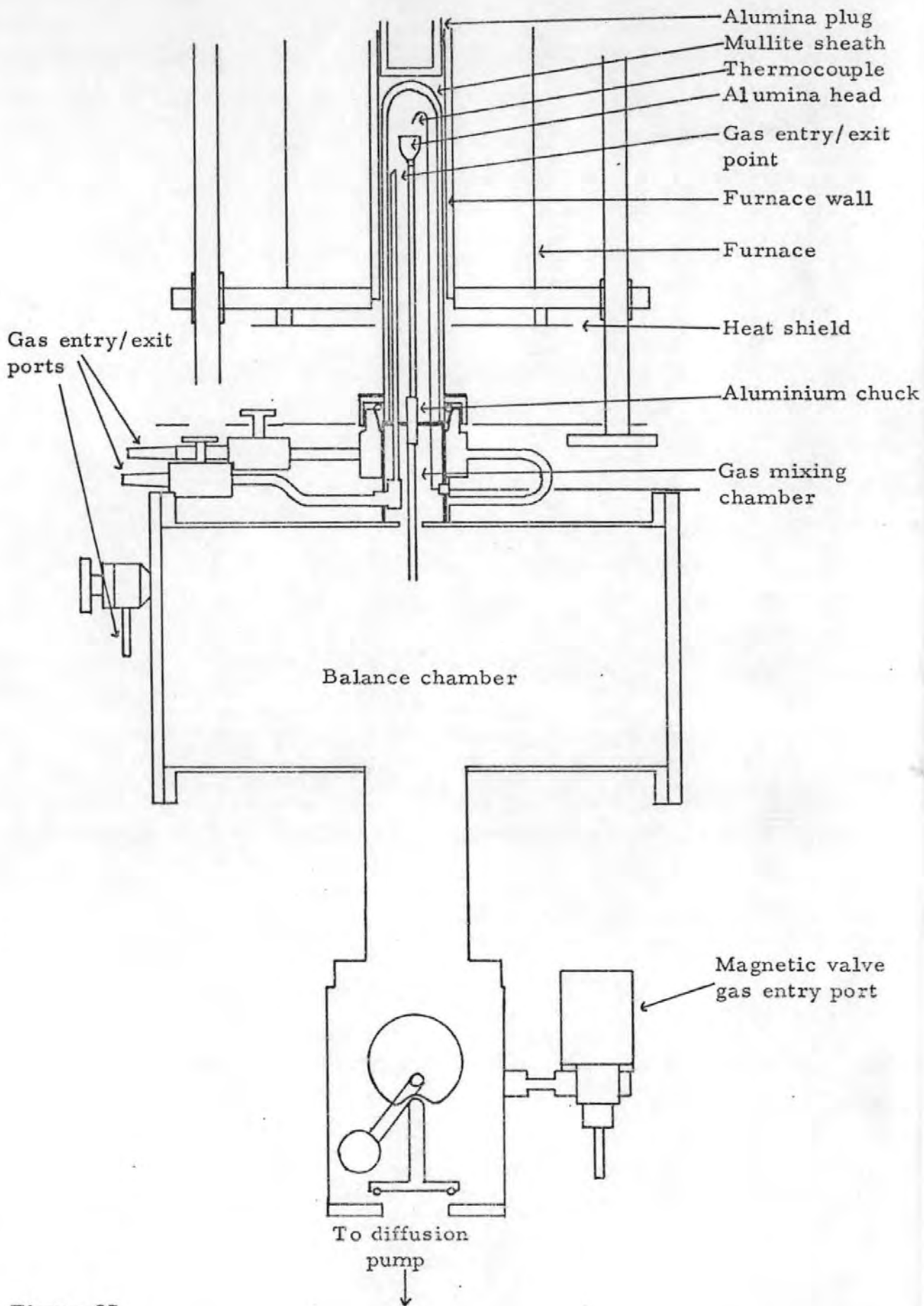
Figure 27.

Gas circuit of the Stanton-Redcroft Massflow Balance MF-H5

regulators, with the gas flow entering the balance monitored by a rotameter.

The vacuum equipment consists of a single-stage rotary and diffusion pump with Pirani and Penning gauges. The rotary pump enabling the pressure to be reduced to 10^{-1} - 10^{-2} mm Hg.(13-1.3 Pa), and with the diffusion pump to $< 10^{-4}$ mm Hg.(<0.013 Pa).

The platinum-rhodium bifilar wound furnace has a 50 mm bore and is closed at the top with a 100 mm deep alumina plug filled with α-alumina powder. The maximum temperature at which the furnace could be used was 1350°C.

The temperature is controlled by a Stanton-Redcroft Eurotherm temperature controller with the sensing Pt/13% Rh.Pt thermocouple trapped between the mullite reaction tube and the furnace wall. The controller enables the heating rate to be continuously varied from 1-20°C min^{-1} with the maximum temperature pre-selected and subsequently held constant indefinitely (isothermal conditions).

Initially, a set of calibration curves were recorded to determine the buoyancy corrections for the thermogravimetric work and the base-line for the differential thermal studies. This was done by using the standard reference material in both the sample and reference crucibles and a heating rate of 5°C min^{-1}. Hence the buoyancy correction curve and differential thermal base-line were obtained up to 1050°C. This procedure was repeated with the appropriate gas atmospheres and flow rates. These correction curves were then applied to the experimental results.

2.1.4 Determination of Sulphur Dioxide

The apparatus

A Leco[74] sulphur determinator was used to monitor the sulphur dioxide given off in the thermal decomposition experiments and some of the oxidation studies. The output gases from the massflow balance were passed through a cell containing potassium iodate, excess potassium iodide with hydrochloric acid and starch as indicator. The iodine released gives the solution a blue colour with starch, the blue intensity being measured by a lamp and photocell with a current meter. The sulphur dioxide is oxidized by the iodine to sulphur trioxide and

enters solution as sulphuric acid.

$$KIO_3 + 5KI + 6HCl \longrightarrow 6KCl + 3H_2O + 3I_2$$
$$SO_2 + I_2 + 2H_2O \longrightarrow H_2SO_4 + 2HI$$
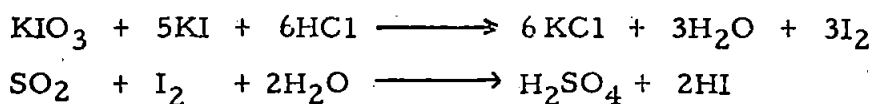
Procedure

The standardized potassium iodate was put in the burette, the potassium iodide, hydrochloric acid and starch were placed in the titration cell. A small aliquot of potassium iodate was added from the burette; with no sulphur dioxide in the gases passing through the titration cell, a constant reading was obtained on the meter. This reading was taken as the zero reading. Another aliquot of potassium iodate was added, its volume recorded and the sulphur dioxide in the gas determined when the meter reading returned to the zero. The sensitivity of detection of sulphur dioxide could be varied by changing the concentration of potassium iodate or the size of the aliquot added. The system was self-mixing by the action of the gases bubbling through the titration cell.

Finally, the values of the potassium iodate added were converted to milligrams of sulphur dioxide. The amount of sulphur dioxide could be plotted against temperature from the DTA record, since the time lag between the evolution and determination of sulphur dioxide was small because of the high gas velocity employed (1 lmin^{-1}).

2.2   GAS SORPTION

When a highly disperse solid is exposed in a closed space to a gas or vapour at a definite pressure, the solid begins to adsorb the gas. The adsorption is a consequence of the forces of attraction emanating from the solid which are of two types viz., physical and chemical, giving rise to physical ("Vander Waals") adsorption and chemisorption.   The amount of gas adsorbed on a solid depends upon the pressure, p, temperature, T, nature of gas and nature of solid.

i. e. $x = f(p, T, gas, solid)$

where x is the amount of gas adsorbed, usually expressed in grams of adsorbate per gram of adsorbent.   When the adsorbate is below its critical temperature, the form:-

$$x = f(P/P_0)_{T, gas, solid}$$

is more useful, where p_0 is the saturated vapour pressure of the adsorbate at T K.

The majority of adsorption isotherms resulting from physical adsorption may be grouped for convenience into five classes - the five types of classification originally proposed by Brunauer, Deming, Deming & Teller[75] (BDDT), nowadays commonly known as the Brunauer, Emmett & Teller[76] (BET) classification.   The five types are illustrated in Figure 28.   Type 4 possesses a hysteresis loop (dotted line), where the lower branch represents progressive addition of vapour to the system and the upper branch represents progressive withdrawal.   It is now possible to use isotherms of Type 2 and 4 to calculate specific surface, and use Type 4 isotherms for making an estimate of pore size distribution.

From the adsorption isotherm, the problem is to calculate the monolayer capacity of the adsorbent by mathematical methods or otherwise.   The monolayer capacity is defined as the quantity of adsorbate which can be accommodated in a completely filled single layer of molecules on the adsorbent surface;   the specific surface, S ($m^2 g^{-1}$), is directly proportional to the monolayer capacity, given by the relationship:-

$$S = \frac{x_m N}{M} \cdot A_m \quad\quad\quad\quad\quad\quad\quad (1)$$

Figure 28. The five types of adsorption isotherm in the B E T classification.

Type 1

Type 2

Type 3

Type 4

Type 5

AMOUNT ADSORBED

RELATIVE PRESSURE
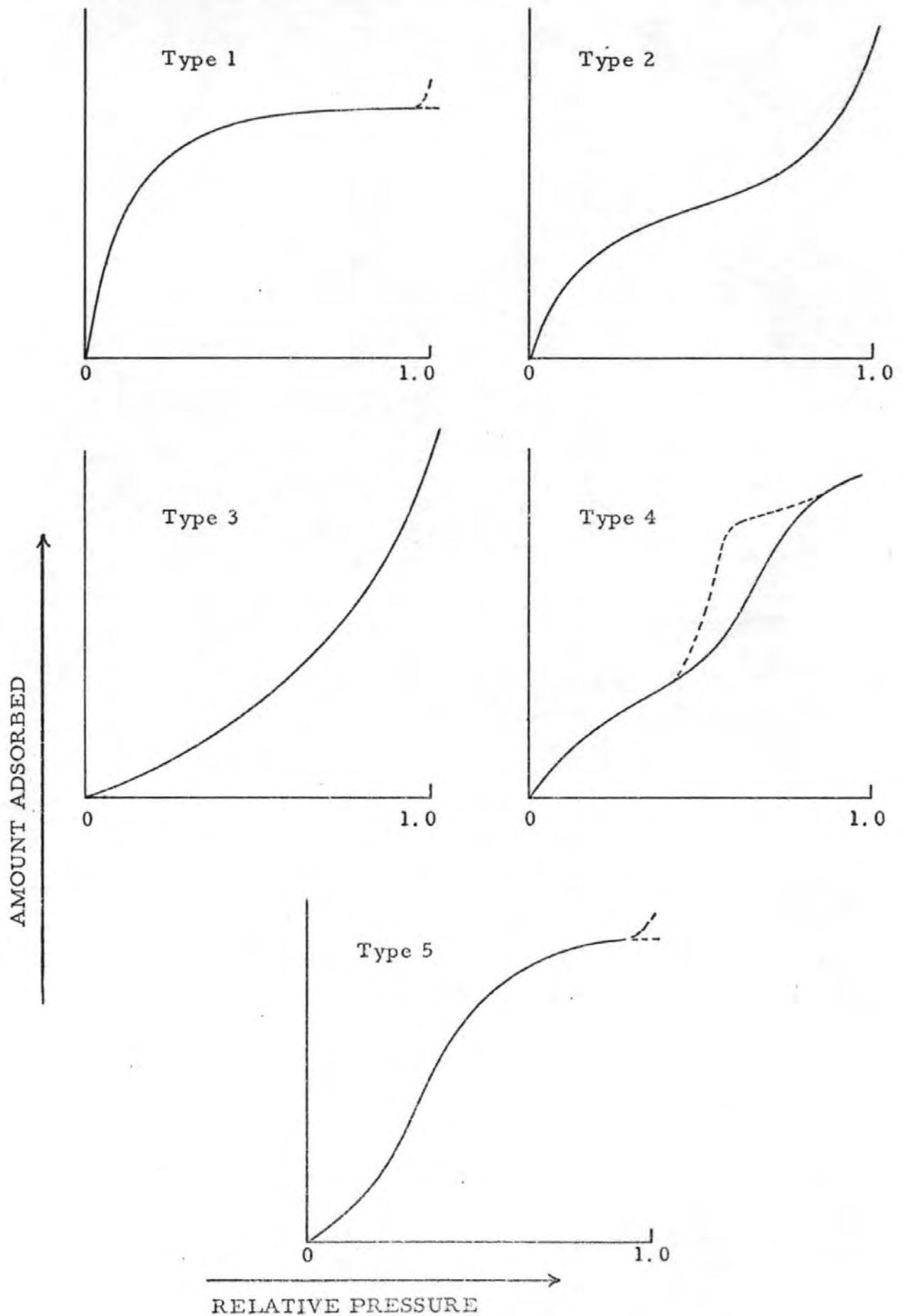
where x_m = monolayer capacity in grams adsorbate per
gram of solid

M = molecular weight of adsorbate

A_m = area occupied per molecule of adsorbate

N = Avogadro's number

A number of theories have been proposed for the interpretation of adsorption isotherms. Brunauer, Emmett & Teller[76] approached the problem of adsorption kinetically, focussing their attention on the interchange of adsorbate molecules between the gas phase and adsorbed layer. The results of their efforts yielded the BET equation:-

$$\frac{p}{x(p_0 - p)} = \frac{C-1}{x_m C} \cdot \frac{p}{p_0} + \frac{1}{x_m C} \tag{2}$$

where x_m = monolayer capacity

C = constant dependent on the heat of adsorption of the first layer of adsorbate, E, and the latent heat of vaporization of the adsorbate, L. Thus $C = e^{(E_1-L)/RT}$ (simplified expression) may be used in theory to calculate the net heat of adsorption, but because of the over simplification of the model the values obtained are of limited validity.

Although the BET equation is an over simplification of the equilibrium involved, it has proved remarkably successful in the calculation of specific surface from Type 2 isotherms.

2.2.1 Assumptions made with the BET Model

The BET model assumes that all adsorption sites are exactly equivalent (the surface is energetically uniform), but there is evidence from variations of heats of adsorption with coverage, that this is not the case. The model neglects horizontal interactions between the molecules within the adsorbed layer, and only takes into account the vertical attractions; also mobility in the adsorbed layer is neglected.

2.2.2 Determination of Surface Area and Particle Size

By plotting $\frac{p}{x(p_0 - p)}$ against $\frac{p}{p_0}$ a straight line of slope $\frac{C-1}{x_m C}$ and intercept $\frac{1}{x_m C}$ is obtained. Elimination of C from the equations yields the monolayer capacity, x_m, and from equation

(1) the specific surface, S.

If the specific surface is known then the average crystallite diameter, d, may be found. Assuming all the crystallites to the spherical then:-

$$S = \frac{4\pi \left(\frac{d}{2}\right)^2 n}{\frac{4}{3}\pi \left(\frac{d}{2}\right)^3 \rho n} = \frac{6}{\rho d}.$$

where   n   is the number of crystallites per gram

ρ is the density of the solid

If the crystallites are cubes of side length d, then:-

$$S = \frac{6d^2}{\rho d^3} = \frac{6}{\rho d}$$

Other relationships may be derived for plate and needle-shaped crystallites.

2.2.3   The Apparatus

Plate 2 shows the apparatus used. The sorption balance was designed and constructed for the determination of surface areas within the range $0.2 \text{ m}^2\text{g}^{-1}$ to $1000 \text{ m}^2\text{g}^{-1}$ using samples of 0.25 g. The balance head used was a "CI microforce balance Mark 2B" marketed by CI Electronics Limited[77] with five weight ranges, 0-25 μg to 0-100 mg with sensitivities of 1×10^{-7}g and 5×10^{-4}g respectively.

The sample was placed in an aluminium foil bucket suspended from the balance with a fine pyrex fibre (27 cm long). This enabled the sample to be at least 15 cm below the level of the liquid nitrogen, keeping the temperature to within $\pm$ 0.1°C as previously determined by Glasson[78]. In practice, the sample is about 1° warmer than the liquid nitrogen outside the balance limb (as determined by Glasson[79] using internal and external thermocouples).

A perspex counterweight was employed to reduce the buoyancy effect to within 2 μg at 760 mm Hg.(101325 Pa) pressure, when using a 250 mg sample of lead sulphide. The balance head was coupled by taps and glass tubing to a two-stage rotary pump (enabling the pressure to be reduced to 10^{-3} Torr), and to a nitrogen reservoir and gauges, the nitrogen pressure being measured by a mercury manometer.
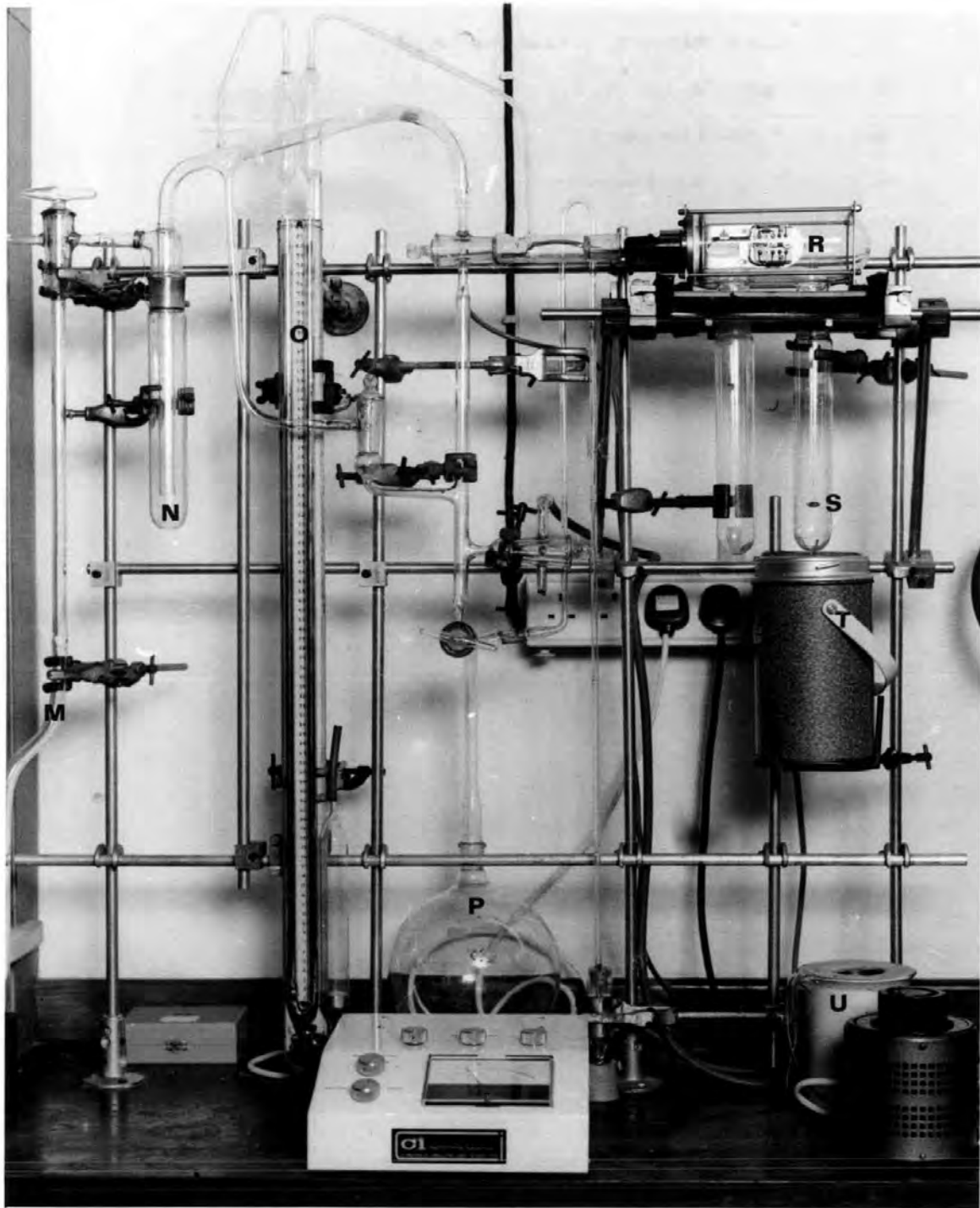
Plate 2   Sorption balance

2.2.4 Procedure

0.25 g samples were taken and mounted on the balance, the whole system was evacuated and the sample degassed by heating to 150°C for 20 min. After allowing to cool to room temperature, the balance was zeroed on range 2 (0-250 µg), the balance limb containing the sample immersed in liquid nitrogen. A pressure of 30-50 mm Hg.(4000-6670 Pa) of nitrogen was introduced and the system allowed to attain equilibrium (~30 min), when the nitrogen pressure and uptake were recorded. Six readings were taken; with the final nitrogen pressure ~220-230 mm Hg (29300-30700 Pa). Weight corrections for buoyancy effects of the sample, container and suspension were applied to the uptake readings. The surface areas were determined by the BET method, as previously described.

2.3   X-RAY DIFFRACTION

A comprehensive survey of the theory and practice of X-ray diffraction is given by Peiser et al[80].

2.3.1   Theory

Crystals consist of regular three-dimensional arrays of atoms in space.   Points which have identical surroundings within a structure are known as lattice points.   A collection of lattice points form a crystal lattice;   when adjacent lattice points are joined together a unit cell is obtained.   This is the smallest convenient repeating unit of the structure.   In general the unit cell is a parallelepiped, but in some cases depending on the symmetry of the crystal, it may have a more regular shape, e. g. in the extreme case, a cube.

The size and shape of a unit cell can be described by the lengths of its three edges (a, b, c) and the angles between them (α, β, γ), i. e. the angle between b and c being α.   Crystals can be classified into seven crystal systems according to their symmetry which are summarized in Table 2. 3a.

Various sets of parallel planes may be drawn through the lattice points.   Each set of planes can be completely described by three intergers (h, k, l), the Miller indices, corresponding to the three axes (a, b, c) respectively.   Index h is the reciprocal of the fractional value of the intercept made by the set of planes on the a axis etc.

As the dimensions of a crystal lattice are of the same order of magnitude as the X-ray wavelength employed, the lattice behaves as a three-dimensional diffraction grating.

Table 2. 3a

Crystal system	Conditions limiting cell dimensions	Minimum Symmetry
Cubic	$a = b = c \quad \alpha = \beta = \gamma = 90°$	Four three-fold axes
Trigonal	$a = b = c \quad \alpha = \beta = \gamma \neq 90°$	One three-fold axis
Tetragonal	$a = b \neq c \quad \alpha = \beta = \gamma = 90°$	One four-fold axis
Hexagonal	$a = b \neq c \quad \alpha = \beta = 90°, \gamma = 120°$	One six-fold axis
Orthorhombic	$a \neq b \neq c \quad \alpha = \beta = \gamma = 90°$	Two perpendicular two-fold axes or two perpendicular planes of symmetry
Monoclinic	$a \neq b \neq c \quad \alpha = \beta = 90°, \gamma \neq 90°$	One two-fold axis or (one plane of symmetry)
Triclinic	$a \neq b \neq c \quad \alpha \neq \beta \neq \gamma \neq 90°$	None

The diffraction is governed by Bragg's Law:-

$$2 \, d \sin \theta = n \lambda$$

where

λ = X-ray wavelength

n = order, in X-ray diffraction = 1

d = interplanar spacing

θ = angle of diffraction

d is related to the unit cell dimensions by the Miller indices.

The intensity and distribution of the diffracted beams with respect to the Bragg angle is characteristic of a particular structure and may be used to identify the phases present. Diffraction patterns for the majority of crystalline compounds are listed in the A.S T M tables.

2.3.2　X-ray Line-broadening

X-ray line-broadening always occurs due to instrumental factors such as specimen size, beam divergence etc. Combined with this there may be intrinsic broadening due to crystallite size, and/or crystal lattice strain. Crystals > 200 nm in size contain numerous parallel planes, where the interatomic distance is constant giving a sharp diffraction maximum. With smaller crystallites the number of atomic planes per crystallite is less, and a small deviation from the ideal leads to line-broadening of the diffraction peaks.

Line-broadening due to cubic crystallites may be expressed by the equation :-

$$B_t = \frac{C \lambda}{d \cos(\frac{1}{2}\theta)} \qquad (1)$$

where C = constant

λ = X-ray wavelength

d = edge length of the crystallites

θ = Bragg angle (measured in terms of 2θ)

B_t = broadening

This equation was agreed upon by Scherrer[81], Bragg[82] & Seljakow[83], from which it can be shown that line-broadening is negligible if $d \geqslant 10^{-4}$ cm.

The constant, C, has previously been assigned values 0.94, 0.89, and 0.92 by Scherrer[81], Bragg[82] & Seljakow[83] respectively, but since the crystallite sizes vary little significance is attached to these values and for convenience it is made equal to unity. This method can only be expected to achieve an overall accuracy of 20%.

2.3.3   Calculation of Intrinsic Broadening

A single calcite crystal is used as a standard to determine the instrumental broadening, Bo.

The Jones[84] method (1938) was employed to calculate the average crystallite size; this method assumes a Gaussian distribution of crystallites.

Copper K_α radiation was employed; this is composed of a doublet with a finite breadth, z, which is calculated from the expression:-

$$z = \frac{360.}{2\pi} \left[\frac{\lambda_{\alpha 2} - \lambda_{\alpha 1}}{\lambda_{av}} \right] . \tan \theta_{av} = C \tan \theta$$

where $\lambda_{\alpha 1}$ = wavelength of $K_{\alpha 1}$ component

$\lambda_{\alpha 2}$ = wavelength of $K_{\alpha 2}$ component

λ_{av} = average wavelength

θ = angle of calcite diffraction peak used

C = constant (0.285 for copper K_α radiation)

Using the Jones[84] correction curve (Figure 29) of $^b/Bo$ against $^z/Bo$ a corrected line breadth, b, for the K_α —doublet is obtained, where Bo is the measured half-peak breadth of the calcite diffraction

Figure 29.   The Jones correction curves.

Curve for correcting observed
line breadth for the fact that it
is formed by a $K\alpha$-doublet.

Curve for correcting line
breadth for the effect of
instrumental broadening.
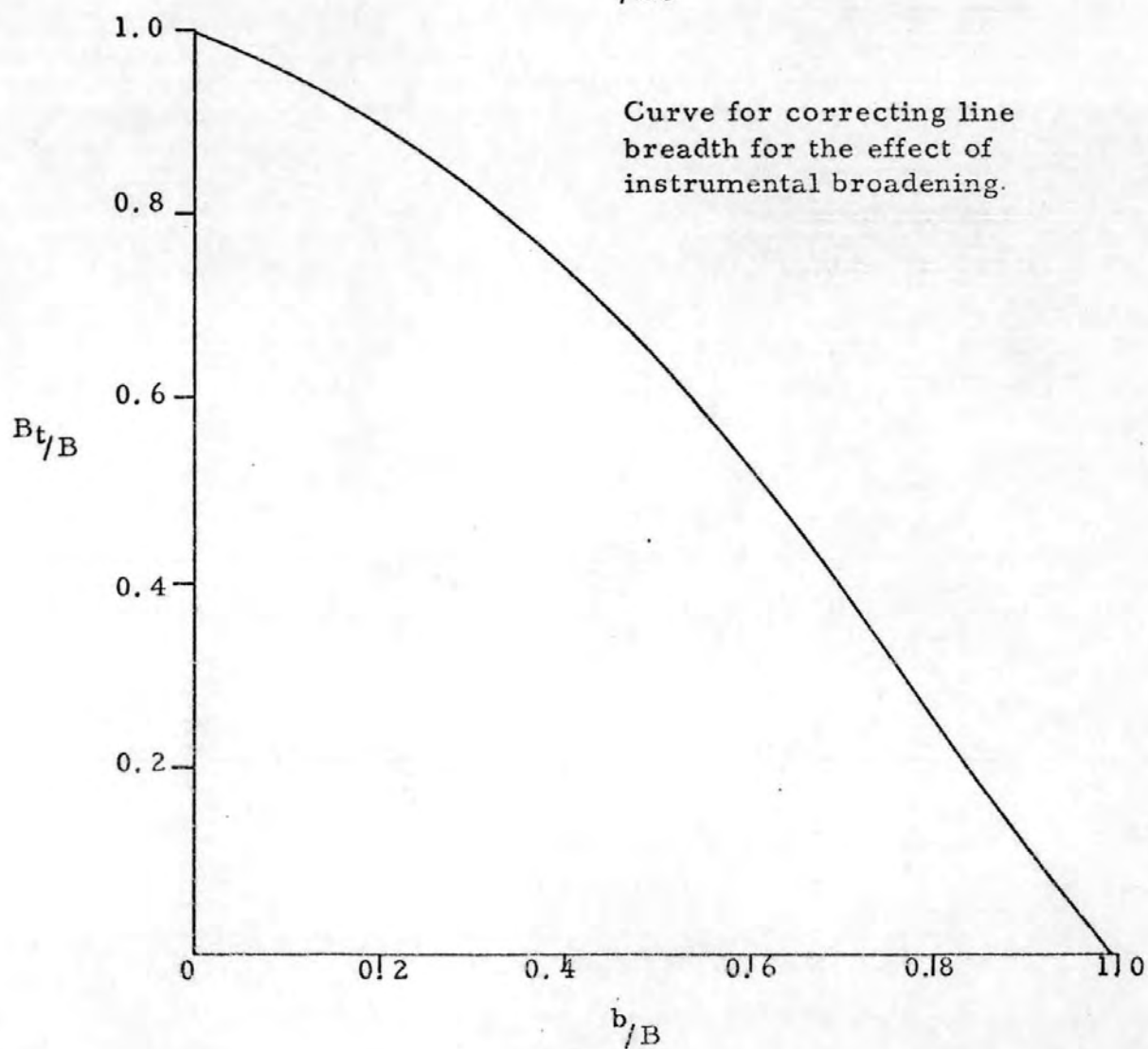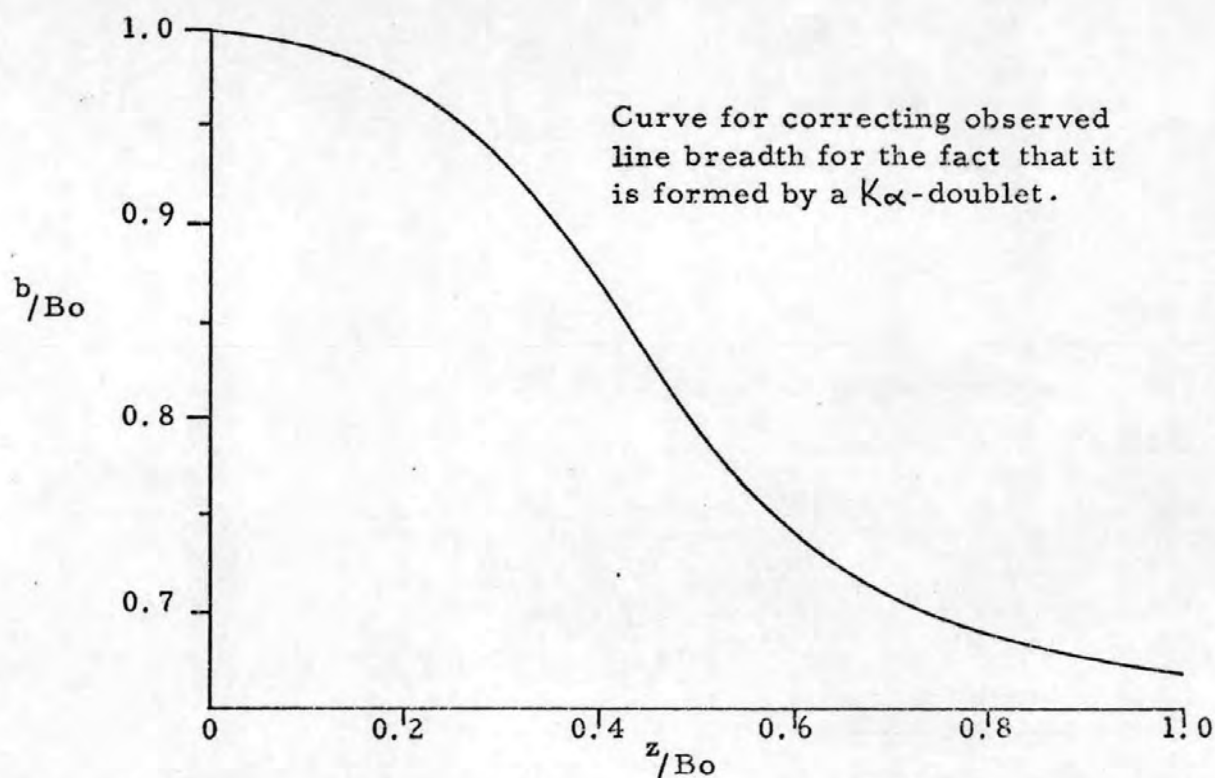
peak after subtraction of the background radiation.

A further correction for instrumental broadening is applied by the curve $^{Bt}/B$ against $^b/B$, (Figure 29) where B_t is the true diffraction breadth, b is the corrected diffraction breadth for calcite and B is the measured half-peak breadth of the specimen.

Hence, the crystallite size is calculated from equation 1.

i.e.
$$d = \frac{\lambda}{B_t \cos\left(\frac{1}{2}\theta\right)} \quad .$$

2.3.4 The Equipment

The Hilger and Watts X-ray generator used was fitted with a Philips X-ray tube and copper target. Voltage and current were set at 40 kV and 20 mA respectively. The X-rays generated were filtered with a nickel foil to reduce the K β component and passed through a collimator and slits before impinging on the sample mounted vertically at the centre of the 50 cm Berthold diffraction table. The diffracted X-rays were detected by a gas-filled proportional counter connected to a discriminator/ratemeter and Enraf-Nonius chart recorder.

2.3.5 Procedure

The table was aligned and calibrated with a single calcite crystal.

Samples were prepared by mixing the powdered material with acetone and a drop of adhesive 'Durofix'. The suspension was poured on to a microscope cover slip and the acetone allowed to evaporate leaving the sample adhering to the slip.

For phase composition analysis the table was rotated at $\frac{1}{3}$ degree per minute, and the chart paper at 60 cm per hour; this gave a trace of the intensity of diffracted radiation against Bragg angle in degrees, with a spacing of 3 cm per degree. To achieve a smooth trace the time constant chosen was 3 seconds.

For line-broadening measurements the table was re-calibrated, and the slits reduced to a minimum to decrease the effect of instrumental broadening, whilst keeping the diffracted radiation sufficiently strong. The table was rotated at 1/10 degree per minute and the selected peak scanned with a time constant of 3 sec.

2.4 TRANSMISSION ELECTRON MICROSCOPY

2.4.1 Principle

De Broglie in 1924 discovered the principle of wave and particle duality, and established the relationship:-

$$\lambda = \frac{h}{mu} \text{\textemdash\textemdash\textemdash\textemdash\textemdash\textemdash\textemdash}(1)$$

The energy given to an electron accelerated through a potential difference of V volts $= eV$ ————————————(2)

which is equivalent to the kinetic energy $\frac{1}{2} mu^2$—————————(3)

From 2 and 3 $mu = \sqrt{2 \ meV}$

By substitution in 1 the wavelength can be determined.

where   m = mass of electron (relativistically corrected)

u = velocity of electrons

e = electronic charge

V = accelerating voltage

h = Planck's constant

λ = wavelength

Due to the high velocities attained by the electrons, relativistic corrections are necessary.

The wavelength of electrons accelerated by a potential difference of 80 kV is 0.0043 nm (4.3 pm).

An electron microscope, like an optical microscope, is employed to provide enlarged images of small objects and the detail shown ultimately depends upon the resolving power of the instrument. The limit of resolution is controlled by the wavelength of radiation employed. In optical microscopy, 200 nm, is the theoretical limit but with electron microscopy it is ~ 1pm. In practice the resolving power is much lower due to lens aberrations caused by:- mechanical asymmetry, magnetic inhomogeneities and deposits on the lens surfaces. Nevertheless, resolving powers down to 0.1 nm are attainable with present instruments.

Figure 30 is a schematic diagram of the Philips EM 300 microscope and the following descriptions apply to this instrument.

Filament

Wehnelt cylinder

Anode

Electron gun

Condenser lens (1)

Condenser stigmator

Condenser lens (2)

Objective stigmator

Objective lens

Specimen

Specimen holder

Diffraction lens

Intermediate lens

Projector lens

35mm. camera

Fluorescent Screen

Plate camera
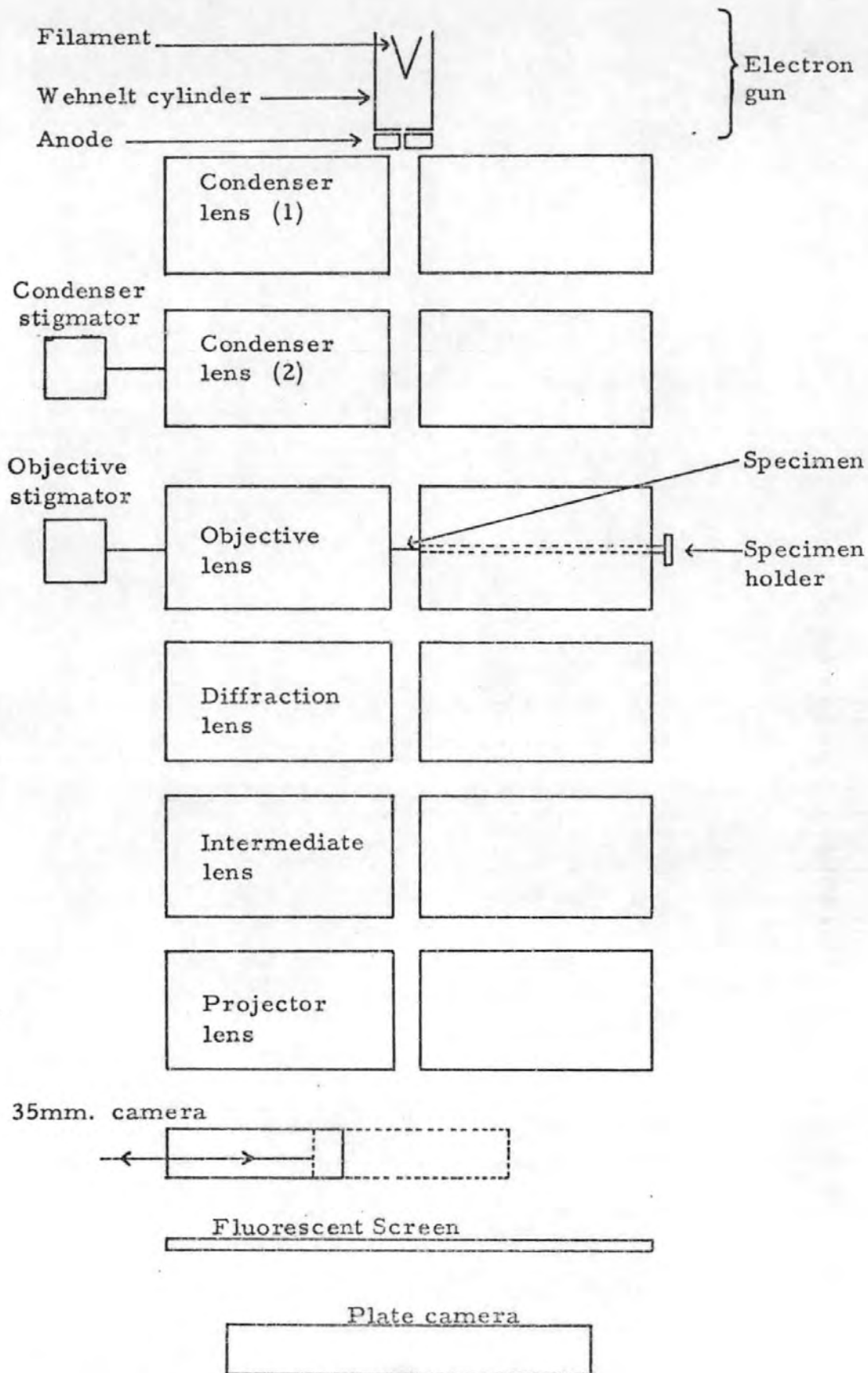
Figure 30.   Philips E. M. 300 Electron Microscope

2.4.2   The Equipment

The gun provides a beam of electrons and is composed of a
hairpin tungsten filament enclosed by a Wehnelt cylinder.   The electrons
are accelerated by a high voltage through a hole in the Wehnelt cylinder
which is negatively biased to converge the beam to a diminished virtual
image of the filament a short distance in front of the filament.   The
beam current is controlled by varying the bias voltage applied to the
Wehnelt cylinder (Emission control).

Lens (1) focusses the diminished virtual image of the electron
source, to a greater extent than that produced by the Wehnelt cylinder.
Lens (2) focusses the beam in the specimen plane.   Usually the first
lens is operated at constant current, and the current varied in the
second lens changing the focal length and thus the area of illumination.

To minimize spherical aberrations, the objective lens must be
operated with small acceptance angles (10^{-2} - 10^{-3} rad.);   this is
achieved by placing an aperture in the beam in front of the lens.   This
lens determines the ultimate resolving power of the instrument and
produces a real image of the specimen, which is further magnified by
the projector lens system.

The three lenses give a wider range of distortion-free
magnification than is possible with one.   Usually the intermediate lens
is kept under constant current conditions for low magnification work
(< 1000 X) and the projector lens current varied;   for higher
magnifications vice versa.   The third lens, the diffraction lens, enables
variations to be made in the magnification of the specimen area selected
for electron diffraction without needing to adjust the objective lens which
has been used to focus the specimen.

An electromagnetic lens invariably suffers from astigmatism,
due to asymmetry of the magnetic field strength about the lens axis
caused by foreign bodies deposited on the pole pieces and electrostatic
charging.   To counteract these effects, stigmators are used in
conjunction with the condenser and objective lenses.

Astigmatic conditions of the objective lens are checked by
observing Fresnel interference fringes seen around a small object
at high magnification, if the lens is astigmatic the fringe is not even.

To correct this the objective stigmators are used.

Condenser lens astigmatism is checked by focussing the condenser so that a bright spot is seen; if the spot does not expand symmetrically when the condenser is defocussed the illumination system is astigmatic, and the condenser stigmator is used to correct it.

2.4.3 Procedure

The samples were prepared as in Section 2.4.7. The specimen grid was mounted in the holder and introduced to the microscope through the objective lens. A voltage of 80 kV was selected and the filament adjusted to saturation current. After alignment of the beam and correction for condenser lens astigmatism, the scanning mode was selected and the grid scanned for a suitable section of specimen. When found, the instrument was set to the magnification mode and the appropriate magnification factor selected. The image was then carefully focussed and photographed after adjusting the illumination and exposure time. Both $3\frac{1}{8}$" by 4" plates and 35 mm film were employed to record the images.

2.4.4 Electron Diffraction

The principle of electron diffraction is almost the same as X-ray diffraction, the difference being the strong scattering of the incident electrons by the atoms due to the electrical charge of the electron. Thus, the depth of penetration is small and only thin crystals ($<$ 30 nm) may be used. As with X-ray diffraction, electron diffraction of single crystals gives an array of points and with polycrystalline material, a set of concentric rings.

When used in conjunction with the hot-stage holder analysis of the products, when crystalline, can be made in situ by electron diffraction at the series of reaction temperatures chosen.

2.4.5 Hot-stage Electron Microscopy

The hot-stage holder was used to study sintering and thermal decomposition of related sulphites.

The general form of the Philips PW6550 heating holder is similar to that of other holders for the goniometer except that the sample is clamped to a small furnace element. The element is insulated from the rest of the holder by three zirconium oxide spheres.

A thermocouple is welded to the furnace and is used to monitor the temperature. The temperature control unit contains the current supplies for the heater and the circuitry necessary to measure the voltage generated by the thermocouple.

Palladium specimen grids with carbon films were employed with the samples (preparation described in Section 2.4.8). The grid is mounted between conduction rings in the holder and held in position by a spring clip. Before use, the conduction rings were cleaned in an ultrasonic bath to reduce the risk of welding the grid to the furnace. By adjusting the voltage and current controls carefully, the specimen is raised to the desired temperature and held. The maximum permissible temperature of the furnace is $1000^{\circ}C$.

2.4.6 Formvar Film Preparation

A 0.25% solution of Formvar (polyvinyl formol plastic) in chloroform was prepared. A clean glass microscope slide was dipped in the solution, the excess removed and the slide allowed to dry. When dry, the edges of the film were scored and the film floated off by "frosting" the slide and slowly dipping in a bowl of distilled water at an angle of 45°.

3 mm-copper grids were laid upon the floating film with their smooth faces touching the film. The film with the grids is removed from the water surface by carefully placing a piece of paper on the film, lifting and inverting the paper and allowing to dry. The grids, for use, were mounted in a cylindrical holder and the sample applied as below (2.4.7).

2.4.7 Sample Preparation

Precipitated samples of lead sulphide were prepared for examination by suspending the sample in a little acetone and placing in an ultrasonic dispersion unit for 5 min , this breaks down the aggregates. A small dropper-tube was used to transfer a drop of the shaken suspension to a prepared 3 mm-copper grid with 100 μm mesh, where the acetone was allowed to evaporate at room temperature.

2.4.8 Carbon Film Preparation

Carbon films of approximately 20 nm thickness were deposited on freshly-cleaned mica by striking an electric arc, in about ten bursts

of 2-3 second duration between two pure carbon electrodes in an "Edwards 306 Vacuum Coating Unit". Prior to deposition, the mica was breathed upon to prevent perfect adhesion of the carbon film. The film was separated from the mica by trimming around and slowly dipping into distilled water at an angle of 45°, allowing the action of surface tension to remove the film. A section of the floating film was removed by a palladium grid held with tweezers, transferred to a vertical cylindrical holder and held in position with an open-ended cap. The specimens were prepared as previously described, and deposited on the prepared grid.

2.5   SCANNING ELECTRON MICROSCOPY

Scanning electron microscopy may be used in a number of modes to provide enlarged three-dimensional images relating to various properties of a specimen, e.g. surface topography, elemental composition and surface voltage. The formation of these different types of image is largely dependent upon the type of signal produced during the electron-probe scan, e.g. light, X-rays or secondary electrons, and used to modulate the intensity of brightness of a cathode ray tube.

Physically a scanning electron microscope consists of three main sections:-

(a)   electron-optical column

(b)   operating and display console

(c)   stabilized power supplies

The three sections are outlined in the schematic diagram Figure 31.

(a)   This includes the electron gun and a series of lenses which demagnify the electron beam, the final lens focussing the beam on the specimen. The resolving power of the microscope can not be less than the electron beam diameter; the better commercial machines achieve a typical resolution of 10 nm. A set of scanning coils are mounted above the final lens; and within the bore of the lens is located a stigmator and a set of three movable apertures. These apertures determine the angular aperture subtended by the electron beam at the specimen surface. At the base of the lens column is a large specimen chamber. On the "Cambridge Stereoscan S4-10" used, the sample was mounted with conducting paint "Silverdag" on a 3cm-diameter aluminium disc and vacuum coated with gold to ensure electrical conductivity. The whole system was evacuated by means of a pumping system.

(b)   The mode of image formation employed was detection of the secondary electrons emitted during the electron-probe scan yielding an image relating to the surface topography of the
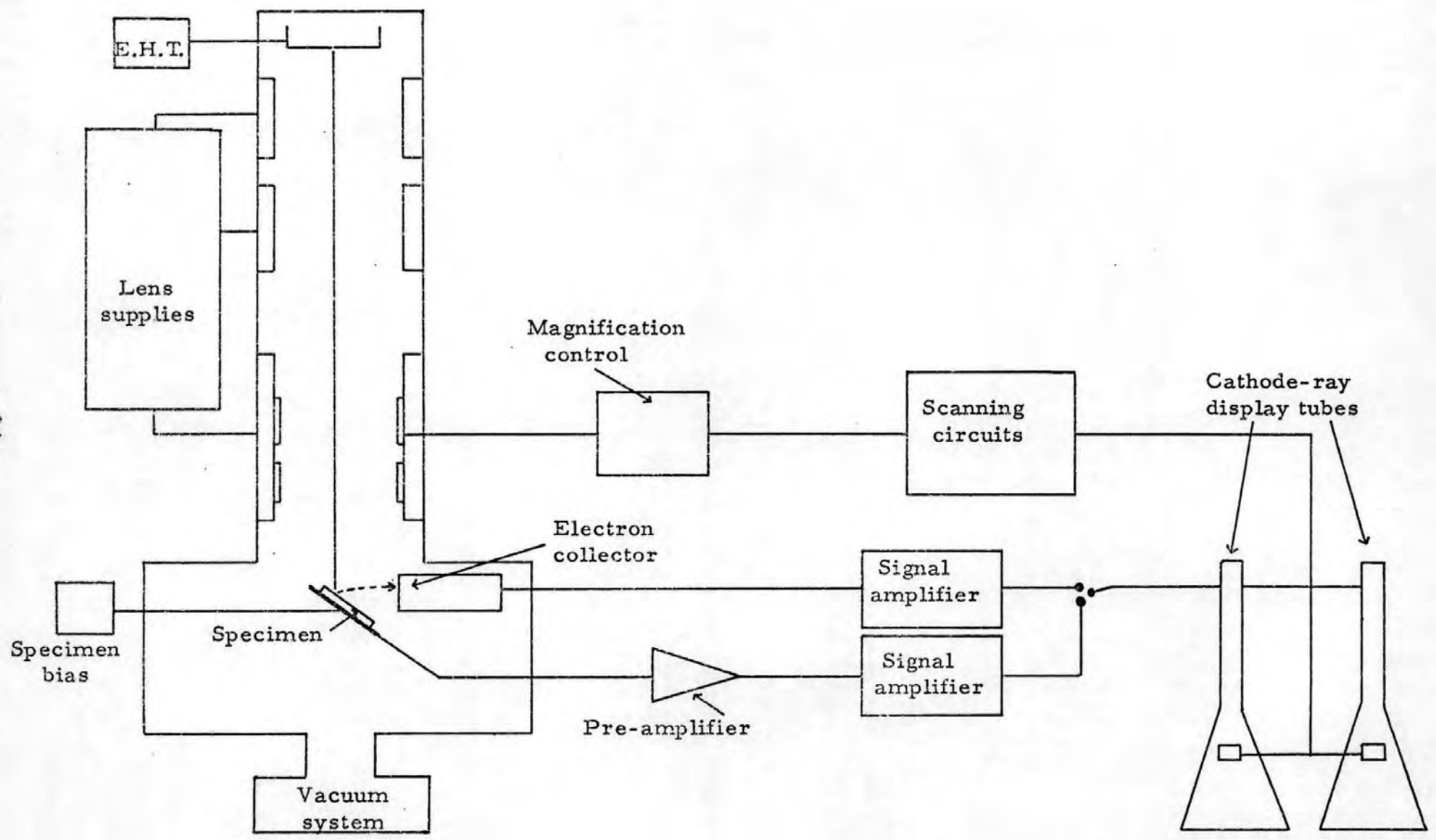
Figure 31. Schematic diagram of a typical scanning electron microscope.

E.H.T.

Lens
supplies

Specimen
bias

Specimen

Vacuum
system

Electron
collector

Magnification
control

Pre-amplifier

Signal
amplifier

Signal
amplifier

Scanning
circuits

Cathode-ray
display tubes

specimen.   The secondary electrons are detected by a
scintillator/photomultiplier system, the resulting signal being
further amplified and applied to the cathode ray display tubes.
Two cathode ray tubes were employed, one having a long
persistence phosphor, used for visual display and a second
having a short persistence phosphor, used solely for
photographic recording.

(c)   Additional electronic equipment was needed to supply the
current for the lenses, the accelerating voltage, control
systems for the cathode ray displays and ancillary equipment
associated with signal detection and amplification.

2.6 OPTICAL MICROSCOPY

In optical microscopy, the resolving power ultimately depends upon the wavelength of light used, and is usually taken as $\sim$200 nm. The other main disadvantage is the depth of focus limitation when observing three-dimensional objects.

With the Tessovar Photomacrographic Zoom system, magnifications of 0.8 to 12.8 were possible using the three lenses available. Three aperture settings were also available enabling the depth of field to be doubled at the expense of illumination. At its best it only gives a depth of field of $\sim$1mm at ten times magnification.

The instrument was used, in conjunction with scanning electron microscopy, to study the well-sintered compacts by reflected light from the oxidation studies. The images were recorded on 35 mm film by a Carl Zeiss Icmarex 35 camera attachment.

CHAPTER 3
PRECIPITATION AND AGEING OF LEAD SULPHIDE

For basic oxidation studies finely divided lead sulphide samples of varying crystallite size and crystallinity were precipitated from solution at different pH levels, electrolyte concentrations and temperature. This research forms part of a wider study of the oxidation of lead sulphide and extends the previous work on precipitation and oxidation of zinc sulphide[71, 85].

3.1 INTRODUCTION

Previous researchers have reported on the preparation of lead sulphide by precipitation from solution using lead salts and both inorganic and organic sulphides. The results varied considerably with respect to the degree of crystallinity and particle shape and size. A comprehensive review of wet precipitation methods is given in Mellor[1].

According to Rodwell[86] lead sulphide precipitated from a solution of lead acetate always contains some of the latter compound. Lucas[87] using pure alkali-free solutions of lead salts obtained a brown-grey sample of colloidal lead sulphide on slow precipitation. Muck[88] reported that lead sulphide prepared from hydrogen sulphide in acetic acid solution is always amorphous, whilst when precipitated in the presence of excess nitric acid is deposited as microscopic cubes. Krivobok & Nakhodova[89], however, found that lead sulphide prepared from pure lead nitrate and hydrogen sulphide is amorphous, the crystalline form being obtained by heating the sample to 700°C in an atmosphere of carbon dioxide (inert atmosphere). According to Natta[90], lead sulphide when precipitated in solution "is seemingly amorphous with X-rays, but gives sharp lines with electronic rays" (electron diffraction). Amorphous lead sulphide was also obtained by Komarova et al[91] in a reaction involving solids. Nixon et al[92] studied the effect of temperature on the ageing of lead sulphide under wet and dry conditions and found that at 200°C sharper diffraction peaks were obtained, but optical examination revealed little significant change, although overall ageing was enhanced at higher temperatures.

A considerable amount of research has been carried out on the preparation of lead sulphide as single crystals and thin films for study

of the semi-conductor properties.

At low temperatures Reuter & Stein[38], Mellgren[44], Leja[45] all report basic lead thiosulphate as the main oxidation product of lead sulphide under moist conditions at room temperature. Eadington & Prosser[47] similarly found basic lead thiosulphate as the main oxidation product up to 12 h, for longer oxidation periods lead sulphate became the predominant species. Further investigations conclude that the oxidation product is dependent upon pH, as well as time of exposure. At pH 1.5 lead thiosulphate is unstable and the major product is sulphur; at pH 7 the dominant product is lead sulphate after 12 h and at pH 9 lead thiosulphate is found.

3.2   EXPERIMENTAL

3.2.1   Materials

BDH Analar lead nitrate and lead acetate were employed as the lead salts.   BDH Analar sodium sulphide and BDH hydrogen sulphide laboratory gas were used as the precipitating agents.   X-ray diffraction of the solid reagents showed the absence of any sulphate and other impurities.

3.2.2   Procedure

Samples of lead sulphide were precipitated from lead nitrate and lead acetate solutions at concentrations 0.1 mol dm^{-3}, 0.5 mol dm^{-3} and 1.0 mol dm^{-3} with hydrogen sulphide at a flow rate of 5 lh^{-1}, and 1.0 mol dm^{-3} sodium sulphide at both 20 and $85^{\circ}C$.

The hydrogen sulphide was passed through a Dreschel bottle containing distilled water and into the solutions via a gas dispersion tube.   Sodium sulphide solution was fed at a rate of 50 cm^3 h^{-1} from a burette.   The solutions were continually agitated by a magnetic stirrer during precipitation.

Samples of the precipitate were taken after 1 h, filtered and washed first with 100 cm^3 of distilled water, then with two 50 cm^3 aliquots of acetone.   The samples were dried in an oven at $60^{\circ}C$ for an hour, and stored in sealed bottles.   This procedure arrests any further ageing as in the treatment of calcareous materials[93].   The remaining precipitate was left in the mother liquor and further samples removed after 24 h and 80 h, and treated as above.   Ageing conditions were kept the same as for precipitation i.e. 20 and $85^{\circ}C$.

3.3   RESULTS

The precipitated samples were studied by electron microscopy, using a Philips EM 300 microscope, after preliminary treatment in an ultra-sonic bath to break down the aggregates. This enabled the crystallinity and crystallite sizes to be directly observed and micrographed for later comparison. The average crystallite size for the 72 samples was also determined by X-ray line-broadening measurements on the "200 reflection" at Bragg angle 15.055° using the Jones method (as described in Chapter 2). Surface area measurements of the samples employed nitrogen as adsorbate at -196°C. From the isotherm obtained the surface areas were calculated using the BET method (as described in Chapter 2). This gave a quantitative value for the potential reactivity of the samples, as well as a value for the average crystallite size.

Attempts were made to determine the relative quantities of lead sulphide and sulphate in the precipitated samples. First, the precipitate was treated with ammonium acetate in order to dissolve the lead sulphate. The remaining sulphide was filtered and the lead ion content of the filtrate determined by:-   (a) cathode-ray polarography, (b) gravimetric analysis as lead chromate,   (c) complexometric titration using EDTA and (d) using a specific lead ion electrode. However, the results indicated unacceptably high concentrations of lead sulphate and it was later concluded that results were high due to basic salts, in addition to lead sulphate. Thus, a method of analysis for determining the sulphate ion content of the filtrate (ammonium acetate extract) was developed.

This involved a reaction between the sulphate ions and barium chloroanilate[94] in acid solution to give barium sulphate and the coloured acid-chloroanilate ion:

$$SO_4^{2-} + BaC_6Cl_2O_4 + H^+ \longrightarrow BaSO_4\downarrow + HC_6CL_2O_4^-$$
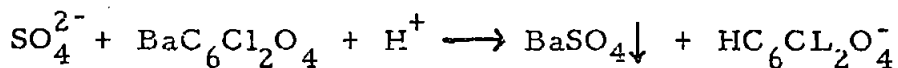
The amount of the acid-chloroanilate ion liberated is proportional to the sulphate ion concentration. However, the lead cation has to be removed since it forms an insoluble chloroanilate, this was effected by passage of the solution through a strongly acidic ion-exchange resin

(Amberlite IR-120). The pH governs the adsorbance of chloroanilic acid solution at a particular wavelength, e.g. at pH 4 the chloroanilate ion gives a broad adsorption peak in the visible region at 530 μm and a much more intense adsorption in the ultra-violet enabling the limit of detection of the sulphate ion to be extended to 0.06 ppm.

However, this technique was found to be very time consuming and therefore impracticable for the analysis of the very large number of precipitate samples. Thus, the sulphate was determined for the six samples used in the oxidation studies; the results are given in Table 4.1a.

The determination of the particle size distribution of the precipitated lead sulphide samples was attempted using a Coulter Counter Model Industrial D, to supplement the particle size range obtained from the electron micrographs. A computer programme (see Appendix I) was written in Fortran IV for use with the ICL 1905 computer to calculate the particle size distribution from the data obtained. An additional programme (see Appendix II) run on an IBM 1300 computer enables the distribution to be represented in a graphical form. However, the particle size range of the lead sulphides was outside that of the instrument, and thus this technique was not suitable for studying the precipitates.

Tables 3.3a, 3.3b, 3.3c and 3.3d give the surface areas and crystallite sizes of the lead sulphide samples precipitated under varying conditions of pH, electrolyte concentration, temperature and time.

Tables 3.3a and 3.3b show the surface areas and crystallite sizes when hydrogen sulphide was the precipitating agent; here the pH decreased to 1 with lead nitrate after ~5 min and to pH ~3 when lead acetate was used. Tables 3.3c and 3.3d give the results when sodium sulphide was the precipitating agent; here the pH remained below 7 for ~50 min and then rose to ~11 as the remaining sodium sulphide was added.

Table 3.3a

Code	Reactants	Ageing time	Surface area	Particle size range measured from electron micrographs	Av. Particle size calculated from line-broadening	Av. Particle size calculated from surface areas
		h	$m^2 g^{-1}$	nm	nm	nm
R	$50cm^3$ x 1.0 mol dm^{-3}	1	2.16	50 - 250	~400	370
		24	2.16	50 - 300	~400	370
	$Pb(NO_3)_2 + H_2S$	80	1.88	100 - 400	~600	425
N	$100cm^3$ x 0.5 mol dm^{-3}	1	2.49	50 - 100	~600	320
		24	2.20	50 - 200	~400	365
	$Pb(NO_3)_2 + H_2S$	80	1.68	50 - 300	> 600	465
A	$500cm^3$ x 0.1 mol dm^{-3}	1	4.29	40 - 100	110	190
		24	3.66	50 - 150	160	220
	$Pb(NO_3)_2 + H_2S$	80	2.55	50 - 200	> 600	315
P	$50cm^3$ x 1.0 mol dm^{-3}	1	10.60	20 - 70	80	75
		24	9.65	20 - 70	90	85
	$Pb(Ac)_2 + H_2S$	80	7.41	20 - 80	160	105
Z	$100cm^3$ x 0.5 mol dm^{-3}	1	8.87	30 - 60	100	90
		24	6.94	30 - 90	120	115
	$Pb(Ac)_2 + H_2S$	80	4.23	40 - 200	190	190
B	$500cm^3$ x 0.1 mol dm^{-3}	1	11.10	20 - 50	95	70
		24	10.52	20 - 60	120	75
	$Pb(Ac)_2 + H_2S$	80	10.89	20 - 60	190	75

Particle size data for samples precipitated with H_2S (5 lh^{-1}) and aged at $20^{\circ}C$.

Table 3.3b

Code	Reactants	Ageing time	Surface area	Particle size range measured from electron micrographs	Av. Particle size calculated from line-broadening	Av. Particle size calculated from surface areas
		h	$m^2 g^{-1}$	nm	nm	nm
S	$50cm^3$ x 1.0 mol dm^{-3}	1	<0.2	40 - 300	>600	4 μm
		24	<0.2	70 - 400	>600	4 μm
	$Pb(NO_3)_2 + H_2S$	80	<0.2	150 - 450	>600	4 μm
U	$100cm^3$ x 0.5 mol dm^{-3}	1	1.72	30 - 400	>600	465
		24	1.90	50 - 300	>600	420
	$Pb(NO_3)_2 + H_2S$	80	1.48	100 - 400	>600	540
X	$500cm^3$ x 0.1 mol dm^{-3}	1	2.27	40 - 300	>600	350
		24	2.17	50 - 300	>600	370
	$Pb(NO_3)_2 + H_2S$	80	2.01	150 - 500	>600	400
K	$50cm^3$ x 1.0 mol dm^{-3}	1	8.89	20 - 80	95	90
		24	7.48	20 - 100	110	105
	$Pb(Ac)_2 + H_2S$	80	6.34	20 - 100	140	125
G	$100cm^3$ x 0.5 mol dm^{-3}	1	7.83	20 - 80	110	100
		24	6.86	20 - 80	120	115
	$Pb(Ac)_2 + H_2S$	80	3.89	40 - 130	160	205
J	$500cm^3$ x 0.1 mol dm^{-3}	1	9.98	20 - 50	140	80
		24	5.11	50 - 150	280	155
	$Pb(Ac)_2 + H_2S$	80	3.00	50 - 250	∼600	265

Particle size data for samples precipitated with $H_2S(5 \ 1h^{-1})$ and aged at $85^{\circ}C$.

Table 3.3c

Code	Reactants	Ageing time	Surface area	Particle size range measured from electron micrographs	Av.Particle size calculated from line-broadening	Av.Particle size calculated from surface areas
		h	$m^2 g^{-1}$	nm	nm	nm
D	$50cm^3$ x 1.0 mol dm^{-3} $Pb(NO_3)_2$ + 1.0 mol $dm^{-3} Na_2S$	1	7.63	20 - 40	80	105
		24	7.25	20 - 40	100	110
		80	8.08	10 - 20	90	100
E	$100cm^3$ x 0.5 mol dm^{-3} $Pb(NO_3)_2$ + 1.0 mol $dm^{-3} Na_2S$	1	10.84	10 - 90	30	75
		24	8.54	20 - 100	50	95
		80	7.29	30 - 100	70	110
N	$500cm^3$ x 0.1 mol dm^{-3} $Pb(NO_3)_2$ + 1.0 mol $dm^{-3} Na_2S$	1	12.79	20 - 50	30	60
		24	10.45	<10 - 40	60	75
		80	11.38	<10 - 60	90	70
F	$50cm^3$ x 1.0 mol dm^{-3} $Pb(Ac)_2$ + 1.0 mol $dm^{-3} Na_2S$	1	4.61	50 - 130	110	170
		24	7.94	10 - 40	80	100
		80	9.39	10 - 40	40	85
Y	$100 cm^3$ x 0.5 mol dm^{-3} $Pb(Ac)_2$ + 1.0 mol $dm^{-3} Na_2S$	1	8.82	10 - 50	120	90
		24	7.78	10 - 60	140	105
		80	6.99	10 - 60	160	115
C	$500cm^3$ x 0.1 mol dm^{-3} $Pb(Ac)_2$ + 1.0 mol $dm^{-3} Na_2S$	1	9.1	20 - 70	60	90
		24	3.49	20 - 60	90	230
		80	3.10	20 - 150	190	260

Particle size data for samples precipitated with Na_2S (50 $cm^3 h^{-1}$) and aged at $20^{\circ}C$.

Table 3.3d

Code	Reactants	Ageing time	Surface area	Particle size range measured from electron micrographs	Av. Particle size calculated from line-broadening	Av. Particle size calculated from surface areas
		h	$m^2 g^{-1}$	nm	nm	nm
TR	$50cm^3$ x 1.0 mol dm^{-3}	1	10.27	< 10 - 40	60	80
		24	7.80	20 - 50	80	100
	$Pb(NO_3)_2 + 1.0$ mol dm^{-3} Na$_2$S	80	5.70	10 - 70	140	140
V	$100cm^3$ x 0.5 mol dm^{-3}	1	4.88	10 - 80	160	165
		24	3.56	10 - 80	190	225
	$Pb(NO_3)_2 + 1.0$ mol dm^{-3} Na$_2$S	80	2.96	10 - 90	160	270
W	$500cm^3$ x 0.1 mol dm^{-3}	1	9.24	20 - 80	80	85
		24	8.49	20 - 80	100	95
	$Pb(NO_3)_2 + 1.0$ mol dm^{-3} Na$_2$S	80	8.06	20 - 80	140	100
L	$50cm^3$ x 1.0 mol dm^{-3}	1	0.60	20 - 150	280	1300
		24	5.56	< 10 - 40	140	145
	$Pb(Ac)_2 + 1.0$ mol dm^{-3} Na$_2$S	80	3.90	< 10 - 60	160	205
H	$100cm^3$ x 0.5 mol dm^{-3}	1	7.49	20 - 70	70	105
		24	6.47	30 - 70	120	125
	$Pb(Ac)_2 + 1.0$ mol dm^{-3} Na$_2$S	80	3.55	20 - 50	200	225
Q	$500cm^3$ x 0.1 mol dm^{-3}	1	7.37	15 - 60	110	110
		24	5.72	20 - 90	140	140
	$Pb(Ac)_2 + 1.0$ mol dm^{-3} Na$_2$S	80	4.69	20 - 100	160	170

Particle size data for samples precipitated with Na$_2$S (50 cm^{3}h^{-1}) and aged at 85°C.

3.4 DISCUSSION

The crystallinity, crystallite size and composition of the products are governed by the conditions of precipitation, namely pH, electrolyte concentration, temperature and time of ageing. Correlations between these factors are discussed below.

3.4.1 Crystallinity and Crystallite Size

The samples precipitated from lead nitrate $(0.1 \text{ mol dm}^{-3})$ and hydrogen sulphide at $85^\circ C$ showed the greatest crystallinity, (cf Figure 32a, b, c), where also the largest crystallites (up to 500 nm) were found. Similar results were obtained at $20^\circ C$, where the crystallites were somewhat smaller (up to 350 nm), (Figure 33a, b, c). In both instances, owing to nitric acid formation, the pH decreases to 1 within 5 min of the commencement of precipitation. This is consistent with the work of Muck[88] who observed microscopic cubes in the presence of nitric acid.

Lead sulphide precipitated from lead nitrate and sodium sulphide shows a lower crystallinity; the crystallites have less uniform external faces and are more irregular in shape and smaller in size (up to 100 nm), (Figure 34a, b, c). The same overall trends are observed with samples prepared from lead acetate which produces lead sulphide of poorer crystallinity, and smaller crystallite size than the nitrate (Figure 35a, b, c). The lead acetate and hydrogen sulphide produces lead sulphide of medium crystallinity, with crystallite sizes up to 200 nm, (Figure 36a. b. c), whilst with sodium sulphide poorly crystalline products of up to 100 nm size are observed, (Figure 35a, b, c).

The degree of crystallinity and crystallite size correlates with the pH of the solution during precipitation and ageing, lower pH values enhancing greater crystallinity. For example, with lead nitrate and hydrogen sulphide (pH $\sim$1) the crystallites have well-defined faces whereas with lead acetate and sodium sulphide (pH up to 11) the samples have poorest crystallinity. This marked effect of pH on crystallite size is probably due to the effect on the solubility of lead sulphide (solubility decreases with increasing pH, see Table 1.1a).

The temperature does not appear to have a great effect on the crystallinity of the samples. However, higher temperatures do favour
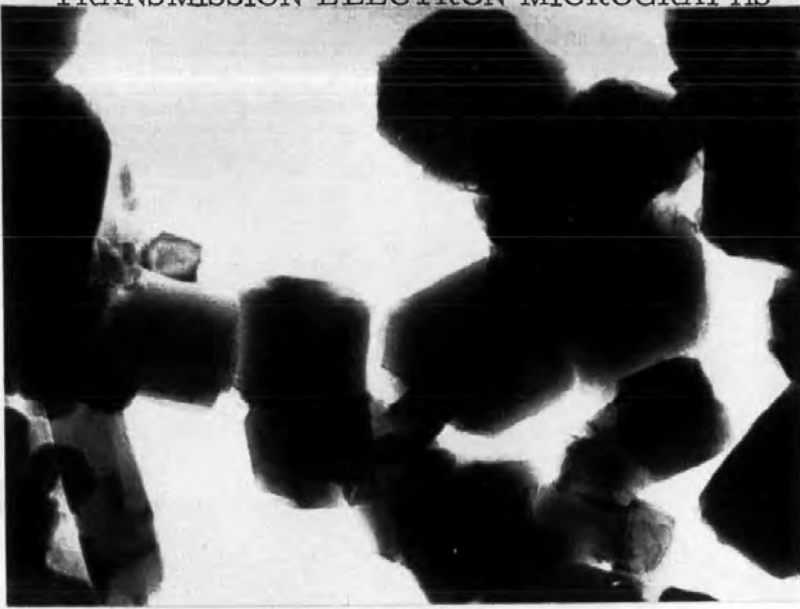
Figure 32a
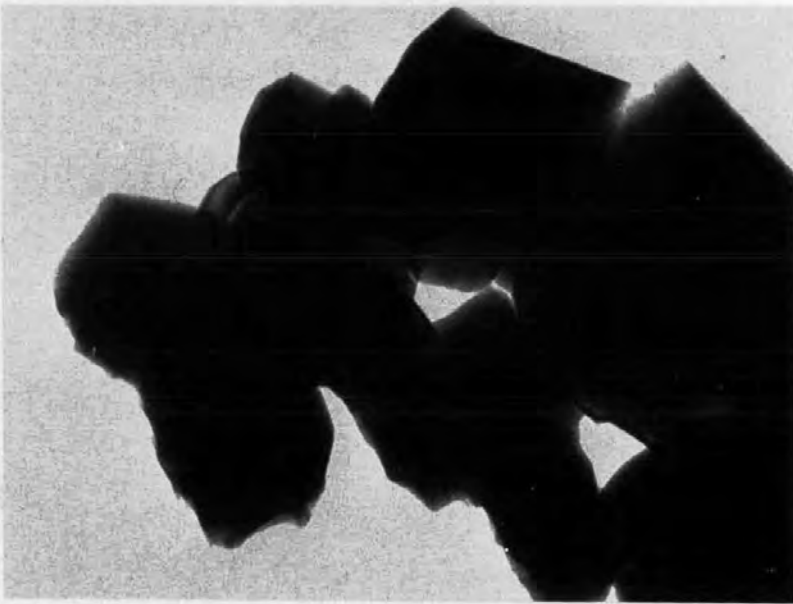Sample X1
Ageing time 1 h
Mag: 110,000 X
Scale 100 nm

Figure 32b
Sample U1
Ageing time 1 h
Mag: 110,000 X
Scale 100 nm

Figure 32c
Sample S1
Ageing time 1 h
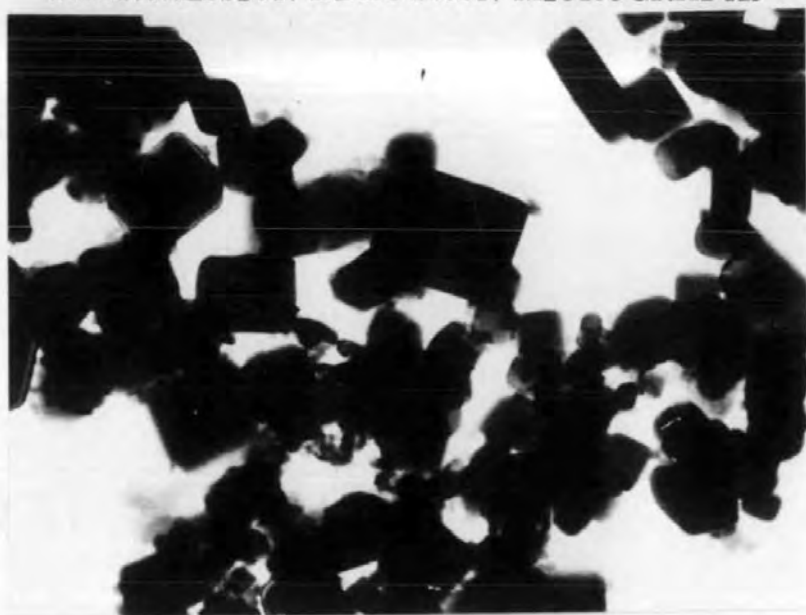Mag: 11,000 X
Scale 1 μm

Figure 33a
Sample A1
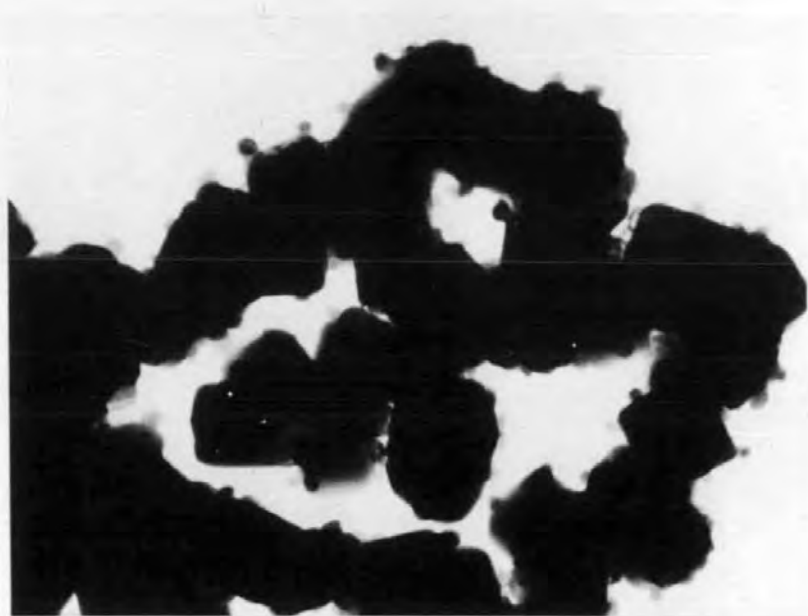Ageing time 1 h
Mag: 110,000 X
Scale 100 nm

Figure 33b
Sample N1
Ageing time 1 h
Mag: 110,000 X
Scale 100 nm

Figure 33c
Sample R1
Ageing time 1 h
Mag: 110,000 X
Scale 100 nm

Figure 34a
Sample W1
Ageing time 1 h
Mag: 110, 000 X
Scale 100 nm

Figure 34b
Sample V1
Ageing time 1 h
Mag: 110, 000 X
Scale 100 nm

Figure 34c
Sample TR 1
Ageing time 1 h
Mag: 110, 000 X
Scale 100 nm

TRANSMISSION ELECTRON MICROGRAPHS

Figure 35a
Sample C1
Ageing time 1 h
Mag: 110, 000 X
Scale 100 nm

Figure 35b
Sample Y1
Ageing time 1 h
Mag: 110, 000 X
Scale 100 nm

Figure 35c
Sample F1
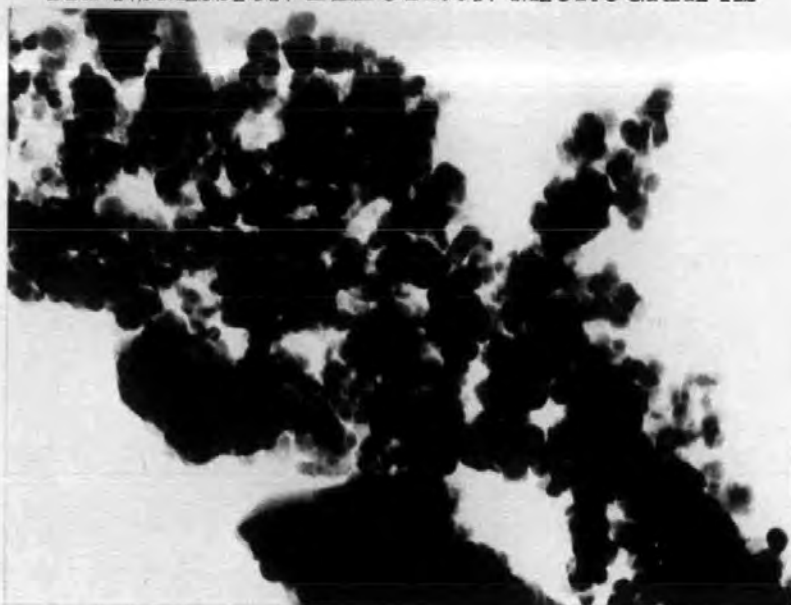Ageing time 1 h
Mag: 110, 000 X
Scale 100 nm

Figure 36a
Sample B1
Ageing time 1 h
Mag: 110, 000 X
Scale 100 nm

Figure 36b
Sample Z1
Ageing time 1 h
Mag: 110, 000 X
Scale 100 nm

Figure 36c
Sample P1
Ageing time 1 h
Mag: 110, 000 X
Scale 100 nm

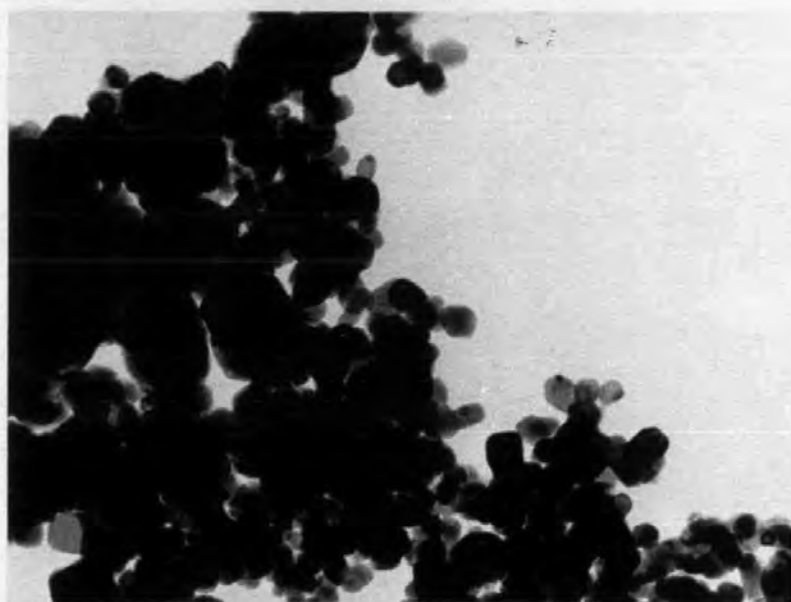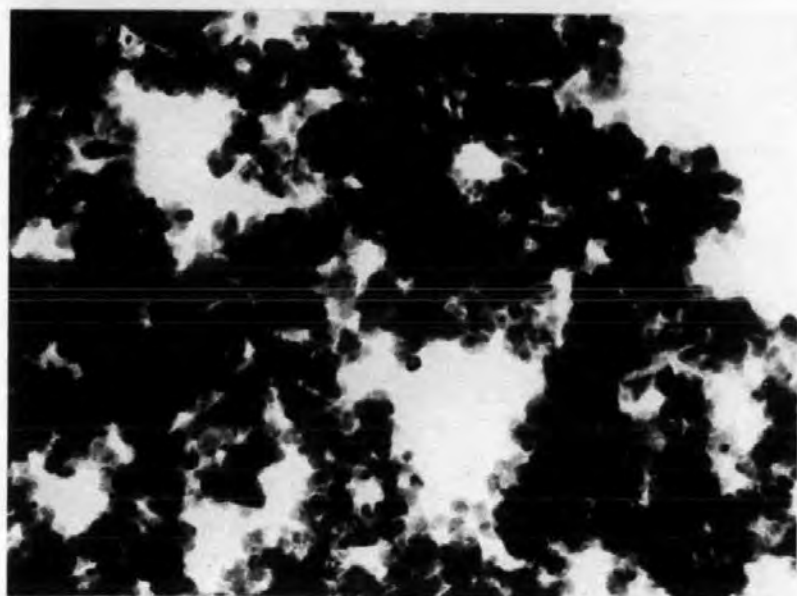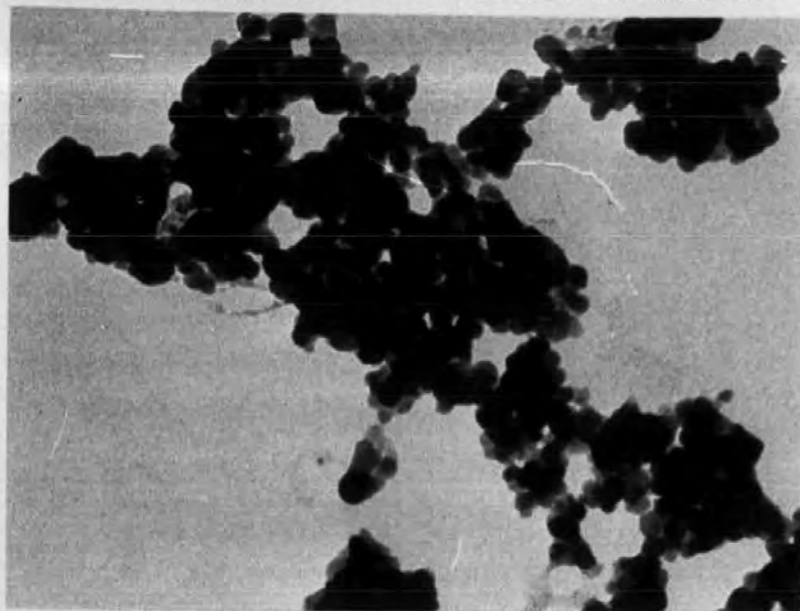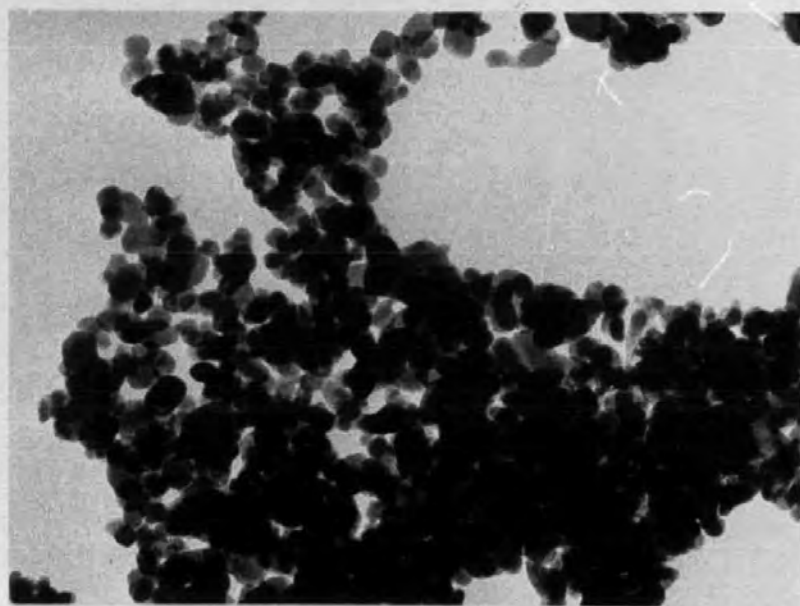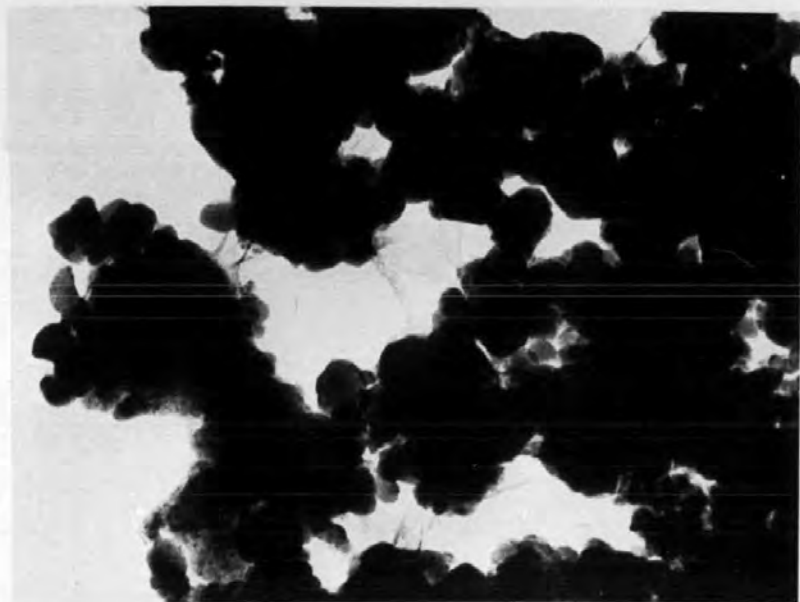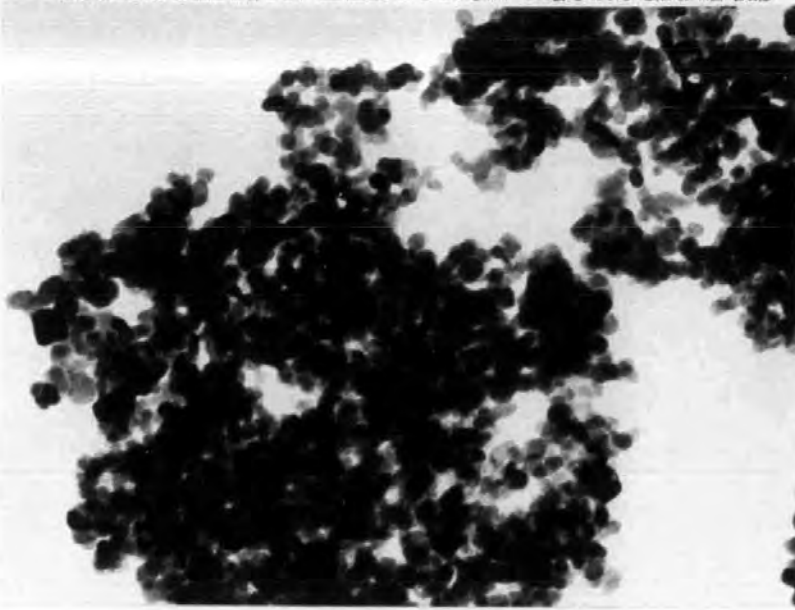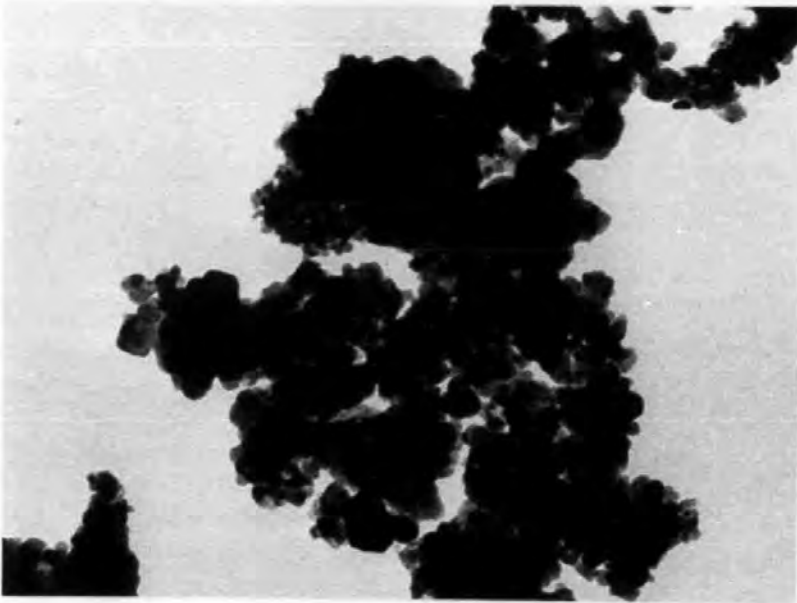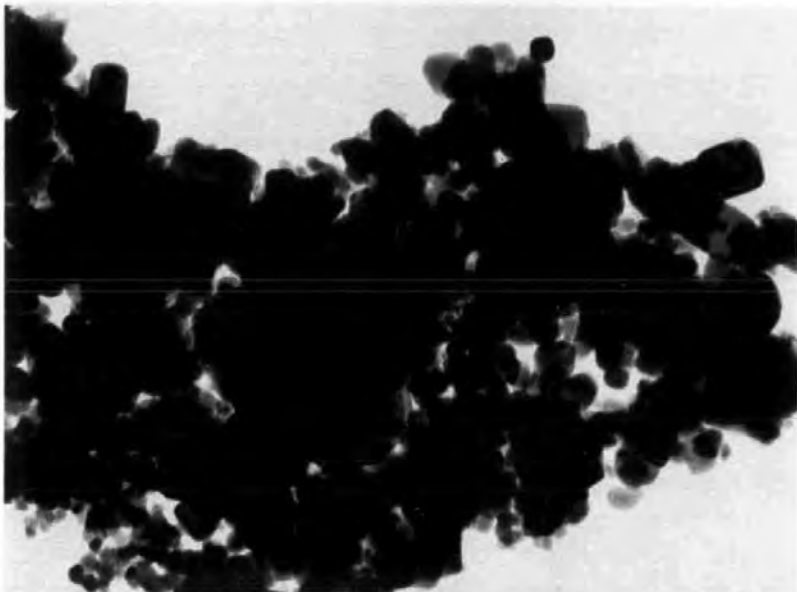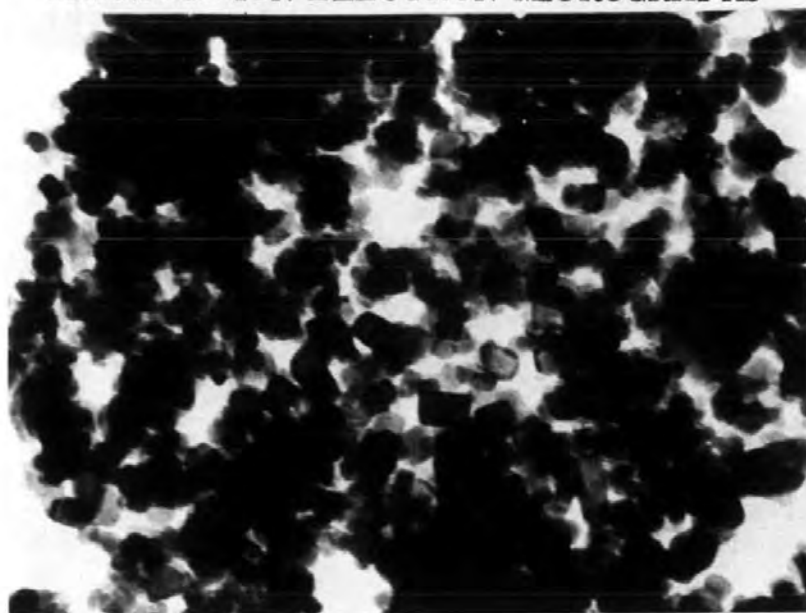Figure 37a
Sample J1
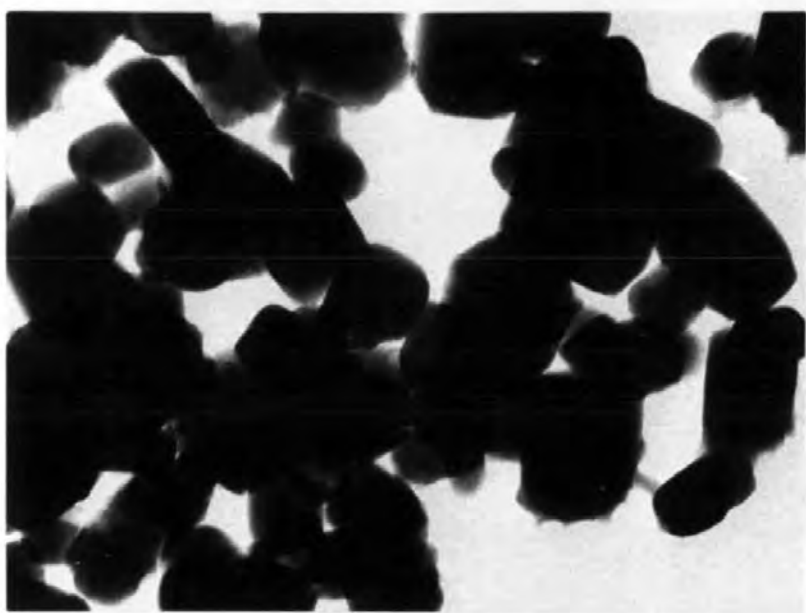Ageing time 1 h
Mag: 110,000 X
Scale 100 nm

Figure 37b
Sample J24
Ageing time 24 h
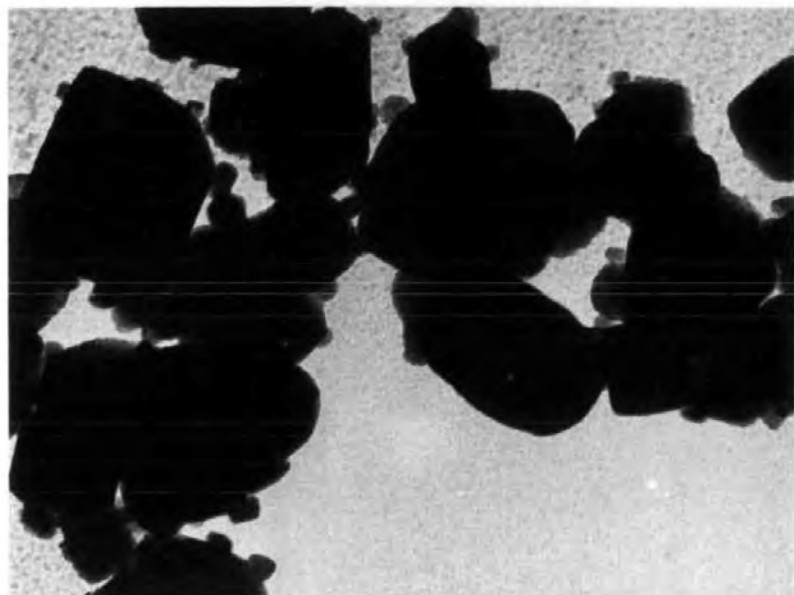Mag: 110,000 X
Scale 100 nm

Figure 37c
Sample J80
Ageing time 80 h
Mag: 110,000 X
Scale 100 nm

larger crystallites (compare Figure 32c and 33c). This is in accordance with the Ostwald ripening process where the smaller crystallites dissolve and recrystallize on the larger ones on ageing. Samples precipitated from higher concentration solutions tend to have larger crystallite sizes, e.g. compare crystallite sizes of samples A, N and R of Table 3.3a and Figure 33a, b, c. Thus, the ageing (see Figure 37a. b. c) of the precipitates proceeds by Ostwald ripening supplemented by coagulation, especially in the presence of higher electrolyte concentration.

All the samples gave good X-ray diffraction traces indicating that the samples were crystalline to varying degrees. Thus the observations of previous workers[88, 89, 90, 91] who report the formation of "amorphous" lead sulphide are not confirmed. Because most of these workers did not use diffraction methods to study the samples, their conclusions are open to question.

3.4.2 Measurement of Crystallite Size

The use of X-ray line-broadening to determine the average crystallite size is limited to the range 2-200 nm; above 1000 nm ($1\mu m$) broadening is negligible. The Jones[84] method employed for the determination of crystallite size can only be expected to achieve an overall accuracy of 20%. This method assumes a Gaussian distribution of particles which may be true in the case of freshly prepared precipitates, but on ageing the very small crystallites dissolve and recrystallize on the larger ones leading to a shift in distribution.

The half-peak breadths were measured to 0.5 mm, this meant the minimum broadening corresponded to an average crystallite size of $\sim$1300 nm (1.3 μm), i.e. ($\frac{1}{2}$ mm peak broadening). One mm broadening corresponds to 600 nm crystallite size, and the next two half mm steps correspond to 400 nm and 280 nm respectively. Thus, in the tabulated results the average crystallite sizes have the symbols $\sim$ and $>$ associated with them above 200 nm, because of the larger errors involved. Although the results above 140 nm are subject to a $>$ 20% error, they show the trends and agree with the other techniques used.

The surface area method employed for the determination of crystallite size assumes all the crystallites to be the same shape and size. In this case it was assumed the crystallites were cubes, although

assuming the crystallites to be spherical gives the same numerical result. The results obtained agreed with those calculated from line-broadening measurements, showing the same trends with ageing and temperature.

The crystallite size-range obtained from the electron micrographs gave values 2-3 fold lower than that obtained from the other two techniques. This is probably because of a sampling error in the preparation of the grids, i.e. the large crystallites settling out faster than the smaller ones. Although the results are 2-3 fold less than the other techniques the trends are nevertheless confirmed.

3.4.3 Formation of Lead Sulphate and Basic Salts

Lead sulphate was detected by X-ray diffraction in a number of precipitated lead sulphide samples.

Only at the highest salt concentration (1.0 $mol\,dm^{-3}$) and at 85°C did lead nitrate yield any lead sulphate with hydrogen sulphide. The high temperature and strong oxidation conditions, due to the nitric acid formation, lead to the formation of lead sulphate. Lead sulphate was formed from lead acetate (1.0 $mol\,dm^{-3}$) and hydrogen sulphide at 20°C to a small extent, and at 85°C to a greater extent. At the higher temperatures only, it is formed at the lower concentration (0.5 $mol\,dm^{-3}$) of lead acetate. Lead sulphate was always formed to varying degrees with sodium sulphide and lead nitrate, the extent increasing with temperature. Whilst sulphation was only detected at the two high concentrations of lead acetate with sodium sulphide.

The oxidation of lead sulphide in strongly acidic conditions (sample S) gave well-crystalline needles of lead sulphate as observed by electron microscopy, Figure 32c, whereas in alkaline conditions the lead sulphate identified by X-ray diffraction was never evident from the electron micrographs.

The precipitation of lead sulphide by the addition of sodium sulphide to lead acetate or nitrate solutions may require a longer time for completion because of the tendency to precipitate the basic lead nitrate or acetate, since much of the sodium sulphide solution is hydrolysed to sodium hydroxide and hydrogen sulphide, viz:

$$Na_2S + H_2O \rightleftharpoons 2NaOH + H_2S$$
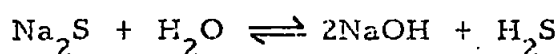
(giving a highly alkaline reaction for sodium sulphide solutions).

The pH range (5-8 mainly) for the precipitation of the basic lead salt is similar to that for lead sulphide by the above mode of addition. At higher pH levels (in the presence of excess sodium hydroxide or sodium sulphide) the basic salt will decompose to the normal hydroxide, $Pb(OH)_2$ or sulphide; this process probably occurs while the precipitates are being aged.

By analogy with other examples, such as decompositions of basic salts to hydrous oxides, this often leads to considerable increases in surface area[95] (or decreases in crystallite size).

e. g. $TiO.SO_4 \longrightarrow TiO_2, \, xH_2O.$
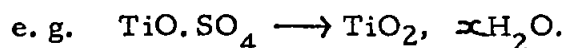
Atmospheric oxidation of some of the excess sulphide in solution produces sulphur to react with the newly-formed activated lead hydroxide producing lead thiosulphate and ultimately lead sulphate, cf similar changes occur in mixtures of lead hydroxide and colloidal suspensions of sulphur[96,]. However, in the present experiments any sulphur formed would be soluble in the excess of sodium sulphide (as polysulphides).

The reactions have been represented as:-

$$4Pb^{2+} + 8OH^- + 4S = 2PbS + PbO.PbS_2O_3.xH_2O + (4 -x) H_2O$$

$$PbO.PbS_2O_3.xH_2O = PbS + PbSO_4 + xH_2O.$$
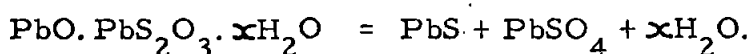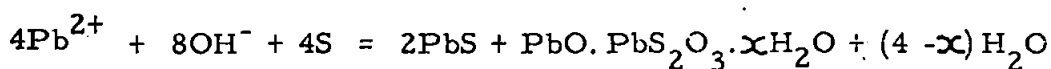
but their proposed initiating reaction:-

$$2PbS + 2H_2O + O_2 = 2Pb^{2+} + 4OH^- + 2S$$
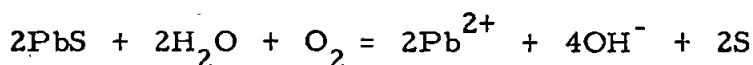
seems improbable in alkaline solutions because of the very low solubility of lead sulphide (Table 1.1a). More probably the first stage involves oxidation of the excess sulphide in solution, viz.,

$$2H_2S + O_2 \longrightarrow 2H_2O + 2S.$$
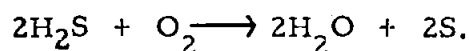
The oxidation of the hydrogen sulphide from the hydrolysed sodium sulphide would cause further hydrolysis by displacing the position of equilibrium of the reaction $Na_2S + 2H_2O) \rightleftharpoons 2NaOH + H_2S$ more to the right.

The formation of basic lead salts during precipitation resulting in the formation of lead sulphide and lead sulphate (in some cases) on

ageing is illustrated by the small increases in average crystallite size on ageing e. g. samples P, K, E, M, V, W and D; whilst with samples F and L, the average crystallite size decreases. In these instances, the loss of surface caused by Ostwald ripening and coagulation is evidently off-set by the increases in surface area from the decomposition of the basic lead salts and completion of the formation of lead sulphide and sulphate.

The formation of basic lead nitrate during the precipitation of lead sulphide has been demonstrated by following the pH changes during precipitation. Figure 38 gives the pH curve for the precipitation of lead sulphide from lead nitrate and sodium sulphide. Thus, there is complete precipitation after about 0.95 moles of sodium sulphide have been added. This is equivalent to 0.80 moles of lead sulphide and 0.05 moles $3Pb(OH)_2, Pb(NO_3)_2$ per mole of initial lead nitrate. Thus, 21.6% of material is basic salt for conversion ultimately to lead sulphide by excess sodium sulphide — a process which may give increases in surface area (like conversion of basic salts to metal hydroxides[95], which may be a stage in the above process).

3.4.4   Comparison with Previous Work on the Precipitation of Sulphides

This ageing behaviour of lead sulphide is comparable with that of copper sulphide samples precipitated by the addition of 1M sodium sulphide to 1M copper sulphate at room temperature where there is a tendency to form basic $3 Cu(OH)_2. CuSO_4$ as an impurity in the original material. James[98] has shown the average particle size decreases from 117 to 65 nm (determined by surface area measurements) on ageing from 1 h to 100 h for copper sulphide. At higher temperatures ($80^{\circ}C$) the precipitate ages more rapidly so that the loss in surface caused by Ostwald ripening and coagulation predominates. There are also progressive decreases in surface areas, as would be expected, for samples precipitated in acidic conditions (thereby precluding basic salt formation). This is the case as well for precipitation of lead sulphide in the present research.

Both the precipitates of lead and zinc sulphide[85], were similar in the fact that they gave the largest and best crystalline crystallites in acid conditions, with the crystallite sizes decreasing as the precipitation conditions become more alkaline. However, the most significant

Figure 38   pH curve for the addition of 1M sodium sulphide to 1M lead nitrate
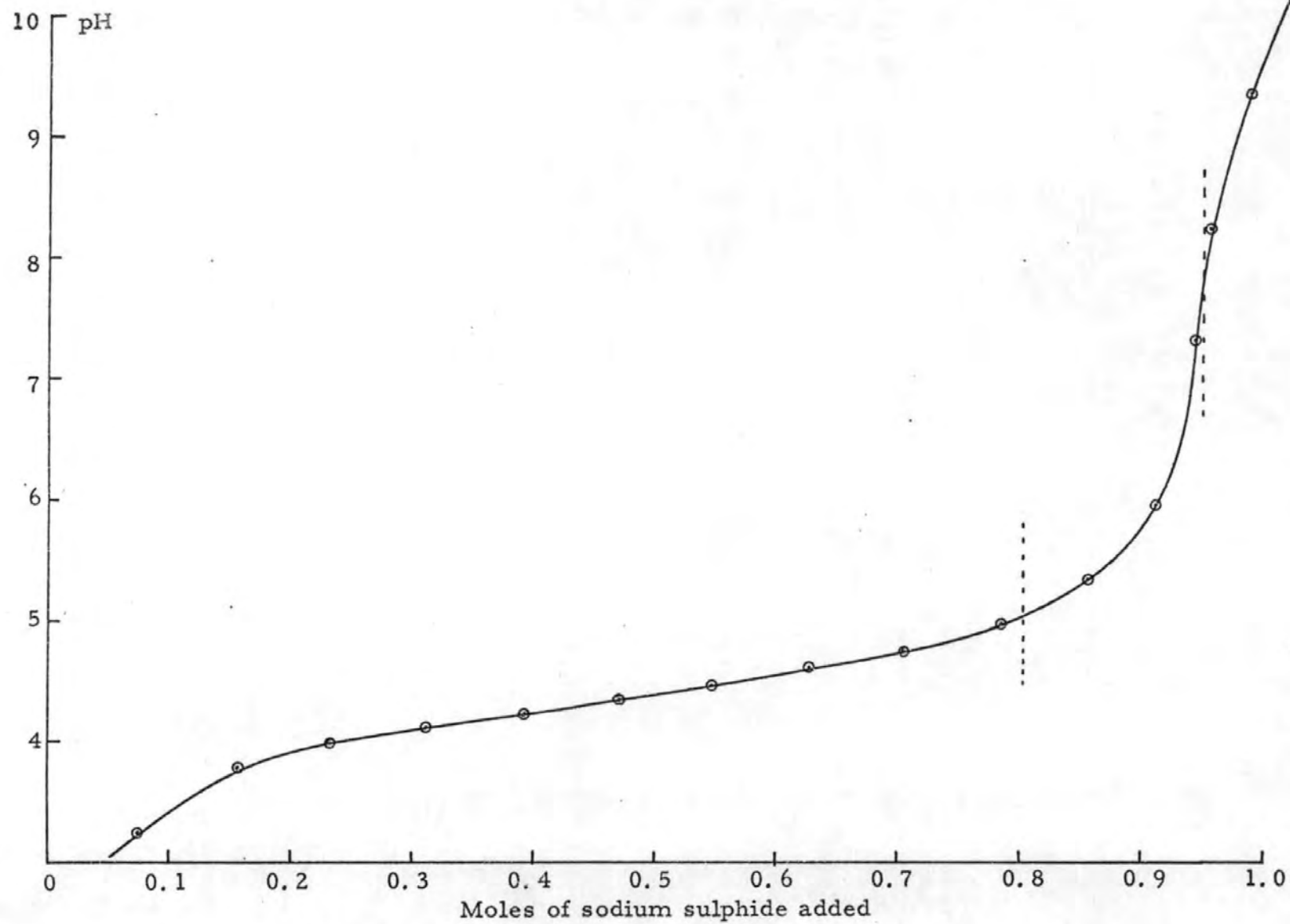
difference is the crystallite size obtained.   With zinc sulphide the surface area measurements range from 54 to 130 m^2g^{-1} corresponding to average crystallite sizes of 27 to 11 nm respectively, with the X-ray line-broadening measurements giving average crystallite sizes of between 2.5 and 6 times smaller.   The present researches on the precipitation of lead sulphide find that the surface area measurements range from 1.5 to 11 m^2g^{-1} with corresponding crystallite sizes of 460 to 30 nm.

Figure 39 shows a typical nitrogen adsorption isotherm of lead and zinc sulphide.   For lead sulphide between 0.4 and 0.8 relative pressure there is slight hysteresis indicating porosity with the pore sizes given by the inset scale, and calculated from the expression[99]:-

$$\ln \frac{P}{P_0} = \frac{2\gamma_0}{RT\rho r}$$

where $\frac{P}{P_0}$ = relative pressure

γ_0 = surface tension of adsorbate

ρ = density of adsorbate

r = radius of pore

R = gas constant

T = adsorption temperature K.

The adsorption isotherm for zinc sulphide was carried out using liquid oxygen at -183°C shows a large hysteresis loop which suggests high porosity, with the pore sizes given by the inset scale.   The relative number of particular sized pores may be gauged from the vertical separation of the adsorption and desorption curves.

In both cases hysteresis does not occur below $\sim$0.4 relative pressure and thus the use of the BET method for determining the monolayer capacity is justified.

Figure 39a
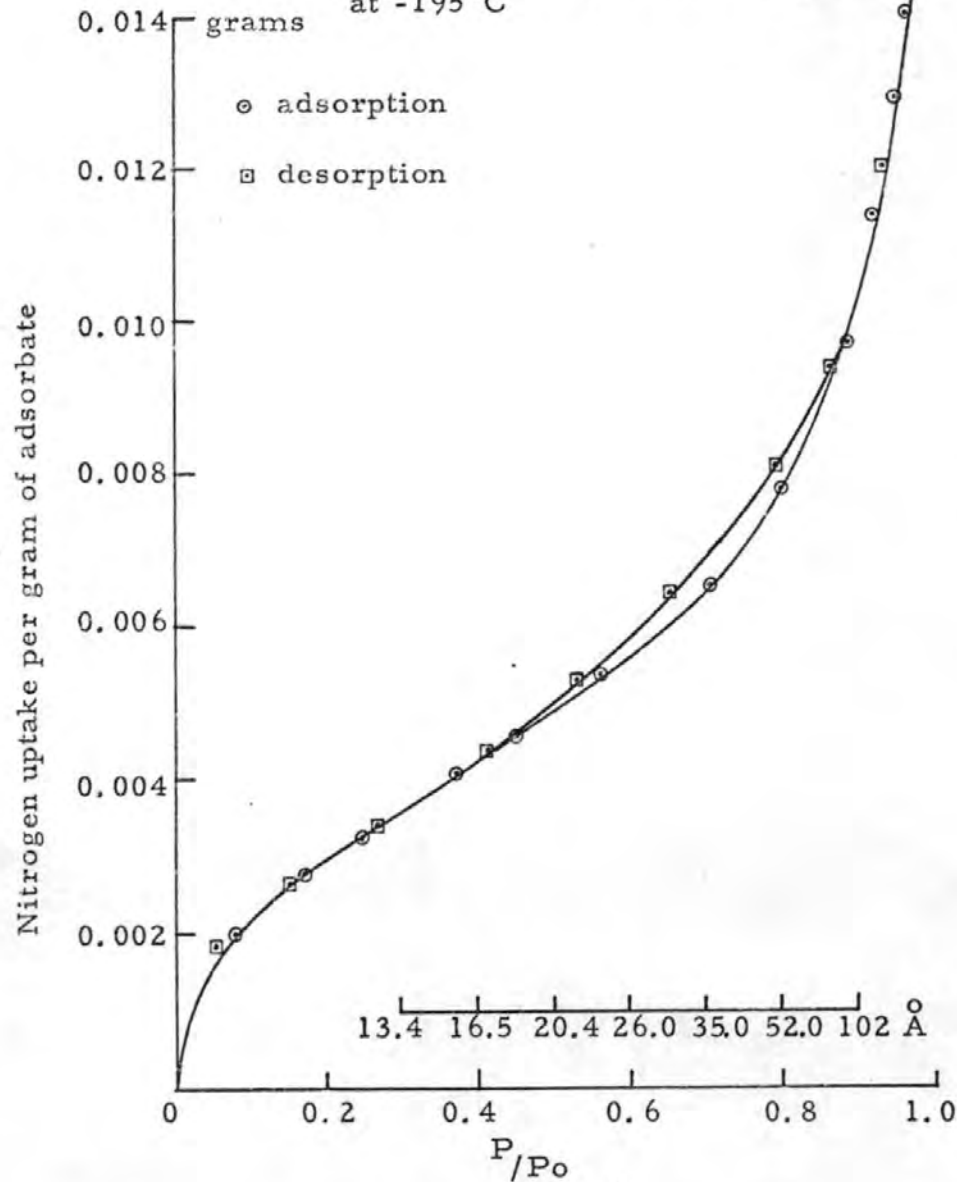Adsorption isotherm of N₂ on lead sulphide at -195°C

Figure 39b
Adsorption isotherm of O₂ on zinc sulphide at -183°C
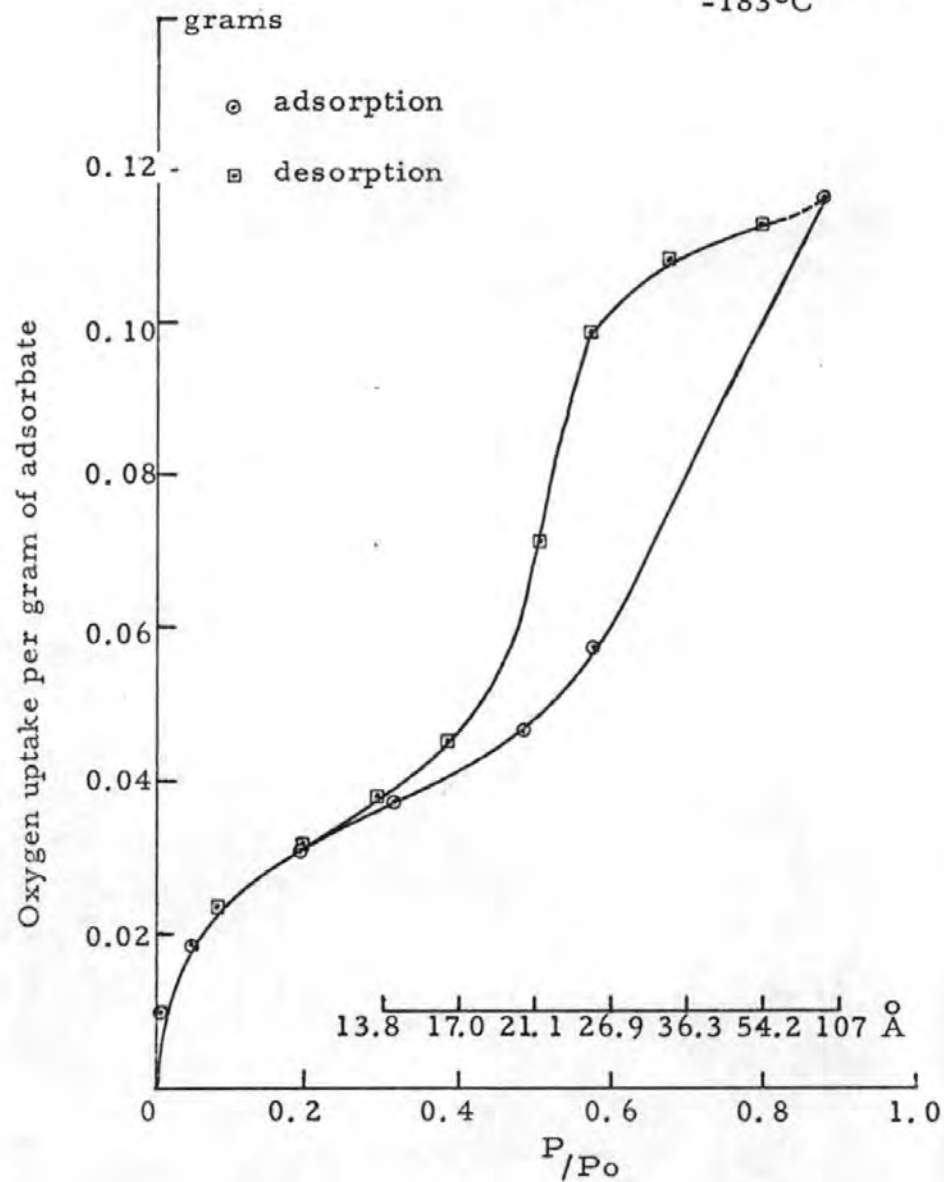
CHAPTER 4

OXIDATION OF LEAD SULPHIDE

The oxidation of lead sulphide has been investigated using DTA and TG in conjunction with X-ray phase analysis and optical and scanning-electron microscopy. The thermal equipment employed was a Stanton-Redcroft Massflow Balance Model MF-H5 as described in Section 2.1

4.1   INTRODUCTION

Six samples were selected for detailed study, viz., five precipitated samples of varying surface area, crystallinity and crystallite size and commercial BDH lead sulphide. From the precipitated samples W, D, Q, J and X were chosen. Table 4.1a gives the details of precipitation, surface area, crystallite sizes and degree of sulphation of the selected samples.

4.1.1   Experimental

A mixed stock sample of the 24 h (50%) and 80 h (50%) aged samples was used in the oxidation studies.

Isothermal oxidation investigations were performed initially on the six samples. The 150 mg samples were contained in alumina crucibles. Small quantities were purposely chosen so that the sample thickness would be low to allow complete oxidation. In practice, the sinter cakes produced were 2-3 mm thick.

The furnace was raised and heated to the pre-selected oxidation temperature, the crucible placed on the TG pedestal and the furnace lowered over the sample. The sample was held at this temperature for 1 h then removed, allowed to cool, and a portion analysed for phase composition by X-ray diffraction. This procedure was repeated for each sample at temperature intervals of 50 degrees from the onset of oxidation, as determined by preliminary experiments, to $950^{\circ}C$.

The resultant traces of weight change against time were replotted as percentage weight gain or loss (after buoyancy corrections were applied) against time, and gave the series of isothermal curves, Figures 40a, b - 45 a, b. The X-ray analysis of phases present were tabulated and are presented in Tables 4.2a - f.

As discussed in Section 1.2, the oxidation of lead sulphide occurs

Table 4. 1a   Details of the six chosen lead sulphide samples

% lead sulphate in sample	Mode of precipitation or source	Code	Surface area m^2g-1	Equivalent spherical diameter calculated from S. A. result $\overset{o}{A}$	Crystallinity as determined from electron micrographs
11	lead nitrate + sodium sulphide @ 85°C	W24/80	8.3	980	poor crystallinity
15	lead nitrate + sodium sulphide @ 20°C	D24/80	7.7	1050	poor crystallinity
< 1	lead acetate + sodium sulphide @ 85°C	Q24/80	5.2	1550	poor crystallinity
< 1	lead acetate + hydrogen sulphide @ 85°C	J24/80	4.1	2100	intermediate crystallinity
< 1	lead nitrate + hydrogen sulphide @ 85°C	X24/80	2.1	3850	well-crystalline
1. 5	commercial BDH	BDH	5.6	1450	poor crystallinity

in two stages.   Stage one is the low temperature oxidation where the rate controlling process is chemisorption of oxygen with an activation energy of 46-50 k J mol^{-1}.   In stage two at higher temperatures (above 600-700°C) sintering of the oxidation products becomes extensive and the reaction rate is dependent upon the diffusion of oxygen inward and product gases outward; here there is a four-fold decrease in activation energy.

4.2   STAGE ONE : Low Temperature Oxidation

There are three main initial oxidation reactions:-

$$PbS + 2O_2 \longrightarrow PbSO_4 \tag{1}$$

$$2PbS + 3O_2 \longrightarrow 2PbO + 2SO_2 \tag{2}$$

$$2PbO + 2SO_2 + O_2 \longrightarrow 2PbSO_4 \tag{3}$$
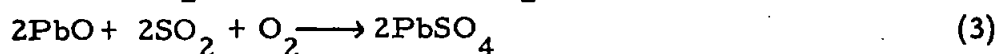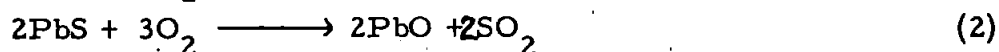
By studying the free energies of the above reactions the feasibility of each may be assessed.   Table 4.2g gives the free energy data for the six main oxidation-reduction reactions.   From the free energy values reaction (1) occurs more readily than reaction (2); to promote reaction (2) it would be advantageous to reduce the sulphur dioxide partial pressure.   Reaction (1) consumes 2 moles of oxygen per mole of lead sulphide whereas reaction (2) only consumes 1.5 moles oxygen.   Thus, initially at the surface of the sample one would expect to find lead sulphate because of the freely available oxygen, and the greater likelihood from the free energy data.   As oxidation proceeds the lead sulphate layer reduces the supply of oxygen to the lead sulphide within the sample and thus makes reaction (2) more likely, because of the reduced oxygen consumption.   Reaction (2) produces sulphur dioxide which like the oxygen entering the sample is inhibited from leaving by the surface lead sulphate and thus reaction (3) is distinctly possible.   Any lead oxide formed will be in a highly active form and may combine with lead sulphate to give monobasic lead sulphate.   Thus the modes of reaction at the lower temperatures (below 600°C) appear to be:-

$$PbS \quad \overset{1.5\,O_2}{\nearrow} \quad \begin{array}{c} PbO \\ + \\ 2SO_2 \end{array} \quad O_2 \longrightarrow PbO.PbSO_4$$
$$\underset{2O_2}{\searrow} PbSO_4$$
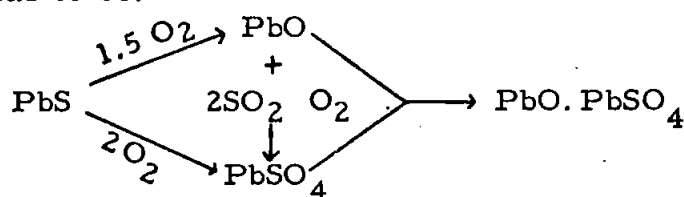
4.2.1   Results and Discussion

The thermogravimetric curves in Figures 40a, b - 45a, b for the oxidation of the precipitated lead sulphides show that oxidation to lead sulphate (requiring a maximum percentage weight gain of 26.75%) is never complete within 1 h at any of the temperatures.   Usually the rate of oxidation decreases considerably and often becomes almost negligible at the end of the hour.   These smaller weight gains are

Table 4.2g

Reaction \ Temperature °C	400	550	700	850	900	1000	1100
$PbS + 2O_2 \longrightarrow PbSO_4$ ———(1)	-645428	-606235	-570190	-543785	-517196	-495956	-472282
$PbS + 1.5O_2 \longrightarrow PbO + SO_2$ ——(2)	-363207	-350740	-338144	-329730	-321286	-312747	-304315
$PbS + O_2 \longrightarrow Pb + SO_2$ ———(3)	-210438	-212947	-214979	-217142	-217376	-220278	-221182
$PbS + 2PbO \longrightarrow 3Pb + SO_2$ ——(4)	98047	67535	37914	9238	- 125	-18547	- 36785
$PbS + PbSO_4 \longrightarrow 2Pb + 2SO_2$ ——(5)	161266	107891	48176	-7368	- 29274	-60225	- 94689
$2Pb + O_2 \longrightarrow 2PbO$ ———(6)	-308243	-280536	-253262	-226359	-217175	-200020	-182761

Values of the free energies according to Kelley from 400-1100°C in $kJ\ mol^{-1}$

ascribed to incomplete oxidation to lead sulphate at lower temperatures and to formation of basic sulphates and lead oxide at higher temperature; formation of the oxide produces percentage weight losses.

X-ray analysis indicates that lead sulphate is the main product at lower temperatures (below 500°C). This evidently inhibits further oxidation by coating the outside of the sulphide particles.

The equivalent spherical diameter of the initial sulphide crystallites can be calculated from the surface areas of the samples. Hence, the thickness of the lead sulphate layer can be estimated from the precentage oxidation of the sulphide (which the percentage weight gain represents) and the change in molecular volume in the conversion of lead sulphide to lead sulphate calculated from the X-ray densities of the phases (7.5 and 6.2g cm^{-3} respectively). Lead sulphide changes its volume 1.534-fold when it forms lead sulphate, so that the fractional oxidation, x, of a sample of lead sulphide causes a proportionate volume change of $(1 - x) + 1.534x = 1 + 0.534x$. The equivalent spherical diameter of the coated sulphide, d, increases from d to $d\left(1 + 0.534x\right)^{\frac{1}{3}}$, while the diameter of the unchanged sulphide core decreases to $d\left(1 - x\right)^{\frac{1}{3}}$. The thickness, t, of the product layer is then given by the equation:-

$$2t = d \cdot \left(1 + 0.534x\right)^{\frac{1}{3}} - \left(1 - x\right)^{\frac{1}{3}} .$$

Results for samples oxidized isothermally at 400°C for times of 8 min and 1 h are given in Table 4.2h.

Table 4.2h

Sample	Specific surface S m^{2}g^{-1}	Equivalent spherical diameter Å d	Product layer thickness t (Å)	
			after 8 min	after 1 hr
poorly crystalline Q	5.2	1550	130	134
intermediate crystallinity J	4.1	1950	30	90
well crystalline X	2.1	3800	15	58
poorly crystalline + lead sulphate W	8.3	960	49	57
D	7.7	1050	25	25
BDH	5.6	1450	130	190

Figure 40a   Sample W24/80 oxidized isothermally in static air
(400-650°C)
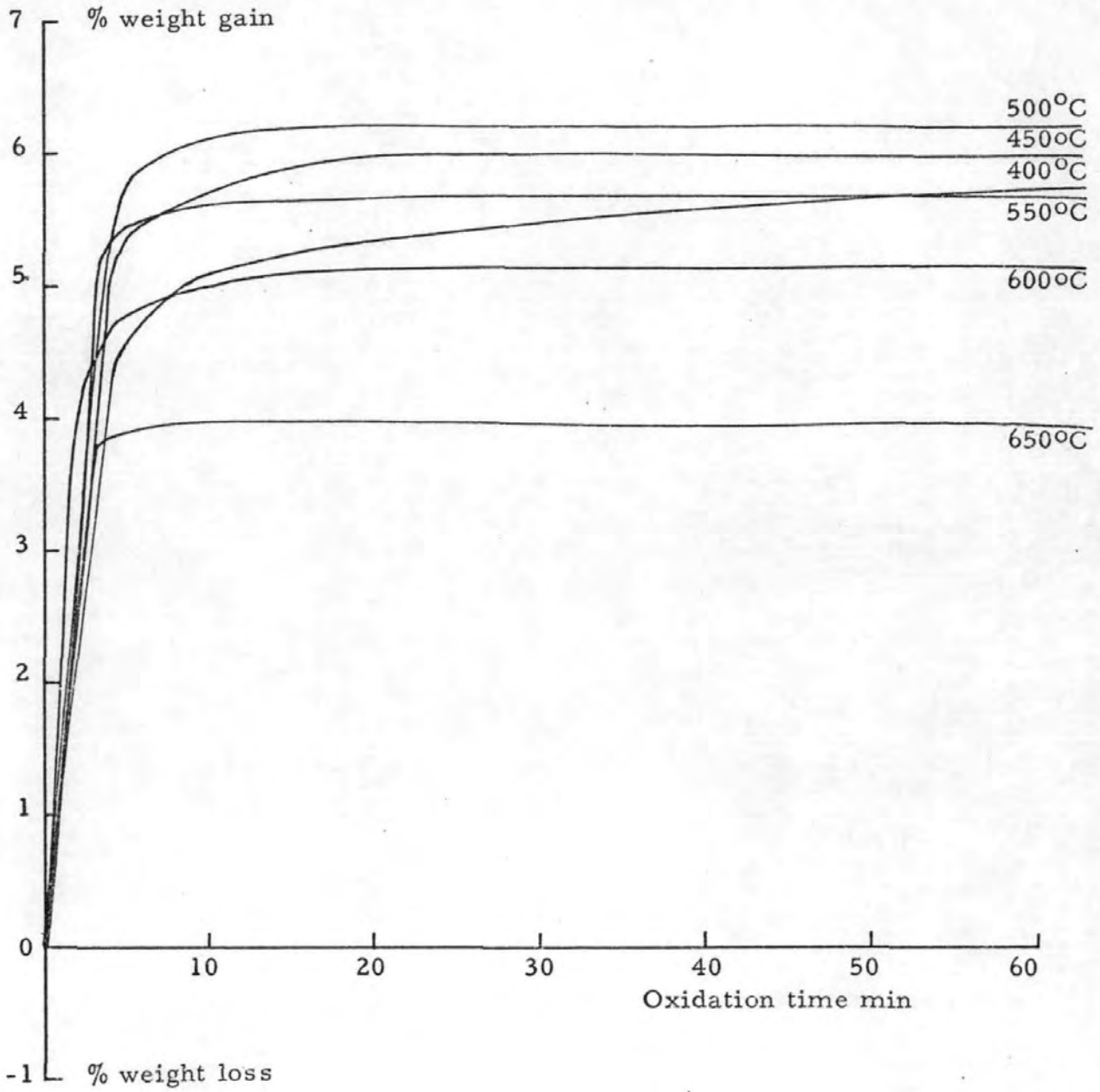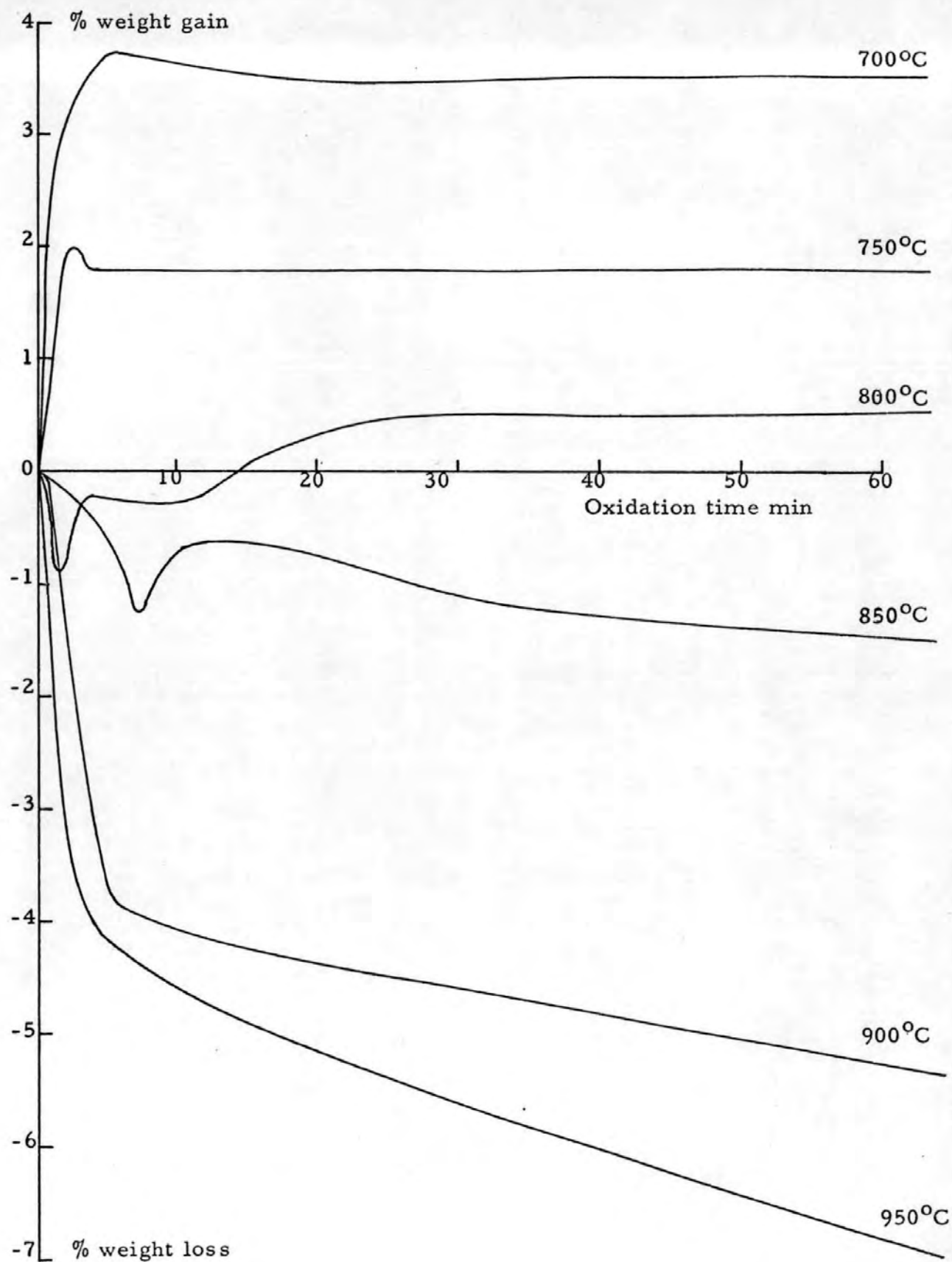
Figure 40b   Sample W24/80 oxidized isothermally in static air
·(700-950°C)

Figure 41a   Sample D24/80 oxidized isothermally in static air
(400-650°C)
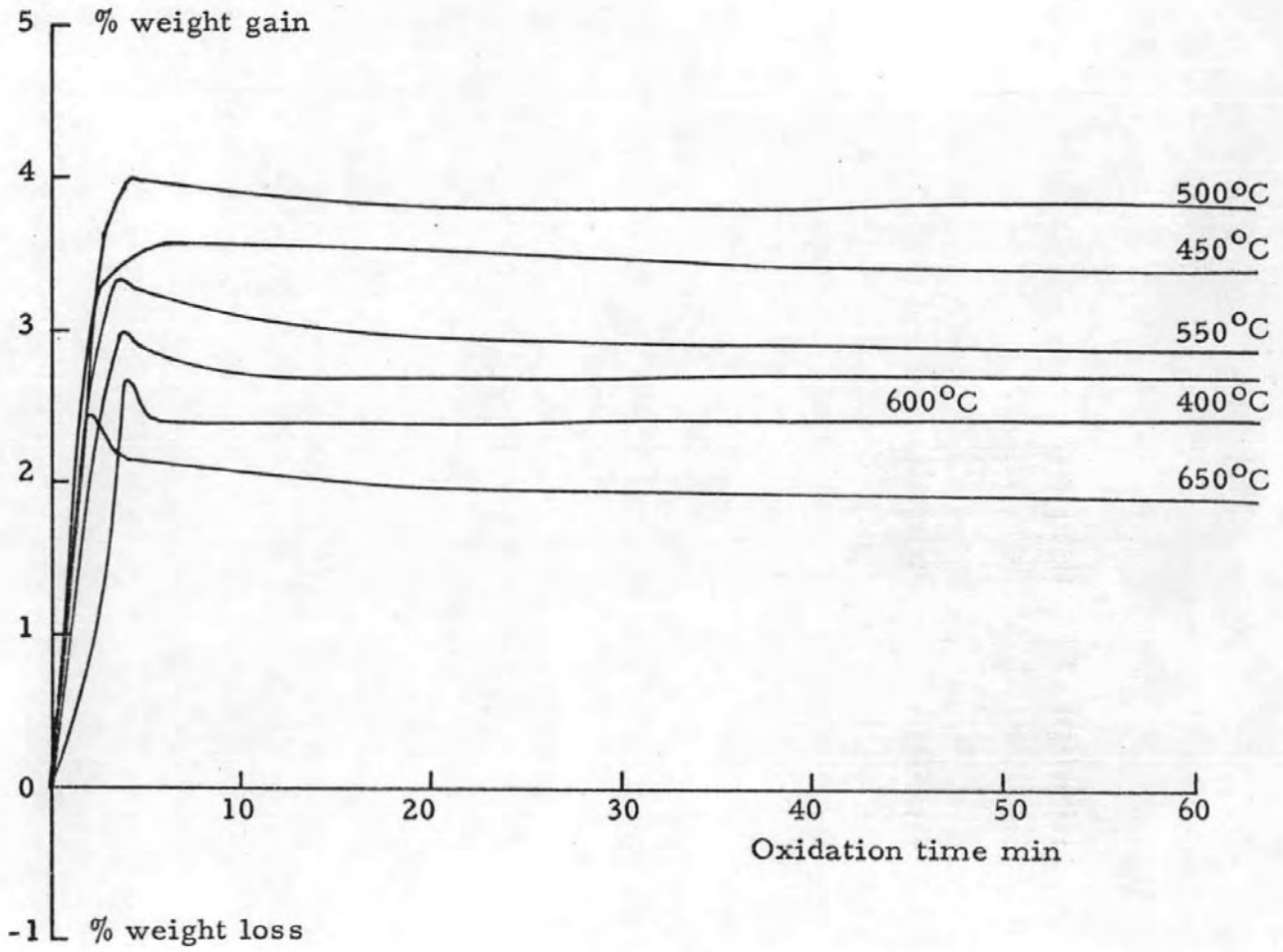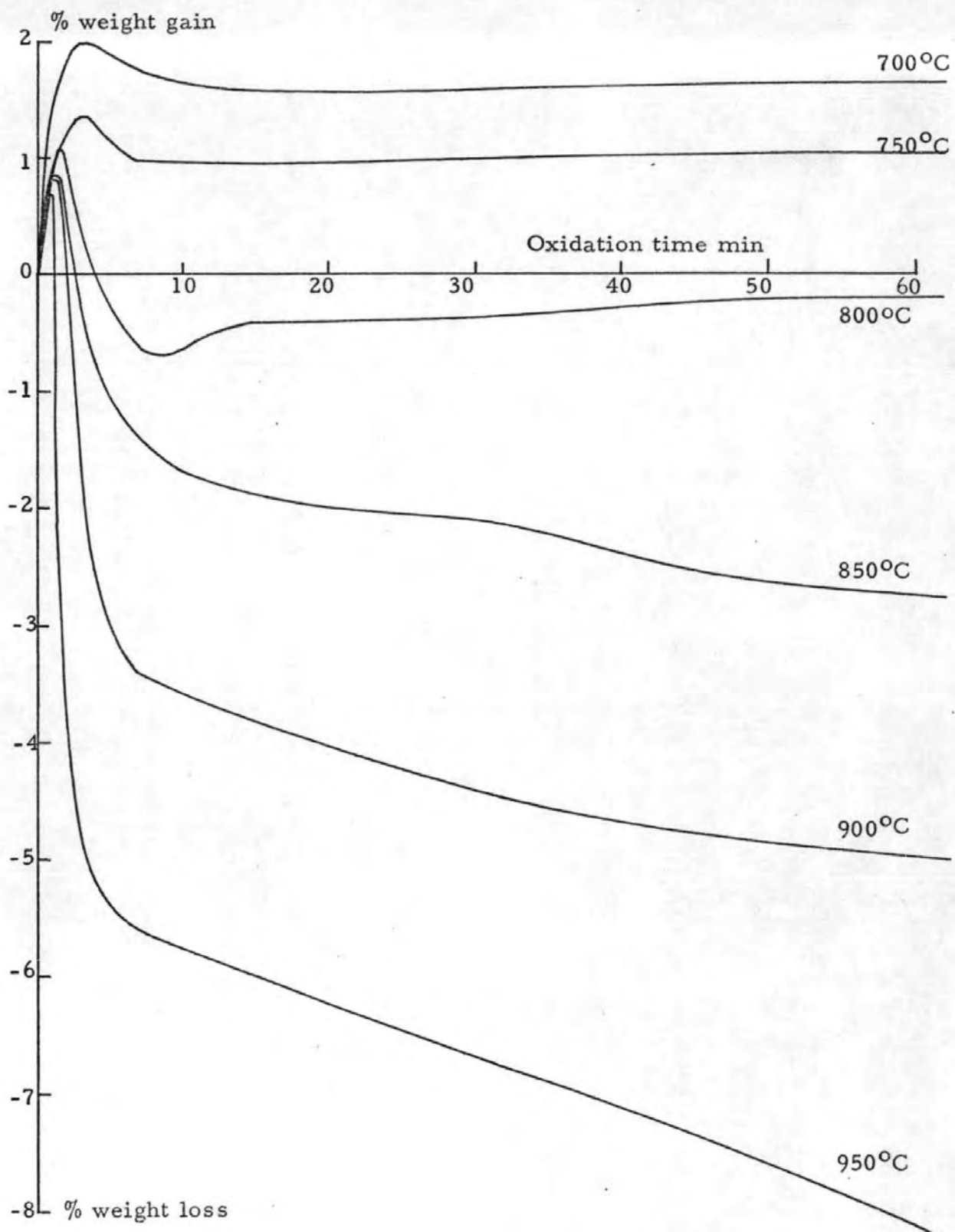
Figure 41b   Sample D24/80 oxidized isothermally in static air
(700-950°C)

Figure 42a   Sample Q24/80 oxidized isothermally in static air
(150-550°C)
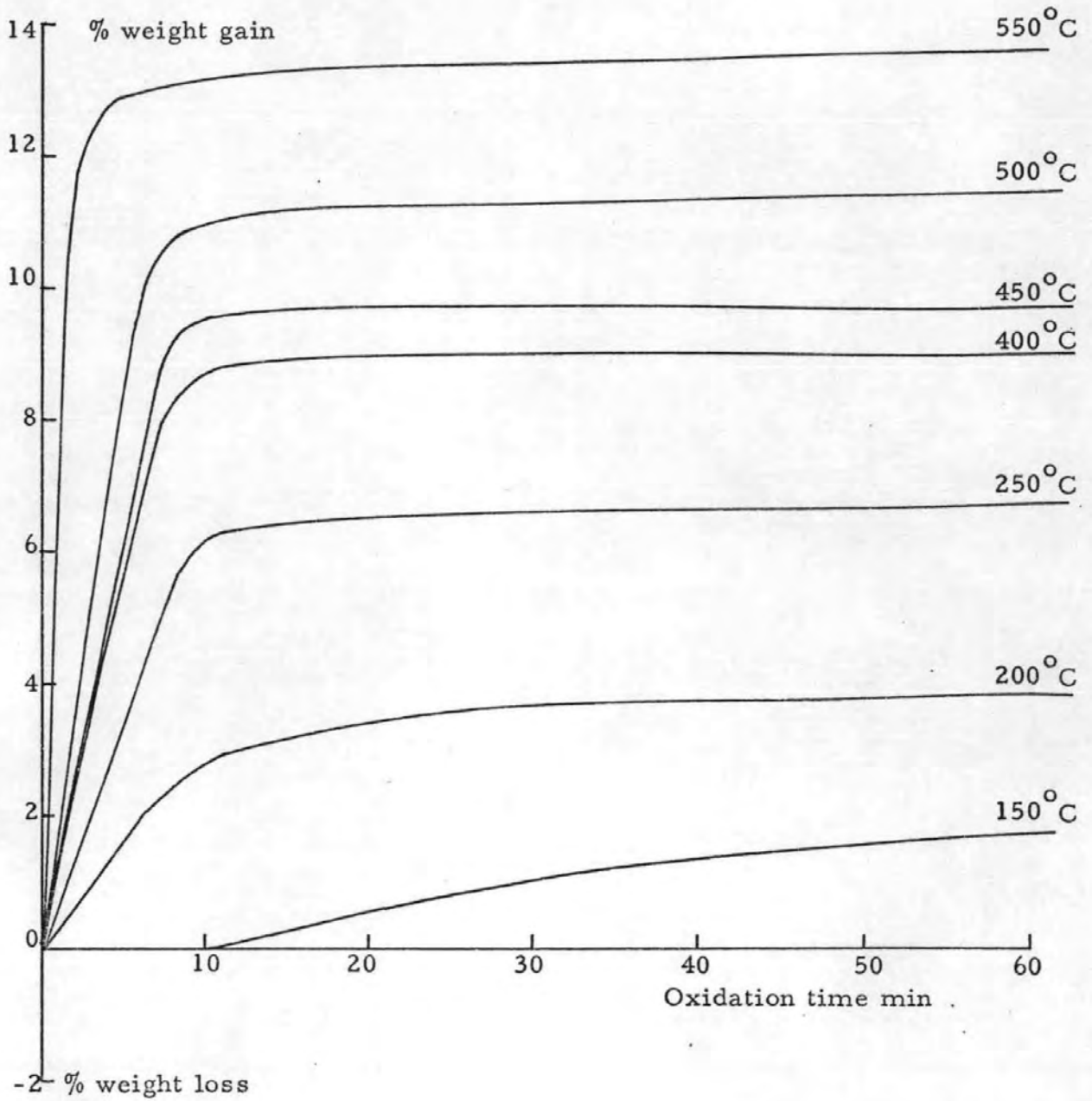
Figure 42b   Sample Q24/80 oxidized isothermally in static air
(600-950°C)
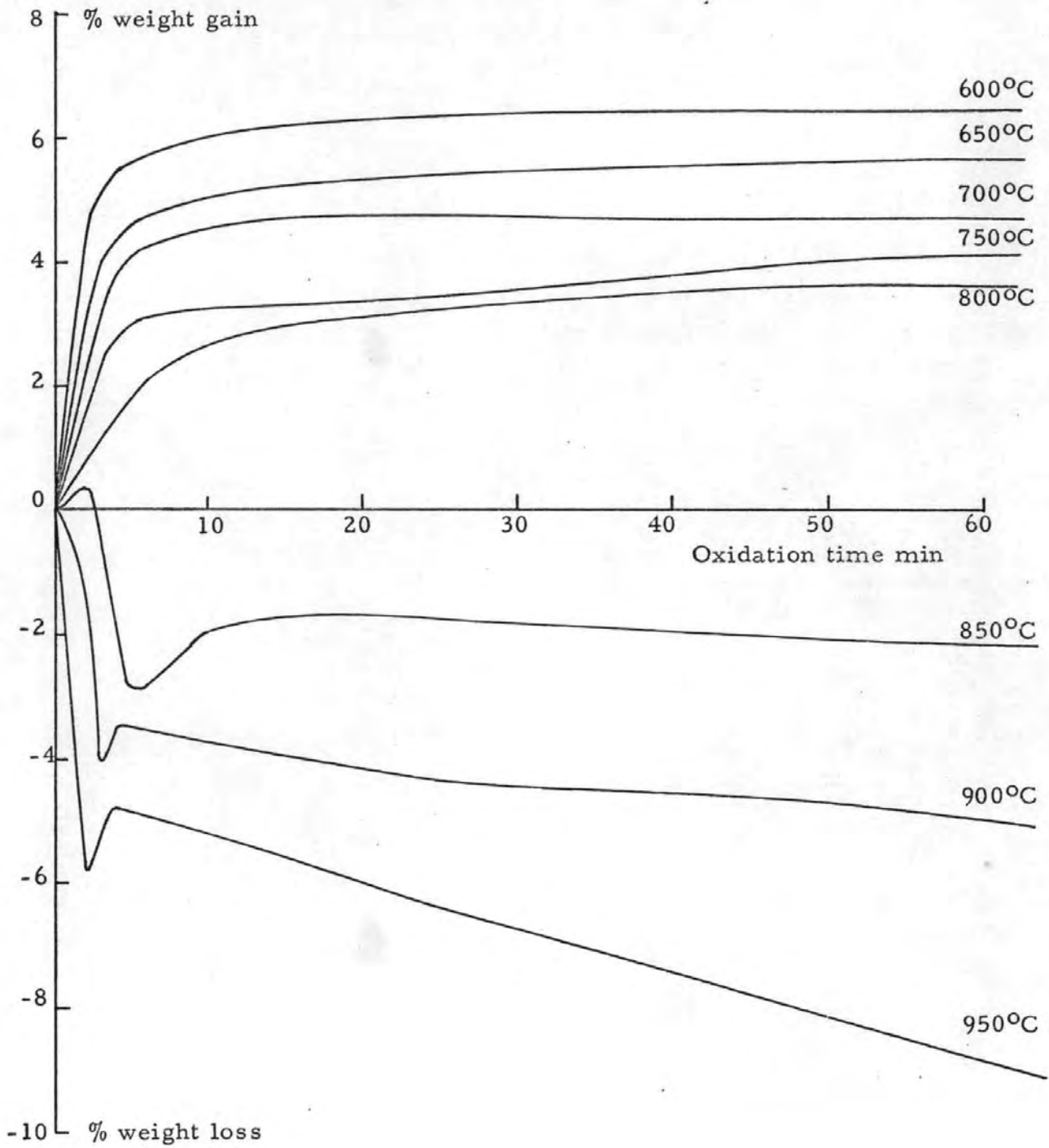
Figure 43a   Sample J24/80 oxidized isothermally in static air
(400-650°C)
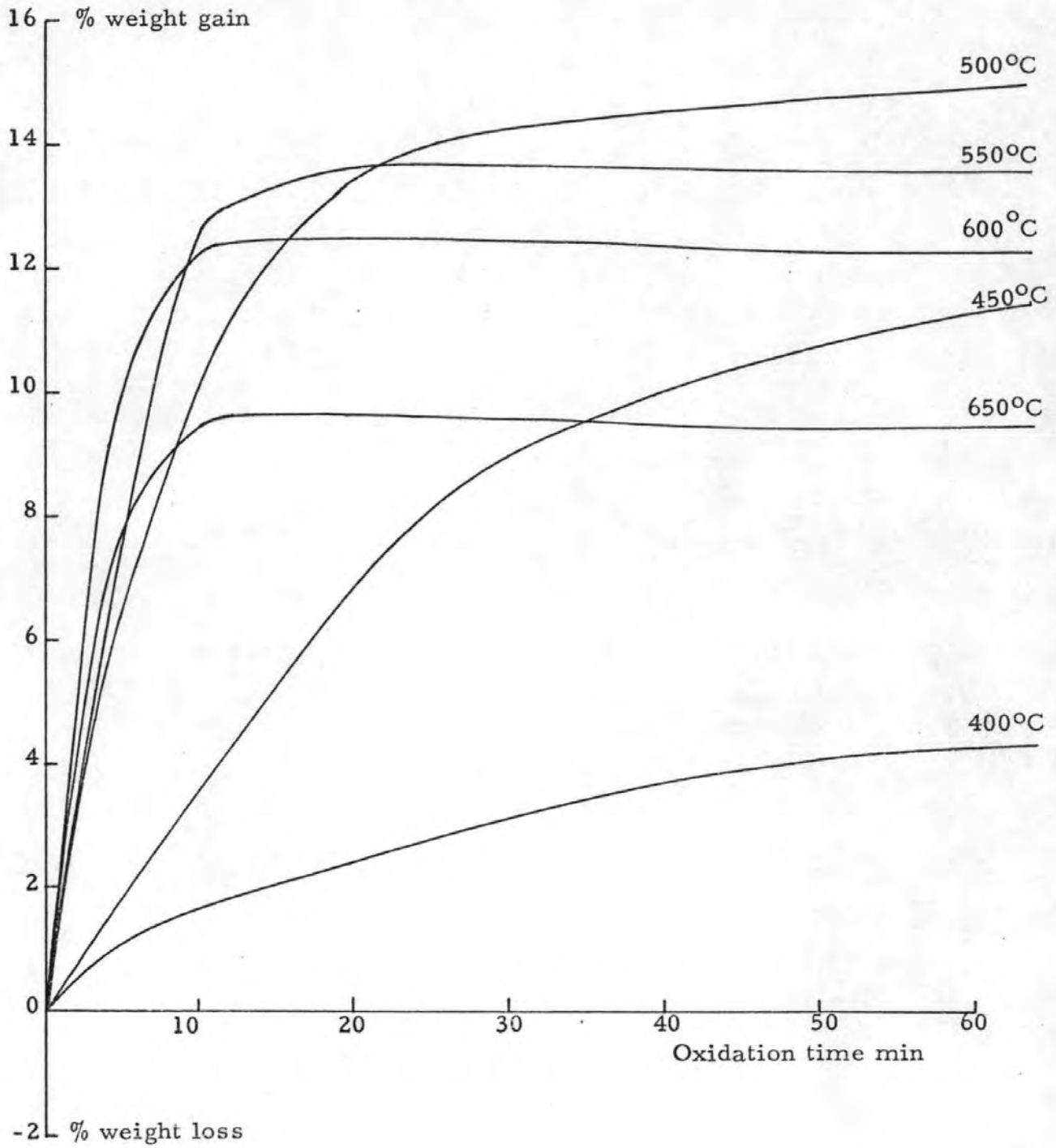
Figure 43b   Sample J24/80 oxidized isothermally in static air
(700-950°C)
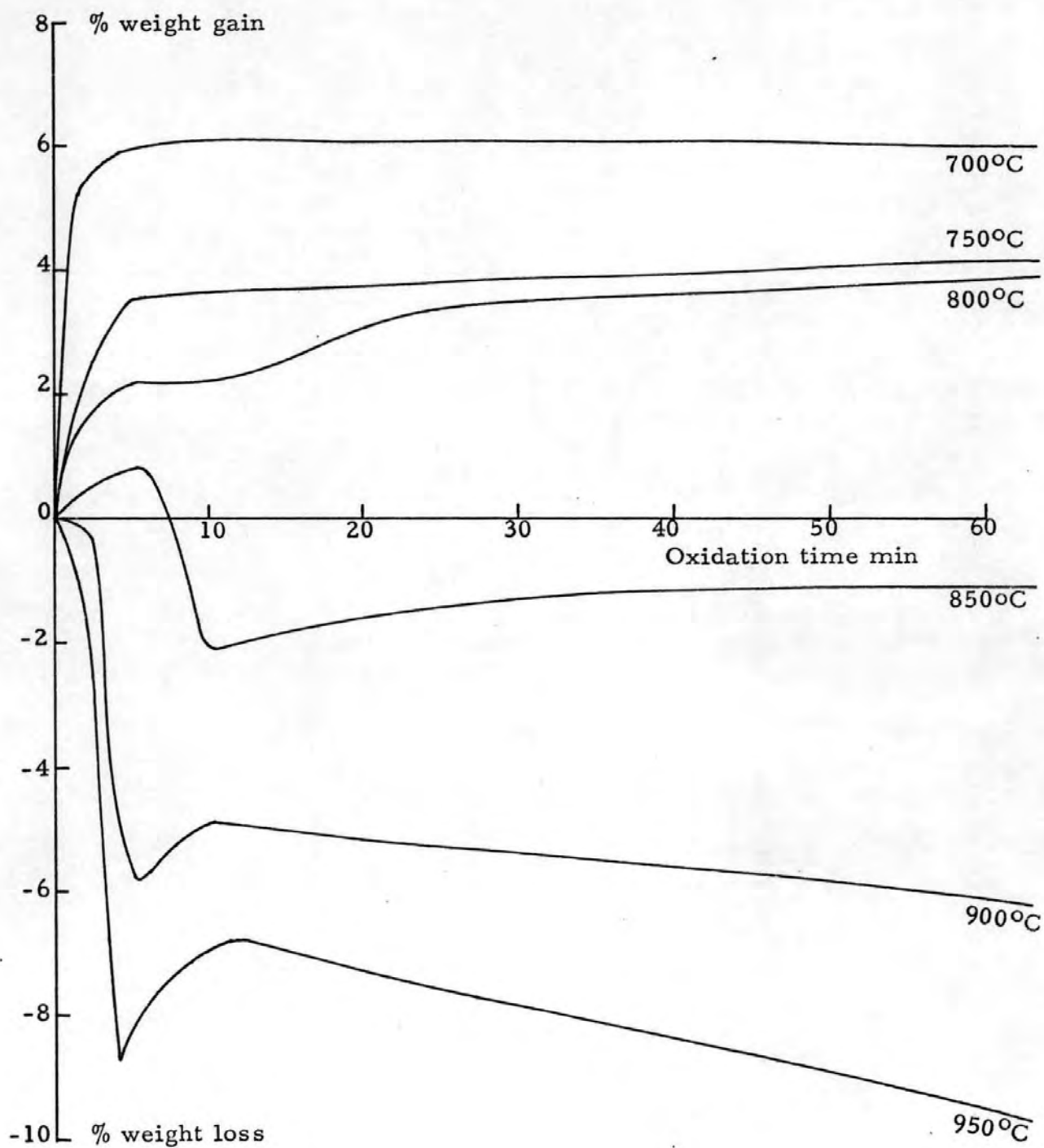
Figure 44a   Sample X24/80 oxidized isothermally in static air
(400-650°C)
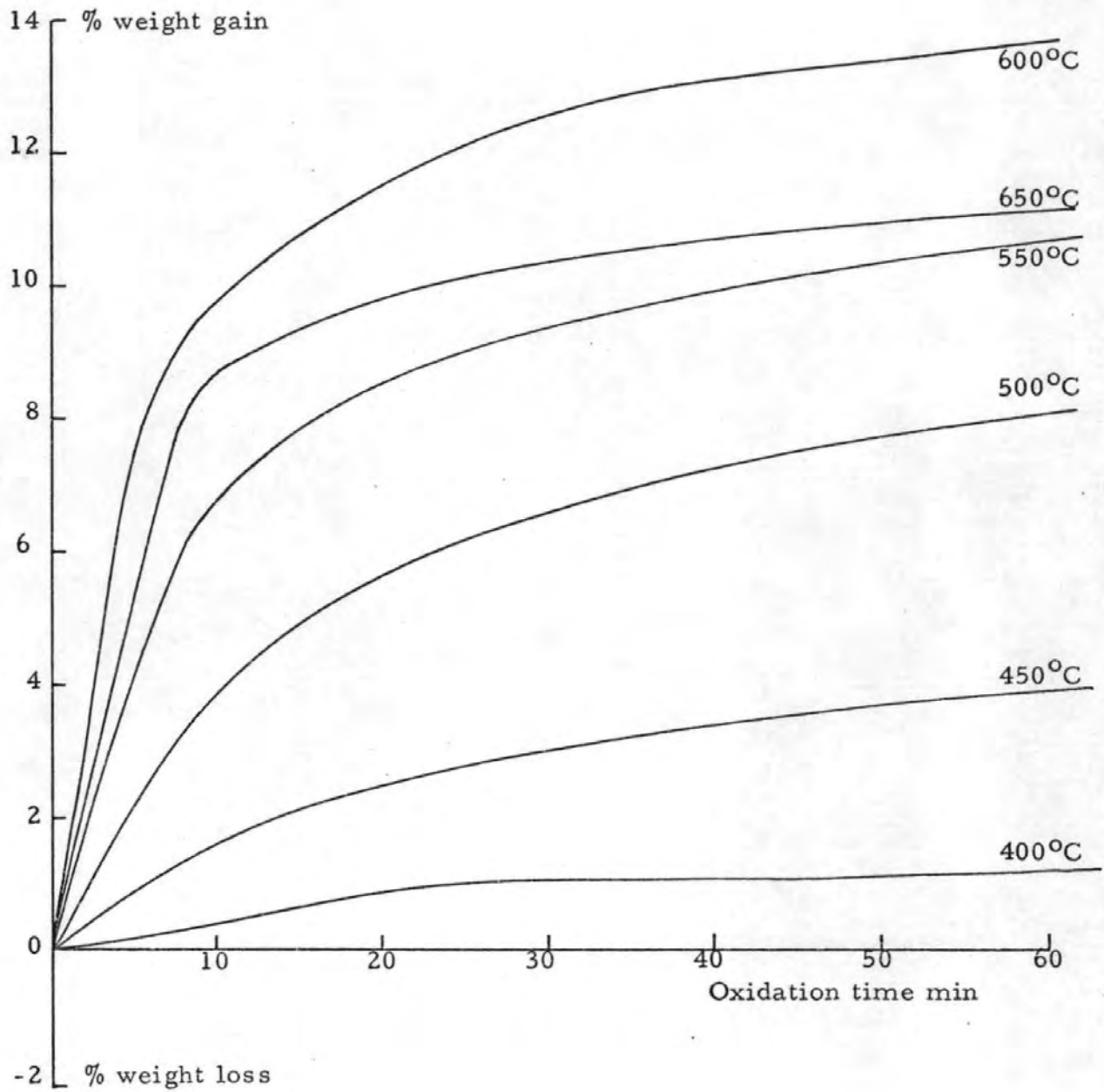
Figure 44b   Sample X24/80 oxidized isothermally in static air
(700-950°C)
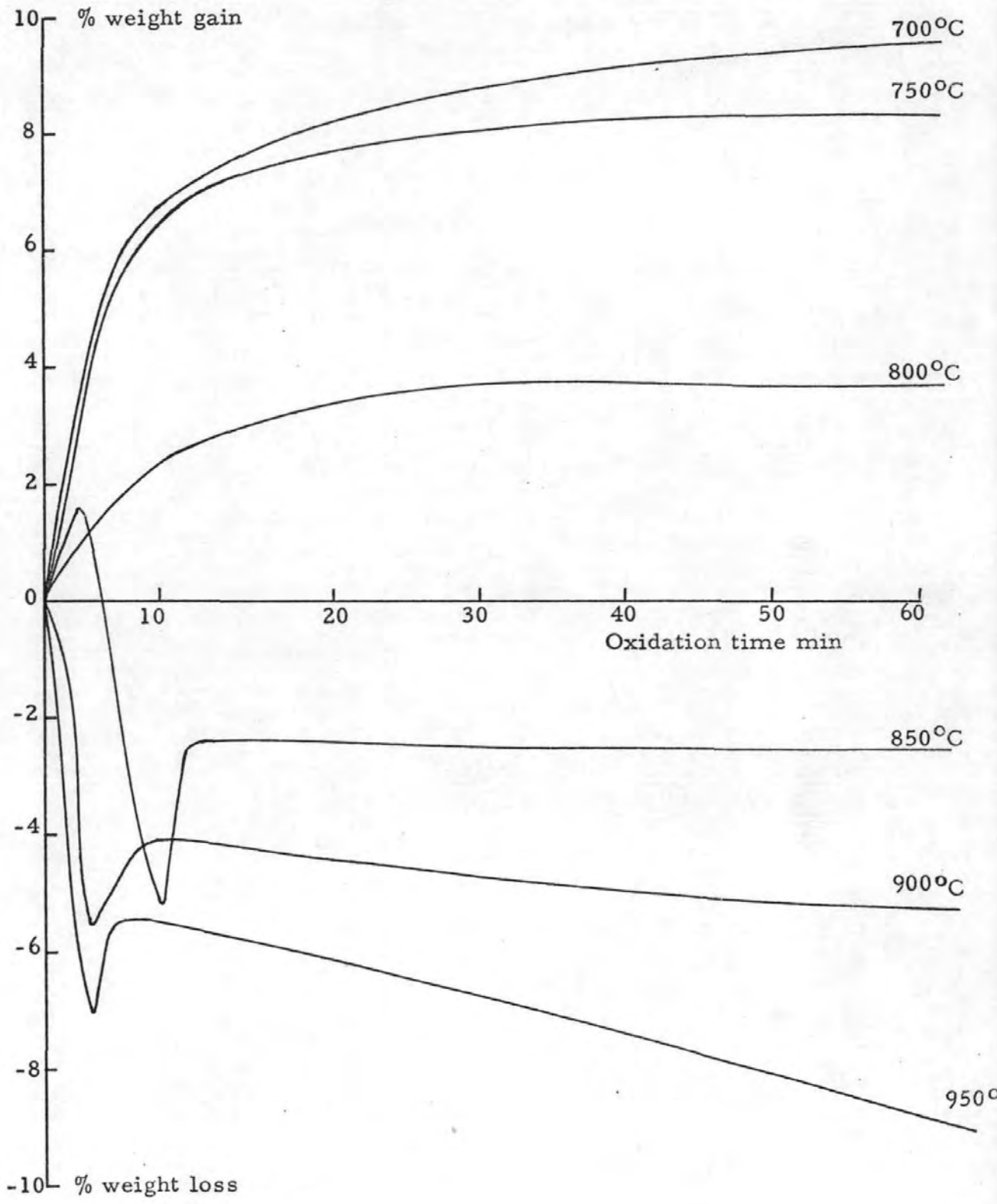
Figure 45a   Sample BDH oxidized isothermally in static air
(200-600°C)
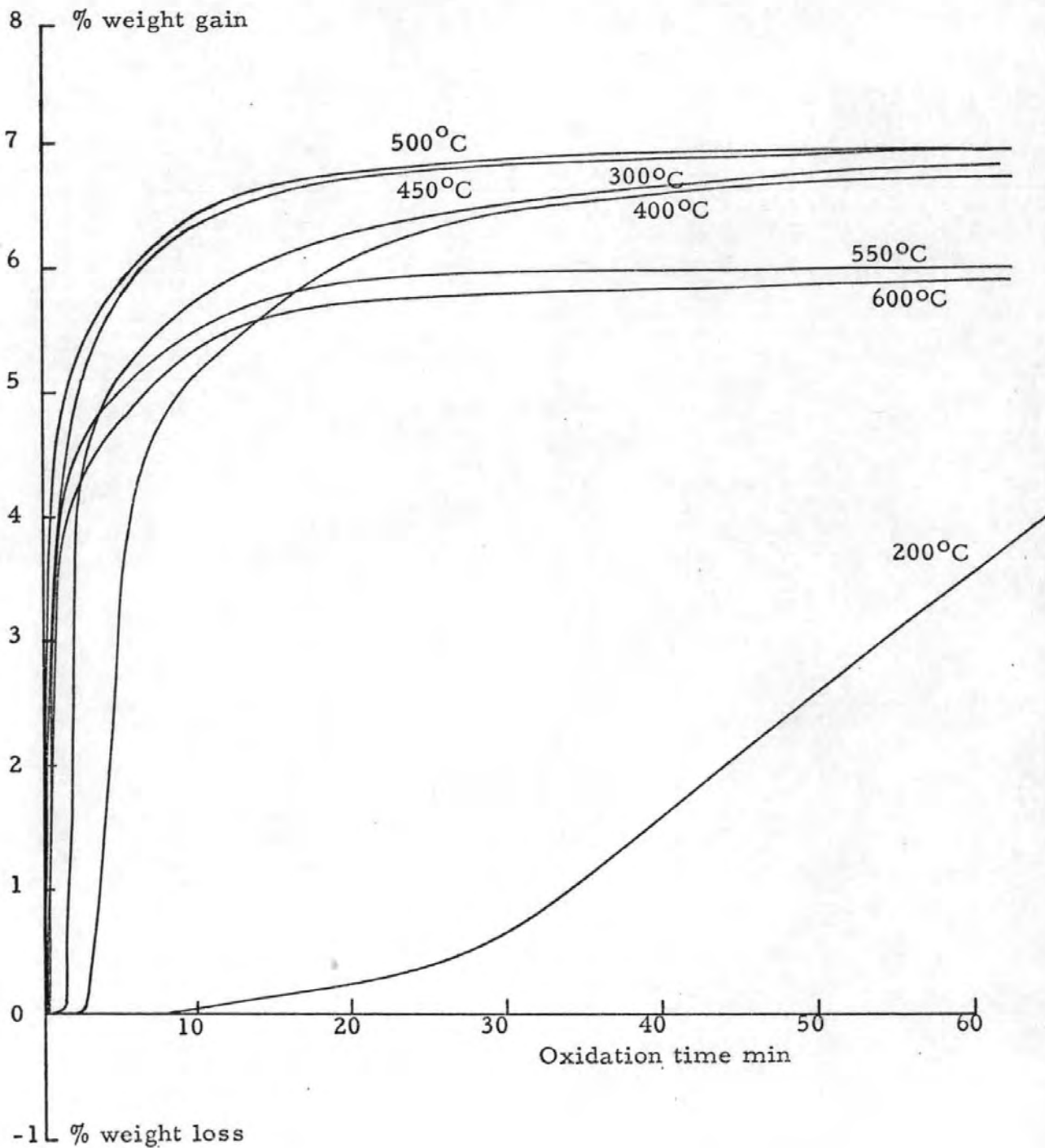
Figure 45b   Sample BDH oxidized isothermally in static air
(650-950°C)
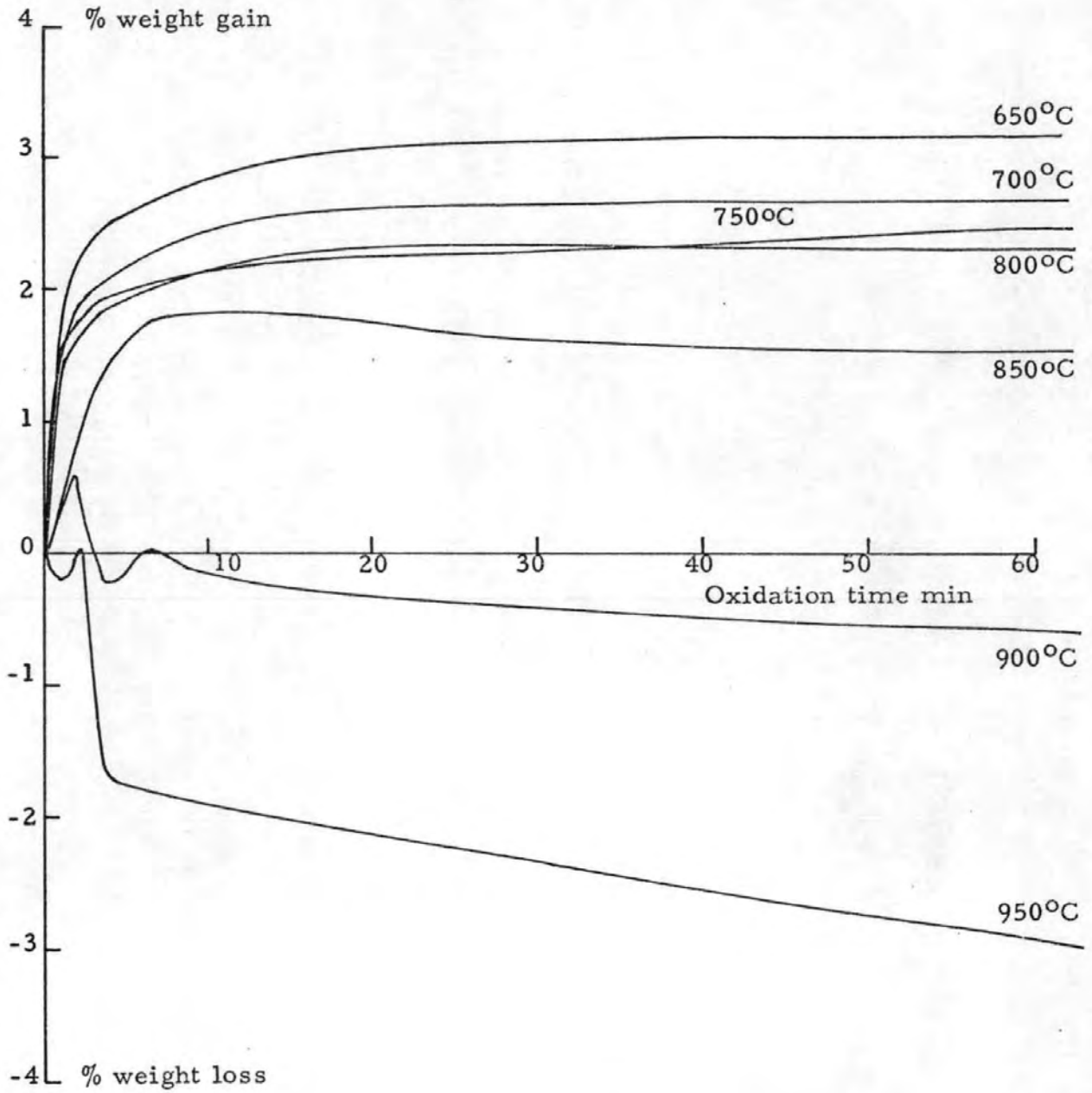
Table 4.2a

Isothermal temperature °C	PbS	PbSO$_4$	PbSO$_4$.PbO	PbSO$_4$.2PbO	PbSO$_4$.4PbO	PbO
400	small	v. strong	weak			
450		v.strong	v. small			
500		v.strong	small			
550		v.strong	medium			
600		strong	medium			
650		strong	strong			
700		strong	strong			
750		strong	v.strong			
800		strong	v.strong			
850		medium	v.strong			
900			strong	medium		
950			medium	strong		

X-ray phase analysis for sample W24/80 oxidized isothermally

weak
v. small
small
medium
strong
v. strong

Table 4.2b

Isothermal temperature ^{o}C	PbS	PbSO$_4$	PbSO$_4$.PbO	PbSO$_4$.2PbO	PbSO$_4$.4PbO	PbO
400	medium	v.strong	medium			
450	weak	v.strong	medium			
500		v.strong	medium			
550		v.strong	medium			
600		v.strong	medium			
650		v.strong	strong			
700		v.strong	strong			
750		strong	strong			
800		strong	strong			
850		weak	strong			
900			v.strong	weak		
950			small	strong		

X-ray phase analysis for sample D24/80 oxidized isothermally

weak
v. small
small
medium
strong
v. strong

Table 4.2c

Isothermal temperature °C	PbS	$PbSO_4$	$PbSO_4 \cdot PbO$	$PbSO_4 \cdot 2PbO$	$PbSO_4 \cdot 4PbO$	PbO
100	v.strong	v.small				
200	v.strong	small				
250	strong	medium				
400	medium	strong	weak			
450	medium	v.strong	weak			
500	medium	v.strong	weak			
550	small	strong	v.strong			
600	small	strong	small			
650	weak	strong	small			
700		v.strong	small			
750		strong	strong			
800		small	v.strong	v.small		
850			small	strong		
900				strong		
950					strong	

X-ray phase analysis for sample Q24/80 oxidized isothermally

weak
v.small
small
medium
strong
v.strong ↓

Table 4.2d

Isothermal temperature °C	PbS	$PbSO_4$	$PbSO_4.PbO$	$PbSO_4.2PbO$	$PbSO_4.4PbO$	PbO
400	v.strong	strong				
450	strong	strong				
500	weak	v.strong	v.small			
550		v.strong	v.small			
600		strong	small			
650		strong	medium			
700		medium	medium			
750		medium	strong			
800		medium	strong			
850		small	medium	small		
900					strong	small
950					strong	strong

X-ray phase analysis for sample J24/80 oxidized isothermally

weak
v. small
small
medium
strong
v. strong ↓

Table 4.2e

Isothermal temperature °C	PbS	PbSO$_4$	PbSO$_4$·PbO	PbSO$_4$·2PbO	PbSO$_4$·4PbO	PbO
400	v.strong	v.small				
500	v.strong	medium				
550	strong	v.strong	weak			
600	medium	v.strong	medium			
650	small	medium	strong			
700	v.small	small	v.strong			
750		v.small	v.strong			
800		v.small	v.strong	v.small		
850			v.small	strong		
900					strong	
950					strong	small

X-ray phase analysis for sample X24/80 oxidized isothermally

weak
v. small
small
medium
strong
v. strong

Table 4.2f

Isothermal temperature °C	PbS	PbSO$_4$	PbSO$_4$.PbO	PbSO$_4$.2PbO	PbSO$_4$.4PbO	PbO
200	strong	small				
300	medium	medium	weak			
400	small	strong	small			
450	small	strong	medium			
500	small	small	medium			
550		v.small	strong			
600		v.small	strong			
650		v.small	v.strong			
700		weak	v.strong			
750		v.small	v.strong			
800		weak	v.strong			
850		weak	v.strong			
900				strong		
950					strong	

X-ray phase analysis for sample BDH oxidized isothermally

weak
v. small
small
medium
strong
v. strong

Initially, the oxidation rates will depend mainly on nucleation and development of the reaction on the surface of the sulphide. Subsequently, it will tend to proceed at an interface advancing inwards from the surface of each particle. The nucleation and surface reaction will be affected by the crystallinity at the surface and any lead sulphate or similar impurities (like basic sulphates) already present. Of the six samples in Table 4.1a, Q, J, X and the BDH samples are initially-sulphate free and the greater reactivity is shown by the samples with the poorer crystallinity (as judged from electron micrographs in Figures 46a-f), these being expected to have a larger number of crystal defects to promote crystal change. In samples W and D, part of the surface is already coated with oxidation product (normal and basic sulphate impurities) and is in effect partly nucleated. The remainder of the surface probably will have poorer crystallinity on account of the impurities and thus will rapidly nucleate. This will give initial overall rates intermediate between those of pure samples which have good and poor crystallinity, as is found experimentally.

The subsequent oxidation by the advancing interface mechanism will depend mainly on the internal crystallinity of the material and the stability of the product layer. If the product layer is very permeable to gases i.e. there is no impedance, the interface can advance inwards from the outside of each particle at a linear rate and $\frac{2}{3}$ order kinetics result. However, if the layer is less permeable a diffusion mechanism produces parabolic kinetics, as often encountered in oxidation of metals[101] (or their nitrides etc)[102].

At lower temperatures, nucleation rates are slower and may even show induction periods so that the oxidation accelerates giving curves which are initially concave upwards (e.g. the commercial BDH sample oxidized at 200°C), before a stable product layer gives parabolic kinetics. After this the oxidation progressively decelerates giving a sigmoid curve. At higher temperatures, where nucleation is more rapid, the parabolic kinetics are established sooner, but if the initial surface is inhomogeneous the formation of a stable product layer is delayed and the initial part of the curve becomes approximately linear as found in many instances in the present research (Gulbransen[103] has
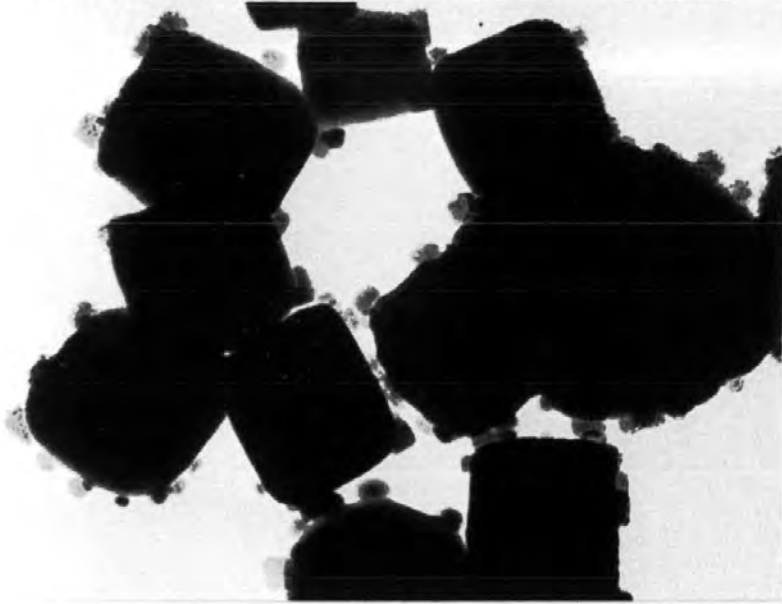
Figure 46a
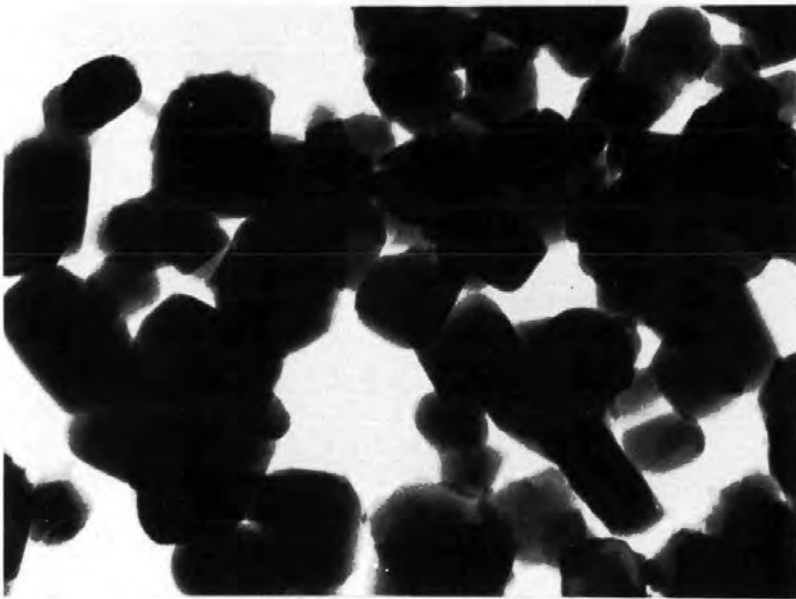Sample X24/80
Mag: 111,000 X
Scale 100 nm

Figure 46b
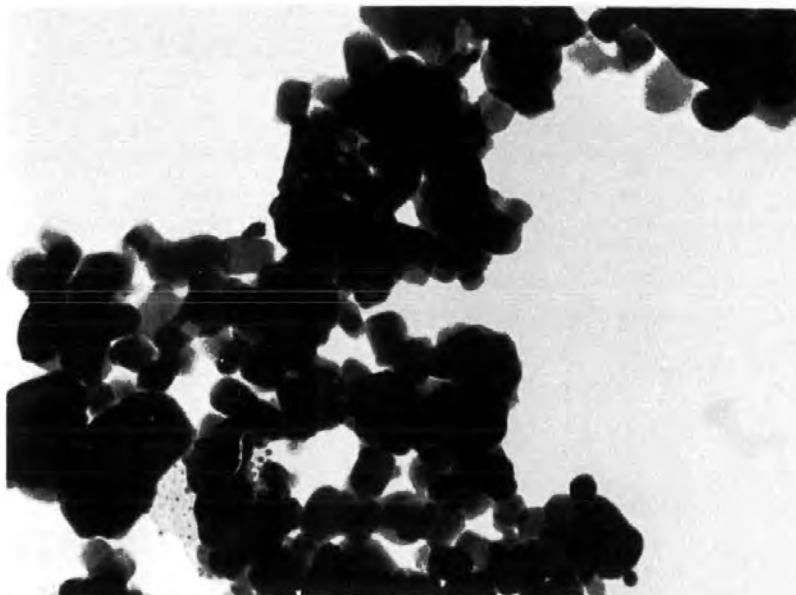Sample J24/80
Mag: 111,000 X
Scale 100 nm

Figure 46c
Sample Q24/80
Mag: 111,000 X
Scale 100 nm
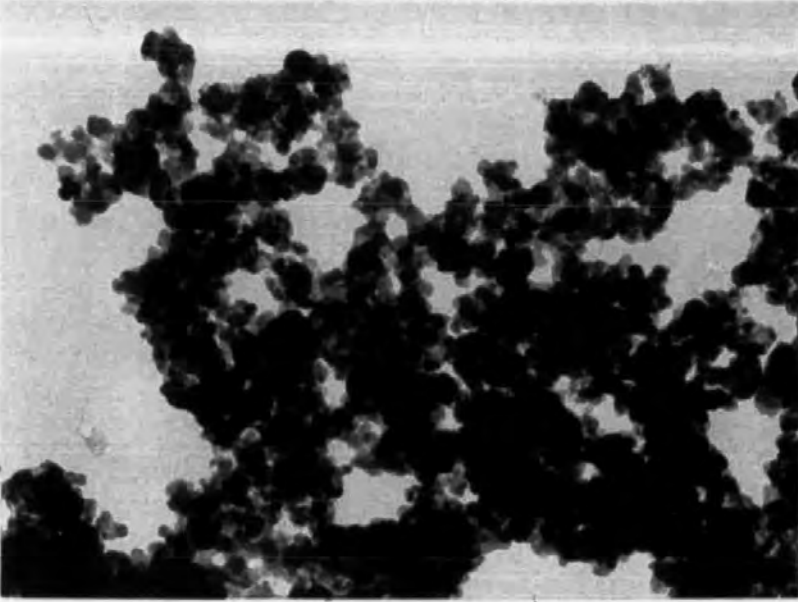
TRANSMISSION ELECTRON MICROGRAPHS

Figure 46d
Sample D24/80
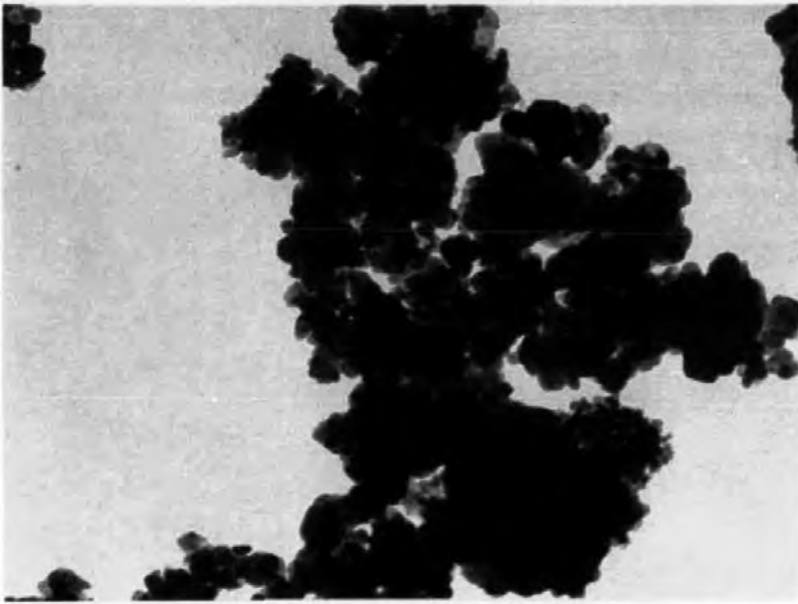Mag: 111,000 X
Scale 100 nm

Figure 46e
Sample W24/80
Mag: 110,000 X
Scale 100 nm
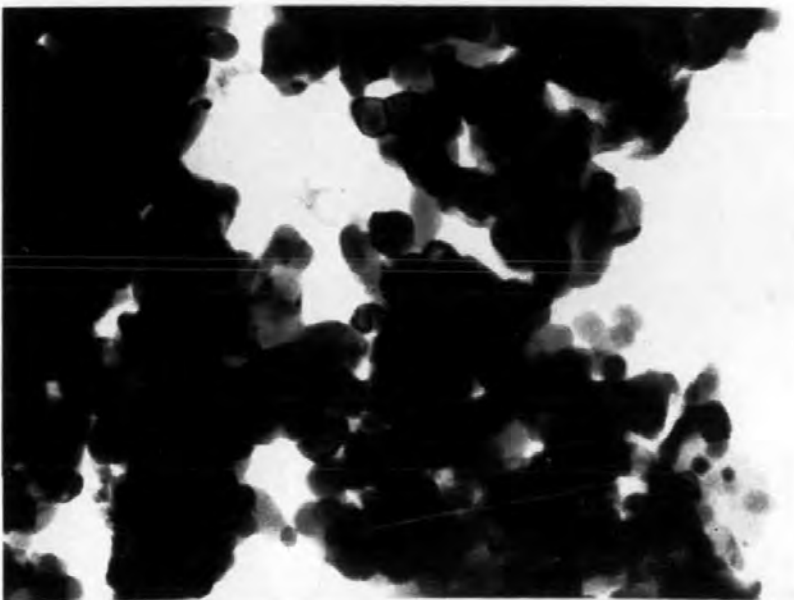
Figure 46f
Commercial BDH lead
sulphide
Mag: 110,000 X
Scale 100 nm

summarized this and other possible contributory factors, viz., decreases in surface heterogeneity and specific surface as the reaction proceeds, changes in local surface temperature caused by heat of reaction, solubility effects and impurity concentrations).

Sintering of the products may cause increased impedance giving ultimately abnormally slow oxidation rates. The behaviour is found for lead sulphide oxidations especially at higher temperatures. Surface diffusion and crystal lattice diffusion which promote recovery of crystallinity and sintering become prominent for ionic solids at temperatures above about $\frac{1}{3}$ melting point and $\frac{1}{2}$ melting point (in K) which corresponds to 190° and 420°C respectively for lead sulphide, 210° and 450°C for lead sulphate. The lead oxide, PbO, formed increasingly at higher temperatures (Tables 4.2a-f) is comparatively low-melting $(880^{\circ}$C) and should be effective in promoting surface diffusion and crystal lattice diffusion at temperatures above about 110° and 300°C respectively.

Kinetics of the oxidations are illustrated further in Figures 47a, b, c where the squares of the weight increases, m, are plotted against time. Linear plots corresponding to parabolic kinetics are found only at the lowest temperatures over all the oxidation ranges studied. At higher temperatures the plots deviate from linearity, decreasing in slope as the oxidation rates become abnormally low. At these temperatures sintering becomes more extensive, so that the outer layers of the particles coalesce, ultimately embedding the unreacted material in the matrix of product, abnormally reducing the diffusion rate. This behaviour is shown also from optical micrographs of the partly oxidized sulphide samples. Sample Q24/80 oxidized for 1 h at 450°, 500° and 550°C (see Figures 48a, b, c) shows increasing amounts of white particles (sulphate product) present tending to coalesce at the highest temperature $(550^{\circ}$C).

Above 600°C, the 1 h samples can be removed from the crucible as solid cakes. Part of the top, side and bottom portions of the sample oxidized at 650°C are compared in Figures 49a, b, c. The greatest amount of sulphated product occurs in the top layer and is much more extensively sintered than that at 550°C (see Figure 48c). There is

Figure 47 a, b, c.   Kinetics of oxidation
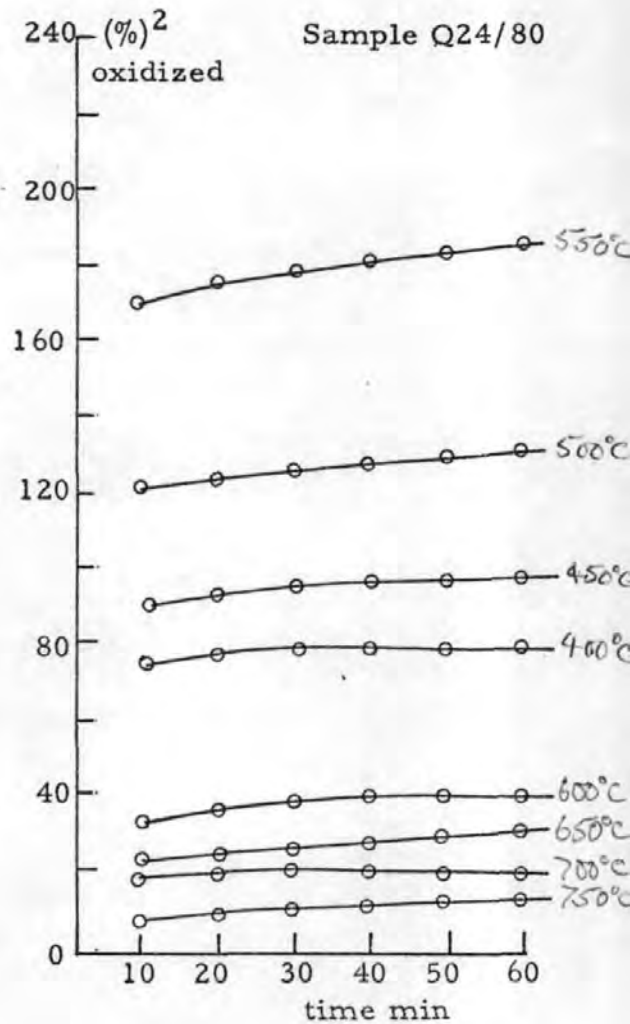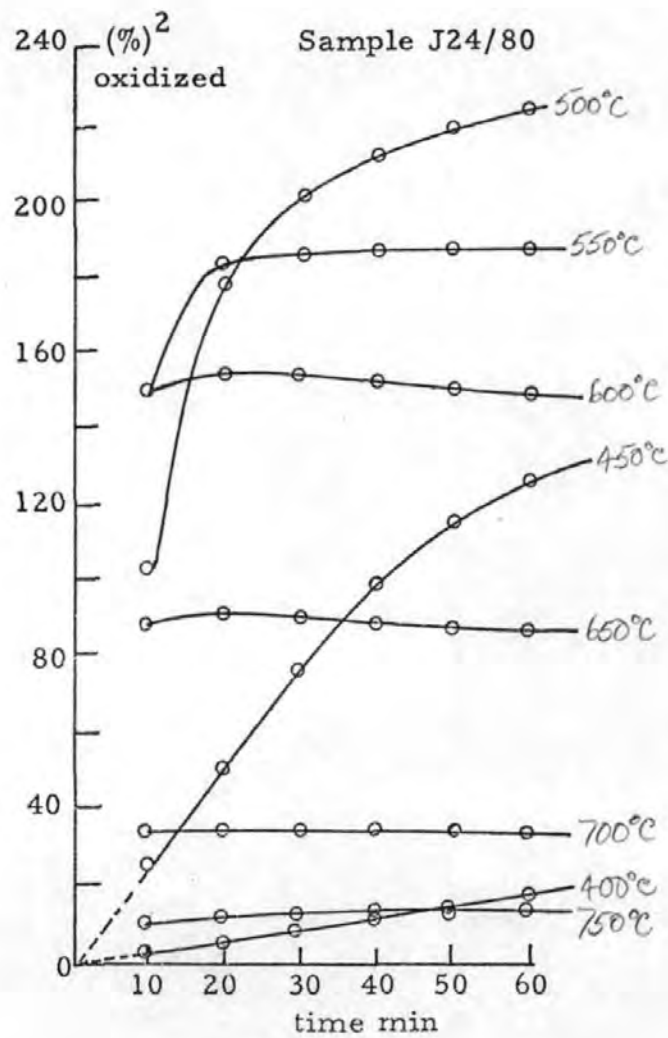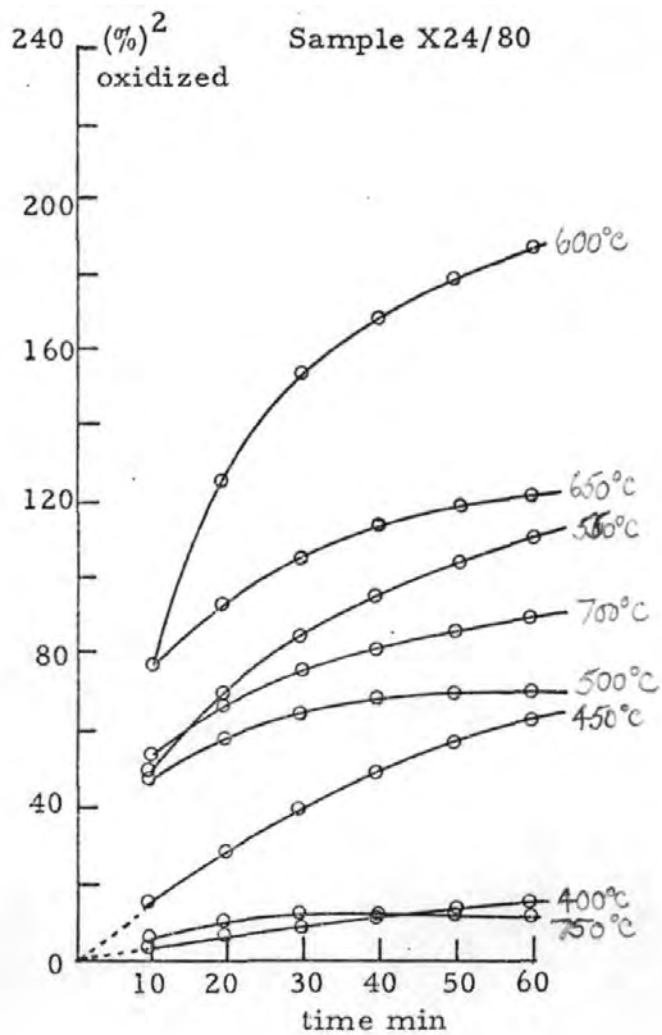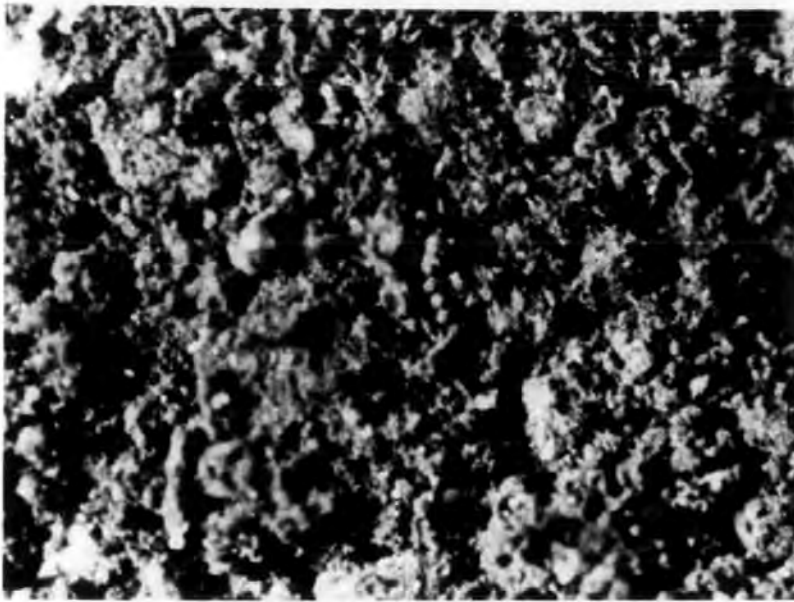
Figure 48a

Sample Q24/80
oxidized for 1 h at 450°C

Mag: 40 X

Scale 500 μm
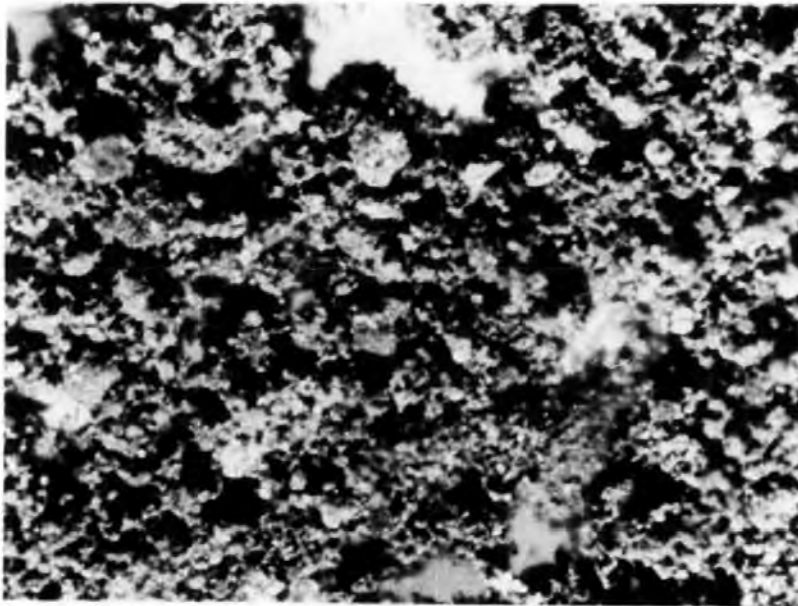
Figure 48b

Sample Q24/80
oxidized for 1 h at 500°C

Mag: 400 X

Scale 500 μm
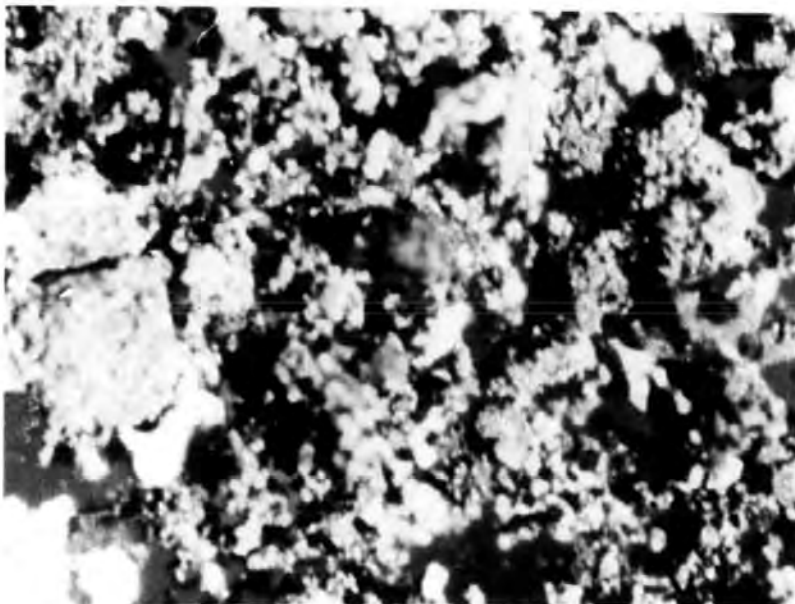
Figure 48c

Sample Q24/80
oxidized for 1 h at 550°C

Mag: 40 X

Scale 500 μm
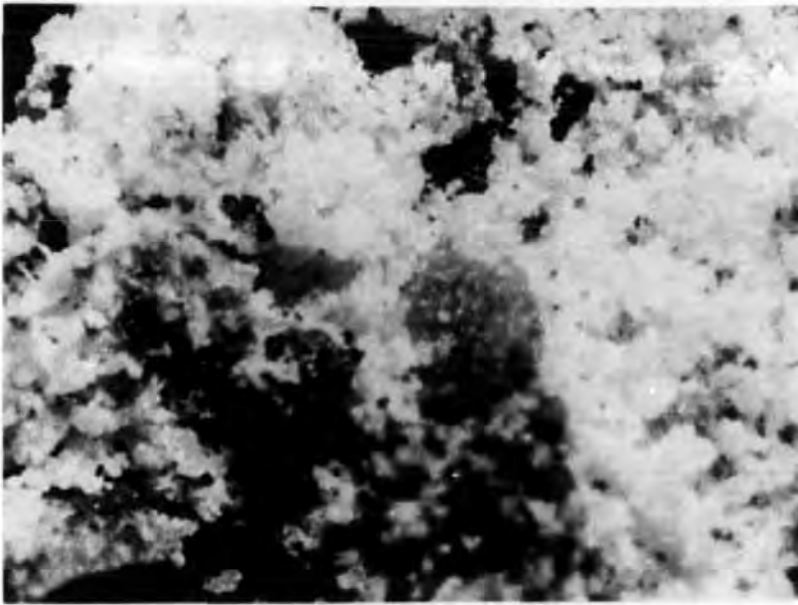
Figure 49a

Sample Q24/80
oxidized for 1 h at 650°C

Top of sample

Mag: 40 X

Scale 500 μm
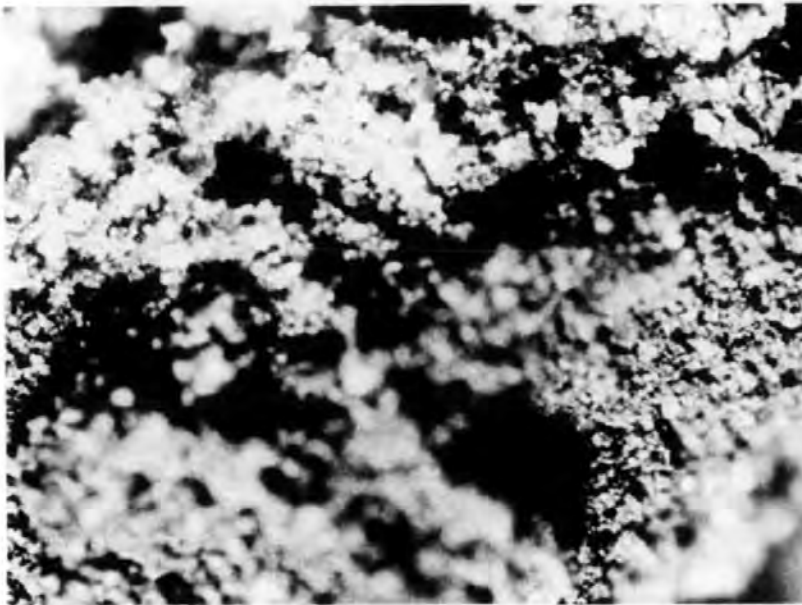
Figure 49b

Sample Q24/80
oxidized for 1 h at 650°C

Side of sample

Mag: 40 X

Scale 500 μm
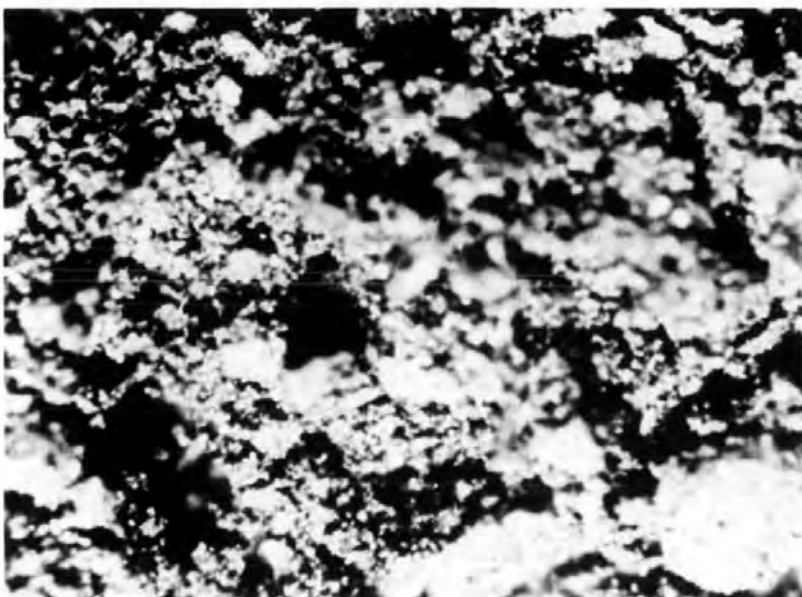
Figure 49c

Sample Q24/80
oxidized for 1 h at 650°C

Bottom of sample

Mag: 40 X

Scale 500 μm

less extensive oxidation in the side and bottom layers, where oxygen diffusion has been impeded by the sintered product layer at the top.

Particle growth increases considerably at 750°C (see Figure 50 a), but nevertheless small amounts of unchanged sulphide can still be seen (small grey particles partly coated with white sulphated product), in too small amounts to be identified from X-ray diffractometer traces. There is less difference in the microstructure of the top and side portions of the product at 750°C compared with 650°C; the higher temperature facilitates crystal lattice diffusion and chemical reaction. This optical examination is somewhat restricted by limitations in depth of focus resulting in blurring in some parts of the micrographs. Thus, further microstructural studies were made by scanning electron microscopy, giving a complete independence of depth of focus and a higher magnification to provide more details of the surface structure.

Samples of D24/80 and BDH sulphide oxidized for 1 h at temperatures between 500° and 750°C gave products showing progressive increases in particle size (see Figures 51 a, b, c, d, e), more clearly than those shown by the optical micrographs for Q24/80 (see Figure 48a,b; 49a, b, c).

A comparison of samples W24/80 oxidized for 1 h at temperatures between 700° and 900°C is presented in Figures 52a-d. The product at 700°C is somewhat porous, but at 800°C most of the pores are absent and there is evidence of grain boundaries throughout the whole structure (see 4-fold enlarged micrographs Figures 53a-e). At 850°C there is further loss of porosity but less evidence of grain boundaries, since liquid phases begin to appear. The latter leads to a rounding of the particles at 900°C.

4.2.2   Formation of Monobasic Lead Sulphate

Lead oxide and lead sulphate will react to give monobasic lead sulphate at 400°C and above. Separate experiments were performed to determine the temperature range over which the reaction between lead oxide and lead sulphate would occur.

A 1:1 molar mix of Analar lead oxide and sulphate was ground to a fine powder, and 2 g samples contained in an alumina crucible heated in a muffle furnace at a series of temperatures for varying lengths of time. Figure 54 shows the X-ray diffraction traces obtained

OPTICAL MICROGRAPH
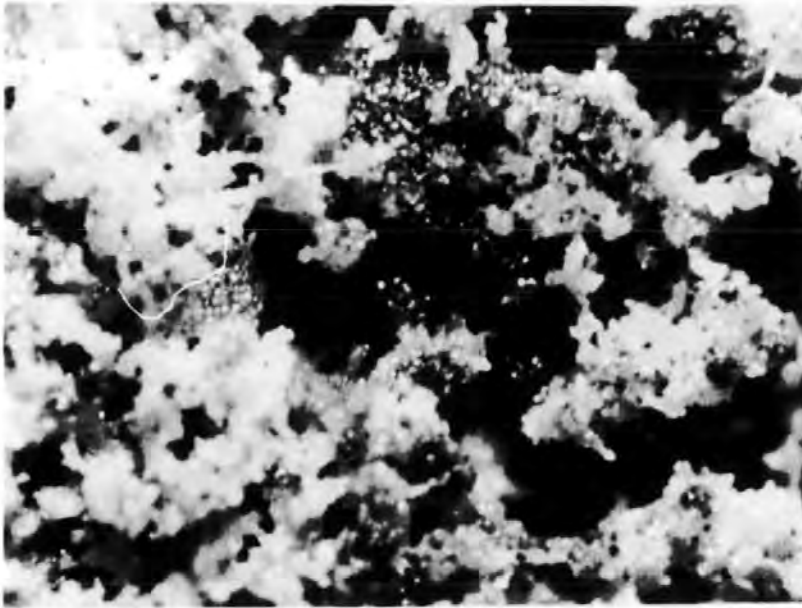
Figure 50a

Sample Q24/80
oxidized for 1 h at 750°C

Mag: 40 X

Scale 500 μm

SCANNING ELECTRON MICROGRAPHS
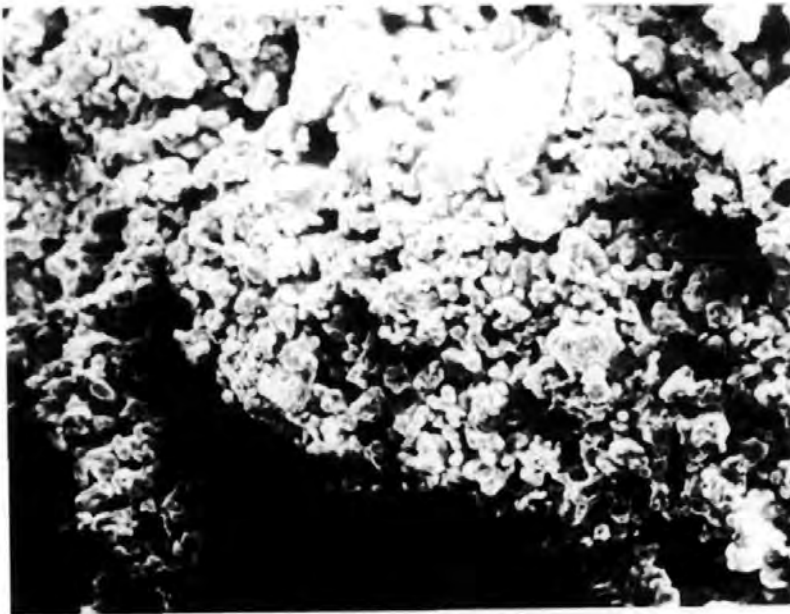
Figure 51a

Sample BDH oxidized for
1 h at 650°C

Mag: 500 X

Scale 40 μm
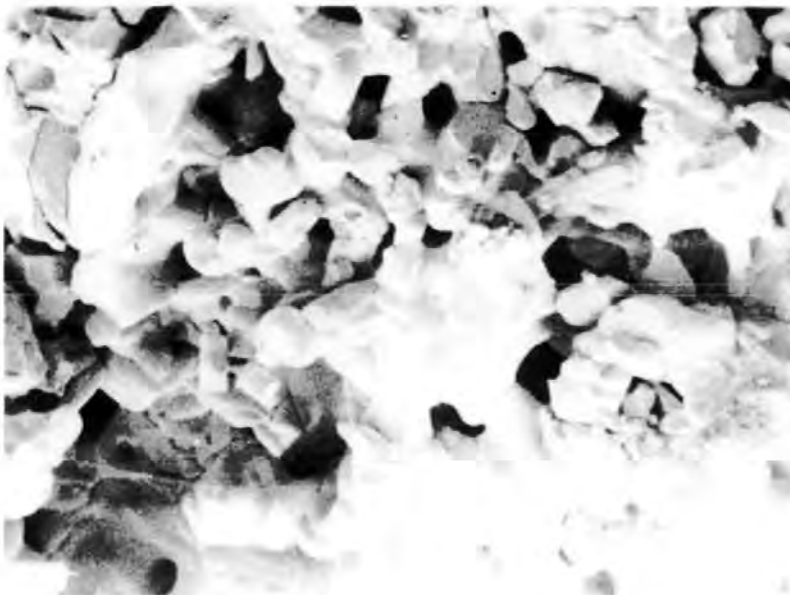
Figure 51b

Sample BDH oxidized for
1 h at 750°C

Mag: 1000 X

Scale 20 μm
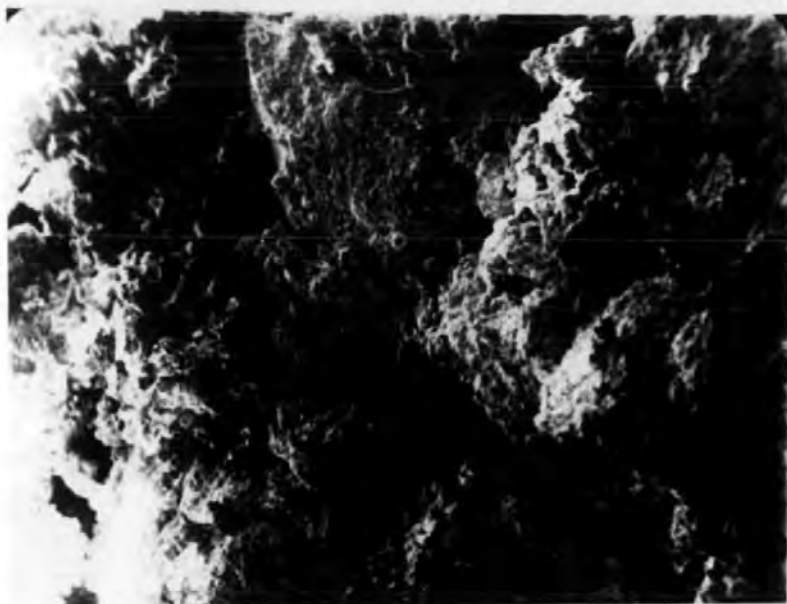
Figure 52a

Sample W24/80
oxidized for 1 h at 700°C

Mag: 500 X

Scale 40 µm
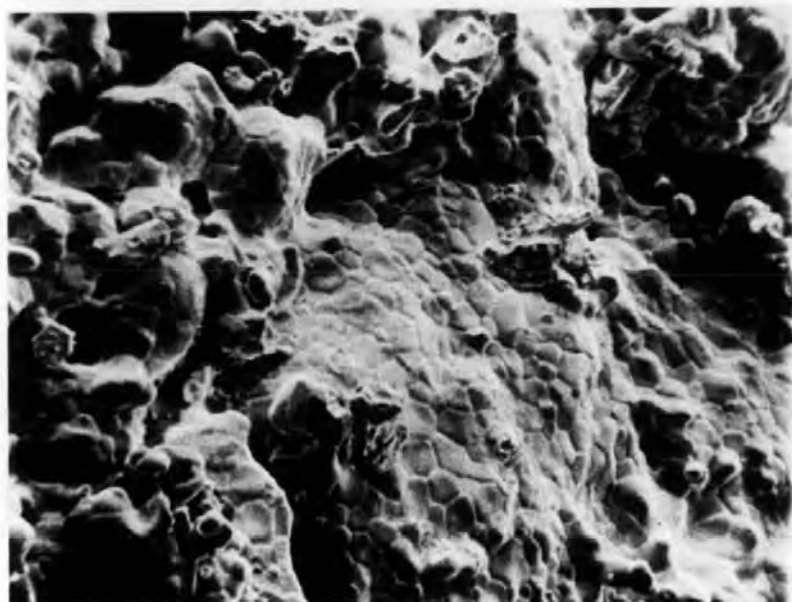
Figure 52b

Sample W24/80
oxidized for 1 h at 800°C

Mag: 500 X

Scale 40 µm
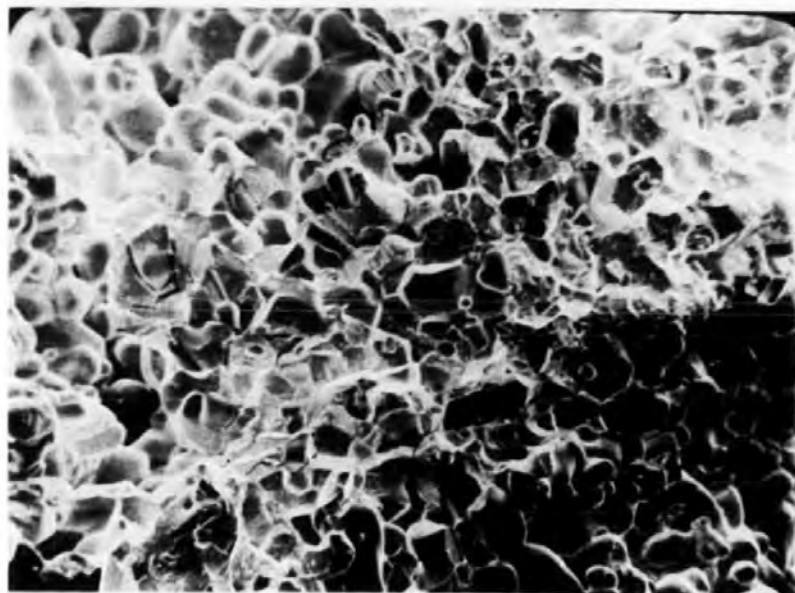
Figure 52c

Sample W24/80
oxidized for 1 h at 850°C

Mag: 500 X

Scale 40 µm
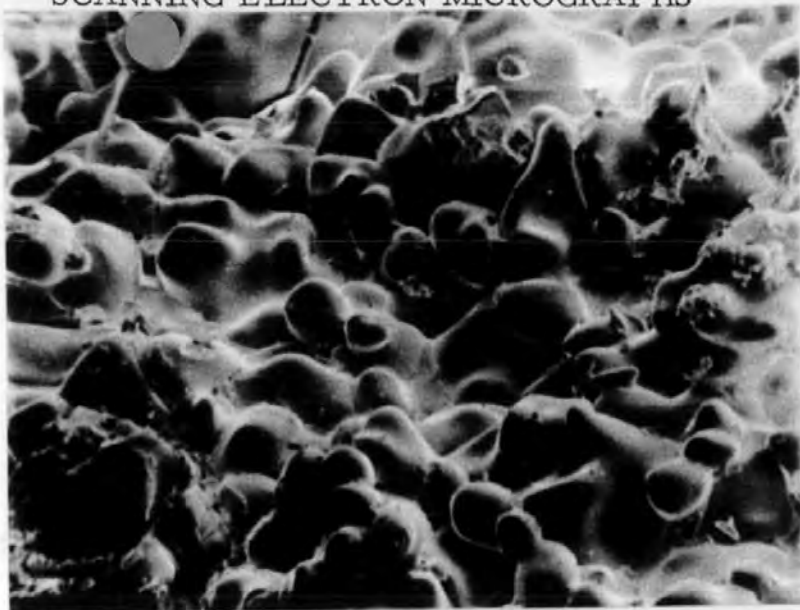
Figure 52d

Sample W24/80
oxidized for 1 h at 900°C

Mag: 500 X

Scale 40 μm
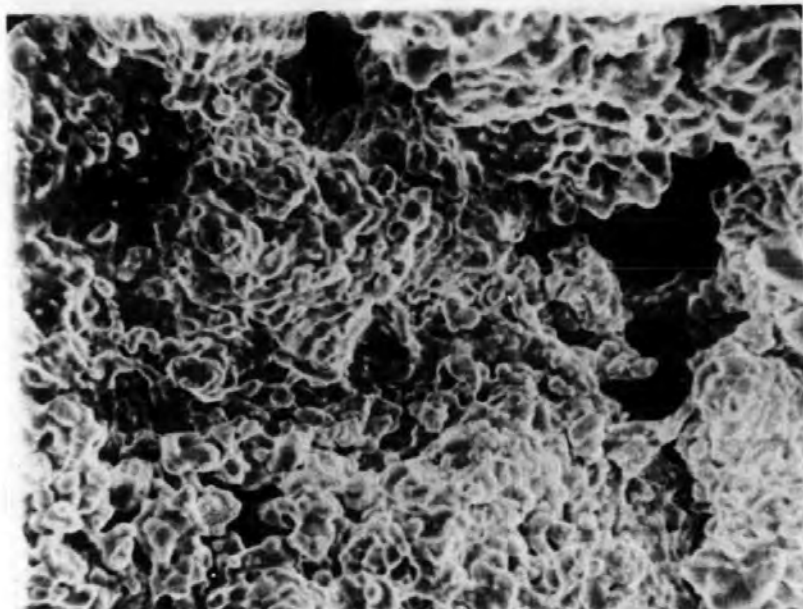
Figure 53a

Sample W24/80
oxidized for 1 h at 700°C

Mag: 2,100 X

Scale 10 μm
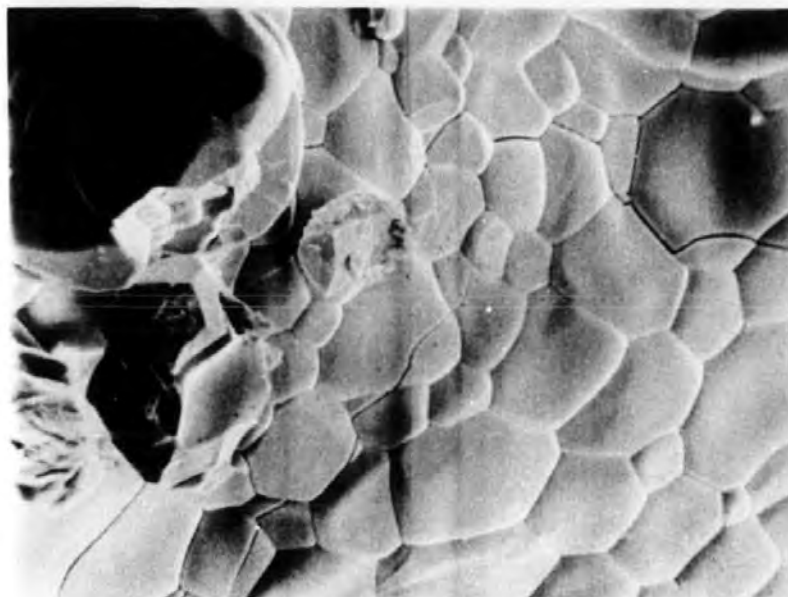
Figure 53b

Sample W24/80
oxidized for 1 h at 800°C

Mag: 2,100 X
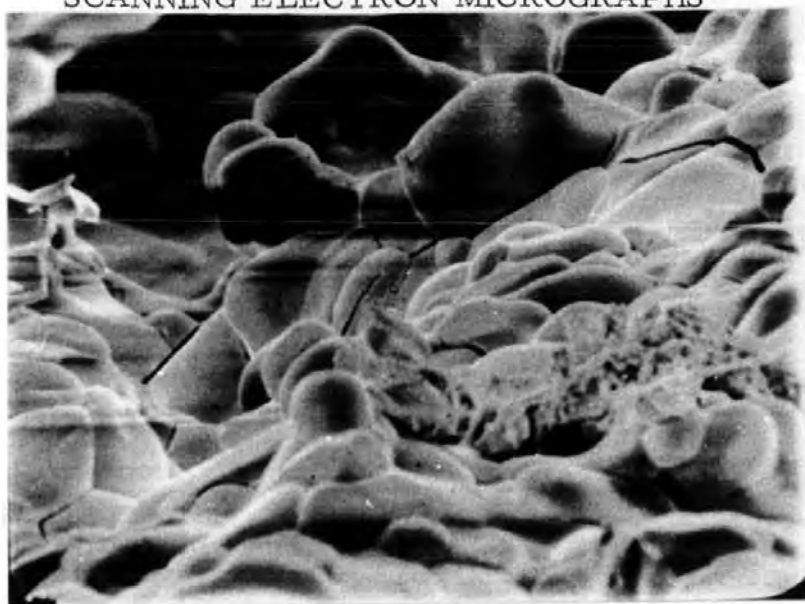
Scale 10 μm

Figure 53c

Sample W24/80
oxidized for 1 h at 800°C

Mag: 2,100 X
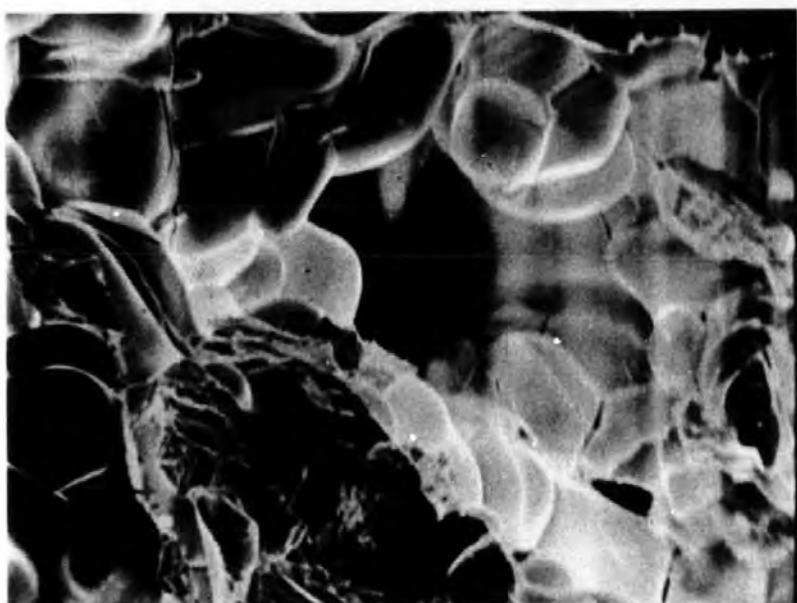
Scale 10 μm

Figure 53d

Sample W24/80
oxidized for 1 h at 900°C

Mag: 1,000 X

Scale 20 μm
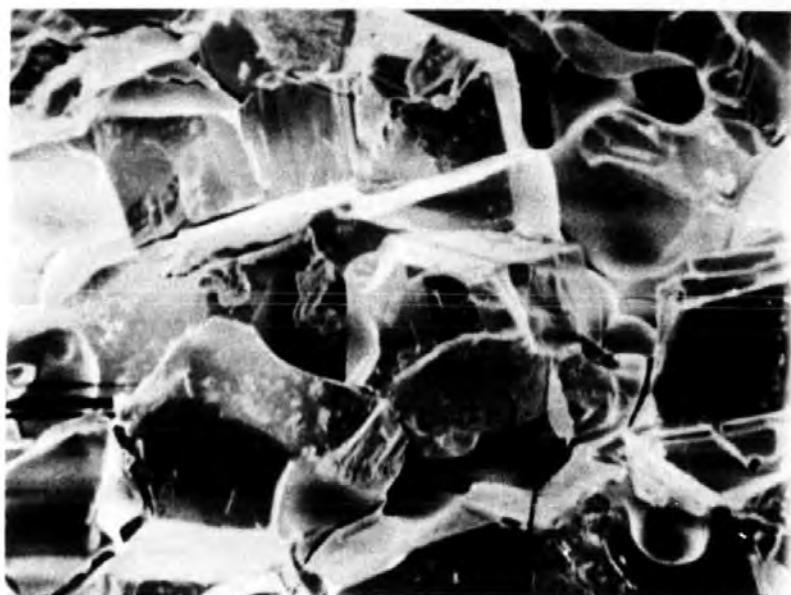
Figure 53e

Sample W24/80
oxidized for 1 h at 850°C

Mag: 2,100 X

Scale 10 μm

Figure 54 illustrating the formation of monobasic lead sulphate

PbSO$_4$.PbO

12°   16°

1:1 mix of lead oxide and lead sulphate heated for 1 h at 400°C

PbSO$_4$.PbO

12°   16°

Heated for 1 h at 500°C

PbSO$_4$.PbO

12°   16°

Heated for 10 h at 500°C

PbSO$_4$.PbO

12°   16°

Heated for 1 h at 700°C

PbSO$_4$.PbO

12°   16°

Heated for 1 h at 800°C

- 147 -
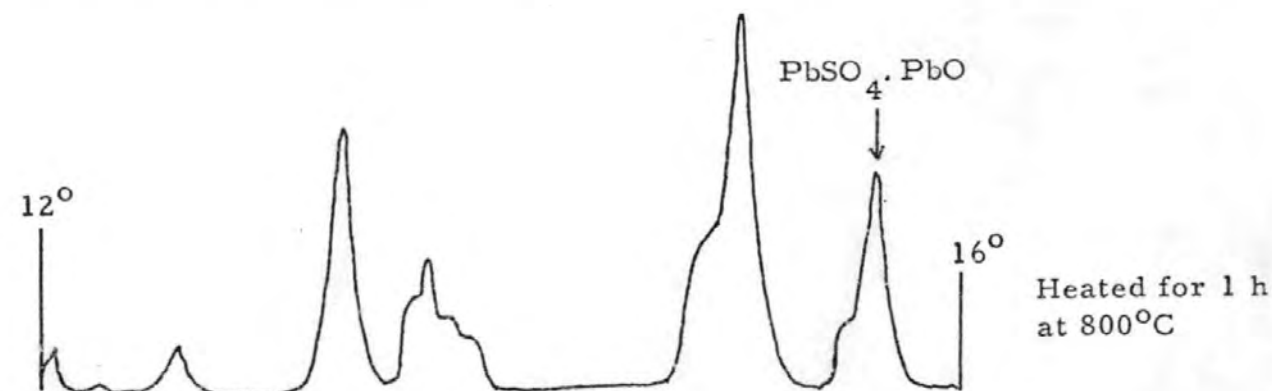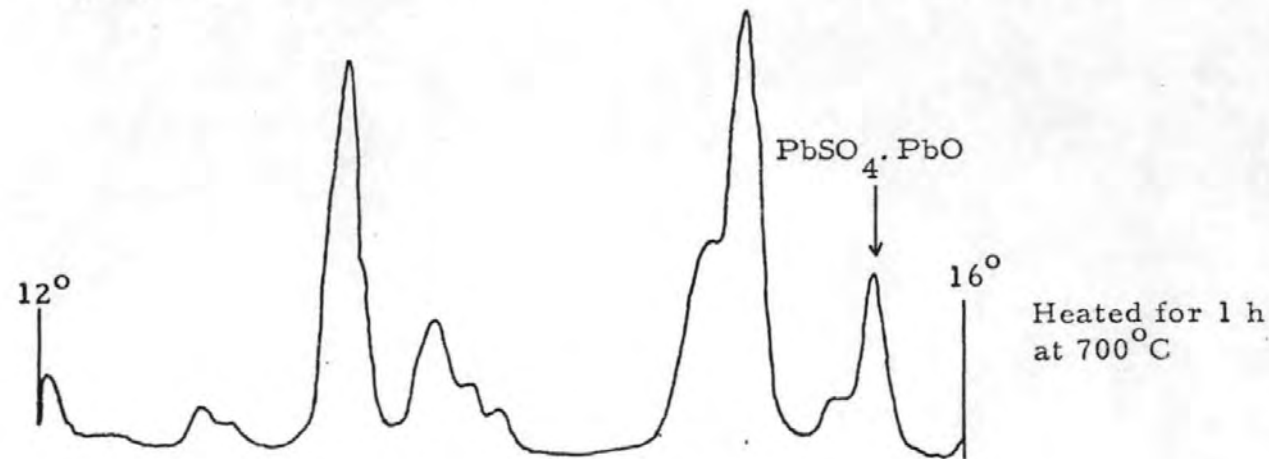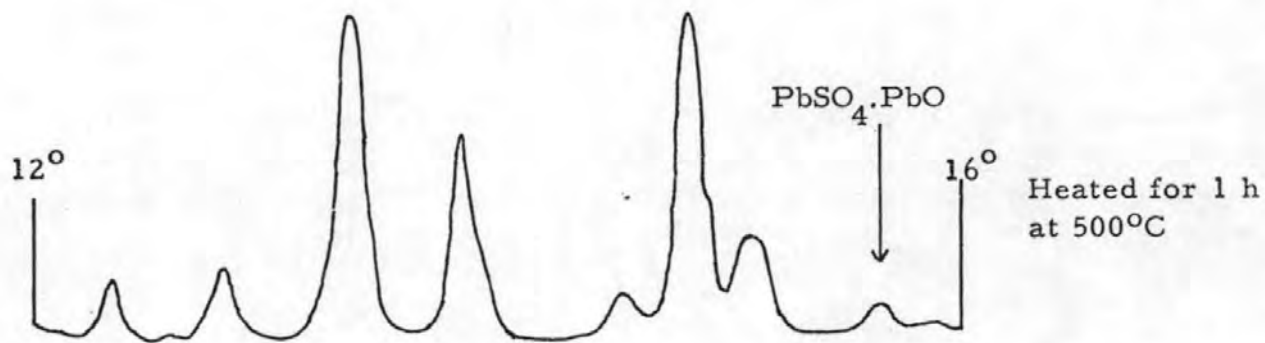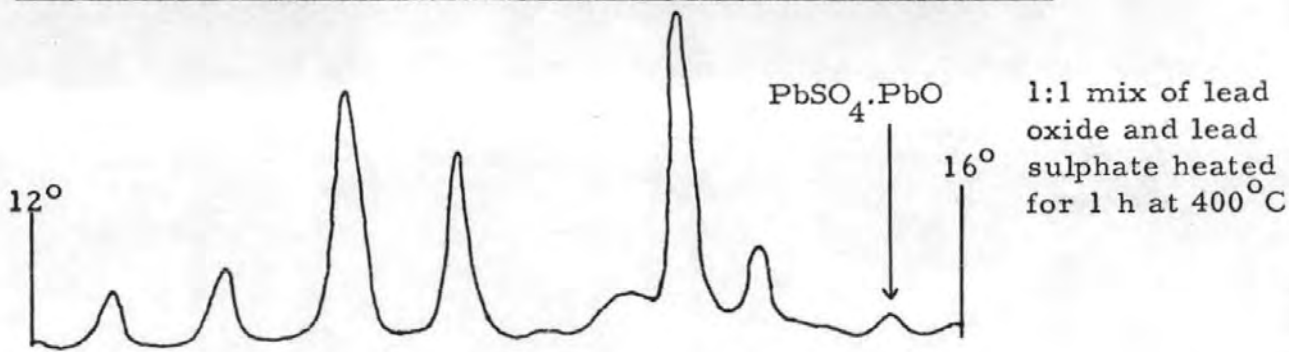
after 1 h at 400°C, 1 h and 10 h at 500°C, 1 h at 700°C and 1 h at 800°C. Thus, even at 400°C for 1 h monobasic lead sulphate is formed, with the rate of formation increasing with temperature and time, as indicated by the peak heights. The mixture was further investigated by DTA, but the resultant trace shows no apparent heat of reaction, with the endothermic peak at 880°C corresponding to a phase change of lead sulphate. X-ray analysis of the product indicated formation of much monobasic lead sulphate. Hence, it appears quite feasible to produce monobasic lead sulphate at temperatures of 300-400°C with the highly active lead oxide and sulphate resulting from the oxidation of lead sulphide.

Monobasic lead sulphate can also be formed by direct oxidation of lead sulphide via reaction: $4PbS + 7O_2 \longrightarrow 2(PbSO_4 \cdot PbO) + 2SO_2$ as reported by a number of workers[13, 16, 17].

The origins of any lead oxide available for direct combination with lead sulphate may be via reaction (2) or by the thermal decomposition of an intermediate, such as, lead sulphite being formed. This is discussed in $(PbSO_3 \longrightarrow PbO + SO_2)$ more detail in Chapter 5.

Tuffley & Russell[13] approached the formation of basic sulphates from the direct oxidation of lead sulphide, but did not consider the reaction of lead oxide and lead sulphate which is possible above ∿ 350°C as experimental evidence has shown. Vander Poorten & Meunier[16] using 44-74 µm galena found monobasic lead sulphate between 550-650°C resulting from direct oxidation of lead sulphide, but did not find lead sulphate until 700°C after 90 min. The proposed mechanism shows the basic sulphate as the top oxidation layer with lead sulphate immediately below and resulting from sulphation of the basic sulphate. This appears to be the reverse of the present findings, in that, lead sulphate was always the premier oxidation product with the basic sulphate resulting probably from both direct oxidation and reaction of lead oxide and sulphate.

The major difference between the experiments performed here and by previous researchers was the particle size of the lead sulphide used. Culver et al[17] used 74 µm galena and found oxidation did not begin until 600°C; this is 200° above the highest temperature needed

to oxidize the most unreactive lead sulphide in the present work.
Margulis & Ponomarev[18] again using 74 μm galena found lead sulphate
first produced at $600^{\circ}C$, with monobasic lead sulphate at $680^{\circ}C$; this
is the reverse order of the findings of Vander Poorten & Meunier[18] who
employed similar sized galena. Polyvannyi & Ponomarev[19] using
62-74 μm galena (air flow 10 $1h^{-1}$) identified both lead oxide and lead
sulphate or monobasic lead sulphate at $400^{\circ}C$, with traces of lead at
$550^{\circ}C$. Thus, the previous researchers results are confusing and
inconsistent. However, they do agree about the reaction kinetics with
the first stage activation energy determined to be 46.7 $kJ\,mol^{-1}$ between
$400-700^{\circ}C$ by Ponomarev & Polyvannyi[19] and 50.2 $kJ\,mol^{-1}$ from DTA
studies made by Kurian & Tamhankar[50]. Above $700^{\circ}C$ the rate constant
changes and a value of 13.9 $kJ\,mol^{-1}$ is given by Ponomarev & Polyvannyi[19]
for the activation energy. This four-fold decrease results from the
sample sintering with the rate-determining mechanism changing from
chemisorption to diffusion of oxygen.

4.3   STAGE TWO : High Temperature Oxidation

The reactions between the oxidation products of lead sulphide are:-

$$PbO + PbSO_4 \longrightarrow PbSO_4.PbO$$

$$2PbO + PbSO_4 \longrightarrow PbSO_4.2PbO$$

$$4PbO + PbSO_4 \longrightarrow PbSO_4.4PbO$$

$$(mPbO + PbSO_4 \longrightarrow PbSO_4.mPbO)$$
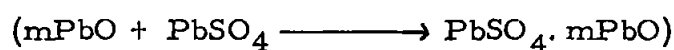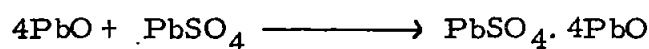
They are all thermodynamically feasible within the reaction temperatures studied, if $m > 1$ to 4 the reactions are further favoured.

The reactions of lead sulphide with the oxidations products are:-

$$PbS + 2PbO \longrightarrow 3Pb + SO_2 \text{ ————————(4)}$$

$$PbS + PbSO_4 \longrightarrow 2Pb + 2SO_2 \text{ ————————(5)}$$

$$p\,PbS + n\,PbO.PbSO_4 \longrightarrow q\,Pb + r\,SO_2$$
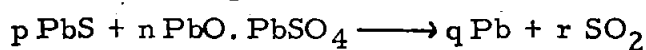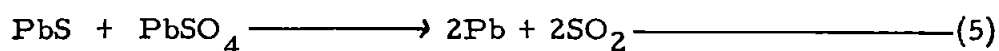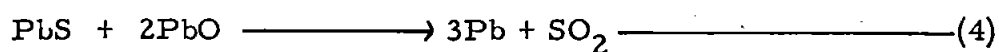
From the free energy data given in Table 4.2g reaction (4) is not feasible until $900^{\circ}C$ and reaction (5) not probable until $\sim 850^{\circ}C$ (when the ΔG value becomes negative).   The free energy data also show that the reaction $2Pb + O_2 \longrightarrow 2PbO$ (6) is possible from $400-1100^{\circ}C$ and only above $900^{\circ}C$ is reaction $PbS + O_2 \longrightarrow Pb + SO_2$ (3) more likely to occur.   Thus, any lead produced by reactions (4) and (5) will be oxidized to lead oxide, below $900^{\circ}C$, via reaction (6) and will only be stable so long as oxygen is absent from the system.   Hence, with severe sintering and thus oxygen prevented from entering the system, lead may be produced below $900^{\circ}C$.

At the higher temperatures it is possible for direct oxidation of lead sulphide to result in the basic sulphates, as shown in Section 1.2, reactions (9), (10) and (11); also sulphation of these basic sulphates can occur with sulphur dioxide to give lead sulphate, e.g. reaction (14) Section 1.2.

The additional reactions possible at the higher temperatures, viz., $850-950^{\circ}C$, modify the TG curves in Figures 40b - 45b. Formation of lead from lead sulphide gives a greater proportionate weight loss than conversion of lead sulphide to lead oxide.   Thus the TG curves at these temperatures show sharp initial weight losses followed by weight gains

ascribed to formation of lead by reaction (3) and its subsequent oxidation by reaction (6) to lead oxide. The ultimate continuous weight losses, especially at 900° and 950° represent the volatilization of the lead oxide, which is known to occur at these temperatures from separate experiments, see Figure 55a; free lead does not volatilize appreciably as illustrated in Figure 55b, and has not been found by optical or X-ray examination in the final products. However, in the TG experiments, the sharp initial weight losses at the higher temperatures are in excess of those required for the complete conversion of the lead sulphide to lead oxide; then reactions in equations (3) and (6) predominate over the possible alternative mechanism, viz., $2PbS + 3O_2 \longrightarrow 2PbO + 2SO_2$, followed by $2PbO + 2SO_2 + O_2 \longrightarrow 2PbSO_4$. This is in accordance with the thermodynamic data in Table 4.3a, where reaction (3) viz., $PbS + O_2 \longrightarrow Pb + SO_2$ should predominate over $2PbS + 3O_2 \longrightarrow 2PbO + 2SO_2$ at temperatures above about $850^{\circ}C$.

The X-ray analyses (Tables 4.2a-f) show as the reaction temperature rises from 600 to $800^{\circ}C$ a shift towards the formation of greater quantities of monobasic lead sulphate, and away from the formation of lead sulphate. Above $800^{\circ}C$, the higher basic sulphates, dibasic and tetrabasic lead sulphate are found, and ultimately free lead oxide in some of the samples at $950^{\circ}C$.

All the samples showed the presence of dibasic lead sulphate at elevated temperatures from the X-ray analyses, even though the phase diagram (Figure 17) predicts it is unstable below $620^{\circ}C$ and decomposes to give a mixture of monobasic and tetrabasic lead sulphate. Furthermore there was no evidence of any decomposition of dibasic lead sulphate, since then both the monobasic and tetrabasic salt would have been observed in the same sample, and this was not the case. Thus, the dibasic lead sulphate must have been in a metastable condition, possibly caused by the rapid cooling of the sample (due to the low sample mass).

Figure 55a   Volatilization of lead oxide in a nitrogen atmosphere
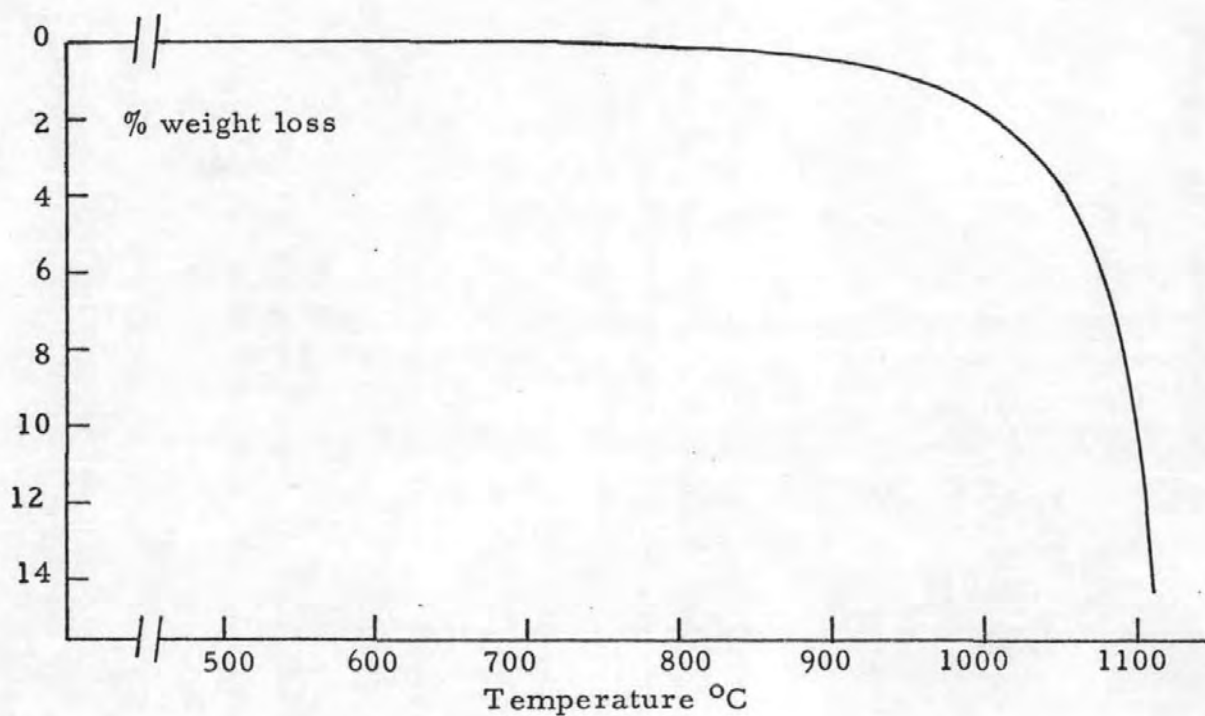
Figure 55b   Volatilization of lead in a nitrogen atmosphere
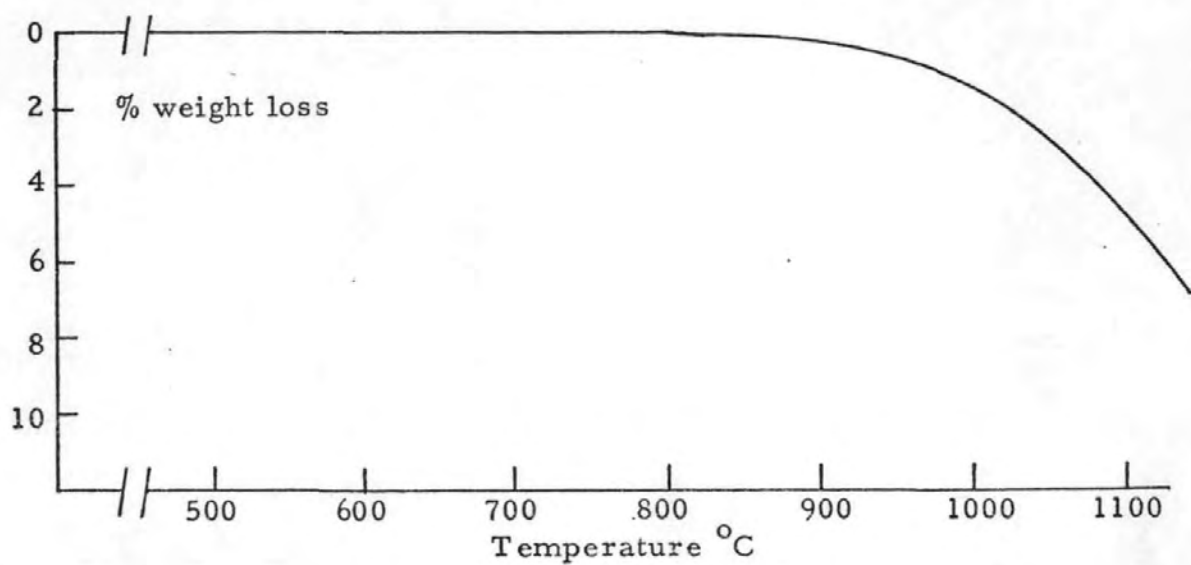
4.4 DIFFERENTIAL THERMAL ANALYSES

Further studies employing simultaneous DTA-TG were planned for the precipitated lead sulphide samples and the ores using various gas atmospheres and flow rates. The experiments were initially intended to run from room temperature to $1200^{\circ}C$, however, it was found that lead alloys with platinum above $\sim 950^{\circ}C$. On attempting to run the lead ores in the platinum crucibles greater problems were encountered with the formation of lead fluxes, with the silica present in the ores, at the higher temperatures. This resulted in the loss of a platinum crucible and serious damage to the alumina head of the balance. The manufacturers could only supply silica or platinum crucibles and thus it was decided to fabricate crucibles from alumina. The holders were constructed from alumina tubing sealed with a plug of fine alumina cement (COS 60) and shaped to fit the thermocouple. However, on testing these crucibles there was an unacceptable loss in the differential thermal signal, caused by the poor conductivity of alumina coupled with the distance the sample was from the thermocouple. After discussions with the manufacturer (who are at present investigating the possibility of alumina holders as an alternative to platinum) it was decided to restrict the oxidation temperature to $900^{\circ}C$ and use the platinum crucibles with the precipitated samples.

Inherent with the balance design the gases could only be passed over the sample and not through it as is desirable. This leads to the DTA traces in some cases having a strong initial exothermic peak, as the surface material is oxidized, but as the temperature rises sintering of the sulphate occurs inhibiting oxygen from reaching the remainder of the sample, giving a broad exothermic peak for the main reaction. The sharp endothermic peak between $870-880^{\circ}C$ occurring with all samples is a phase change from orthorhombic to monoclinic for lead sulphate.

The simultaneous DTA-TG traces are given in Figures 56-61 and the DTA traces are summarized in Tables 4.4a, b.

The samples under investigation were heated at $4.75^{0}C$ min^{-1} in a 6 mm diameter by 10 mm depth platinum crucible and mounted in the alumina DTA head, as described in Section 2.1. These samples were oxidized in static air, air flowing over the sample (500 ml min^{-1}) and pure oxygen (500 ml min^{-1}).

Figure 56

Heating rate 5°C min⁻¹
DT sensitivity 100 μV

Sample W24/80 oxidized in static air

Sample W24/80 oxidized in air flowing at 500 cm³ min⁻¹

Sample W24/80 oxidized in oxygen flowing at 500 cm³ min⁻¹
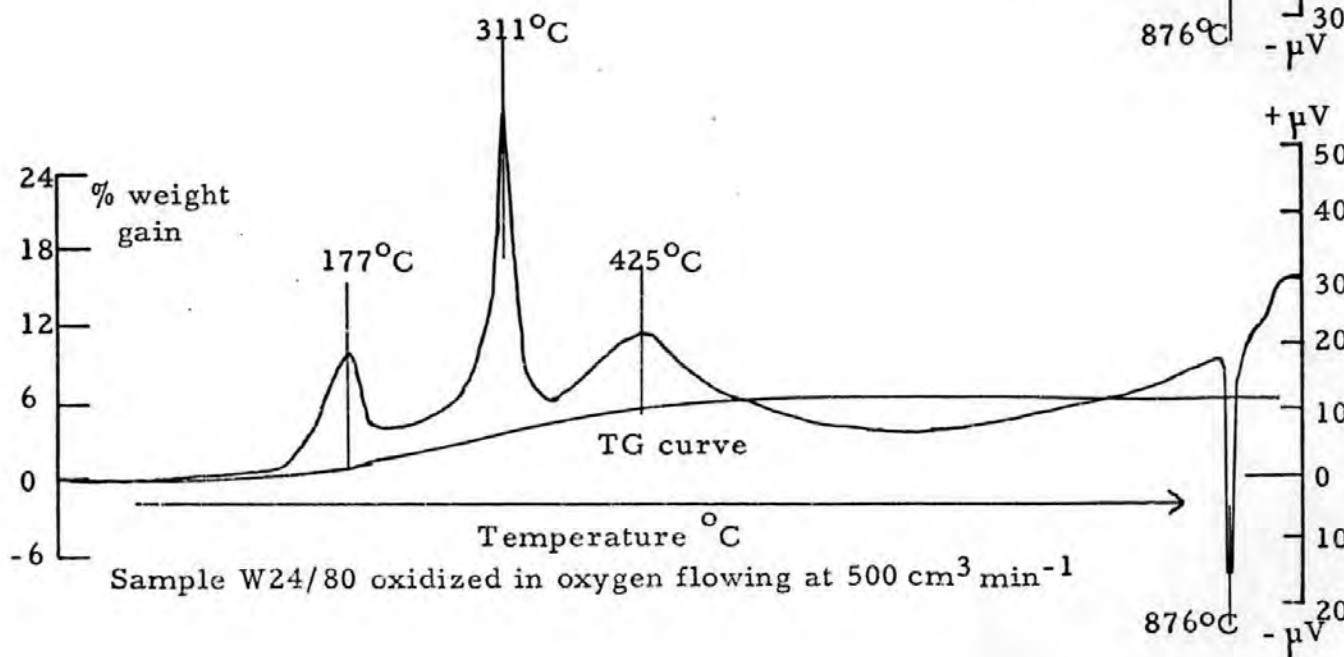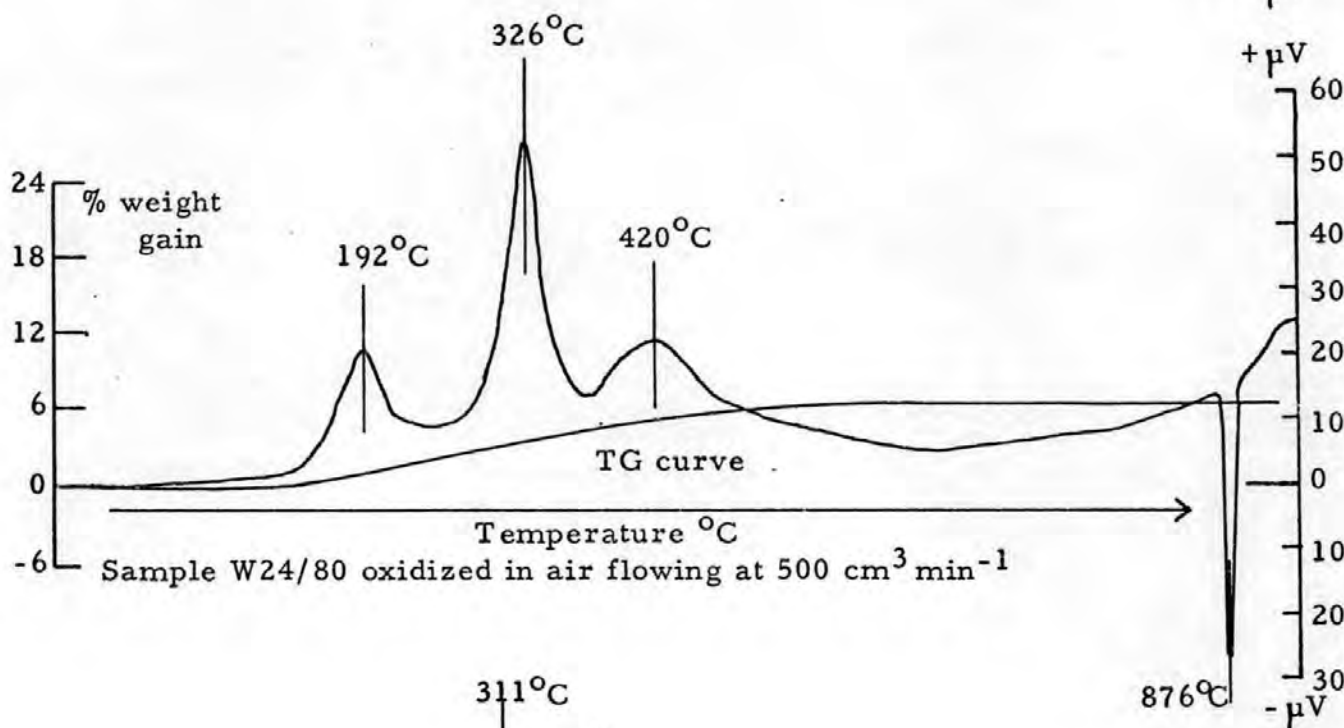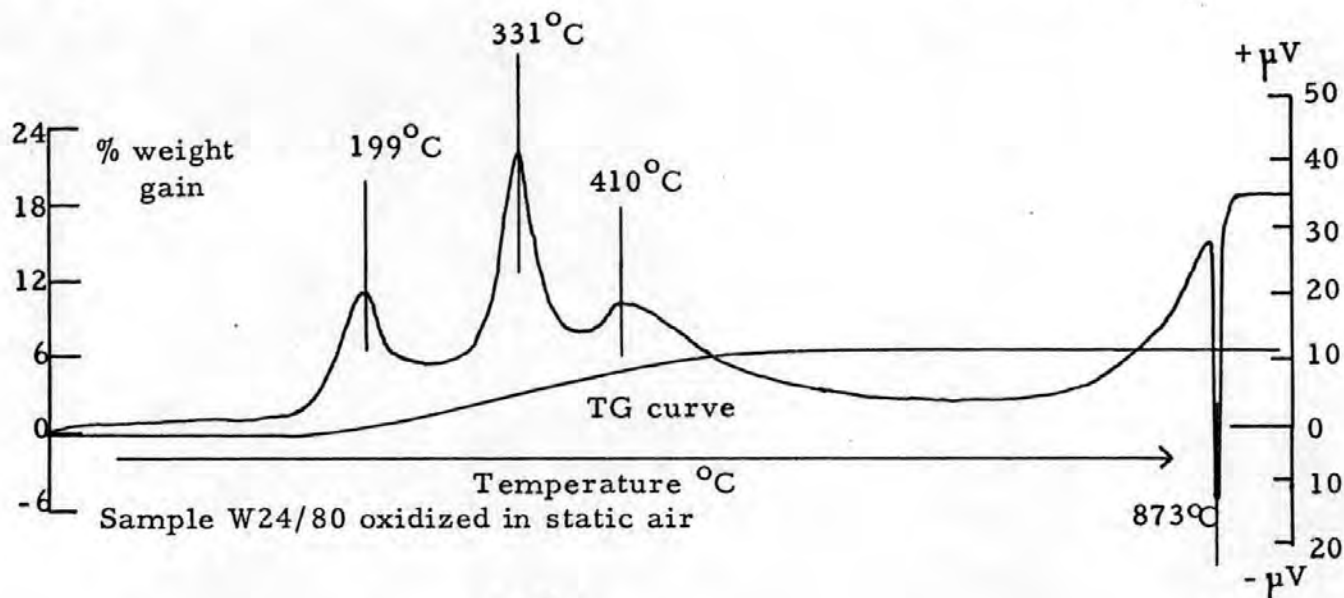
Figure 57

Heating rate 5°C min⁻¹
DT sensitivity 100 μV

Sample D24/80 oxidized in static air

Sample D24/80 oxidized in air flowing at 500 cm³min⁻¹

Sample D24/80 oxidized in oxygen flowing at 500 cm³min⁻¹
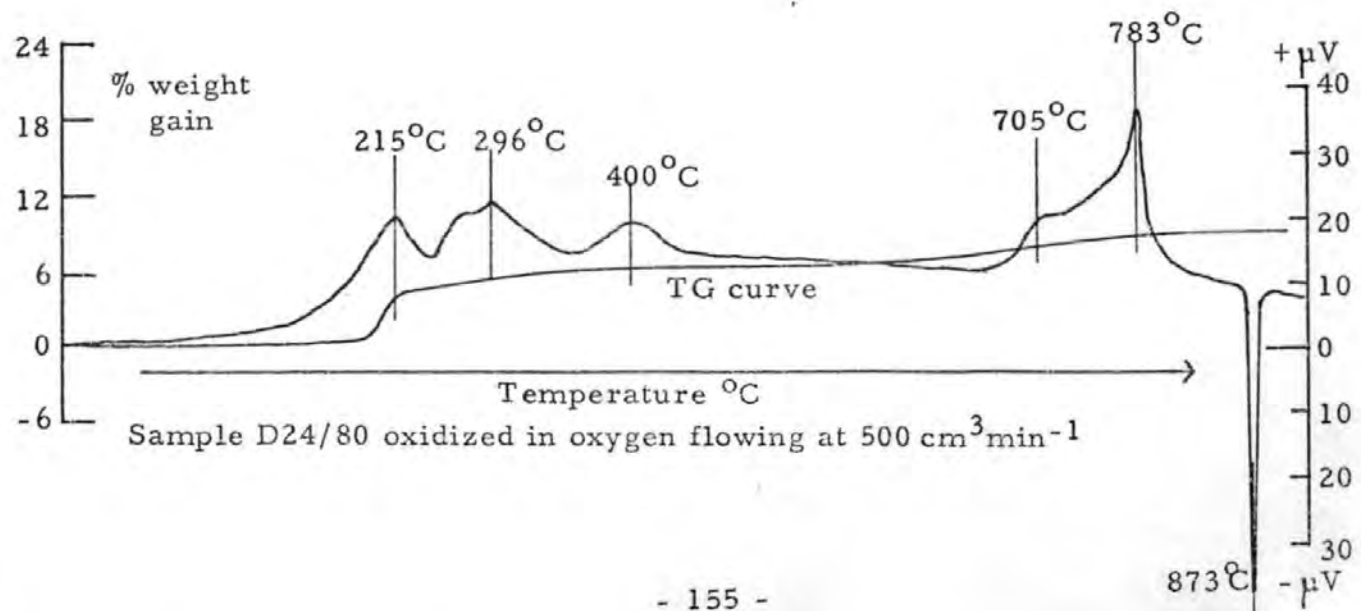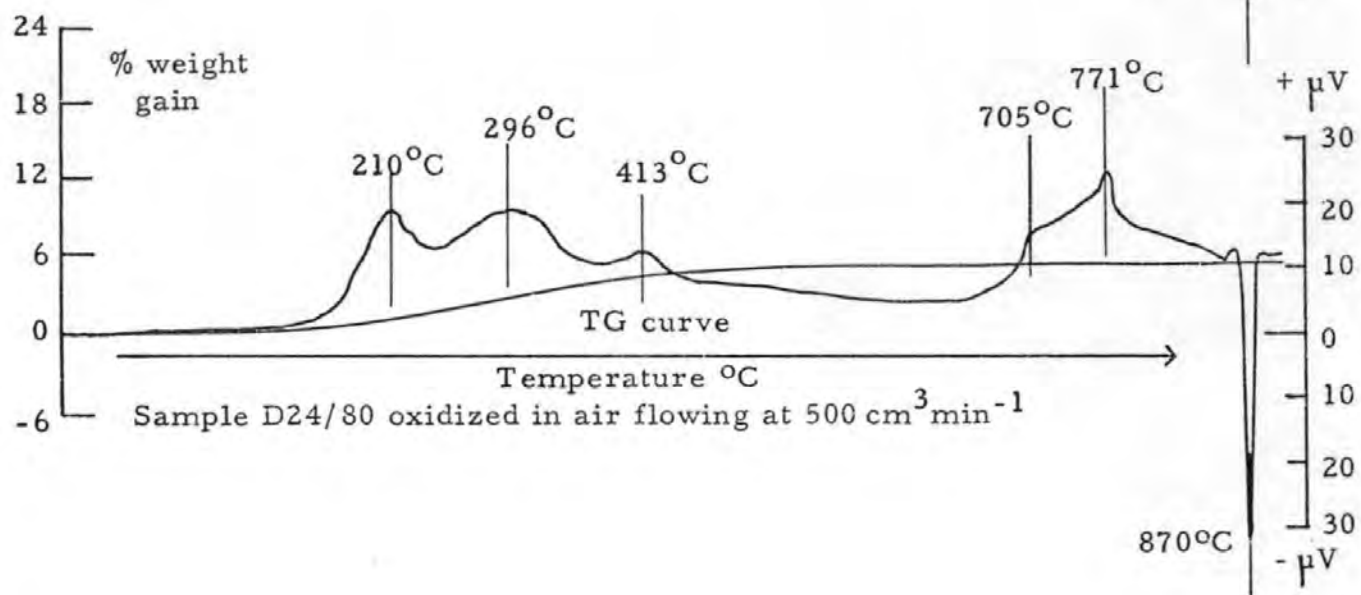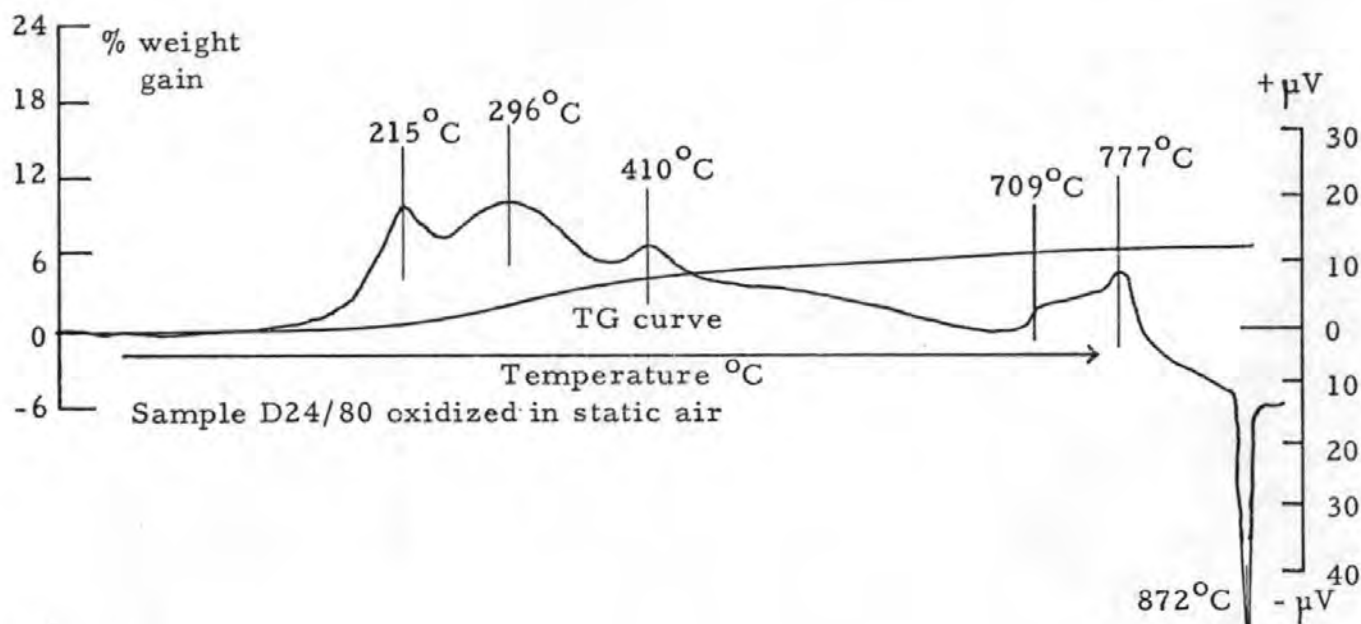
Figure 58

Heating rate 5°C min⁻¹
DT sensitivity 100 μV

Sample Q24/80 oxidized in static air

Sample Q24/80 oxidized in air flowing at 500 cm³min⁻¹

Sample Q24/80 oxidized in oxygen flowing at 500 cm³min⁻¹
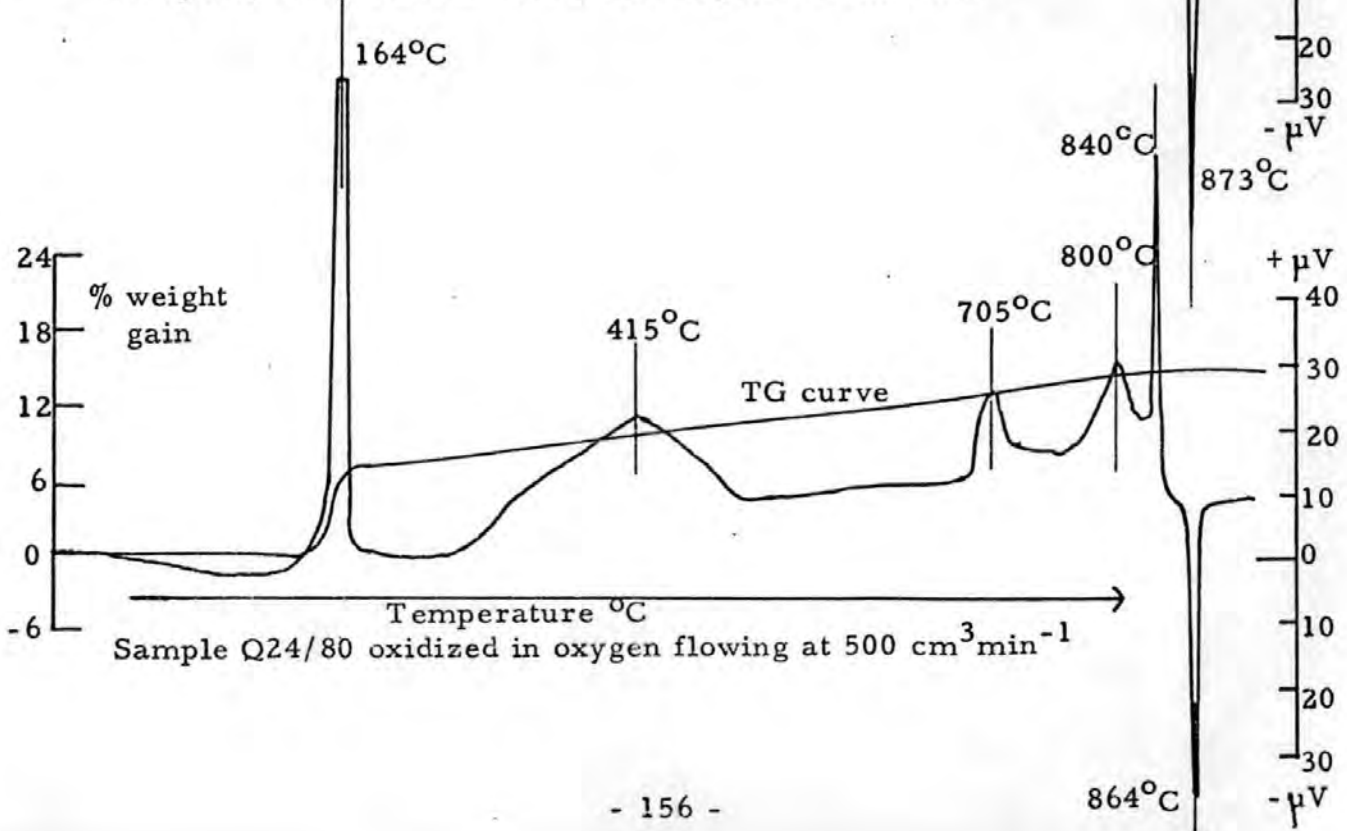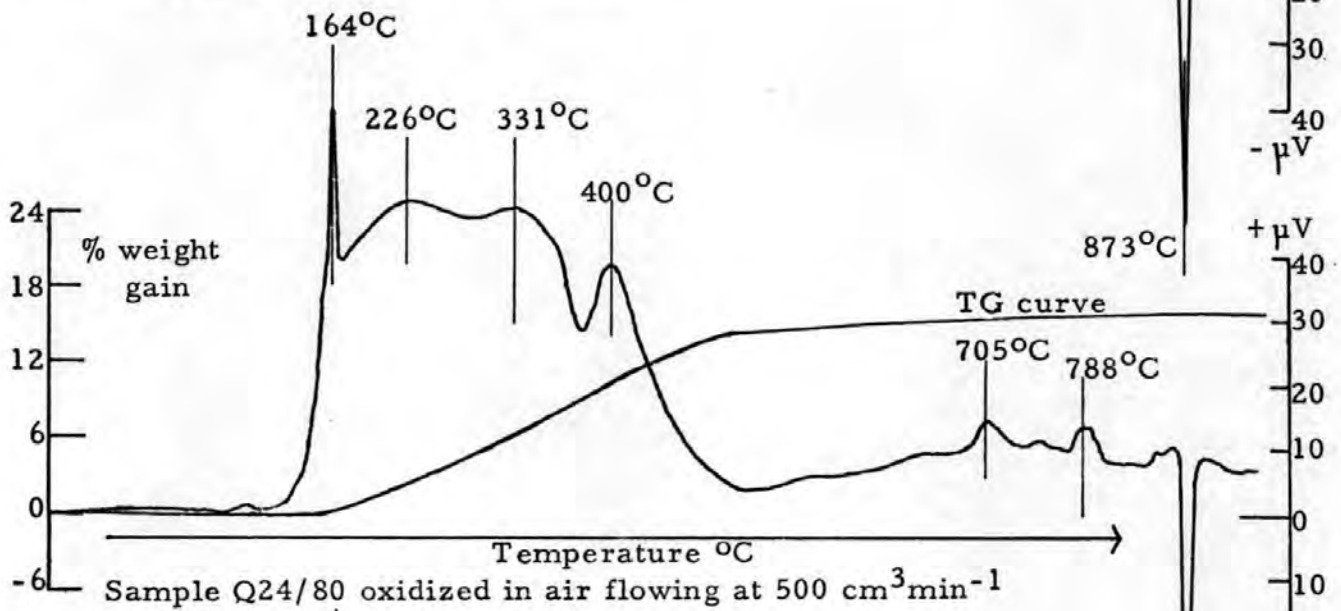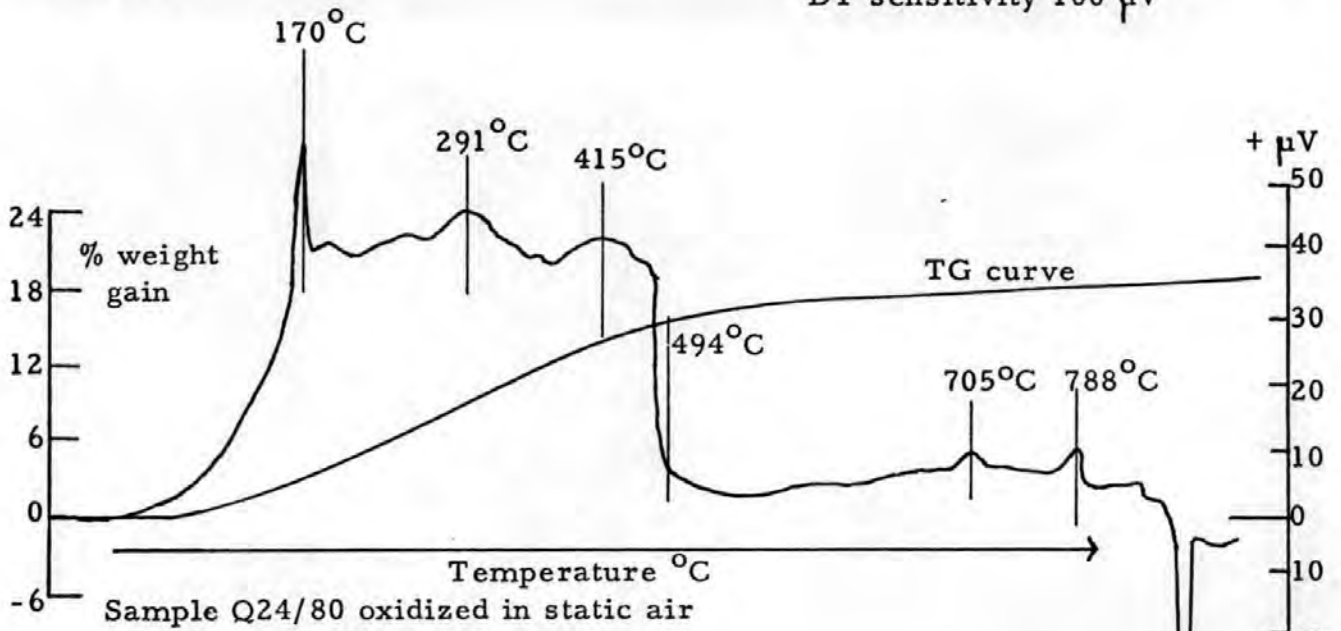
Figure 59

Heating rate 5°C min⁻¹
DT sensitivity 100 μV

Sample J24/80 oxidized in static air

Sample J24/80 oxidized in air flowing at 500 cm³min⁻¹

Sample J24/80 oxidized in oxygen flowing at 500 cm³min⁻¹
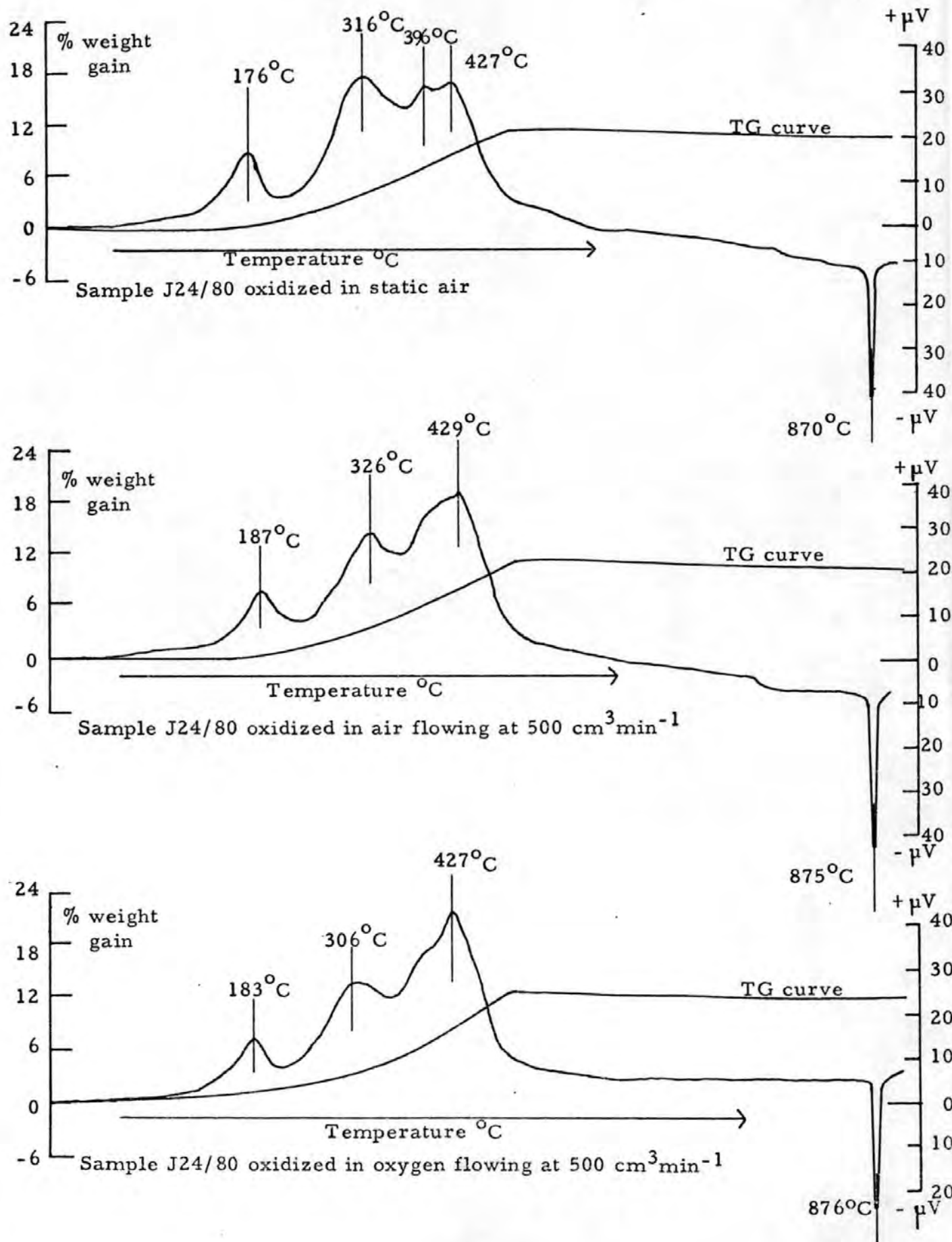
Figure 60

Heating rate 5°Cmin⁻¹
DT sensitivity 100 μV

Sample X24/80 oxidized in static air

Sample X24/80 oxidized in air flowing at 500 cm³min⁻¹

Sample X24/80 oxidized in oxygen flowing at 500 cm³min⁻¹
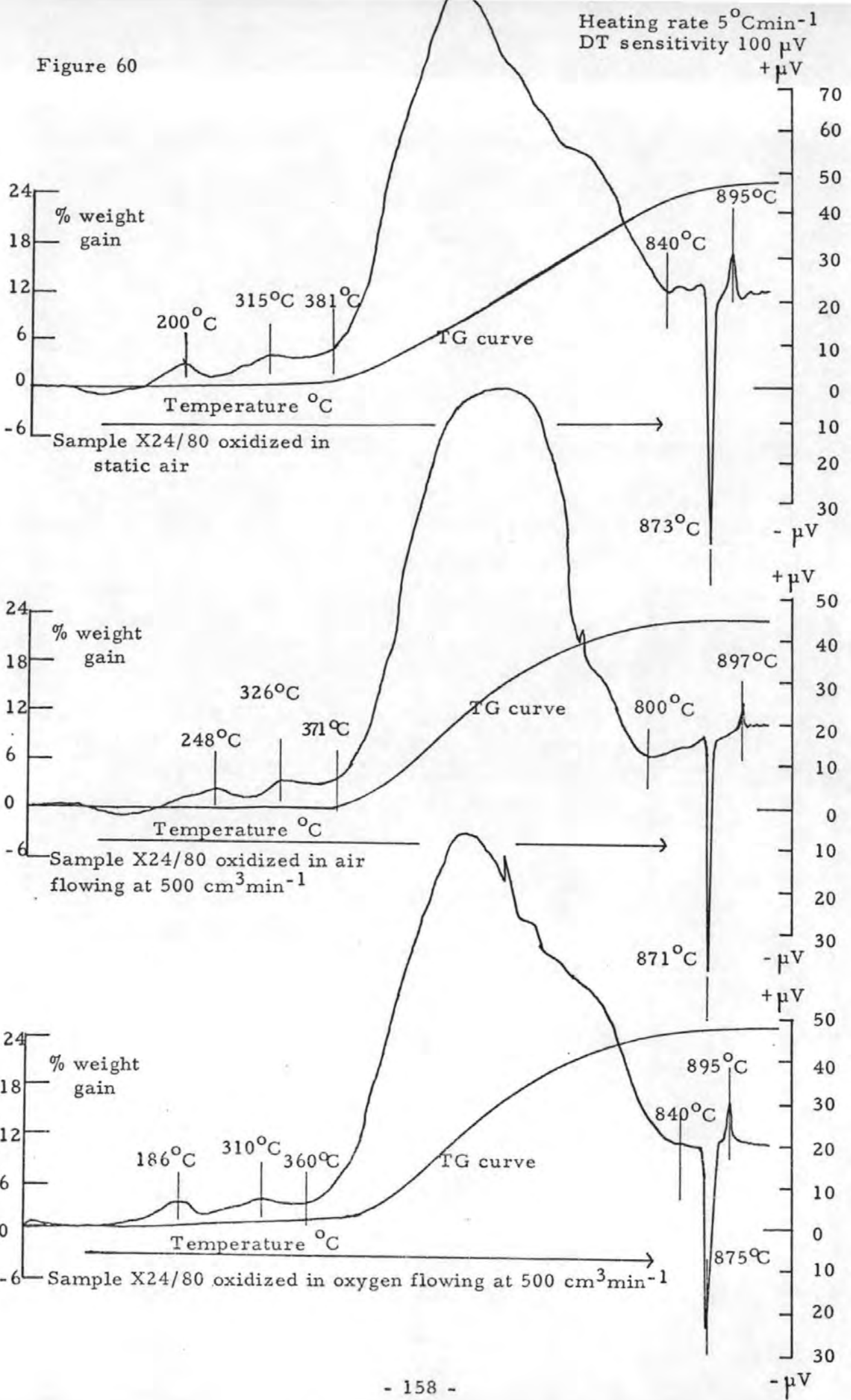
Figure 61

Heating rate 5°C min⁻¹
DT sensitivity 100 μV

Sample BDH oxidized in static air

Sample BDH oxidized in air flowing at 500 cm³min⁻¹

Sample BDH oxidized in oxygen flowing at 500 cm³min⁻¹

	X24/80	J24/80	Q24/80
STATIC AIR	Small exoth.pks at 200,315°C Large broad exoth.(381 - 840°C), with max. 562°C. Phase change $PbSO_4$ - 873°C Small exoth.895°C Total weight gain - 25.0% Analysis: only $PbSO_4$	Exoth.pk. 176°C Broad exoth.pk. 215 - 549°C Smaller broad pks.at 316,396, 427°C $PbSO_4$ phase change - 870°C Total weight gain - 11.3% Analysis: $PbSO_4.PbO$ and $PbSO_4$	Large broad exoth. 120 - 476°C, sharp pk.170°C; broader small pks.at 291, 415°C. Small exoth.pks. at 705, 788°C $PbSO_4$ phase change - 870°C Total weight gain - 18.6% Analysis: mainly $PbSO_4$, little $PbSO_4.PbO$
AIR FLOWING $500 \, cm^3 \, min^{-1}$	Very small exoth.pks.at 248, 326°C Large broad exoth.pk. (371 - 800°C), with max. at 630°C. $PbSO_4$ phase change - 871°C Small exoth.pk. 897°C Total weight gain - 23.1% Analysis: mainly $PbSO_4$,little $PbSO_4.PbO$	Exoth.pk. 187°C Broad exoth.pk. 248 - 522°C Smaller broad pks. at 326,408,429°C $PbSO_4$ phase change - 875°C Total weight gain - 11.0% Analysis: $PbSO_4.PbO$ and $PbSO_4$	Large broad exoth. 120 - 494°C, sharp pks 164, 400°C; broad small pks. at 226, 331°C. Small exoth.pks.at 705, 788°C. $PbSO_4$ phase change - 873°C Total weight gain - 16.7% Analysis: mainly $PbSO_4$,little $PbSO_4.PbO$
OXYGEN FLOWING $500 \, cm^3 \, min^{-1}$	Small exoth.pks. 186, 360°C Large broad exoth.pk.(360 - 840°C) with max. 615°C $PbSO_4$ phase change - 875°C Small exoth.pk. 895°C Total weight gain - 25.0% Analysis: mainly $PbSO_4$, very little $PbSO_4.PbO$	Exoth.pk. 183°C Broad exoth.pk. 240 - 485°C with pks. at 306, 427°C $PbSO_4$ phase change - 876°C Total weight gain - 11.7% Analysis: $PbSO_4.PbO$ and $PbSO_4$	Very strong sharp pk. 107 - 186°C Smaller broad exoth. 240 - 522°C, max. at 415°C Small sharp exoth.pks.705,800°C Very sharp exoth.pk. - 840°C $PbSO_4$ phase change - 864°C Total weight gain - 14.9% Analysis: mainly $PbSO_4$, medium $PbSO_4.PbO$

exoth.= exothermic;   pk.= peak;   max.= maximum

Table 4.4a Characteristic temperatures for DTA studies of the lead sulphide samples

Table 4.4b Characteristic temperatures for DTA studies of the lead sulphide samples

	D24/80	W24/80	BDH
STATIC AIR	Broad shallow exoth. 146-476°C with small exoth.pks.at 215,296,410°C. Small exoth.pk. 709 - 787°C. $PbSO_4$ phase change - 872°C Total weight gain = 6.6% Analysis: mainly $PbSO_4 \cdot PbO$, little $PbSO_4$	Medium exoth.pks.at 199,331,410°C $PbSO_4$ phase change - 873°C Total weight gain = 6.4% Analysis: mainly $PbSO_4 \cdot PbO$, little $PbSO_4$	Large strong exoth. 158 - 395°C with max. at 237°C Smaller broad pks. 457,603,722°C $PbSO_4$ phase change - 868°C Total weight gain = 11.2% Analysis: strong $PbSO_4 \cdot PbO$ and $PbSO_4$
AIR FLOWING 500 $cm^3 min^{-1}$	Broad shallow exoth. pks.148-448°C with small exoth.pks. at 210,296,413°C Small exoth. 705 - 781°C $PbSO_4$ phase change - 870°C Total weight gain = 5.1% Analysis: mainly $PbSO_4 \cdot PbO$, little $PbSO_4$	Medium exoth.pks.at 192,326,420°C $PbSO_4$ phase change - 876°C Total weight gain = 6.6% Analysis: mainly $PbSO_4 \cdot PbO$, little $PbSO_4$	Strong exoth. 146-336°C, with max.at 230°C Smaller broad pks. 460, 620, 730°C $PbSO_4$ phase change - 868°C Total weight gain = 12.6% Analysis: strong $PbSO_4 \cdot PbO$ and $PbSO_4$
OXYGEN FLOWING 500 $cm^3 min^{-1}$	Broad shallow exoth. 138 - 439°C with small exoth.pks. 215, 296, 400°C. Small exoth. 705 - 793°C $PbSO_4$ phase change - 873°C Total weight gain = 8.2% Analysis: mainly $PbSO_4 \cdot PbO$, little $PbSO_4$	Medium exoth.pks. at 177,311,425°C $PbSO_4$ phase change - 876°C Total weight gain = 6.2% Analysis: mainly $PbSO_4 \cdot PbO$, little $PbSO_4$	Strong sharp exoth. 165 - 254°C, with max. at 230°C Slow exoth.reaction 351 - 850°C with small maxima at 476, 700,800°C Sharp max.exoth. 852°C $PbSO_4$ phase change - 865°C Total weight gain = 10.6% Analysis: strong $PbSO_4 \cdot PbO$ and $PbSO_4$

exoth. = exothermic; pk.= peak; max.= maximum

Platinum catalyses the $2SO_2 + O_2 \longrightarrow 2SO_3$ reaction and as a consequence the samples sulphated to a greater extent than was found in the isothermal studies carried out in alumina crucibles. Analysis of the products at $900^{\circ}C$ shows that the only products were lead sulphate and monobasic lead sulphate in all cases. Samples X24/80 gained 25% weight as a result of sulphation (a maximum weight gain of 26.75% is possible for complete sulphation). This strong catalytic effect of platinum on the rate of sulphation agrees with similar findings in the previous study on the oxidation of zinc sulphide[71].

There was little difference in the overall weight gains or the DTA traces obtained when the sample was oxidized in static or flowing air. This is possibly caused by the geometry of the crucible with the relatively low surface contact with the atmosphere. As the temperature rises, sintering of the products begins, further impeding the exchange of reaction and product gases, thus favouring the formation of sulphur trioxide and ultimately sulphation.

With an oxygen atmosphere, in general, the DTA traces show a sharper, stronger initial exothermic peak with the associated greater weight gains.

The comparatively rapid formation of lead sulphate at the lower temperature in oxygen apparently produces an almost impermeable layer of reaction product when only a quarter of the sample is sulphated. At temperatures of about $160^{\circ}C$ only surface diffusion is possible, and there is little additional reaction until temperatures of over 300° are reached when crystal lattice diffusion becomes appreciable. The amount of sulphation gradually increases with further rise in temperature, when it is accompanied by basic salt formation.

The sulphate layer is formed less rapidly in static or flowing air conditions, requiring correspondingly higher temperatures when there is evolution of some sulphur dioxide in the formation of lead oxide leading to basic sulphates. This gas evolution may destabilize the product layer and reduce the impedance. Hence, more sulphate can be formed ultimately in air than in oxygen as the temperature rises to $\sim 450^{\circ}C$.

The abscissa of the DTA figures are in microvolts, this is

because the output from the thermocouples is not linear with temperature. A calibration graph of microvolts against reaction temperature was constructed and is given in Figure 62 for the conversion microvolts to change in temperature, ΔT, at a particular reaction temperature.

As can be seen from Figures 56-61 the DTA traces varied to a great extent, depending on the crystallinity and particle size of the sample used, i.e. the poorly crystalline material oxidizing at a lower temperature with the associated shift in the exothermic peaks. After the initial oxidation exothermic peak there were a series of smaller broader exothermic peaks which could not be assigned to any particular reactions, i.e. Q24/80 had a small exothermic peak at $705^{\circ}C$ in all atmospheres. These peaks were investigated by oxidizing the sample to the peak temperature and then quenching the reaction by evacuation, and studying the phases present by X-ray diffraction. However, no significant results were obtained; but because of the regular pattern of the peaks it suggests the cause is more than the surface cracking, thus promoting oxidation for a short period.
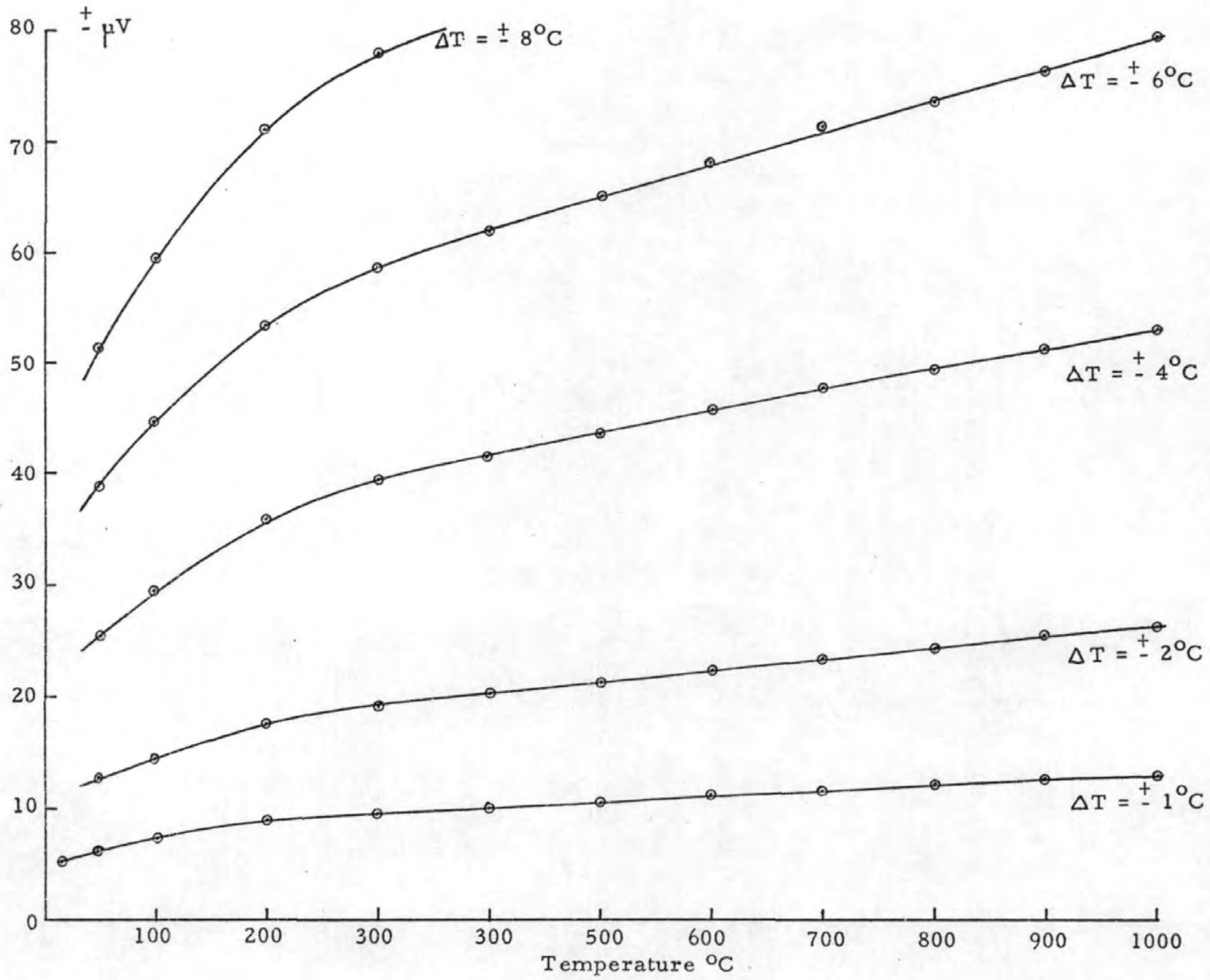
Figure 62   Plot of µV against temperature

4.5 STABILITY OF LEAD SULPHATE

INTRODUCTION

Richards[104] has calculated the stability of the lead sulphate with respect to temperature, sulphur dioxide and oxygen concentration in blast furnace roasting from thermodynamic data. The resulting phase diagram (Figure 63) indicated that lead sulphate was more stable than suggested by the present researches. In calculating the phase diagram the thermodynamic quantities were calculated for the solids so that an error due to the extrapolation into the liquid region exists. On re-calculating, after allowing for liquid phases, the line of stability of lead sulphate/monobasic lead sulphate is about 100° lower.

4.5.1 Experimental

To test the stability of lead sulphate between 850 and 1250°C in atmospheres of varying amounts of oxygen, nitrogen and sulphur dioxide it is necessary to have good control over the flow of the gases. Oxygen and nitrogen were obtained from pressurized cylinders fitted with pressure regulators and calibrated rotameters, thus the gas flow could be controlled closely and consistently. The greatest problem was controlling the sulphur dioxide over long time periods, especially at the higher flow rates. The best control was achieved by placing the cylinder in an ice-bath (thus reducing the sulphur dioxide pressure and keeping the temperature constant).

The oxygen and nitrogen were introduced into the balance chamber of the Stanton-Redcroft Massflow Balance MF-H5 with the sulphur dioxide added to the mixing chamber, giving an overall flow rate of 1 lmin^{-1}.

BDH lead sulphate (5g) was contained in an alumina crucible placed on the TG pedestal. The sample was heated to $\backsim 800^{\circ}$C in the controlled oxygen-nitrogen atmosphere when the sulphur dioxide was introduced at the desired flow rate. The overall gas composition, with respect to sulphur dioxide was determined by the Leco[74] determinator by adding aliquots of iodate and recording the time necessary for the released iodine to be consumed. The procedure of adding aliquots was repeated so as to give time intervals of $\backsim 3$ min up to 1250°C with a heating rate of 4.75°C min^{-1}. The sample temperature

Figure 63   Stability of lead sulphates in roasting gas
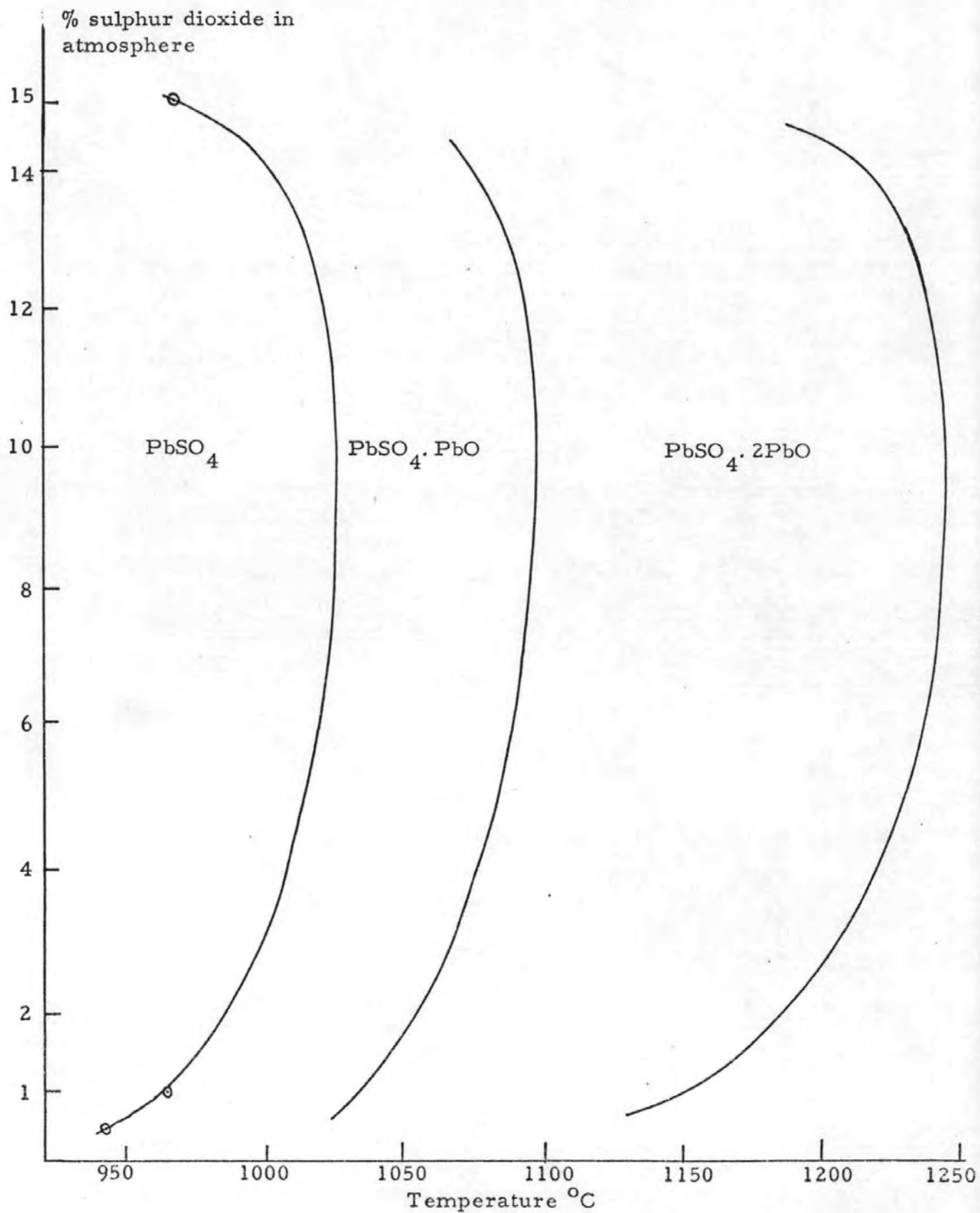
was recorded by an internal thermocouple, as the aliquots were added.

The resulting plots of percentage lead sulphate decomposed against temperature are given in Figures 64a, b, c, d, e, f.

4.5.2 Discussion

In a stream of nitrogen ($1 \ 1 \ min^{-1}$) practically all the lead sulphate decomposes as the temperature rises from 892 to $1250^{\circ}C$, (Figure 64a) 50% being decomposed when the temperature reaches $1047^{\circ}C$. The shape of the curve is sigmoidal, like that given generally for isothermal experiments, where the initial part (up to 20%) represents the induction period - nucleation and decomposition at the surface of the particles. The intermediate part covers decomposition by an advancing interface mechanism from the outside of each particle, and the final part (over 80%) is the "decay period" where the remaining isolated portions of the reactant decompose. The steepness of the curve would correspondingly increase with greater linear heating rates.

When the flow gas contains sulphur dioxide, e. g. 15% in Figure 64b, higher temperatures are required to effect the corresponding amounts of decompositoon, so that 50% of the lead sulphate is not decomposed until the temperature reaches $1099^{\circ}C$. The added sulphur dioxide has partly stabilized the lead sulphate by tending to reverse the decomposition.

$$2PbSO_4 \longrightarrow 2PbO + 2SO_2 + O_2$$
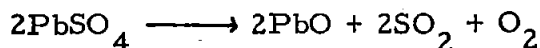
Similarly, added oxygen tends to stabilize the lead sulphate, and 50% is not decomposed until $1087^{\circ}C$ is reached (Figure 64b).

Progressively larger amounts of sulphur dioxide and smaller amounts of oxygen (Figures 64c-f) increasingly stabilize the lead sulphate as indicated by the displacements of the curves relative to each other and the increased temperature required for initial and 50% decomposition.

Figure 64b   Thermal stability of lead sulphate in an atmosphere of 21% O$_2$, 79% N$_2$
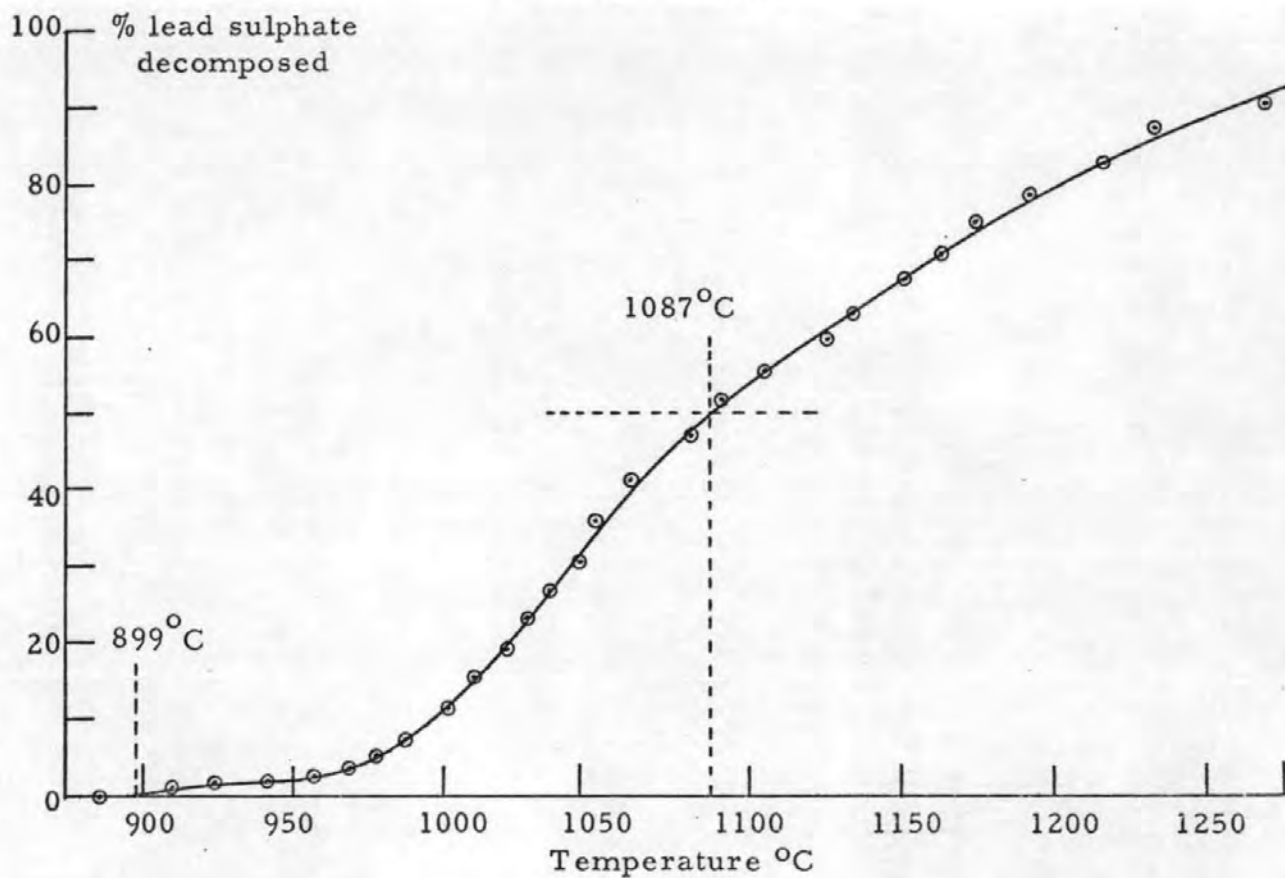
Figure 64a   Thermal stability of lead sulphate in an atmosphere of 100%N$_2$
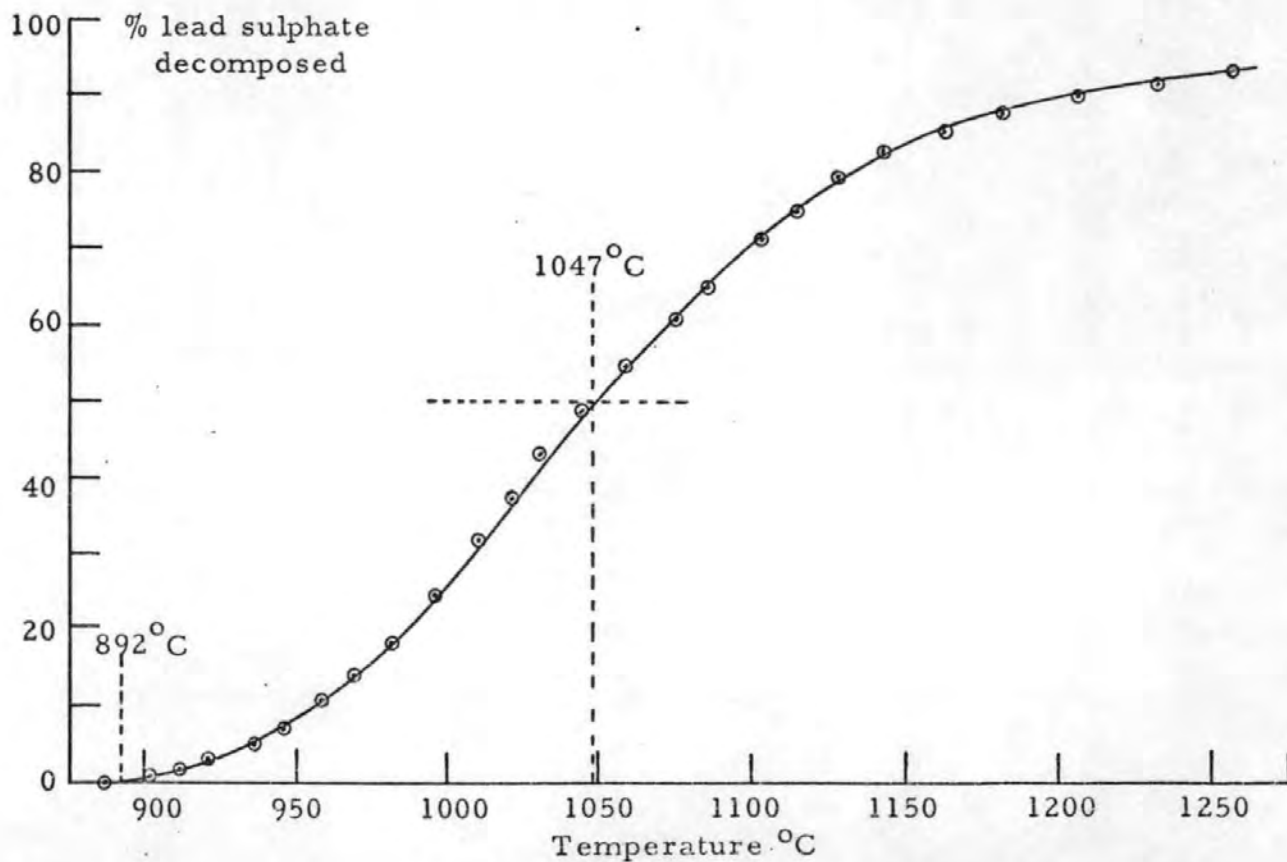
Figure 64c   Thermal stability of lead sulphate in an atmosphere of 3. 8% SO_2, 15% O_2, 81% N_2
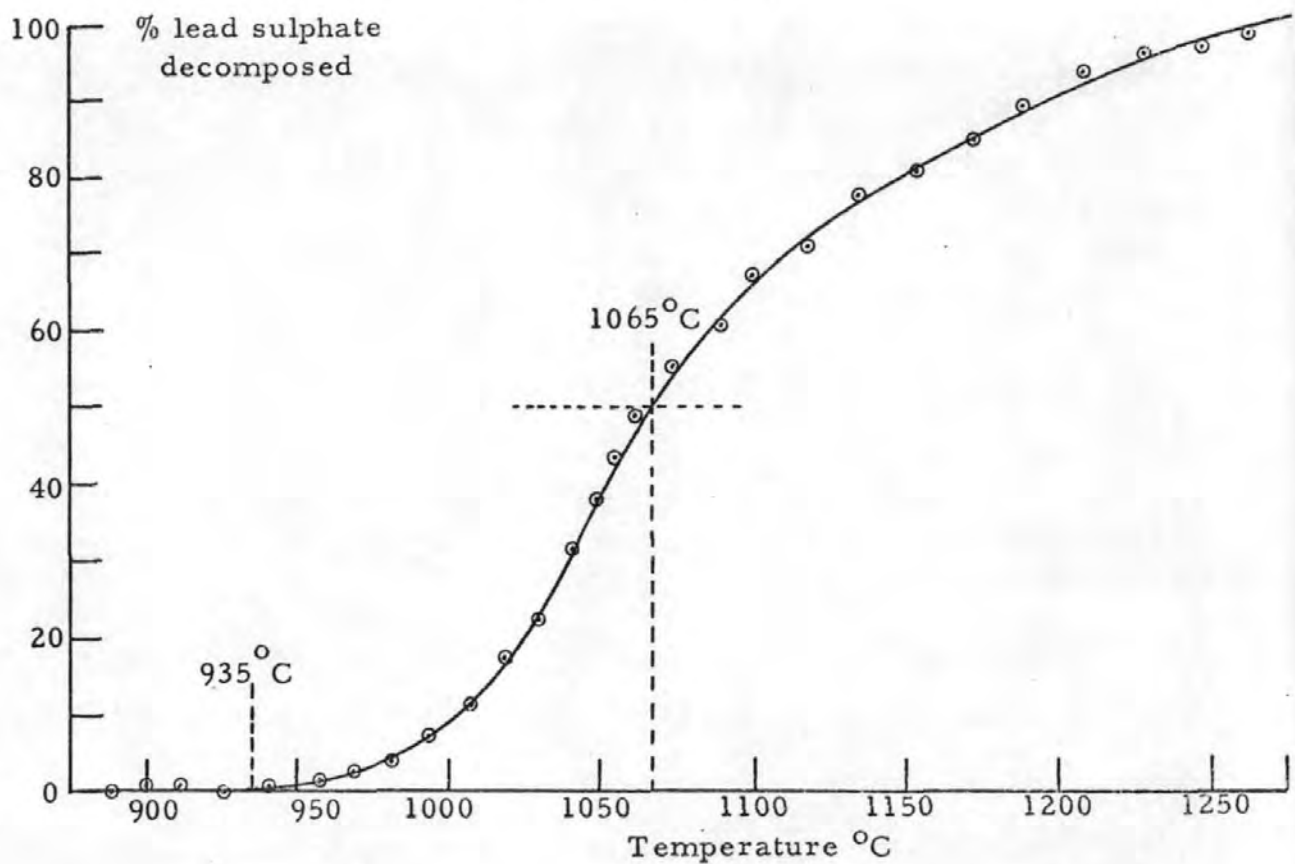
Figure 64d   Thermal stability of lead sulphate in an atmosphere of 8. 1% SO_2, 10% O_2, 82% N_2
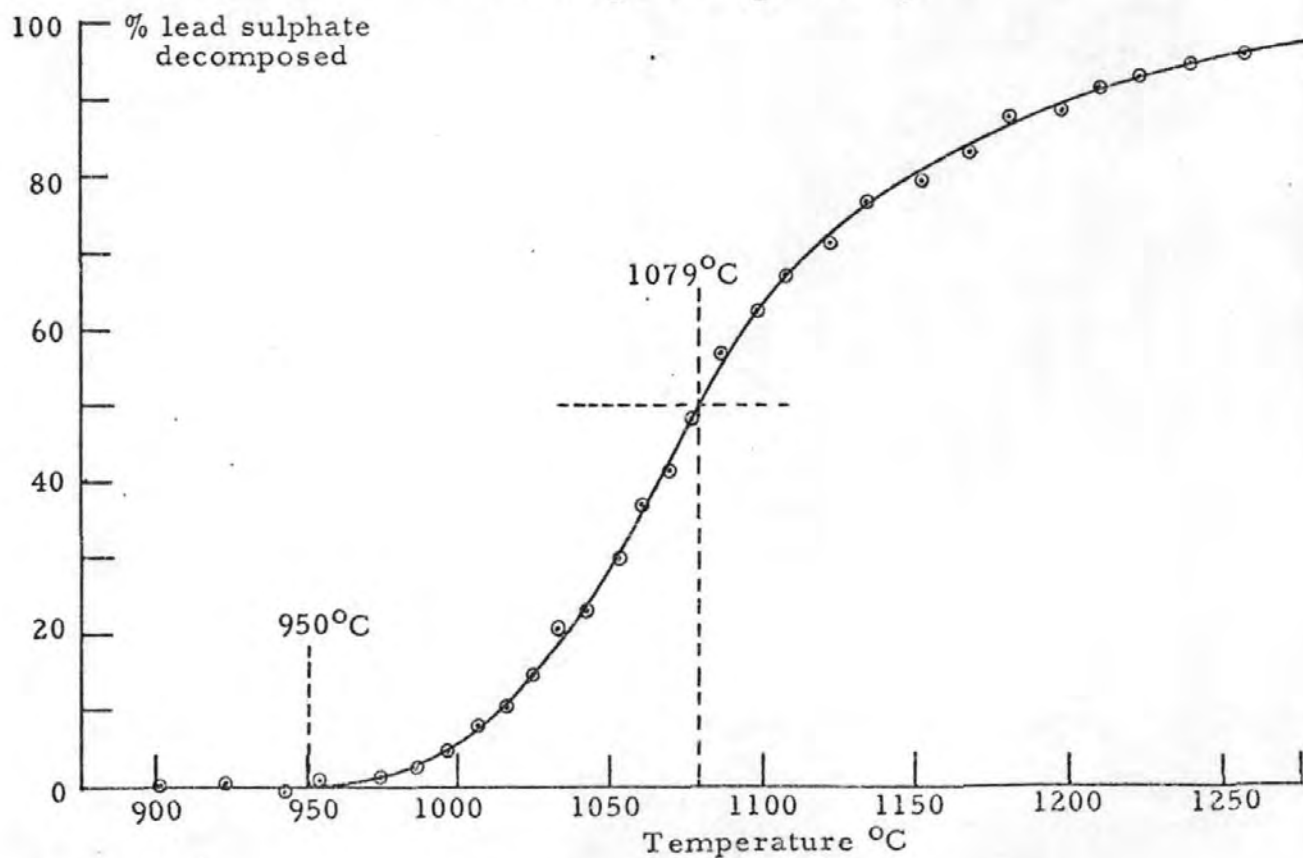
Figure 64e   Thermal stability of lead sulphate in an atmosphere of
12. 2% SO_2, 5% O_2, 83% N_2
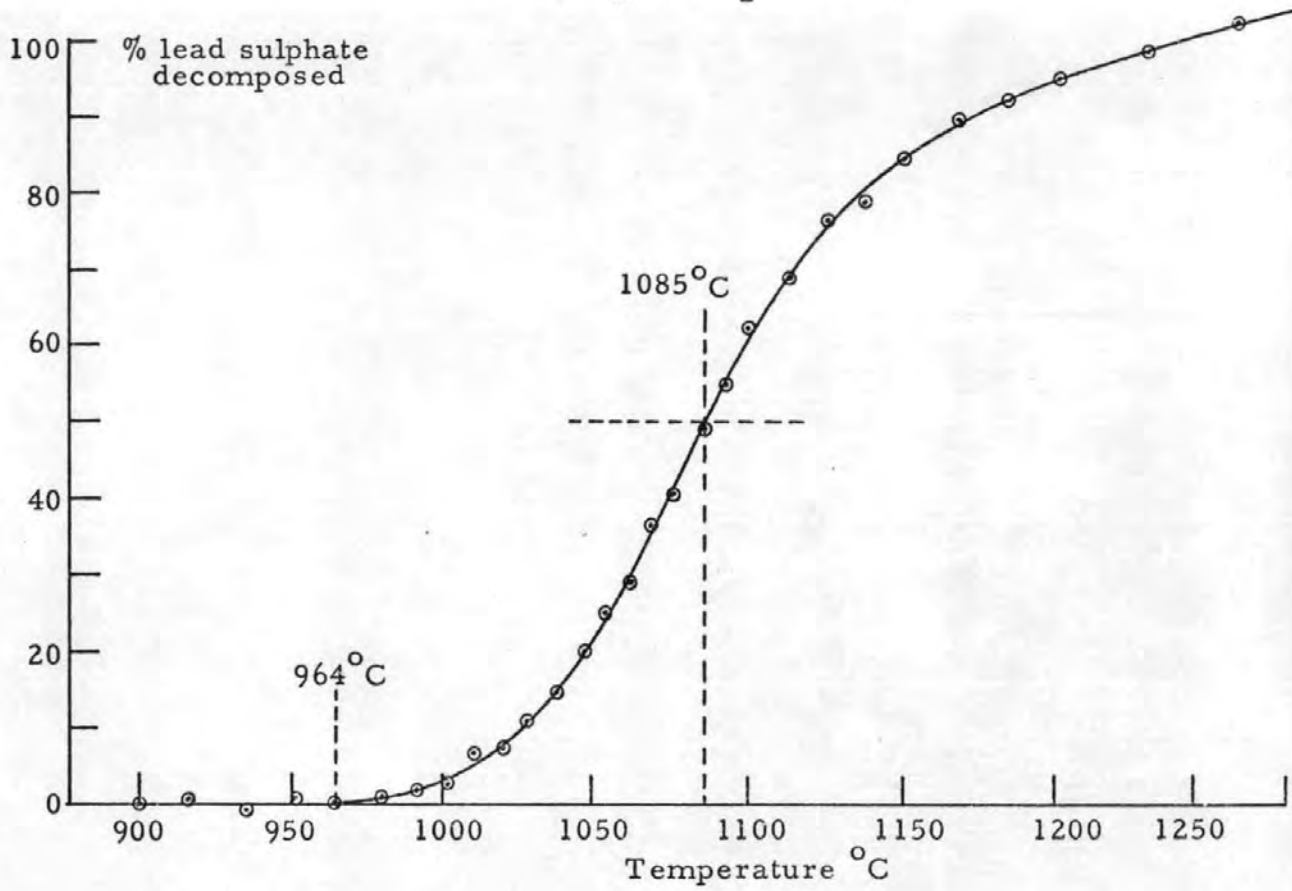
Figure 64f   Thermal stability of lead sulphate in an atmosphere of
14. 8% SO_2, 85% N_2
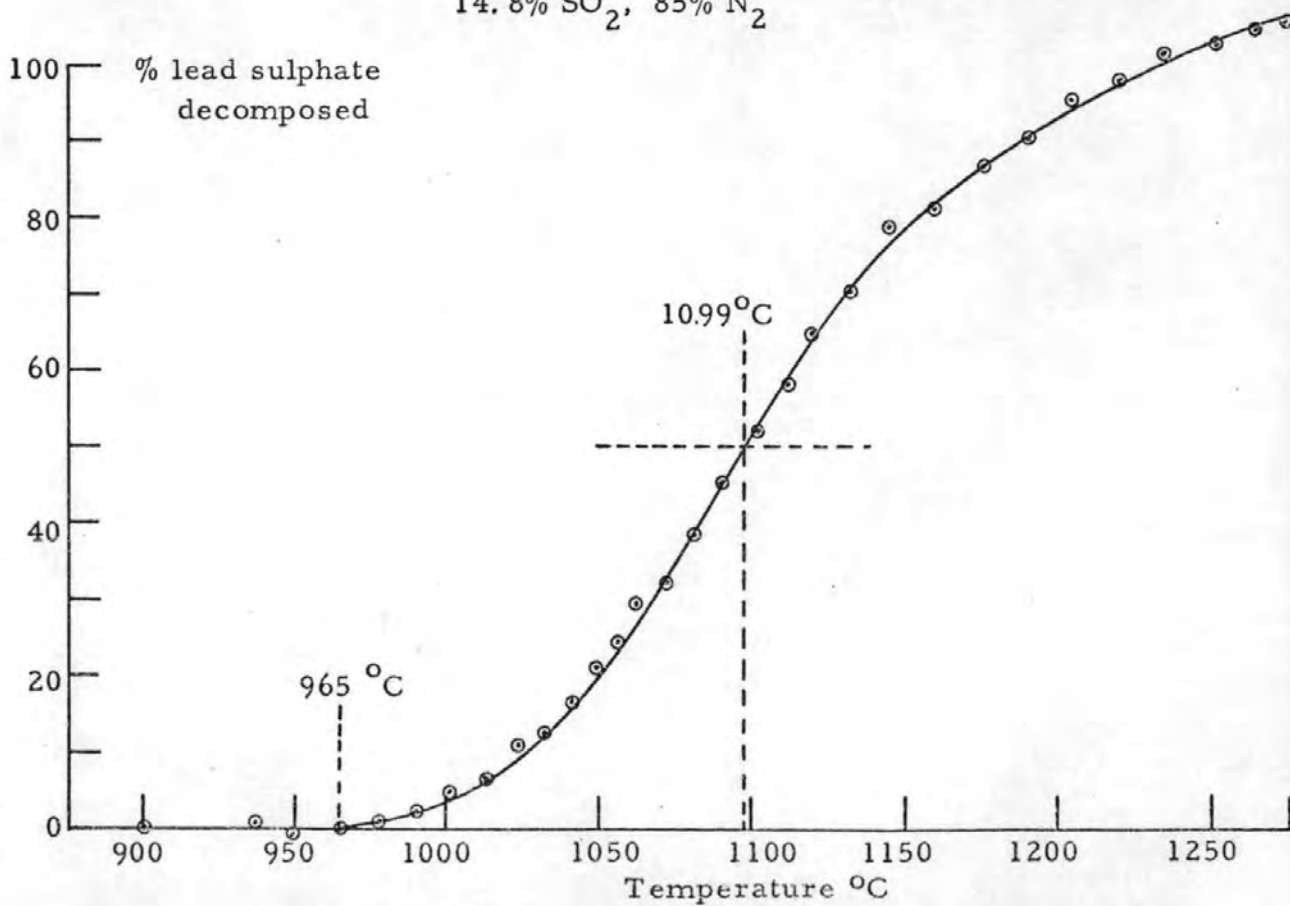
CHAPTER 5

COMPARISON OF THE OXIDATION OF LEAD AND RELATED SULPHIDES

5.1 INTRODUCTION

The research described in Chapter 4 has shown the formation of basic sulphates in the oxidation of lead sulphide, over a wide range of temperature. The tendency to form basic salts is not normally as great in the oxidation of other metal sulphides. This is illustrated by researches on the oxidation of zinc and calcium sulphide which are summarized below.

5.1.1 Oxidation of Zinc Sulphide

In the isothermal oxidation of zinc sulphide below 850°C the quantity of zinc sulphate formed in the early stages reaches a maximum value before decreasing on further roasting. At higher temperatures ($\sim$850°C), the thermodynamics are favourable for the reaction of zinc sulphate and zinc sulphide to give zinc oxide. The basic sulphate $ZnO.2ZnSO_4$ has been identified by X-ray diffraction in the roasted samples particularly at temperatures $\sim$650°C for finely divided α-ZnS and $\sim$700°C for the coarser β-ZnS. Sulphate formation becomes more prominent in the presence of platinum crucibles, resulting in up to 35% of zinc sulphide being converted to sulphate at 620°C compared with $\sim$1% in the absence of platinum. A 2-stage oxidation mechanism is indicated from the 2 exothermic peaks given by the DTA curves:-

(i) nucleation of zinc sulphide and development of the reaction across the surface of the particle (cf kinetic region)

(ii) penetration of oxygen through the oxide layer, promoting further oxidation by an advancing interface mechanism inwards (cf. diffusion region). The oxidation rates, particularly in the diffusion region are lowered by sintering of the products at the higher temperatures.

5.1.2 Oxidation of Calcium Sulphide

The mode of oxidation of this metal sulphide is typical of alkaline earth metal sulphides which do not form any basic salts on oxidation but form sulphites as intermediates. Thus, calcium sulphide slowly oxidizes in air at room temperature to form calcium sulphite,

$CaSO_3$, and γ-$CaSO_4$. The hemihydrates of these compounds dehydrate in air or _in vacuo_ at temperatures below 400°C and the sulphite oxidizes more rapidly with increasing temperature. _In vacuo_ above 500°C, there is some disproportionation to sulphate and sulphide, i.e. $4CaSO_3 \longrightarrow 3CaSO_4 + CaS$ and some decomposition to oxide, i.e. $CaSO_3 \longrightarrow CaO + SO_2$.

5.1.3 Comparison with the Oxidation of Lead Sulphide

By analogy with calcium sulphide, there is the possibility of initial oxidation of lead sulphide to lead sulphite, especially in conditions with limited amounts of oxygen present. Above ~ 300°C, lead sulphite can either decompose, viz.,

$$PbSO_3 \longrightarrow PbO + SO_2 \quad\text{————————(1)}$$

disporportionate, viz.,

$$4PbSO_3 \longrightarrow 3PbSO_4 + PbS \quad\text{———(2)}$$

oxidize, viz.,

$$2PbSO_3 + O_2 \longrightarrow 2PbSO_4 \quad\text{———(3)}$$
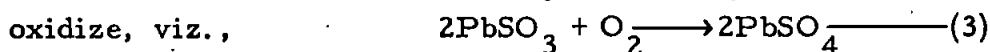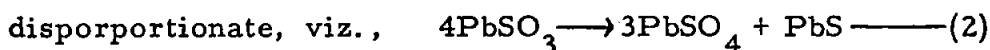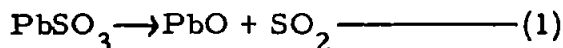
Reaction (3) occurs more readily than (1) or (2) at lower temperatures.

Separate experiments on precipitated lead sulphite (described more fully later in the Chapter) show that oxidation rates in air become appreciable above 220°C in air and at lower temperatures in oxygen. Newly-formed lead sulphite would be expected to oxidize more rapidly in air and still more so in oxygen. Thus, no lead sulphite is detected in the low-temperature (ca 160°C) oxidation of lead sulphide in oxygen.

Accordingly, when precipitated lead sulphite oxidizes at temperatures between 150 and 280°C in oxygen and 220 and 300°C in air, there is less basic sulphate formed in the presence of oxygen, i.e. reaction (3) predominates more over reactions (1) and (2).

5.2 PREPARATION AND STRUCTURE OF LEAD AND ZINC SULPHITE

Lead sulphite is unavailable commercially and so it was prepared by precipitation from solution by the double decomposition reaction of lead nitrate and sodium sulphite. To reduce the possibility of precipitating lead sulphate the sodium sulphite was dissolved in boiled water. Precipitation was achieved by slowly adding 100 cm^3 of 0.5M sodium sulphite to 100 cm^3 of 0.5M lead nitrate. The product was filtered and washed with distilled water and dried in a desiccator.

A sample was X-rayed for phase composition and the analysis showed the absence of any lead sulphate, lead nitrate, sodium nitrate and sodium sulphite. Lead sulphite was analysed for sulphite by decomposition in iodine-acid solution and titrating the remaining iodine with sodium thiosulphate. This gave 101.2% purity with respect to sulphite. However, later studies indicated the presence of 5.5%, by weight, adsorbed water in the sample (see Figure 65 c$_{1, 2}$), applying this correction to the quantity of lead sulphite taken originally gives a result of 97.4% for purity with respect to sulphite.

The ASTM data for lead sulphite appeared incomplete as the prepared sample had extra peaks which could not be assigned to any impurity. Attempts were made to grow single crystals of lead sulphite from very dilute solutions of lead salts and sodium sulphite by allowing the solutions to slowly diffuse across a bridge over a period of three months. However, the resultant crystals were $\sim$ five times too small for mounting, and thus the crystal lattice constants were determined from the powder data.

Almost all the peaks conformed with an orthorhombic type lattice with:-

$\underline{a}$ = 6.26 Å ($\pm$ 0.02 Å)

$\underline{b}$ = 7.51 Å   "

$\underline{c}$ = 5.15 Å   "

giving an X-ray density D_X = 7.87 g cm^{-3}

c.f.   ASTM data which corresponded to:-

$\underline{a}$ = 6.23 Å

$\underline{b}$ = 7.46 Å

$\underline{c}$ = 5.17 Å

Zinc sulphite was prepared similarly from solution by double decomposition of zinc chloride and sodium sulphite.

The product $ZnSO_3 \cdot 2H_2O$ gave X-ray powder diffraction data which agreed with the ASTM data card number 1-0189 and appears to conform to a monoclinic crystal lattice, since attempts to index on an orthorhombic system failed because of the high number of low angle reflections.

5.3   THERMAL DECOMPOSITION OF LEAD SULPHITE

The thermogravimetric curves are shown in Figures 65a-e for samples of lead sulphite heated in (a) vacuo, (b, $c_{1, 2}$) nitrogen, (d) air and (e) oxygen, corrected for buoyancy where applicable.

In <u>vacuo</u>, the adsorbed water is lost at temperatures up to 300°C (see Figure 65a) and sulphur dioxide at temperatures up to 500°C, after which the weight of the residue remains constant up to 600°C. The loss of sulphur dioxide corresponds to 47% of the lead sulphite being decomposed to lead oxide. Since no lead sulphite remains in the residue, the remaining 53% has evidently disproportionated, viz., $4PbSO_3 \longrightarrow 3PbSO_4 + PbS$. The X-ray diffraction analysis showed the presence of tetrabasic lead sulphate, resulting from reaction of the lead oxide produced by decomposition and lead sulphate from disproportionation.

There is almost the same amount of decomposition (44.3%) and disproportionation (55.7%) when lead sulphite is heated in nitrogen flowing at 500 ml min^{-1} (Figure 65b) at similar temperatures, but the main basic sulphate in the residue is monobasic lead sulphate, with less free lead sulphate. Although lead sulphide was difficult to identify from the X-ray traces (because of similarity of its main peaks with the other components) the grey colour of the residue was indicative of its presence.

The simultaneous TG and sulphur dioxide determination curves for the thermal stability of lead sulphite in a flowing nitrogen atmosphere (500 ml min^{-1}) are given in Figures $65c_{1, 2}$. From Figure $65c_2$, 320°C is the temperature when the sample begins to evolve sulphur dioxide and thus decompose to lead oxide, whereas Figure $65c_1$, shows a slow continuous loss from $\sim 80^{\circ}$ to $\sim 400^{\circ}$C. Taking point, X, at 540°C the total weight loss is 77.0 mg and the corresponding quantity of sulphur dioxide is 48.5 mg, thus the discrepancy of 28.5 mg is apparently adsorbed water (5.5% by weight).

There is a further sulphur dioxide loss between 620°C and 788°C which is accounted for by the reaction of lead sulphide and lead oxide giving lead and sulphur dioxide,

i.e. $PbS + 2PbO \longrightarrow 3Pb + SO_2$
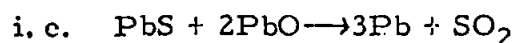
with the quantity of lead sulphide formed during disproportionation

Figure 66a Differential thermogram for the decomposition of lead sulphite in vacuo

Heating rate 4.75°C min⁻¹
DT sensitivity 100 μV

301°C

462°C

415°C

Figure 65a TG curve for the decomposition of lead sulphite in vacuo

% weight loss

Temperature °C
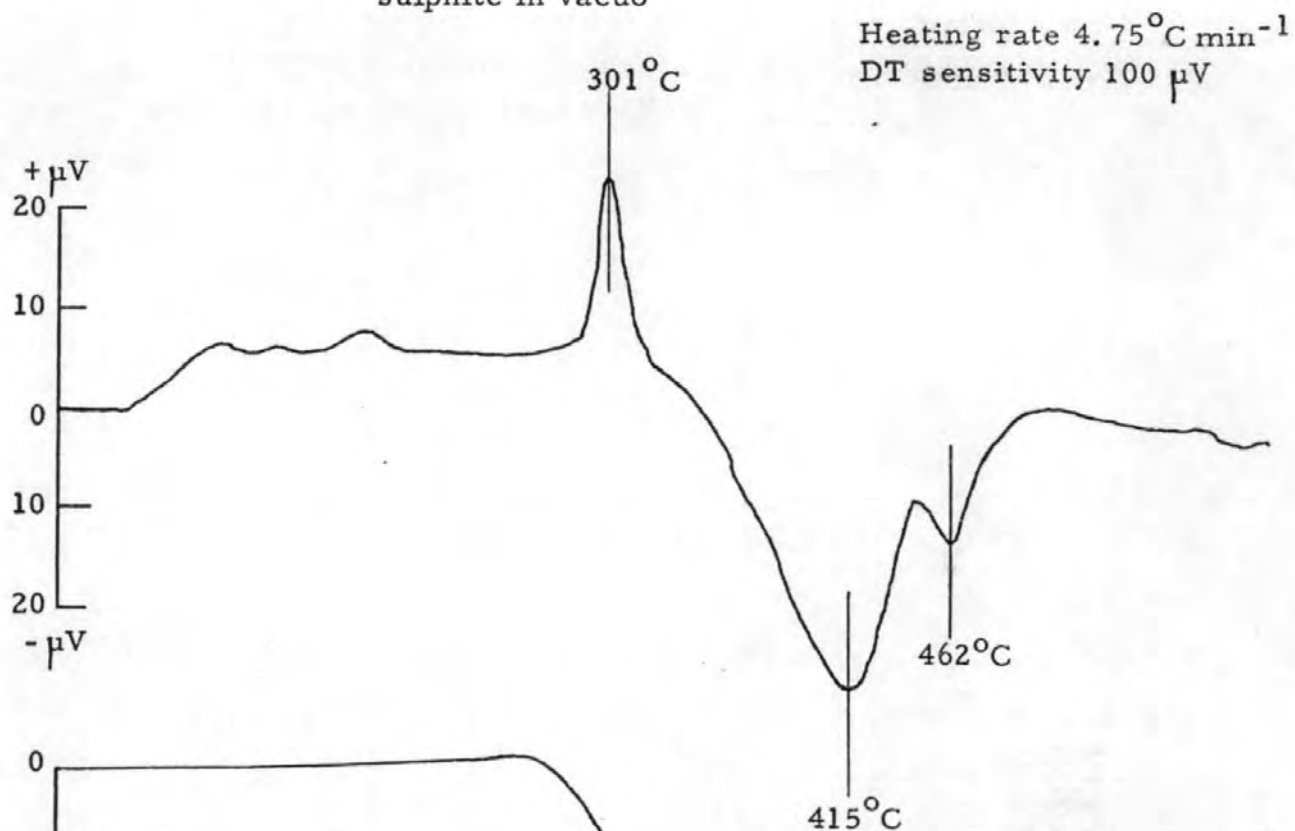
Figure 66b   Differential thermogram for the decomposition of lead
sulphite in nitrogen (500 ml/min⁻¹)

DT sensitivity 100 μV
Heating rate 4. 75°C min⁻

296°C

500°C

480°C

Figure 65b   TG curve for the
decomposition of
lead sulphite in
nitrogen

% weight
loss

Temperature °C
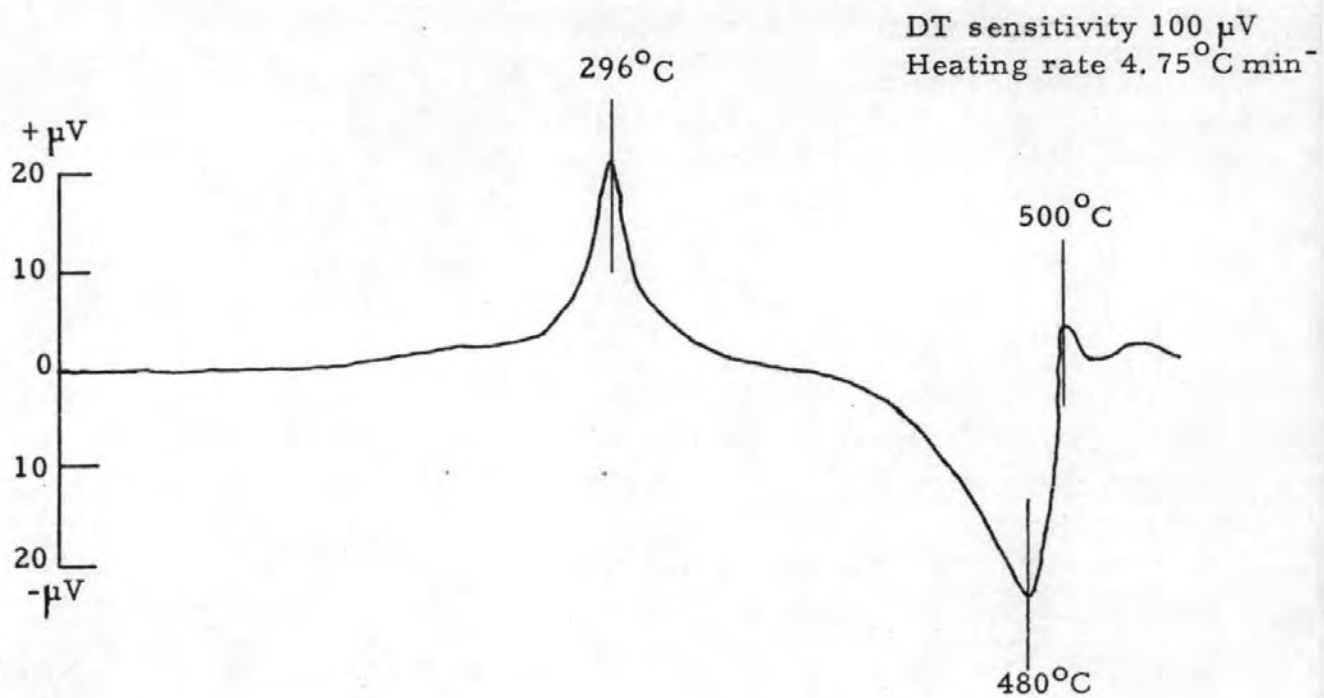
Figure 65c₁, c₂   Thermal decomposition of lead sulphite in nitrogen (500 ml min⁻1)

Figure 66d

Differential thermogram for the
oxidation of lead sulphite in air (500 ml min⁻¹)

Heating rate 4.75°C min⁻¹
DT sensitivity 100 µV
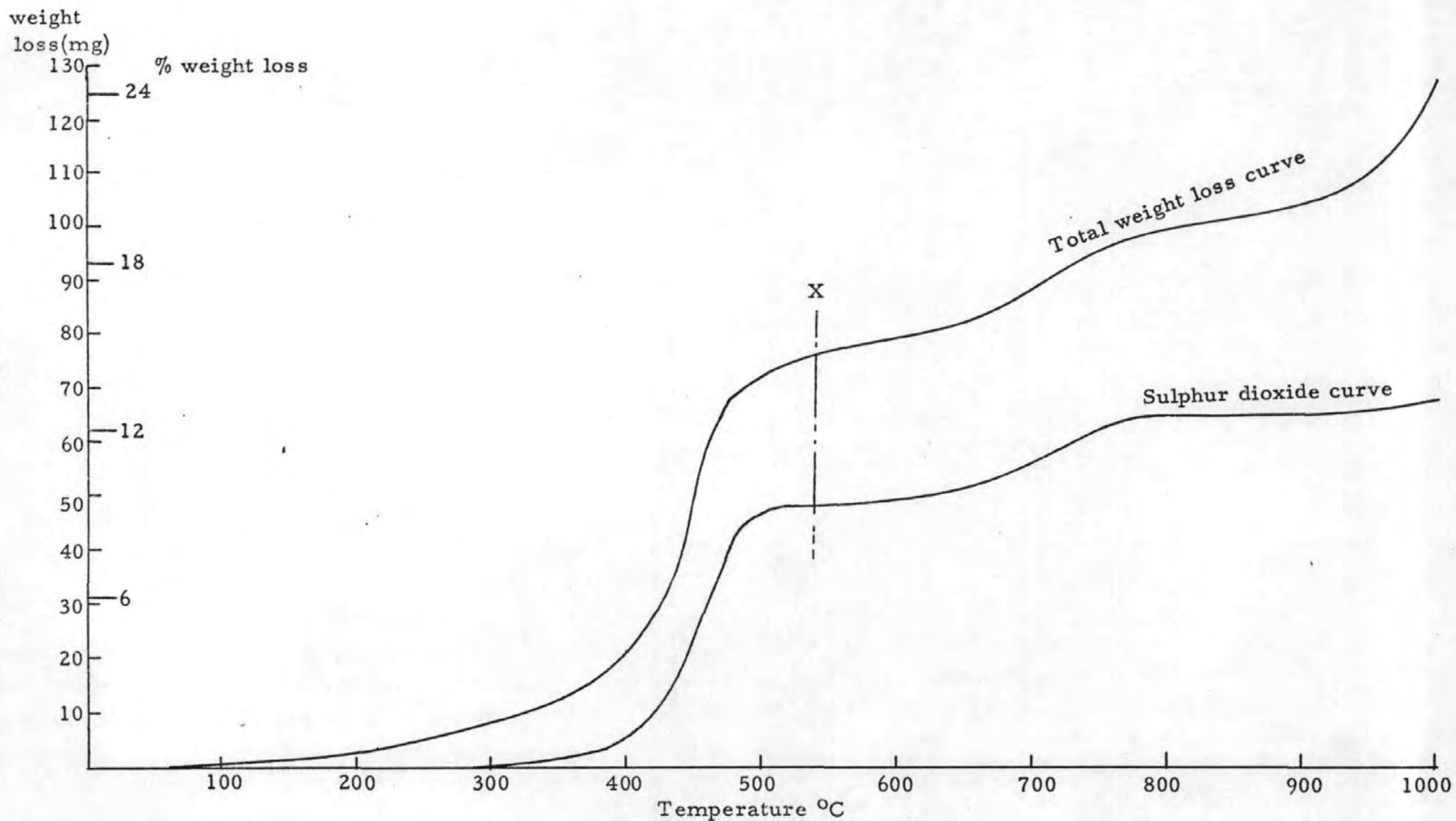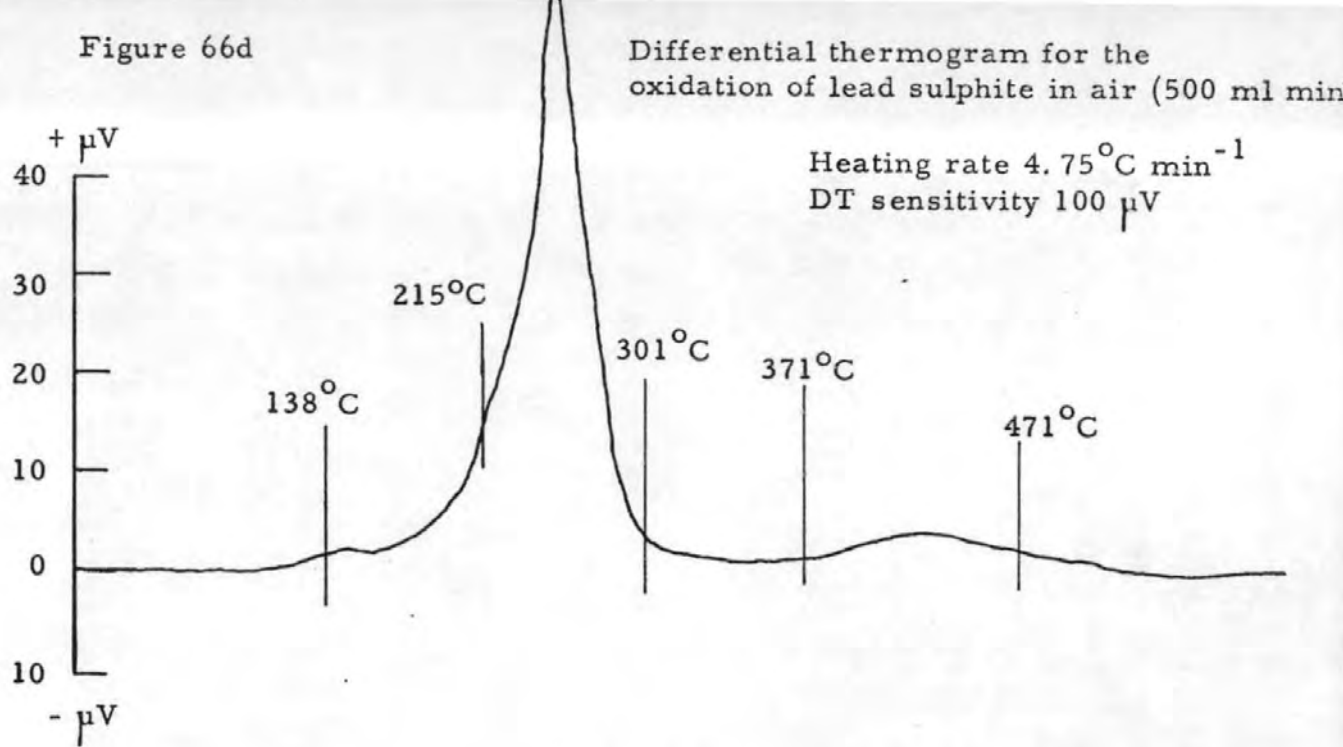
Figure 65d   TG curve for the oxidation of lead sulphite in air

Figure 66e

230°C

Differential thermogram for the
oxidation of lead sulphite in oxygen
(500 ml min⁻¹)

Heating rate 4.75°C min⁻¹
DT sensitivity 100 µV

+ µV

40

30

20

10

0

10

- µV

272°C

156°C

346°C

439°C

535°C
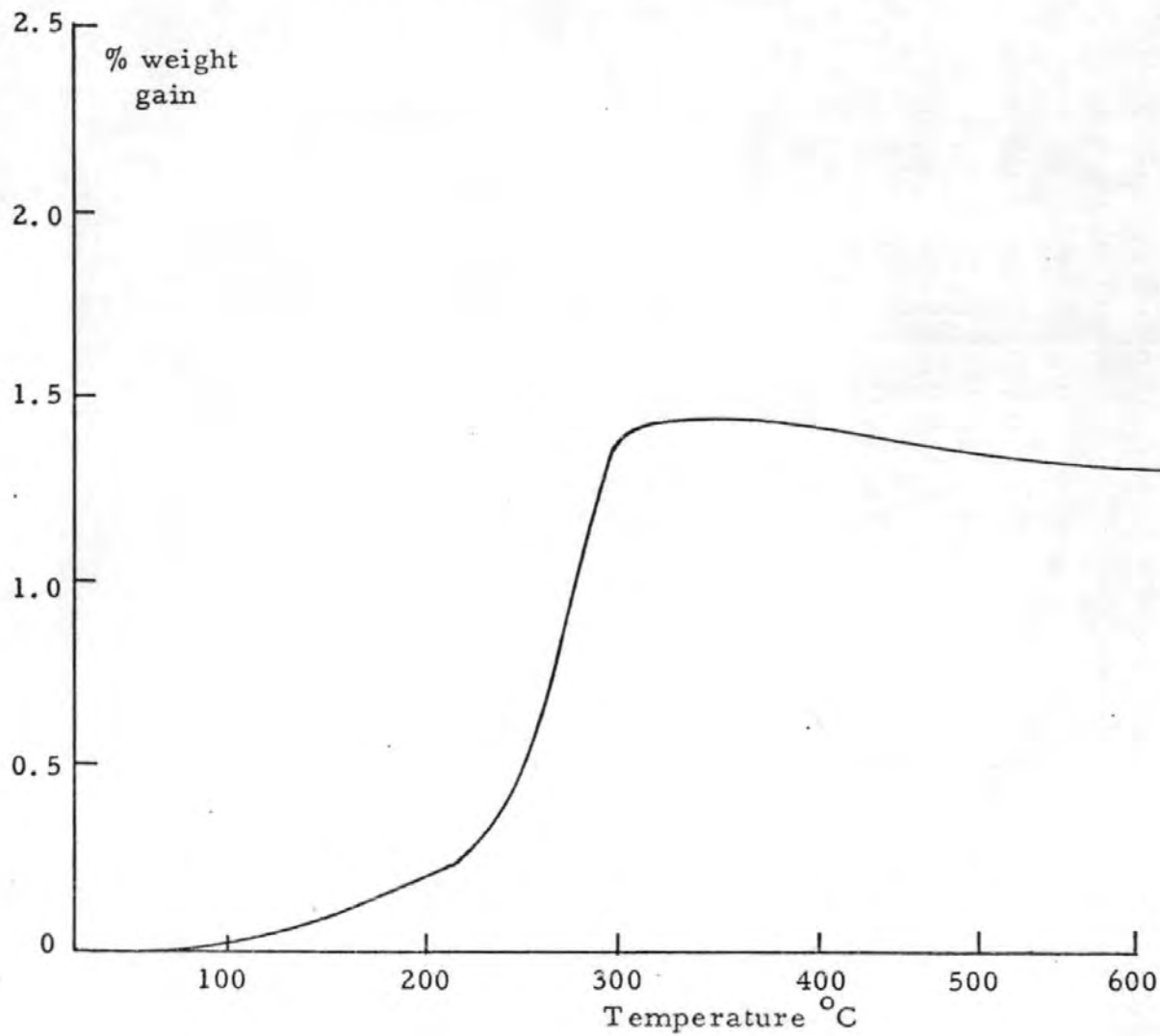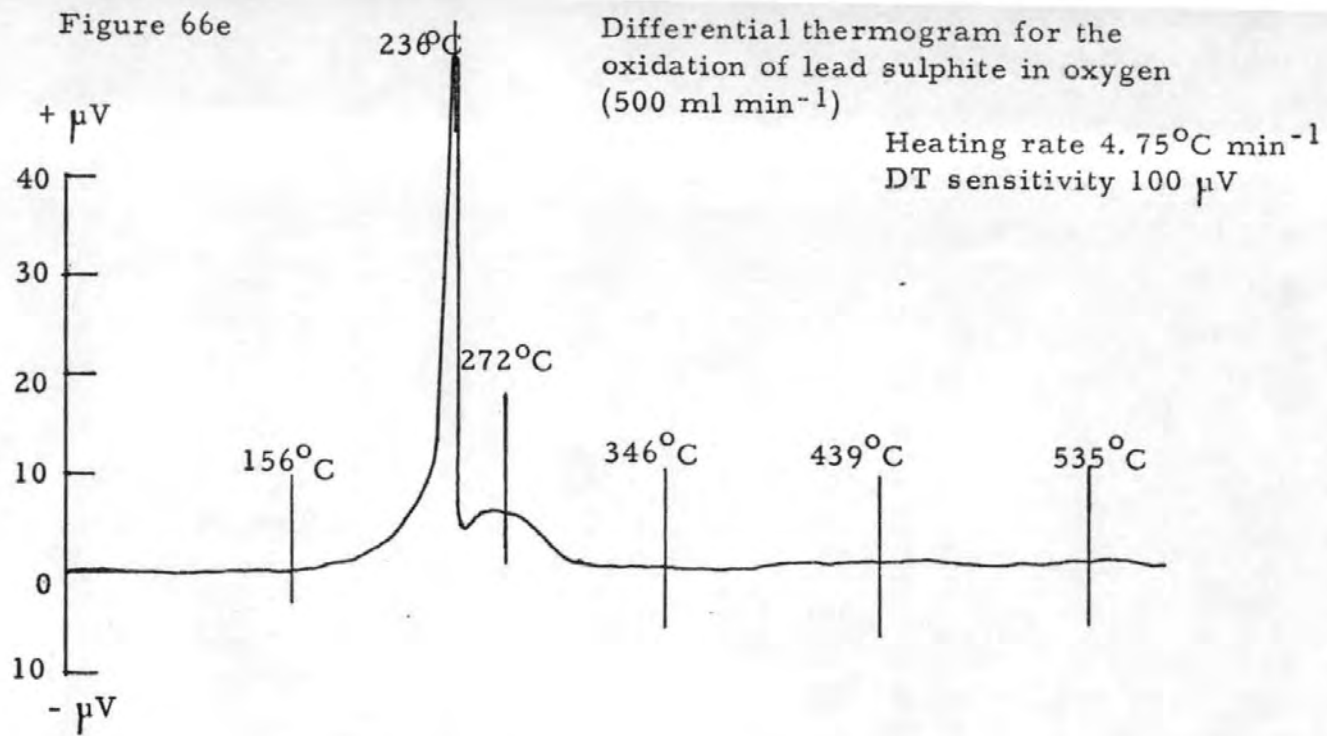
Figure 65e   TG curve for the oxidation of lead sulphite in oxygen

2.5

% weight
gain

2.0

1.5

1.0

0.5

0

100   200   300   400   500   600

Temperature °C
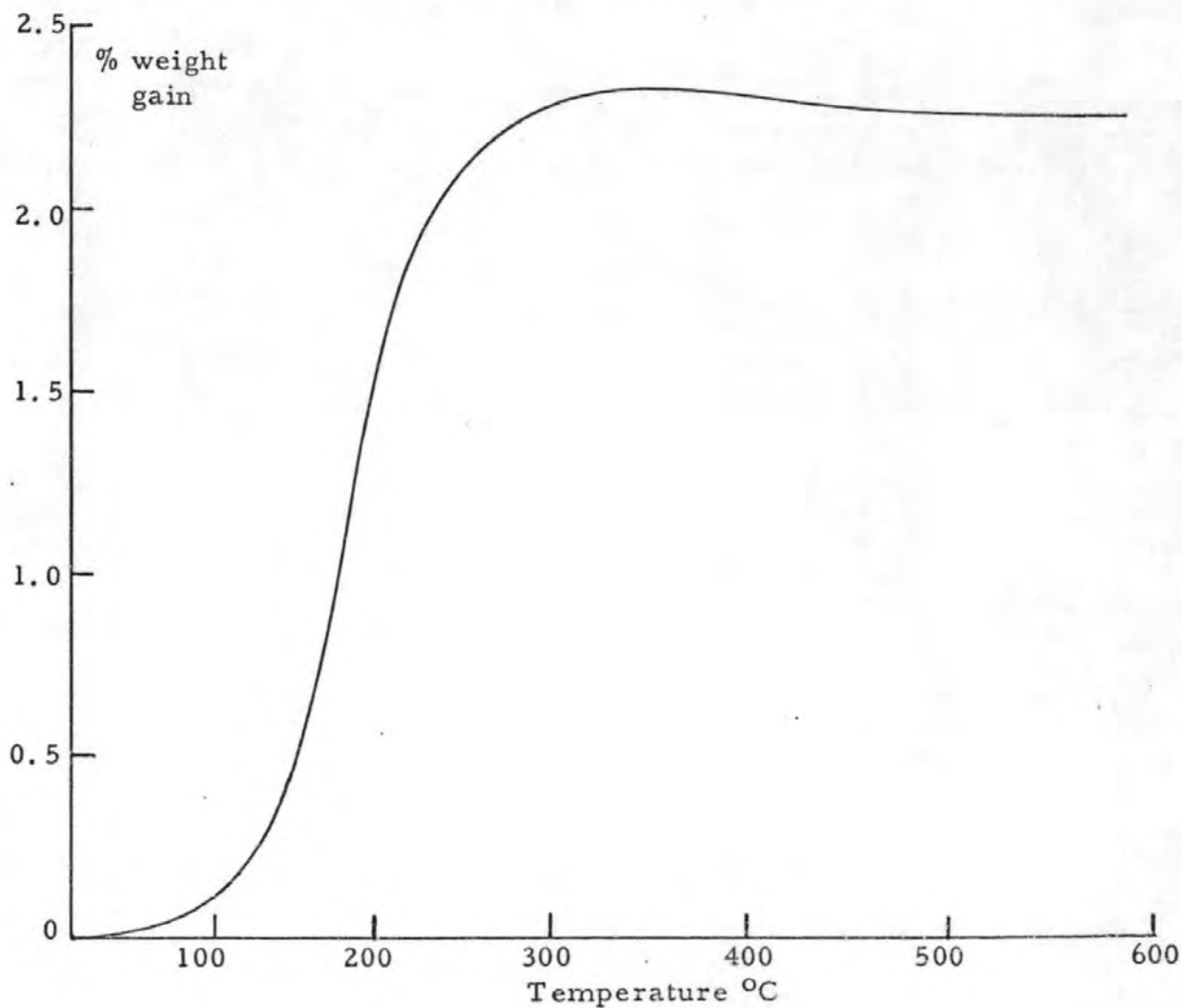
corresponding to the amount of sulphur dioxide evolved. Above $930^{\circ}C$ the sulphur dioxide is produced by the decomposition of lead sulphate.

When lead sulphite is heated in a stream (500 ml min^{-1}) of air or oxygen (Figures 65d, e), small weight gains are recorded corresponding to 15.3% decomposition and 84.7% oxidation in air, and 11.9% decomposition and 88.1% oxidation in oxygen. As expected, there is more oxidation in oxygen than air (20% oxygen).

The oxidation of the lead sulphite to lead sulphate occurs via direct oxidation at the lower temperatures and probably by a combination of direct oxidation and disproportionation followed by oxidation of the resulting lead sulphide at higher temperatures (ca $\sim350^{\circ}C$). The comparatively low oxidation temperature for lead sulphide makes it impossible to distinguish the relative importance of each mechanism of sulphite oxidation, but direct oxidation is the chief mechanism for zinc sulphite.

In the DTA traces for lead sulphite oxidation (Figures 66a, b, d, e), the peaks were much sharper in oxygen and occurring at a somewhat lower temperature than in air. These effects have been found previously in the oxidation of metal sulphides e.g. Zn, Fe, Pb and are probably applicable as well in direct sulphite oxidation.

In vacuo and nitrogen (Figures 66a, b), small exothermic peaks were followed by large endothermic peaks as the temperature was raised. Accompanying weight changes (on the TG curves) show that the endotherms correspond to decomposition and disproportionation reactions. The decomposition process is probably inhibited by the lead oxide produced, which is lower-melting and sinters more readily than the other components. This allows disproportionation to become more significant, accounting for the splitting of the endotherm into two peaks, especially in vacuo.

Microstructural changes during heating of lead sulphite in vacuo ($<10^{-5}$ mm Hg) have been followed by hot-stage electron microscopy (Figures 67a-h). There are only minor changes at low temperatures ($<260^{\circ}C$) during which the water is removed (c.f. Figures 67a, b). Small amounts of water soluble material, e.g. dissolved ionic salts such as sodium nitrate formed in the preparation of lead sulphite, have
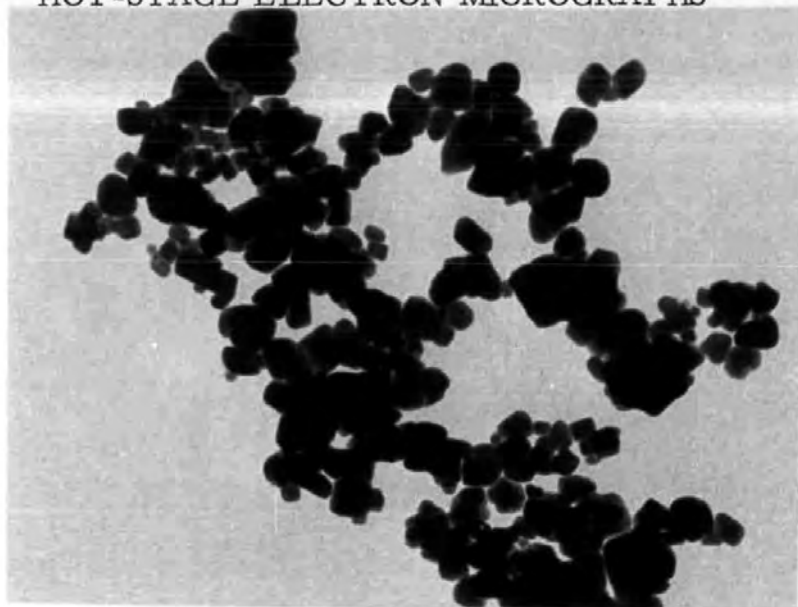
Figure 67a
Lead sulphite at 21°C
Mag: 65,000 X
Scale 0.5 µm
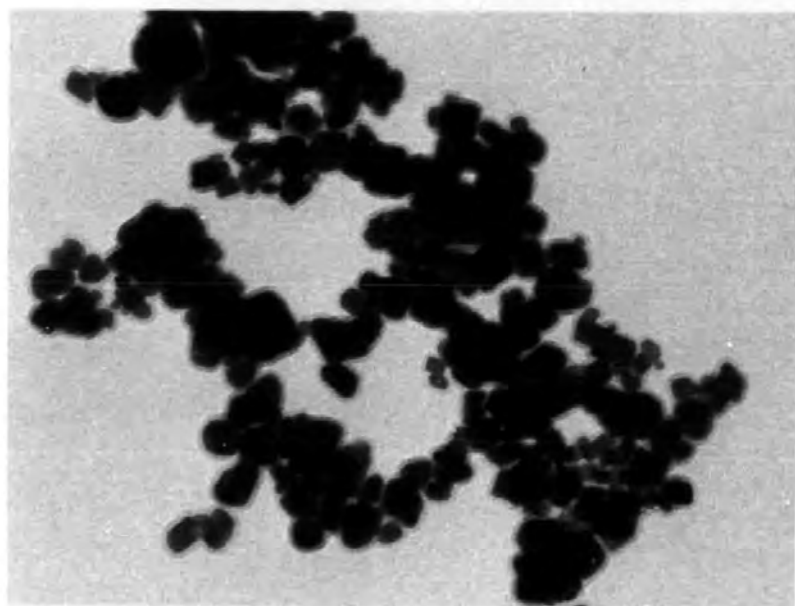
Figure 67b
Lead sulphite after
1 min at 160°C
Mag: 65,000 X
Scale 0.5 µm
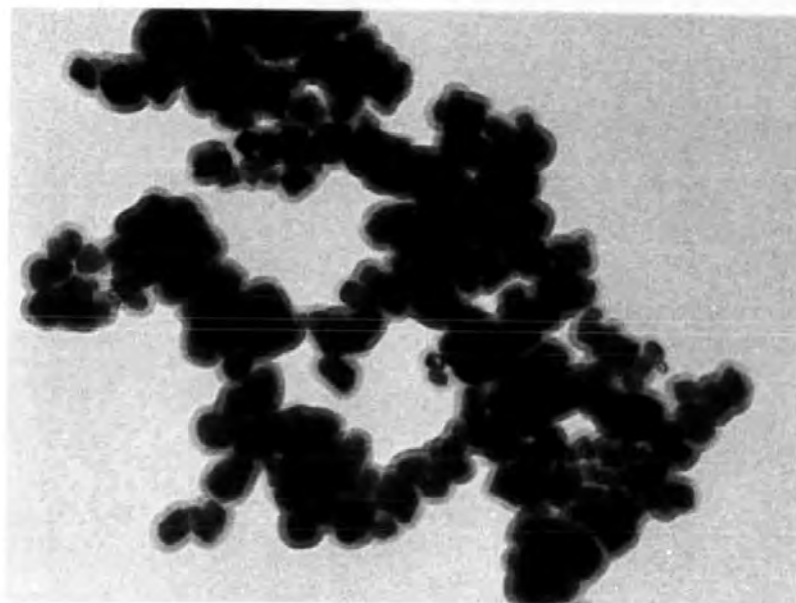
Figure 67c
Lead sulphite after
1 min at 263°C
Mag: 65,000 X
Scale 0.5 µm
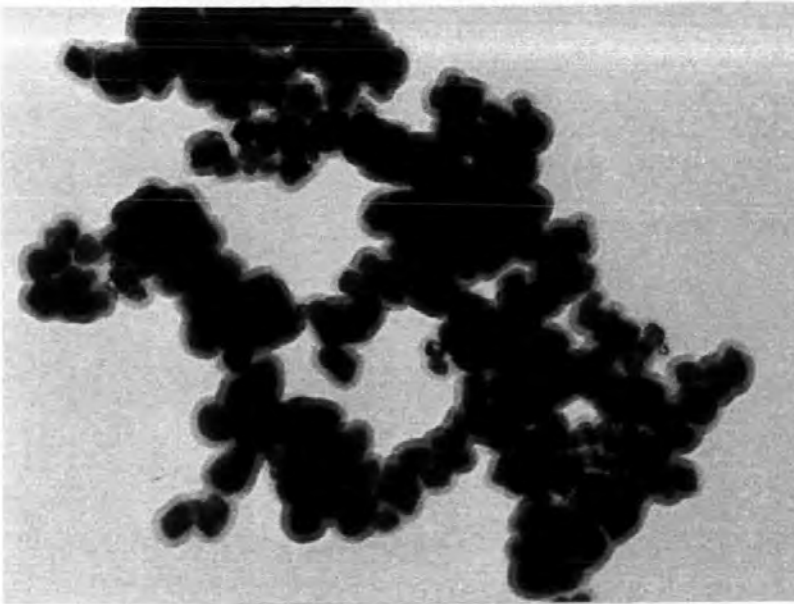
Figure 67d

Lead sulphite after 1 min at 277°C

Mag: 65,000 X

Scale 0.5 μm
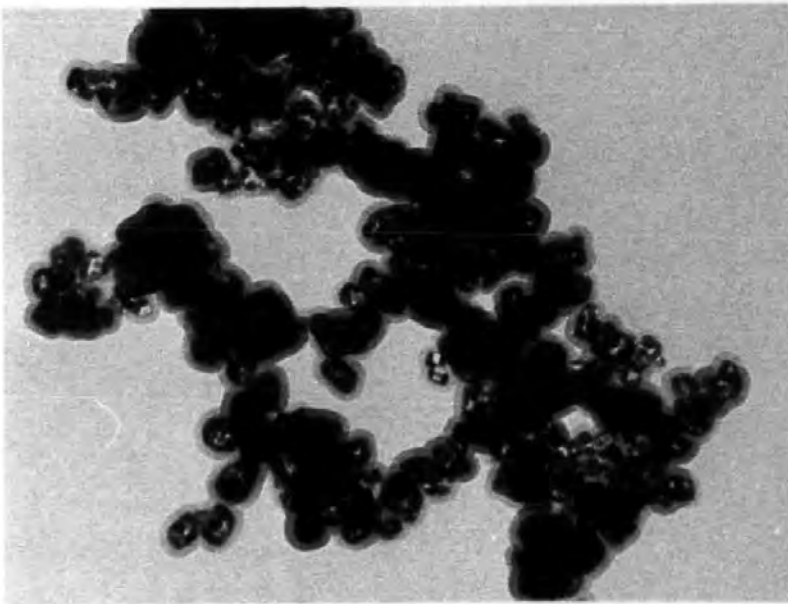
Figure 67e

Lead sulphite after 4 min at 330°C

Mag: 65,000 X

Scale 0.5 μm
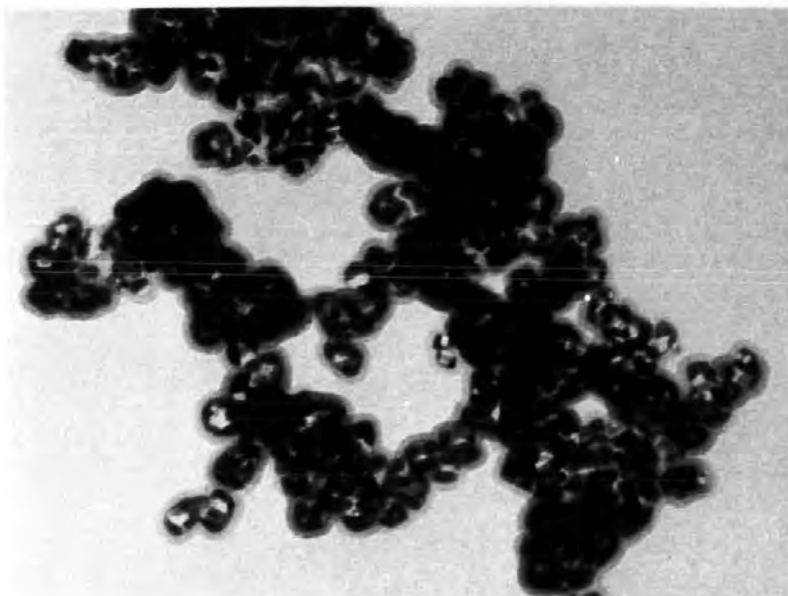
Figure 67f

Lead sulphite after 2 min at 355°C

Mag: 65,000 X

Scale 0.5 μm
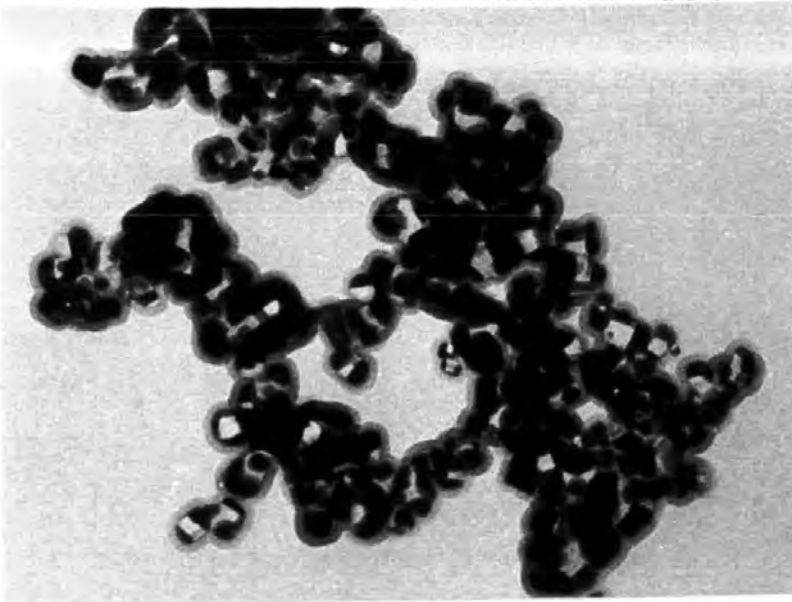
Figure 67g

Lead sulphite after
1 min at 438°C

Mag: 65,000 X

Scale 0.5 µm
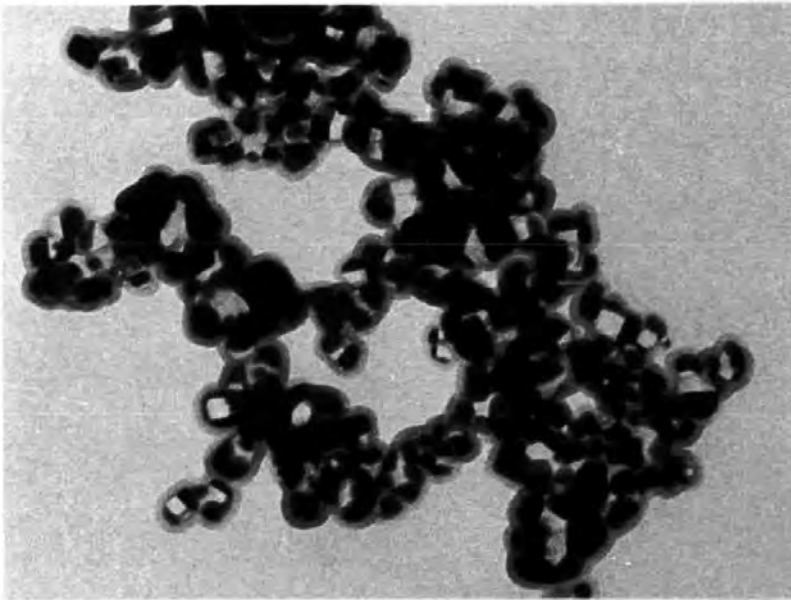
Figure 67h

Lead sulphite after
1 min at 511°C

Mag: 65,000 X
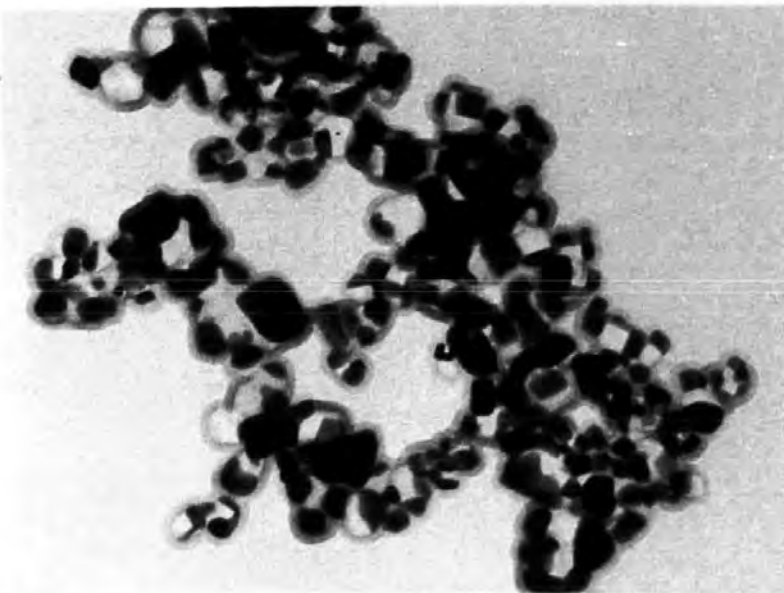
Scale 0.5 µm

Figure 67i

Lead sulphite after
40 min at 511°C

Mag: 65,000 X

Scale 0.5 µm

evidently migrated to the outside of the aggregates, and diffused into the carbon film giving haloes. The first signs of thermal decomposition are seen at $\sim 260^{\circ}$C (Figure 67d) and become more extensive at 330° and 354°C (near first peak of endotherm of the DTA trace) and at 438°C (near completion of the endotherm). At the last-named temperature the crystallite size has increased in accordance with the expectation that sintering will become extensive at temperatures above 400°C; further increases are shown at higher temperatures, viz., 511°C (Figure 67i).

The electron microscopy hot-stage studies were performed a number of times, and it was found that the dehydration and decomposition temperatures varied over a range of $\sim 30^{\circ}$C. This is accounted for by the heating effect of the electron beam on the sample, i.e. the sample was hotter than the thermocouple controlling the grid temperature indicated. To reduce this effect the beam current was kept as low as possible and studies were carried out on particles close to a grid mesh. The micrographs and associated temperatures shown are those which gave the highest temperature for the dehydration and decomposition.

## 5.4   THERMAL DECOMPOSITION OF ZINC SULPHITE

The thermogravimetric curves are shown in Figures 68a-d for samples of commercial zinc sulphite heated in (a) vacuo, (b) nitrogen, (c) air and (d) oxygen.

In vacuo (Figure 68a), the water of crystallization ($+ 2H_2O$) is lost at temperatures up to $200^{\circ}C$ and sulphur dioxide at temperatures up to $400^{\circ}C$, after which the weight of the residue remains constant (up to $600^{\circ}C$). The loss of sulphur dioxide corresponds to 86.1% of the zinc sulphite being decomposed to zinc oxide. Since no zinc sulphite remains in the residue, the remaining 13.9% has evidently disproportionated, viz., $4ZnSO_3 \longrightarrow 3ZnSO_4 + ZnS$.

There is more decomposition (94.9%) and less disproportionation (5.1%) when zinc sulphite is heated in a stream of nitrogen ($1 \ 1min^{-1}$) at similar temperatures (Figure 68b).

Dehydration of salt hydrates in vacuo compared with nitrogen or air generally produces much smaller crystallites of anhydrous product. This is typical of decompositions of the type:-

Solid A $\longrightarrow$ Solid B + gas.
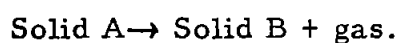
c.f. also metal hydroxides and carbonates and is thought to be connected with the larger concentration gradients of gas or vapour in the capillaries of the solids in vacuum decompositions.[78] Thus, the smaller crystallites of zinc sulphite evidently tend to disproportionate more.

When zinc sulphite is heated in streams of air or oxygen (Figures 68c, d), there is apparently 85.0% and 78.2% decomposition with 15.0% and 21.8% disproportionation respectively. In these experiments, the anydrous zinc sulphite crystallites are probably similar in size to those formed in nitrogen, yet the apparent disproportionation is greater even than that in vacuo. However, in the presence of air or oxygen any disproportionated material would be oxidized at temperatures above $500^{\circ}C$, but there are no weight gains on subsequent heating at the higher temperature when the weight remains constant.

Hence, the smaller weight losses are accountable in terms of zinc oxide and zinc sulphate as the only products. Therefore in air and in oxygen 88.5% and 83.4% of the zinc sulphite decomposes and 11.5% and 16.6% oxidizes to zinc sulphate respectively, the higher amount of

Figure 69a   Differential thermogram for the decomposition of zinc
sulphite in vacuo
Heating rate 4.75°C min⁻¹
DT sensitivity 50 μV
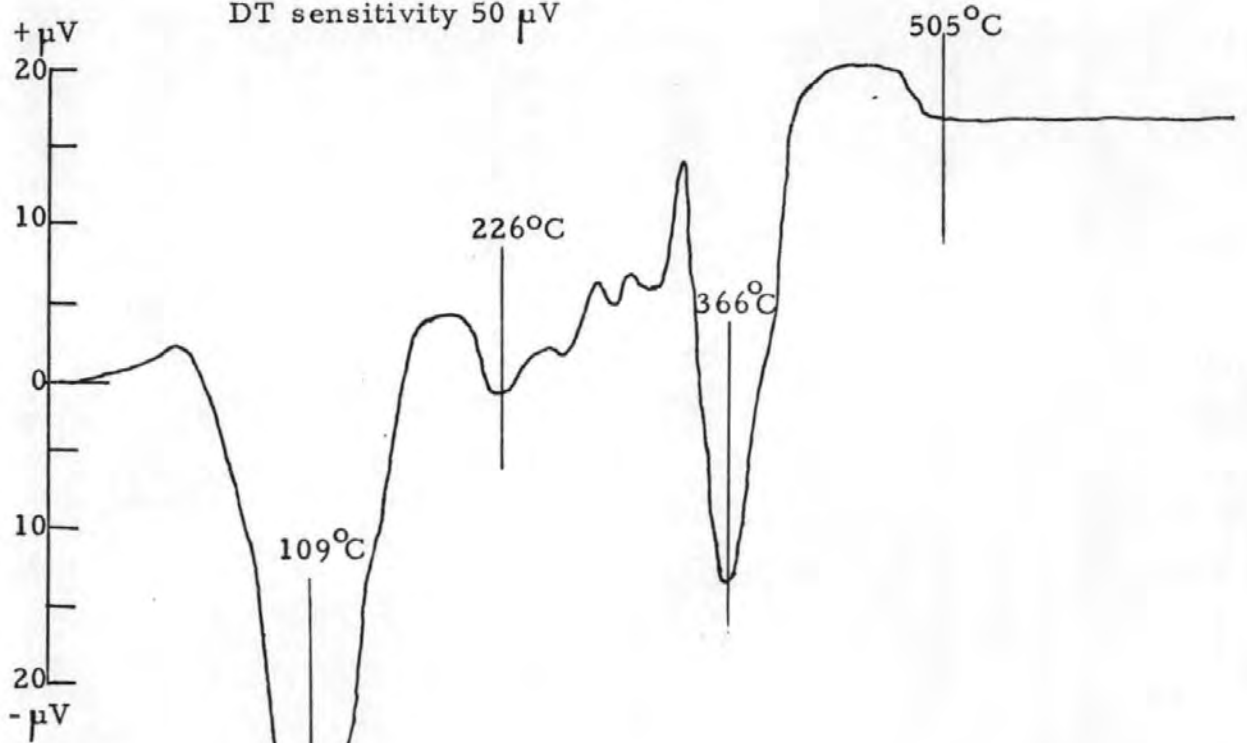
Figure 68a   TG curve for the decomposition
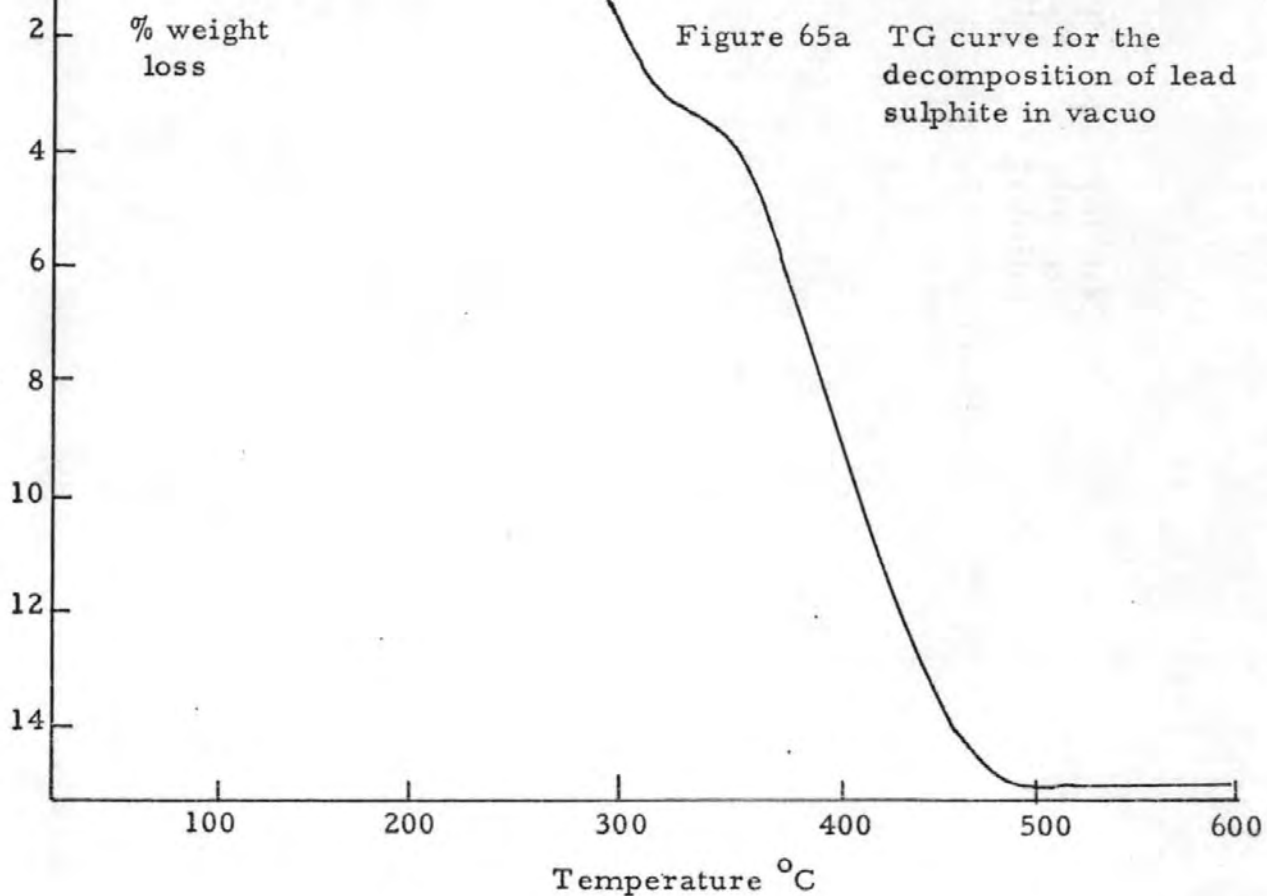of zinc sulphite in vacuo
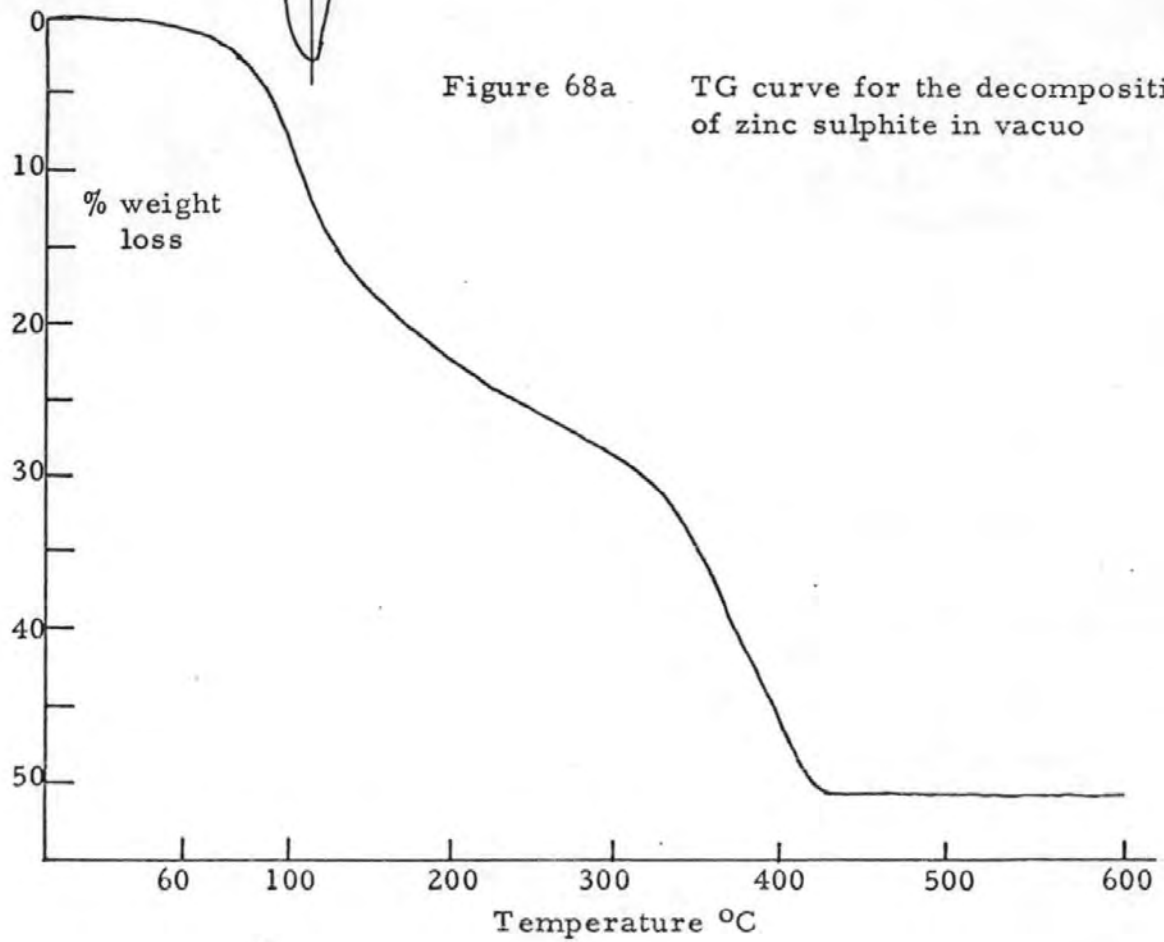
Figure 69b   Differential thermogram for the decomposition of zinc sulphite in nitrogen (500 ml min^{-1})
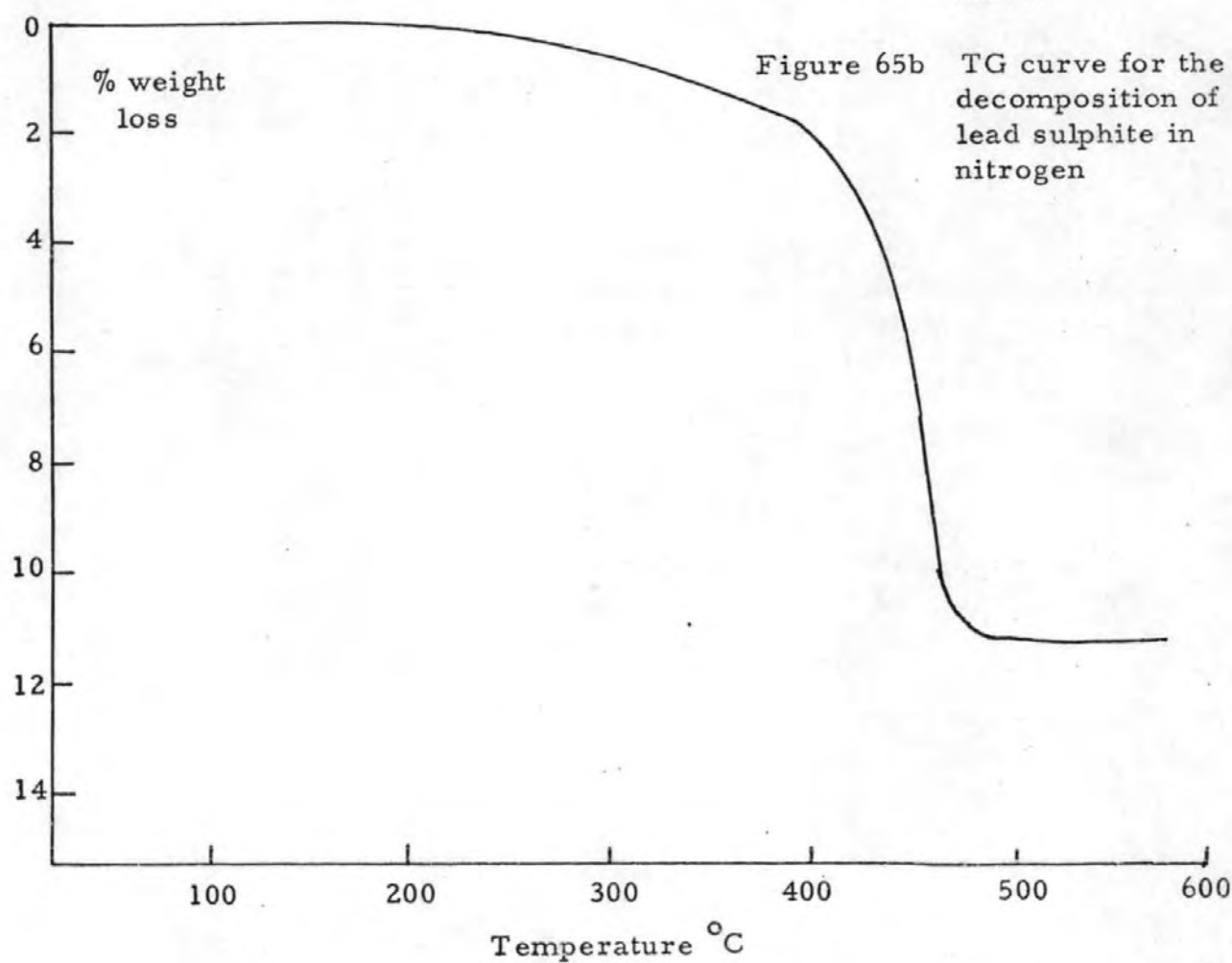
Heating rate 4.75^{o}C min^{-1}
DT sensitivity 50 μV
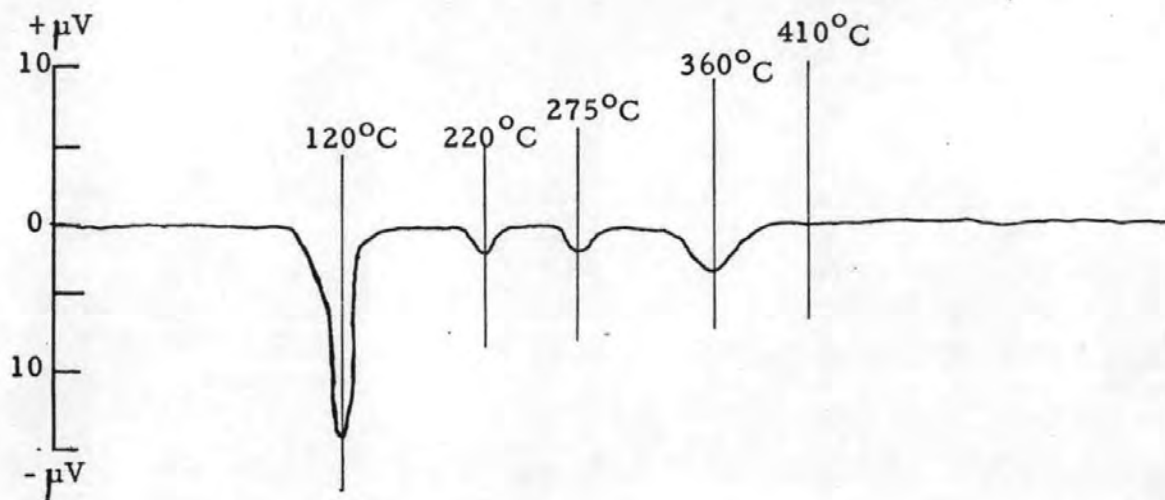
Figure 68b   TG curve for the decomposition of zinc sulphite in nitrogen
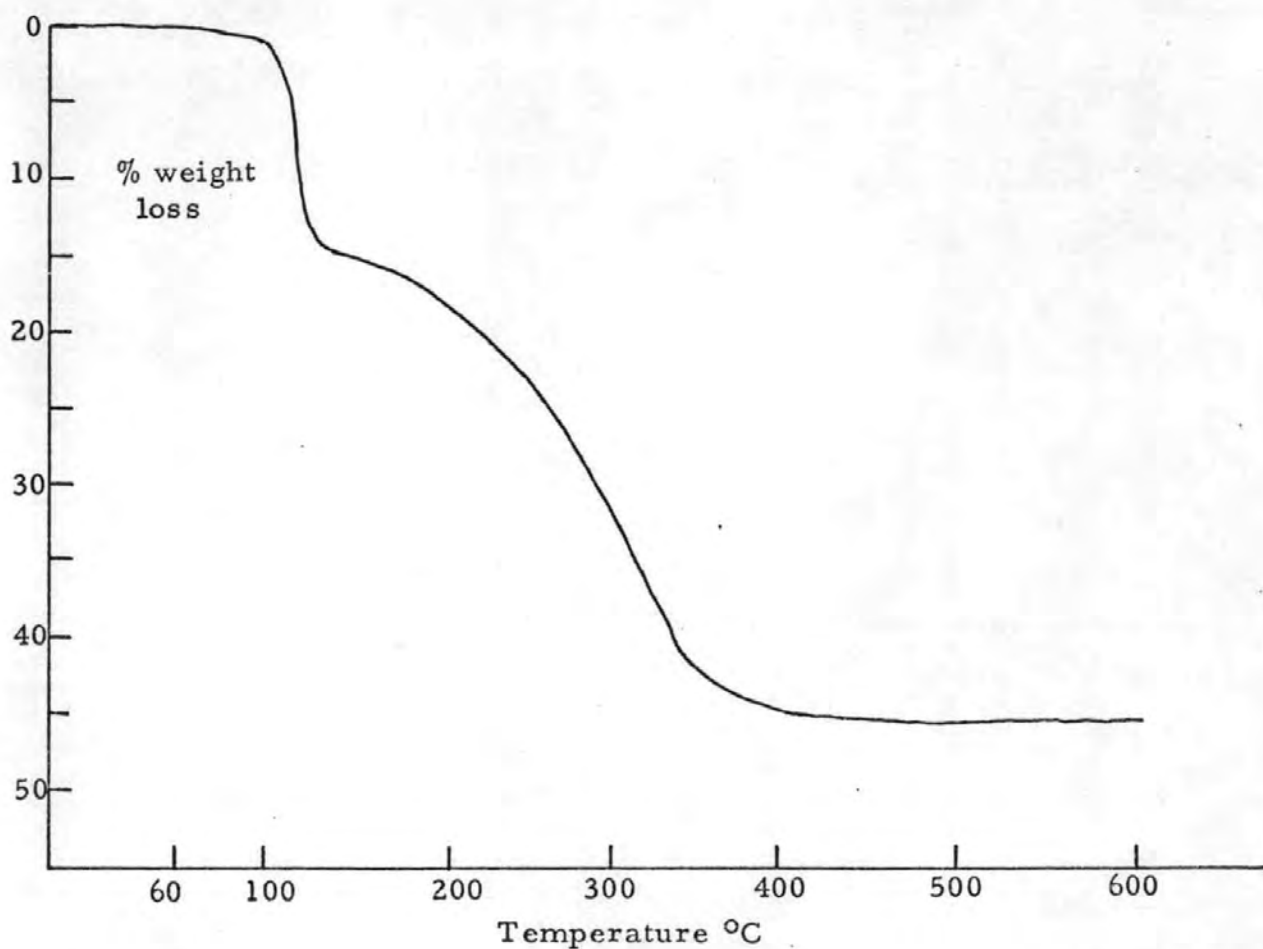
Figure 69c   Differential thermogram for the decomposition of zinc
sulphite in air (500 ml min^{-1})
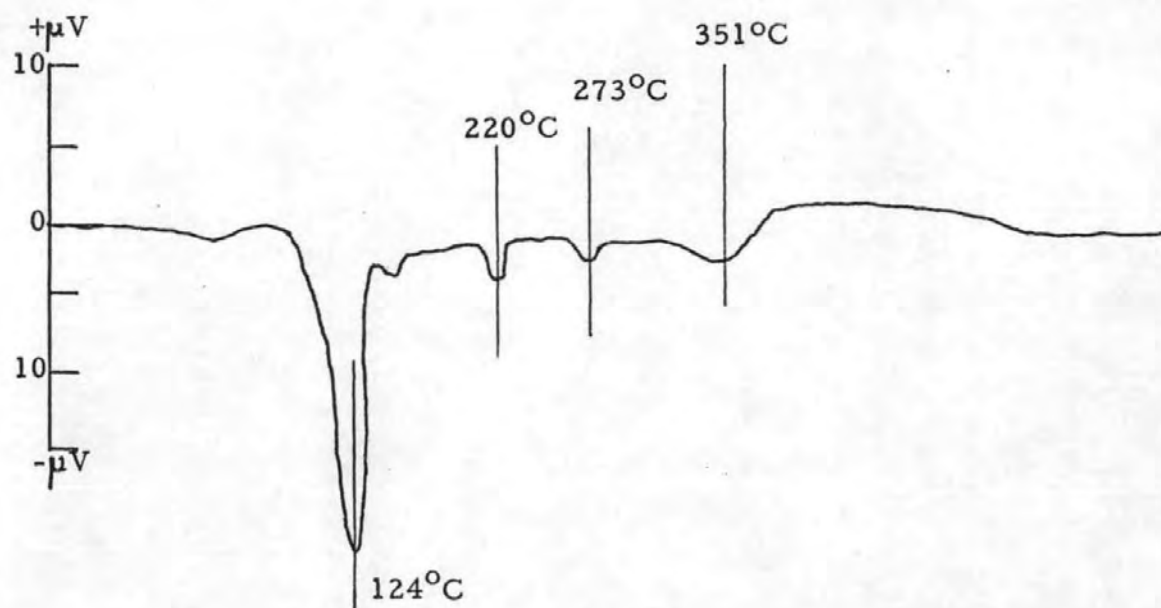
Figure 68c   TG curve for the decomposition of zinc sulphite in air
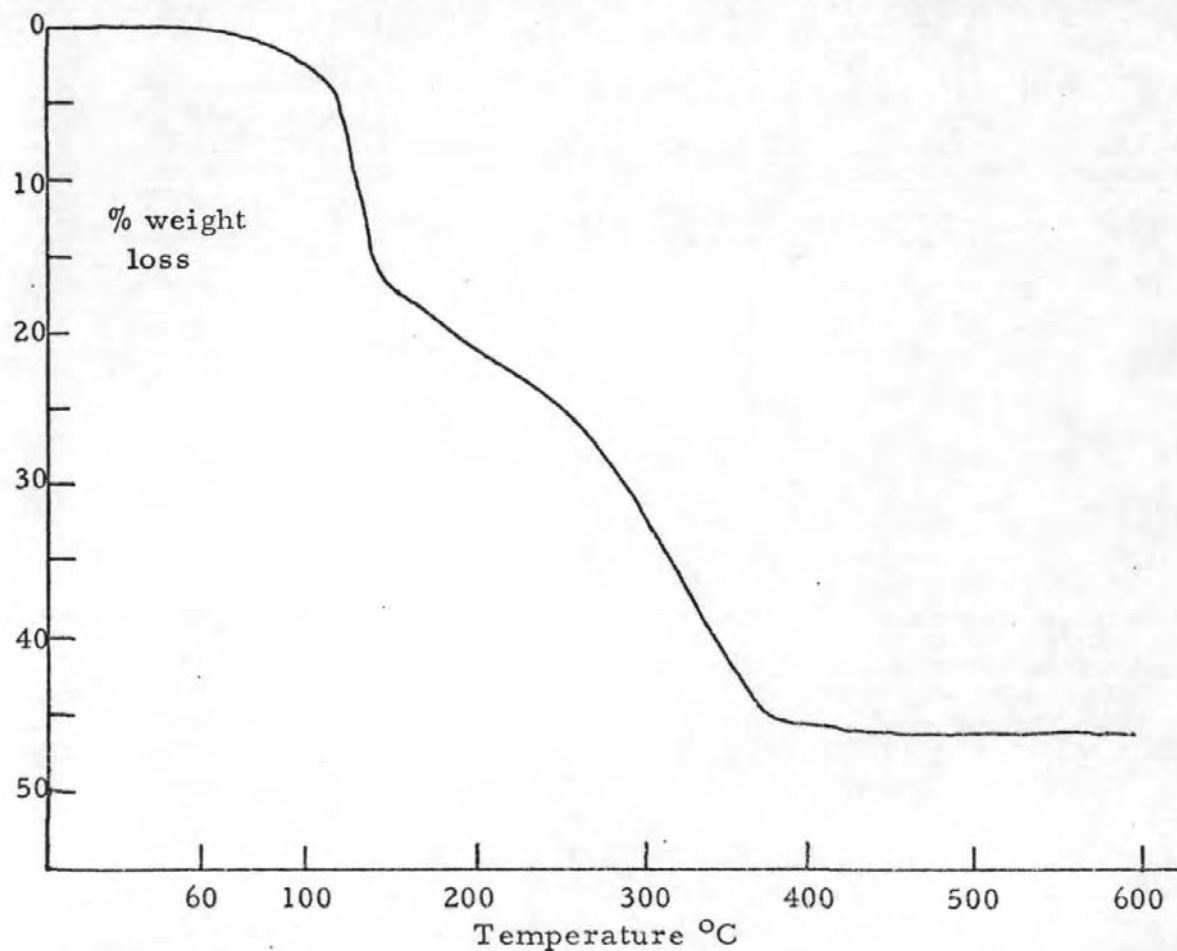
Figure 69d   Differential thermogram for the decomposition of zinc
sulphite in oxygen (500 ml min^{-1})

Heating rate 4.75°C min^{-1}
DT sensitivity 50 μV
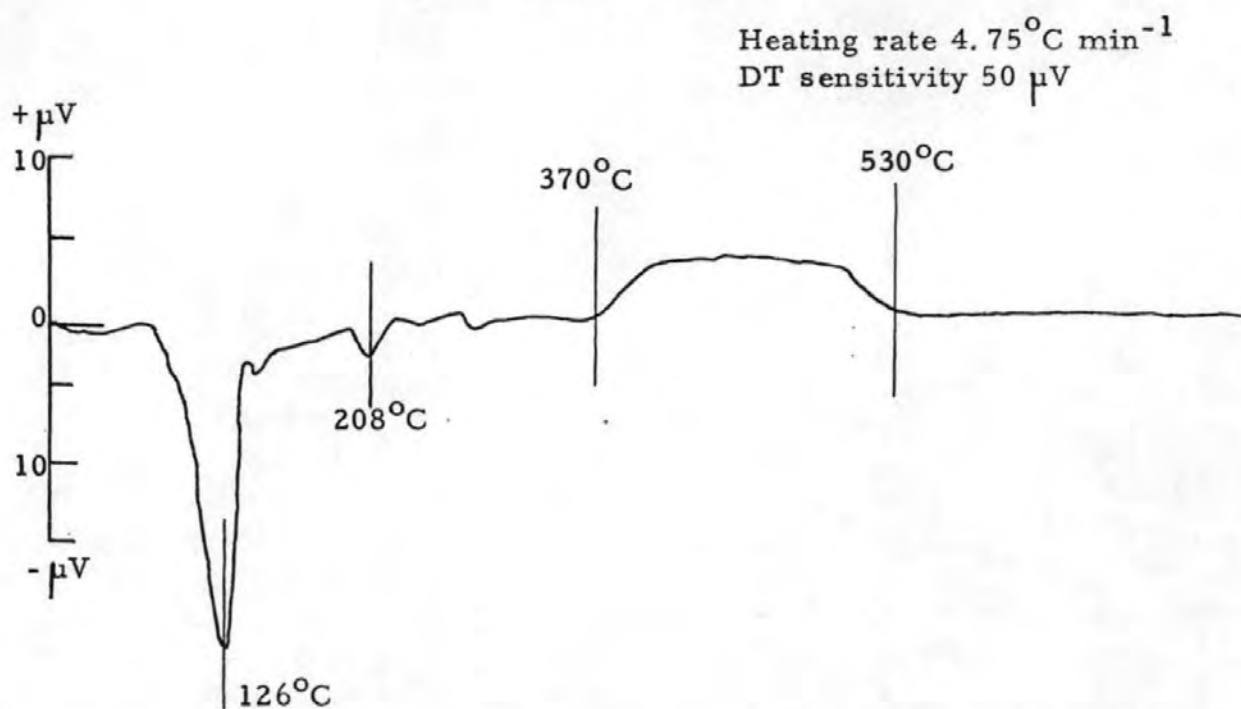
Figure 68d   TG curve for the decomposition of zinc sulphite in oxygen

Temperature $^{\circ}$C
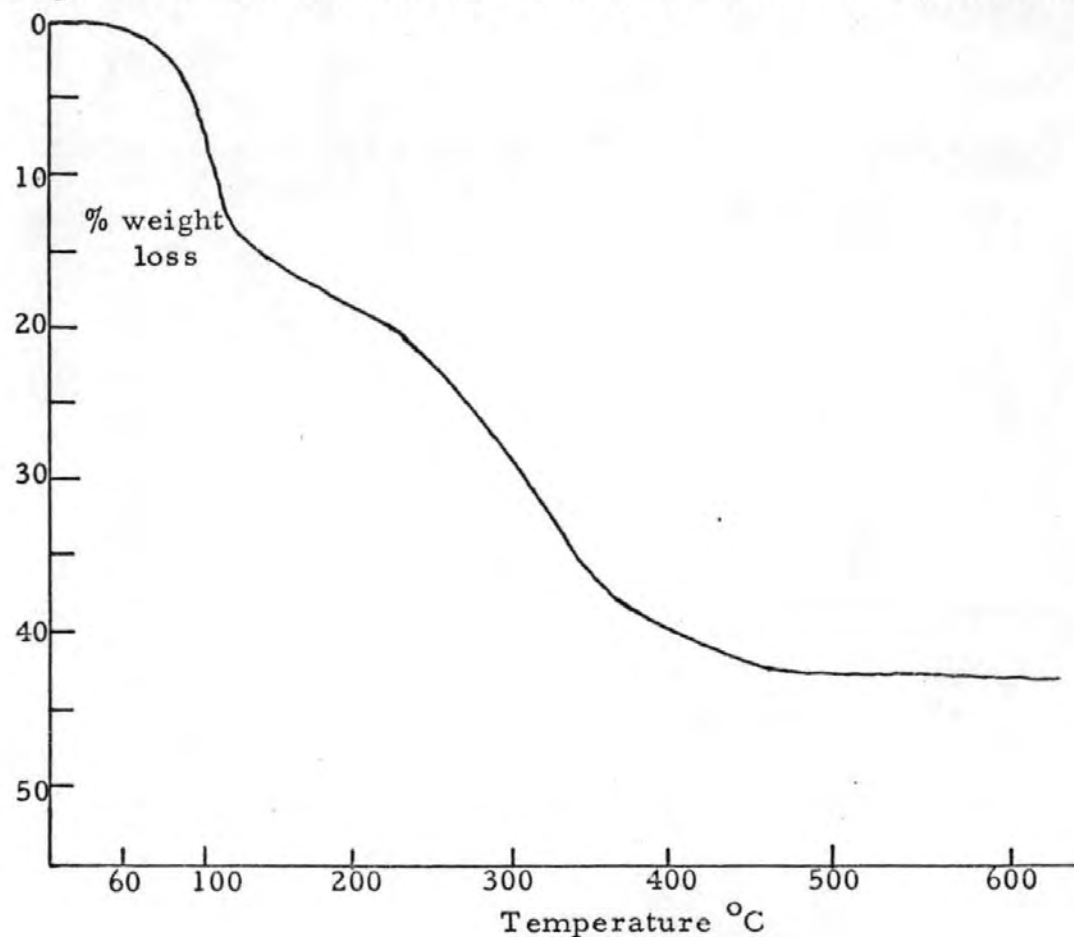
oxygen present producing the greater percentage of oxidation.

In the DTA traces for zinc sulphite (Figures 69a-d), the loss of water of crystallization gives an endothermic peak at 109°C in vacuo and about 125°C in nitrogen, air and oxygen. The decomposition of the anhydrous zinc sulphite at higher temperatures in vacuo and nitrogen gives a series of smaller endothermic peaks. In air and oxygen, these smaller endothermic peaks are followed by a long shallow exotherm corresponding to oxidation of the zinc sulphite to sulphate over temperature ranges of about 370 to 530°C and 360 to 490°C respectively.

The differential thermal trace in vacuo, in both cases, although carried out with the same sensitivity and sample mass as those in nitrogen etc. appears as a magnified version because of the absence of any heat being conducted or converted away by an atmosphere.

5.5 SULPHITE FORMATION DURING OXIDATION OF METAL SULPHIDES

The present researches and those of others[105,106] in the laboratories indicate that the stability of divalent metal sulphites to oxidation to sulphate is in the order:-

$$BaSO_3 > SrSO_3 > CaSO_3 > ZnSO_3 > PbSO_3$$

The sulphides of the alkaline earth metals are less stable to oxidation to sulphates and thus form appreciable amounts of intermediate sulphites during the complete conversions to sulphate. In contrast, the zinc and lead sulphides are more stable to oxidation compared with their sulphites and hence no appreciable amounts are present during the overall oxidations to sulphates, basic sulphates and oxides.

The possible disproportionation of lead sulphite to sulphate and sulphide could be initiated crystallographically by the re-arrangement of the lead sulphite lattice, so that the 001 plane (c - axis of the orthorhombic cell, $5.15\overset{o}{A}$) becomes the 111 plane of the lead sulphide (diagonal of the cubic - F - cell = $10.3\overset{o}{A}$). This is analogous to the aragonite - calcite crystal transformation on heating or milling, where the orthorhombic lattice becomes a deformed cubic (rhombohedral) lattice, by similar axial changes[107,108,109].

The changes from lead sulphite to sulphide and aragonite to calcite involve only small changes in density, viz., 7.87 to 7.60 (4%) and 2.93 to 2.71 (7%) respectively. This would be the case also for the initial oxidation of lead sulphide to lead sulphite and in the reverse transformation of calcite to aragonite; reversibility in the latter has been demonstrated by milling until an equilibrium mixture is obtained[110].

Further direct oxidation of lead sulphite to lead sulphate would involve increases in the size of the orthorhombic lattices, viz;

$\underline{a}$ = 6.26 to 6.96 $\overset{o}{A}$ (11.2%)

$\underline{b}$ = 7.51 to 8.48 $\overset{o}{A}$ (12.9%)

$\underline{c}$ = 5.15 to 5.39 $\overset{o}{A}$ (4.7%)

with decrease in density from 7.87 to 6.32 g cm^{-3} (19.7%).

On the other hand decomposition of lead sulphite to orthorhombic lead oxide (massicot) would involve decreases in the size of the lattices,

viz;

$$\underline{a} \quad = \quad 6.26 \text{ to } 5.49 \text{ Å} \quad (12.3\%)$$

$$\underline{b} \quad = \quad 7.51 \text{ to } 5.89 \text{ Å} \quad (23.7\%)$$

$$\underline{c} \quad = \quad 5.15 \text{ to } 4.76 \text{ Å} \quad (7.6\%)$$

with increase in density from 7.87 to 9.64 g cm^{-3} (22.6%).

Thermal transformation of aragonite to calcite, disproportionation of calcium sulphite and its oxidation at higher temperatures are all accompanied by sintering which is found also with the oxidation of lead sulphide.

CHAPTER 6

INVESTIGATION INTO THE EFFECTS OF PELLETIZATION, BENTONITE AND MOISTURE ON A POOR SINTERING MIX.

6.1 INTRODUCTION

At the 1975 ISP Conference[111] a licensee claimed that the addition of bentonite improved the permeability of sinter mixes, and thus also the sinter strength. This investigation was planned to test the effect of adding 1% bentonite on a poor sinter mix, under varying preparative conditions. It was decided to choose a poor sintering mix initially, so that any improvements in sinter strength would become obvious. The mix was formulated to give a target analysis of 43-44% zinc, with 15% of the new zinc supplied in the form of Waelz oxide; with lead at 20%, iron 7.5%, lime 5%, silica 3.5% and 5% sulphur as fuel.

The investigation was planned as a duplicated factorial experiment with 3 factors at 2 levels; the 2 levels of water addition gave either a normal moisture content or a high moisture level, when 100 cm^3 above the normal amount was added. After mixing, the mix was either burnt in its original form, or pelletized. This gave 2^3 = 8 experiments, with duplication a total of 16.

Table 6.1a   Summary of plan

		Normal moisture	High moisture
Ordinary mixing	No bentonite	1, 2	3, 4
	1% bentonite	5, 6	7, 8
Pelletized	No bentonite	9, 10	11, 12
	1% bentonite	13, 14	15, 16

6.2 EXPERIMENTAL

The mix constituents were restricted to the minimum number necessary to achieve a sinter composition as outlined in Section 6.1. Fresh sinter was obtained from the sinter plant on site, and the analysis of this sinter used in calculation of the sinter mixes. Moisture tests were applied to all constituents, and this value used in the final calculation of composition. Additions of silica were in the form of sand and lime in the form of limestone. The fresh sinter was crushed to $< \frac{1}{4}"$ (< 6.4 mm).

The fuel level chosen for the work was 5% new sulphur in the mix. This has been shown to be close to optimum by previous experiments[69], and is near to the level used by many operating plants.

6.2.1 Calculation of Sinter Mix

An algebraic method (see Appendix III) was used to achieve the desired composition of the sinter mix, from the basic components. Table 6.2a gives the complete analysis of the constituents. Table 6.2b gives the "effective analyses" in which a correction has been made for the loss of volatile components on combustion. It was these "effective analyses" values which were used to calculate the composition from the components. The mixes actually used to make the returns of the desired compositions are shown in Table 6.2c.

6.2.2 Procedure

The 16 mixes for each set of experiments were made up at the same time and stored with the sinter on the top, so as to keep the initial moisture content constant. After the addition of water to the first mix to give the correct moisture content, the water addition was held at this level, or at 100 cm^3 above, throughout the experiments.

The raw materials were mixed in an Eirich SKG II mixer for 4 min with the water being added after 1 min. When required, the mix was pelletized in a disc pelletizer set at an angle of 55° and rotated at 20 rpm for 2.5 min.

The grate bars of the sinter pallet were first cleaned, the inner and outer formers placed in position and the space between them packed with dampened soft sinter fines, crushed to $< \frac{1}{16}"$ (1.6 mm). The ignition layer was then applied (1 kg of the sinter mix).

Table 6.2a **Actual Analysis of Constituents**

Material	Zn	Pb	Fe	S	MgO	Al$_2$O$_3$	SiO$_2$	CaO	Moisture
B.H. Zinc	52.7	1.00	10.00	32.2	0.03	0.4	1.4	0.24	7.6
B.H. Lead	3.5	75.5	2.5	15.5	0.02	0.19	1.0	0.13	5.6
Blue powder	26.1	22.0	4.5	-	-	0.5	-	4.5	3.0
Waelz oxide	42.0	8.0	5.7	3.5	3.4	2.2	7.6	8.0	1.0
Limestone	-	-	0.5	-	1.5	-	4.9	49.4	5.0
Sand	-	-	1.5	-	-	1.5	80.2	6.5	0.0
Sinter returns*	44.7	19.6	10.0	0.7	0.1	2.3	3.1	5.0	0.0

* Sinter analysis for 15. 9. 75 (average for the day)

Table 6.2b **"Effective" Analysis of Constituents**

Material	Effective weight	Zn	Pb	Fe	S	MgO	Al$_2$O$_3$	SiO$_2$	CaO
B.H. Zinc	0.82	64.26	1.21	9.81	39.26	0.036	0.34	1.7	0.29
B.H. Lead	0.67	5.2	75.2	2.97	23.1	0.03	0.28	1.5	0.19
Blue powder	0.88	29.65	25.00	4.11	-	-	-	-	5.00
Waelz oxide	0.96	43.8	8.3	4.74	3.6	3.5	2.4	7.9	8.3
Limestone	0.58	-	-	0.8	-	2.6	1.03	8.4	85.2
Sand	0.94	-	-	1.6	-	-	1.6	85.3	6.9
Sinter returns	1.00	44.7	19.6	10.0	0.7	0.1	2.3	3.1	5.0

Table 6.2c **Actual Mix Used**

Material	Dry weight (g)	Wet weight (g)
B.H. Zinc	2,718	2,895
B.H. Lead	1,088	1,137
Blue powder	54	56
Waelz oxide	861	860
Limestone	353	366
Sand	165	163
Sinter returns	16,753	16,583

The igniter box was lit, and pulled over the pallet, the ignition layer was ignited for 1.25 min at a downdraught air velocity of 50 cfm (1.41 m^{3}min^{-1}). After sliding the ignition box back, the remainder of the mix was applied to the ignition layer, by pouring the mix through a funnel onto the edges of the ignition layer whilst moving the funnel around the inner former. This was essential to avoid pouring the mix directly onto the centre of the ignition layer to avoid uneven sintering. The inner former was lifted out with a slight twisting motion, the mix levelled and the waste gas hood placed in position.

Sintering was achieved with an updraught air flow of 35 ft^{3}min^{-1} (0.99 m^{3}min^{-1}) for 120% of the time necessary to reach the peak waste gas temperature. The bed temperature was monitored at the top and in the middle with Pt/Pt13%Rh sheathed thermocouples. Windbox pressure was recorded at 2 min intervals. The sinter was then rattle tested.

Three sets of 16 sinters were made. The first was to homogenise the returns. In this case the water was held at a constant value, and there was no pelletization or bentonite addition. These returns were employed to make the second set of mixes, and the second burns returns used to make the third mixes. Both the second and third burns were monitored as above, and variations of moisture, bentonite and pelletization applied as in Table 6.1a.

6.3   RESULTS

The results are presented in Tables 6. 3a and 6. 3b.

The primary interest in this work is the effect of the variables on the sinter strength, the rattle index normally being considered the prime indicator of sinter strength.

As the initial plan was to achieve a duplicated factorial of 3 factors at 2 levels, a standard statistical technique may be adopted to assess the significance of the results.   Presentation of the analyses of variance are given in Tables 6. 3c, d, e, f, for the first and second rattle indices of the second and third burns, and sintering times in Tables 6. 3g, h.

A deliberately poor mix was selected in the beginning to make any improvements more obvious.   The rattle indices for the second burn lie between 58-71 (first rattle index), and for the third burn 49-61 (with one at 68), thus showing there was an overall decrease in sinter strength, on burning a third time.

As the sinter was soft (50-70 rattle index), the mean of only three rattle tests were used to give the average rattle index; the selection of samples and grading is given in Technical Report D. 143.

Peak bed temperatures were monitored at 2 levels in the bed. These peak temperatures are listed in Tables 6. 3a, b, with the associated times at which the peaks occurred.   There were no obvious variations in top or middle peak bed temperatures with any of the variables. Temperatures for the second burn at the top were within the range 1235-1310°C, and 1245-1305°C for the third burn; similarly the mid-bed temperatures for the second burn were between 1135-1290°C and 1170-1280°C for the third burn.

Overall sinter times were between 12. 0 and 14. 4 min; these were statistically analysed, as were the rattle indices, and the results tabulated in Tables 6. 3g, h).

Windbox pressure readings are tabulated for the start and finish of the sinters.   With high moisture content the back pressure tended to be lower than with a normal moisture content, similarly with pelletization and non-pelletization.

Table 6.3a   Second Burn

MIX	RATTLE INDEX		MID-BED TEMPERATURE		TOP-BED TEMPERATURE		SINTER Time (min.)	WINDBOX PRESSURE IN cm OF WATER	
	I	II	°C	Time(min.)	°C	Time(min.)		Start	Finish
Normal moisture	67.4	74.2	1260	6.0	1260	9.5	13.2	7.0	4.2
No bentonite	67.7	72.9	1240	6.0	1255	9.5	13.2	8.0	4.3
Ordinary mixing									
Normal moisture	58.4	67.6	1250	5.5	1250	9.0	14.0	8.8	4.2
1% bentonite	62.4	71.5	1250	5.5	1265	9.0	14.3	8.0	4.3
Ordinary mixing									
High moisture	61.7	65.5	1135	6.0	1235	8.5	12.2	5.5	4.0
No bentonite	61.9	65.7	1195	5.5	1265	8.5	13.0	6.0	4.0
Ordinary mixing									
High moisture	58.2	59.0	1235	6.0	1235	10.0	14.7	5.0	2.5
1% bentonite	59.7	61.9	1220	6.0	1230	10.0	12.0	4.8	2.5
Ordinary mixing									
Normal moisture	64.7	65.3	1205	5.0	1270	9.0	13.2	7.2	4.0
No bentonite	70.5	78.0	1190	6.0	1260	10.0	14.3	7.0	4.3
Pelletized									
Normal moisture	69.5	74.6	1290	5.5	1300	9.5	13.4	6.9	3.2
1% bentonite	66.2	69.7	1260	5.5	1280	9.5	13.1	5.2	3.4
Pelletized									
High moisture	71.2	75.3	1220	5.5	1260	10.5	14.2	5.0	3.2
No bentonite	67.8	74.4	1265	6.0	1310	10.5	14.3	6.2	3.8
Pelletized									
High moisture	67.2	73.7	1200	5.5	1255	9.0	13.2	4.9	3.2
1% bentonite	69.5	74.9	1255	5.5	1270	10.0	12.8	6.7	3.5
Pelletized									

Normal moisture - 630 cm^3 water addition

High moisture - 730 cm^3 water addition

Pelletization - 2.5 min;   mixed 4.0 min

Table 6.3b   Third Burn

MIX	RATTLE INDEX		MID-BED TEMPERATURE		TOP-BED TEMPERATURE		SINTER Time (min)	WINDBOX PRESSURE IN cm OF WATER	
	I	II	°C	Time(min.)	°C	Time(min)		Start	Finish
Normal moisture No bentonite Ordinary mixing	54.8 58.1	61.5 61.4	1245 1280	5.0 5.0	1260 1275	9.0 8.5	12.8 12.4	8.0 7.2	4.4 4.1
Normal moisture 1% bentonite Ordinary mixing	52.1 59.0	56.4 58.9	1275 1260	5.0 5.0	1270 1305	10.0 8.5	13.8 13.4	7.9 8.3	3.8 4.0
High moisture No bentonite Ordinary mixing	49.0 53.7	59.5 60.7	1220 1240	5.0 5.5	1250 1300	10.0 9.5	14.4 13.0	6.9 7.8	3.8 4.1
High moisture 1% bentonite Ordinary mixing	50.4 50.9	58.0 57.3	1170 1240	5.0 5.5	1245 1260	8.0 9.5	12.6 13.0	7.2 7.2	4.0 3.0
Normal moisture No bentonite Pelletized	59.1 68.1	66.3 74.0	1210 1275	5.0 5.0	1260 1280	8.5 8.5	12.2 13.8	5.6 8.0	3.4 4.1
Normal moisture 1% bentonite Pelletized	55.8 59.3	60.7 67.7	1225 1240	5.0 5.0	1255 1230	8.5 9.5	13.4 13.4	7.0 6.2	3.8 3.0
High moisture No bentonite Pelletized	56.4 61.5	60.4 68.7	1225 1245	5.5 7.0	1245 1280	9.0 10.0	12.8 13.8	6.8 5.5	3.7 4.0
High moisture 1% bentonite Pelletized	57.8 58.7	63.8 71.2	1220 1220	5.5 6.0	1250 1305	9.5 9.0	12.7 14.4	6.5 4.8	3.7 3.7

Normal moisture   -   640 cm^3 water addition

High moisture   -   740 cm^3 water addition

Pelletization   -   2.5 min;   mixed 4.0 min

Table 6.3c(i)   Second Burn: First Rattle Test
Rattle Indices

		Normal Moisture	High moisture
Ordinary mixing	No bentonite	67.4 67.7	61.7 61.9
	1% bentonite	58.4 62.4	58.2 59.7
Pelletization	No bentonite	64.7 70.5	71.2 67.8
	1% bentonite	69.5 66.2	67.2 69.5

Table 6.3c(ii)   Analysis of Variants

Source of variance	Sum of squares	φ	Mean squares	F	p
Pelletization A	151.29	1	151.29	35.59	<0.1%
Bentonite B	29.70	1	29.7	6.98	<5%
Moisture C	5.76	1	5.76	-	
A x B interaction	2.1	1	2.1	-	
B x C interaction	23.04	1	23.04	5.42	<5%
C x A interaction	20.705	1	20.705	4.87	5%
A x B x C interaction	8.12	1	8.12	-	
Residual	39.88	8	4.98	-	
TOTAL	280.6	15			

φ Degrees of freedom

F   Variance ratio

p   Significance level

Table 6.3d(i)   Second Burn: Second Rattle Test
Rattle Indices

		Normal moisture	High moisture
Ordinary mixing	No bentonite	74. 2 72. 9	65. 5 65. 7
	1% bentonite	67. 6 71. 5	59. 0 61. 9
Pelletization	No bentonite	68. 3 78. 0	75. 3 74. 4
	1% bentonite	74. 6 69. 7	73. 7 74. 9

Table 6.3d(ii)   Analysis of Variants

Source of variance	Sum of squares	φ	Mean squares	F	p
Pelletization A	141. 6	1	141. 6	29. 5	< 0. 1%
Bentonite B	21. 2	1	21. 2	4. 41	> 5%
Moisture C	34. 2	1	34. 2	7. 12	< 5%
A x B interaction	20. 7	1	20. 7	4. 31	> 5%
B x C interaction	1. 2	1	1. 2	-	
C x A interaction	125. 5	1	125. 5	26. 14	< 0. 1%
A x B x C interaction	0. 0	1	0. 0	-	
Residual	106. 5	8	13. 31		
TOTAL	450. 8	15			

φ Degrees of freedom

F   Variance ratio

p   Significance level

Table 6.3e(i)   Third Burn: First Rattle Test
Rattle Indices

		Normal moisture	High moisture
Ordinary mixing	No bentonite	54.8 58.1	49.0 53.7
	1% bentonite	52.1 59.0	50.4 50.9
Pelletization	No bentonite	59.1 68.1	56.4 61.5
	1% bentonite	55.8 59.3	57.8 58.7

Table 6.3e(ii)   Analysis of Variants

Source of variance	Sum of squares	ϕ	Mean Squares	F	p
Pelletization A	148.23	1	148.23	17.31	0.1%
Bentonite B	17.43	1	17.43	2.04	-
Moisture C	48.65	1	48.65	5.67	< 5%
A x B interaction	6.7	1	6.7	-	
B x C interaction	7.8	1	7.8	-	
C x A interaction	9.2	1	9.2	-	
A x B x C interaction	6.6	1	6.6	-	
Residual	100.4	8	12.5		
TOTAL	344.88	15			

ϕ Degrees of freedom

F   Variance ratio

p   Significance level

Table 6.3f(i)   Third Burn: Second Rattle Test
                          Rattle Indices

		Normal moisture	High moisture
Ordinary mixing	No bentonite	61.5 61.4	59.5 60.7
	1% bentonite	56.4 58.9	58.0 57.3
Pelletization	No bentonite	66.3 74.0	60.4 68.7
	1% bentonite	60.7 67.7	63.8 71.2

Table 6.3f(ii)   Analysis of Variants

Source of variance	Sum of squares	φ	Mean Squares	F	p
Pelletization A	218.3	1	218.3	30.79	< 0.1%
Bentonite B	21.39	1	21.39	3.01	> 5%
Moisture C	3.33	1	3.33	-	
A x B interaction	2.64	1	2.64	-	
B x C interaction	26.30	1	26.30	3.7	> 5%
C x A interaction	0.3	1	0.3	-	
A x B x C interaction	14.2	1	14.2	-	
Residual	120.10	8	15.0		
TOTAL	406.47	15			

φ Degrees of freedom

F   Variance ratio

p   Significance level

Table 6.3g(i)   Second Burn - Sinter Times

		Low moisture	High moisture
Ordinary mixing	No bentonite	13.2 min 13.2	12.2 min 13.0
	1% bentonite	14.0 14.3	14.7 12.0
Pelletization	No bentonite	13.2 14.3	14.2 14.3
	1% bentonite	13.4 13.1	13.2 12.8

Table 6.3g(ii)   Analysis of Variants

Source of variance	Sum of squares	Ø	Mean Squares	F	p
Pelletization A	0.22	1	0.22	-	
Bentonite B	0.00	1	0.00	-	
Moisture C	0.33	1	0.33	-	
A x B interaction	2.98	1	2.98	12.52	< 1%
B x C interaction	0.23	1	0.23	-	
C x A interaction	0.69	1	0.69	2.9	> 5%
A x B x C interaction	0.06	1	0.06	-	
Residual	4.75	8	0.59		
TOTAL	9.26	15			

Ø   Degrees of freedom

F   Variance ratio

p   Significance level

Table 6.3h(i)   Third Burn - Sinter Times

		Low moisture	High moisture
Ordinary mixing	No bentonite	12.8 min 12.4	14.4 min 13.0
Ordinary mixing	1% bentonite	13.8 13.4	12.6 13.0
Pelletization	No bentonite	12.2 13.8	12.8 13.8
Pelletization	1% bentonite	13.4 13.4	12.7 14.4

Table 6.3h(ii)   Analysis of Variants

Source of variance	Sum of squares	$\emptyset$	Mean squares	F	p
Pelletization A	0.09	1	0.09	-	
Bentonite B	0.03	1	0.03	-	
Moisture C	0.09	1	0.09	-	
A x B interaction	1.16	1	1.16	7.83	< 5%
B x C interaction	0.00	1	0.00	-	
C x A interaction	0.12	1	0.12	-	
A x B x C interaction	0.68	1	0.68	4.6	5%
Residual	4.50	8	0.56		
TOTAL	6.67	15			

$\emptyset$ Degrees of freedom

F   Variance ratio

p   Significance level

6.4 DISCUSSION

The initial plan was to prepare a poor sintering mix which contained 15% new zinc in the form of Waelz oxide. It was hoped that this mix would produce a sinter which gave a rattle index of 70-80. As can be seen from the results the sinter strength was poorer than anticipated, giving an average rattle index of 55-65. Since these results were unexpectedly low, the whole apparatus and method were checked. Then a well-catalogued sinter mix was burnt, and the resultant rattle indices were within 3-4 points of the original results, thus confirming that there was no fault with the apparatus or method. The complete set of experiments were then repeated, and a similar set of results obtained, these were tabulated, analysed and presented in Tables 6.3a-6.3h.

From the statistical results of Tables 6.3c, d, e, f, bentonite does not apparently effect the sinter strength significantly (above the 5% significance level). Taking a mean value of rattle indices when bentonite was present, and when bentonite was not present, the result shows there was an overall decrease in sinter strength of 2-3 points on the first rattle index.

Analysis of the sintering time shows there was no single significant factor (Tables 6.3g, h) affecting the sintering time, but a combination effect of pelletization and bentonite addition does not have a small reducing effect on sinter time.

Similarly the effect of moisture on the sinter strength is of little significance in the statistical analysis, although the amount of water present does affect the permeability of the sinter bed initially. This is illustrated by the windbox back pressure values for the second burn (Table 6.3a), where an average pressure reduction of 2 cm of water is achieved by adding extra water.

The statistical results for the second and third burns, in each case, show the effect of pelletization on the sinter strength, being better than 0.1% in significance. The mean increase in rattle index due to pelletization is 4-8 points. The pelletization of a mix depends upon the moisture content of mix; in general terms the more moisture present the better the pelletization. Taking Table 6.3c for example, with

ordinary mixing and a low moisture content the associated rattle indices are greater than when the mix had a high moisture content. After the sets of experiments are repeated with pelletization, there is a greater increase in rattle index of the higher moisture mixes than with the low moisture mixes, showing that better pelletization occurs with a high moisture content. These trends are confirmed in Tables 6.3d, e, f.

Similarly there is an increase in the permeability of the sinter bed due to pelletization, this being illustrated by the mean values of back pressure for pelletization and ordinary mixing. In the second burn during ordinary mixing the average initial back pressure was 6.6 cm of water; with pelletization it reduced to 6.1. Similarly with the third burn the reduction in back pressure was from 7.5 to 6.3 cm of water.

Before burning the mix, the aim is to achieve a coating of new materials on the old sinter returns, this being achieved by mixing the constituents for 4 minutes with the correct amount of water. When the mix is burnt, the new material binds the whole aggregate together to produce a strong sinter. The effect of pelletization is to roll the sinter returns over and over, thus coating them with more and more new material.

The combination of moisture and pelletization to produce a good sinter strength is confirmed in the analysis of variants of Table 6.3d(ii), where the significance level of the CxA interaction (moisture x pelletization), is less than 0.1%.

6.5   CONCLUSIONS

1.   Pelletization has the effect of increasing the sinter strength by 4-8 points overall, and increasing the bed permeability by approximately 2 cm water pressure.

2.   The adverse effect on the sinter strength of having a high moisture content with ordinary mixing, is outweighed by the effect on pelletization, which is better achieved using a high moisture content, and the overall effect of increasing the sinter strength by 4-8 points.

3.   Additions of bentonite at the 1% level make little difference to the bed permeability or sinter strength.

CHAPTER 7

CONCLUDING SUMMARY

7.1 Precipitation and Ageing of Lead Sulphide

For basic oxidation studies, lead sulphide samples of widely different specific surfaces were prepared. They were precipitated from solution at various pH levels in the presence of different concentrations of electrolyte, at two temperatures.

The properties of precipitated lead sulphides are a function of the conditions of precipitation. The crystallinity was best and crystallite size greatest when the reagents were lead nitrate and hydrogen sulphide, i.e. strongly acid solution because of the formation of nitric acid, giving crystallites of 190-425 nm at 20°C and 350-540 nm at 85°C. In less acidic conditions there was a greater proportion of smaller crystallites (70-265 nm) as found with lead acetate and hydrogen sulphide at both temperatures. In alkaline conditions with lead nitrate and sodium sulphide the crystallites were small 60-110 nm at 20°C and poorly crystalline, similarly lead acetate and sodium sulphide formed crystallites of 90-260 nm at 20°C. Overall, the lower pH values favour both crystal growth and crystallinity.

Higher temperatures and longer times of ageing further encourage crystal growth as illustrated by sample J where the average particle size increases from 80 to 265 nm on ageing for 80 h at 85°C. In general, higher salt concentrations also lead to increased crystallinity and particle size.

The formation of lead sulphate as an impurity in lead sulphide precipitates appears to be derived in two ways. At the low pH levels, in the presence of nitric acid and the highest electrolyte concentration at 85°C, the lead sulphate is obtained as well-crystalline material, as observed by electron microscopy. On the other hand, the lead sulphate obtained in alkaline precipitation conditions is derived from the decomposition of the basic salts. This lead sulphate does not appear as well-crystalline material, and was only identified by X-ray diffraction.

7.2 Oxidation of Lead Sulphide

The oxidation of lead sulphide proceeds in two stages; stage one, low temperature oxidation (up to $\sim 600^{\circ}C$) where the oxidation mechanism is dependent upon the chemisorption of oxygen with an associated activation energy of $48-50 \text{ kJ mol}^{-1}$. Above $\sim 600^{\circ}C$, stage two, the oxidation mechanism changes to diffusion of oxygen inward and diffusion of the product gases outward through the sintered product layer with an associated 4-fold reduction in activation energy.

From the studies on the selected precipitated lead sulphide samples, the products of oxidation were governed by temperature. At the lower temperatures lead sulphate is produced initially; as the temperature rises, the basic lead sulphates are obtained by direct oxidation of lead sulphide and by interaction of the oxidation products lead oxide and lead sulphate. The isothermal thermogravimetric curves show the oxidation reaction is over in ~ 10 min (depending on temperature) even though the resultant X-ray analysis shows oxidation is incomplete. This is because of the low sintering temperatures of lead oxide and sulphate, thus preventing the ingress of oxygen and release of sulphur dioxide. The sintering of the products modifies the reaction kinetics from parabolic or $\frac{2}{3}$ order. The sintering phenomena are demonstrated by optical and scanning electron microscopy, where large particle size increases are observed above $\sim 550^{\circ}C$.

As the oxidation temperature rises the products tend to become more basic. The thermogravimetric isothermal curves in some cases show the formation of lead between 850 and $900^{\circ}C$, with its immediate oxidation to lead oxide. Samples of poorly crystalline material begin to oxidize at lower temperatures (ca $200^{\circ}C$) than the larger well-crystalline samples; also the quantity of lead sulphate in the original sample considerably reduces the overall amount of oxidation.

Simultaneous DTA/TG studies carried out in platinum crucibles show an overall increase in formation of sulphate, with up to 25% weight gain in some cases (a maximum weight increase of 26.75% is possible for complete conversion of sulphide to sulphate)with the highest basic salt produced in any of the samples being monobasic lead sulphate at $900^{\circ}C$.

This is due to the catalytic effect of platinum on the $2SO_2 + O_2 \longrightarrow 2SO_3$ reaction, thus promoting sulphate formation.

The characteristic temperatures of oxidations varied with the crystallinity and crystallite sizes of the samples used, i.e. the smaller poorly crystalline samples oxidized at lower temperatures than the larger well-crystalline samples. In general, the initial oxidation temperature is reduced when using pure oxygen rather than air.

The stability of lead sulphate was studied under roast gas atmosphere composition and from the results it is concluded that progressively larger amounts of sulphur dioxide and smaller amounts of oxygen increasingly stabilize the lead sulphate. These findings agree with the predictions of the phase diagrams in Figures 11, 13, 15 and 17 regarding the stability of lead sulphate at elevated temperatures.

7.3   Comparison of the Oxidation of Lead and Related Sulphides

By analogy with alkaline earth metal sulphides, the possibility was considered that lead sulphide would oxidized initially to lead sulphite, especially in conditions with limited amounts of oxygen present.

Thermoanalytical and X-ray techniques indicated that the stability of divalent metal sulphites is in the order :-
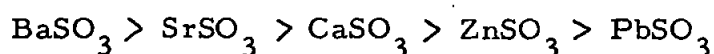
$$BaSO_3 > SrSO_3 > CaSO_3 > ZnSO_3 > PbSO_3$$

The sulphides of the alkaline earth metals are less stable to oxidation to sulphates and thus form appreciable amounts of intermediate sulphites during the complete conversion to sulphate. In contrast, the zinc and lead sulphides are more stable to oxidation compared with their sulphites and hence no appreciable amounts are present during the overall oxidations to sulphates, basic sulphates or oxides. Crystallographic changes during the oxidation of lead sulphide are also discussed.

7.4   Investigation into the Effects of Pelletization, Bentonite and moisture on a Poor Sintering Mix

Pelletization had the overall effect of increasing the sinter strength by 4-8 points and increasing the bed permeability by approximately 2 cm water pressure. The adverse effect on sinter strength by having a high moisture content with ordinary mixing was

outweighed by the effect on pelletization, which is better achieved using a high moisture level. Additions of bentonite at the 1% level make little difference to the bed permeability or sinter strength.

7.5   Other Developments

The acquisition of new information regarding the oxidation of lead sulphides at intermediate temperatures (400-1000°C) is also of value in relation to the preliminary treatment of the ores in connection with the newer electrolytic refining process.

Further useful background development work is required on industrial aspects of sulphide roasting and sintering including:-

1.   Laboratory and pilot plant studies of possible new roasting techniques such as high temperature desulphurization of pelletized material.

2.   Laboratory studies of thermodynamic and reactivity of sulphide-sulphate systems involved in the roasting processes.

REFERENCES

1. Mellor, J. W., "A comprehensive treatise on Inorganic and Theoretical chemistry", 1946, Vol. IX, p. 779-803 (Longmans)

2. Wittung, L., Scand. J. Met., 1972, 1(2), 91-96.

3. Eriksson, G., (SOLGAS), Acta Chem. Scand., 1971, 25, 2651-2658

4. Sillen, L. G., & Rengen, T., Sv. Pappertidn, 1952, 55, 622-631

5. Fuller, F. T., J. Metals, 1968, 20(12), 26-30

6. Yasaka, A., & Gubcova, A., Trans. Met. Soc. AIME., 1967, 239(19), 2004-2005

7. Polyvannyi, I. R., & Gaivoronskii, A. G., Demchenko R. S., Vestn. Akad Nauk. Kaz., USSR., 1967, 23(9), 13-26

8. Melin, A., & Winterhager, H., Z. Erzebergbau Metalluettenw., 1967 20(12), p. 561-569

9. Kellogg, H. H., & Basu, S. K., Trans. Met. Soc. AIME., 1960, 218(1), 70-81

10. Lander, J. J., Trans. Electrochem. Soc., 1949, 95, p. 174

11. Kirkwood, D. H., & Nutting, J., Trans. Met. Soc. AIME., 1960, 218(1), 191

12. Kubaschewski, O., & Evans, E. L., "Metallurgical Thermochemistry", 3rd edn., 1958, London (Pergamon Press)

13. Tuffley, J. R., & Russell, B., J. Australian Inst. Metals, 1962, 7(2), 122-129

14. Tuffley, J. R., & Russell, B., Trans. Met. Soc. AIME, 1964, 230(5), 950-956

15. Gray, N. B. & Culver, R. V., Trans. Met. Soc. AIME., 1967, 239(11), 1835-1840

16. Vander Poorten, H., & Meunier, L., Metallurgie (Mons. Belg.), 1962, 3(1), 15-25

17. Culver, R. V., & Gray, N. B., & Spooner, E. C. R., J. Australian Inst. Metals, 1962, 7(2), 130-135

18. Margulis, E. V., & Ponomarev, V. D., Ser. Met. Obogashch. i Ogneuporov, 1960, 3, 36-51

19. Ponomarev, V. D., & Polyvannyi, I. R., Isv. Akad. Nauk Kaz. USSR., 1956, 9, 3-34

20. Chizhikov, D. M. & Balikina, G. S., Tsventnye Metal, 1937, 4, 72-74

21. Polyvannyi, I. R., Ser. Met. Obogashch. i Ogneuporov, 1958, 3, 23-32

22. Margulis, E. V., & Ponomarev, I. R., Ser. Met. Obogashch. i Ogneuporov, 1960, 3, 38

23. Vander Poorten, H., & Meunier, L., Metallurgie (Mons Belg.), 1962 3(1), 15-25

24. Polyvannyi, I. R. & Gaivoronskii, A. G., & Demchenko, R. S., Vestn. Akad. Nauk Kaz. USSR., 1967, 23(9), 13-26

25. Vander Poorten, H., & Meunier, L., Metallurgie (Mons Belg.), 1962, 3(1), 24

26. Spasov, A. V., & Lenchev, A., & Stanchev, G., God. Sofii Univ. Khim. Fak., 1970, 62, 157-169

27. Spasov, A. V., & Machov, God. Sofii Univ. Khim. Fak, 1970, 62, 143-150

28. Saito, H., Sci. Rept. Tohoku Imp. Univ., 1927, 16, 170

29. Friedrich, K., Metallurgie (Halle), 1909, 6, 179

30. Polyvannyi, I. R., Ser. Met. Obogashch. i Ogneuporov, 1957, 4, 84-96

31. Polyvannyi, I. R., Ser. Met. Obogashch. i Ogneuporov, 1958, 3, 61-70

32. Gaivoronskii, A. G. & Polyvannyi, I. R. Vestn. Akad. Nauk Kaz. USSR, 1967, 23(10), 11-19

33. Saito, H., Sci. Rept. Tohoku Imp. Univ., 1927, 16, 156-157

34. Trifonov, I., Metall Erz., 1932, 29, 429-431

35. Kirkwood, D. H., & Nutting, J., Trans. Met. Soc. AIME, 1965, 233(4), 708-713

36. Collett-Descostils, H. V., J. Mines, 1810, 27, 472.

37. Paduchev, V. V., & Toporova, V. V., & Diev, N. P., Zhur. Priklad Khim., 1961, 34, 676-679

38. Reuter, B., & Stein, R., "Die Oxydation von Bleisulfid bei nederen Temperaturen" Z. Elektrochem., 1957, 61, 440-454

39. Hillenbrand, L., J. Chem. Phys., 1964, 41(12), 3971-3977

40. Kirkwood, D. H., & Nutting, J., Trans. Met. Soc. AIME., 1965, 233(4), 708-713

41. Hagihara, H., J. Phys. Chem., 1952, 56, 610-615

42. Hagihara, H., Proc. Phys. Math. Soc. Japan, 1942, 24, 762-768

43. Sosonowski, L., & Starkiewicz, J., Simpson, O., Nature, 1947, 159, 818-819

44. Mellgren, O., Trans. Met. Soc. AIME, 1966, 235, 46-60

45. Leja, J., & Little, L. H., & Poling, G. W., Trans. Inst. Min. Metall., 1963, 72, 407-423

46. Percy, J., "Metallurgy of Lead", 1870, 47 (London)

47. Eadington, P., & Prosser, A. P., Inst. Mining Met. Trans. Sect. C., 1966, 75(712), 125

48. Eadington, P., & Prosser, A. P., Inst. Mining Met. Trans. Sect. C., 1969, 78(751), 74-82

49. Myuller, R. L. & Danilov, A. V., Ying-Kuei Yang, Zh-Prikl. Khim., 1961, 34, 71-78

50. Kurian, E. M., & Tamhankar, R. V., Trans. Indian Inst. Metals, 1970, 23(4), 59-64

51. Dimitrov, R., & Khekimova, A., Natura (Plovdiv), 1972, 5(1), 67-72

52. Huttig, G. F., Koloidzeitschrift, 1941, 97, 281

53. Kingery, W. D., & Berg, M., J. Appl. Phys., 1955, 26, 1205

54. Coble, R. L., J. Am. Chem. Soc., 1958, 41, 55

55. Kuczynskii, G. C., J. Appl. Phys., 1950, 21, 632

56. White, J., "Science of Ceramics", Proc. Br. ceram. Soc., 1962, 1, (london: Academic Press) 305; ibid., 1965, 3, 155

57. Stickland-Constable, R. F., & Mason, R. E. A., Nature, 1963, 197, 897

58. Kahweit, M., Z. Physik. Chem., 1963, 36, 292

59. Overbeek, J. T. G., Colloid Science, 1952, Chap. II, IV, VII, VIII

60. Tezak, B., Discussion Faraday Society, 1954, 18, 63 and 194

61. Kratshvil, J., & Orhanovie, M., & Malyevie, E., J. Phys. Chem., 1960, 64, 1216

63. Todes, O. M., Zh. fiz. khim., 1946, 21, 629

64. Lifshitz, C. M., & Slyozov, V. V., Phys. Chem. Solids, 1961, 19, 35

65. Klein, E., & Moiser, Ber. Bunsenges Physik Chemic., 1963, 67, 349

66. Kahlweit, M., Z. Physik. Chem., 1963, 36, 292

67. Knox, Trans. Faraday Soc., 1908, 4, 43

68. Harris, C. F., & Bryson, J. L., & Sarkar, K. M. Inst. Mining and Metallurgy, 1967, C76, 12-17

69. Woods, S. E., & Harris, C. F., Sintering Symposium, Port Pirie, (Australian Inst. of Mining and Metallurgy), 1958, 193-218

70. Harris, C. F., ISP Conference 1975, Paper 10

71. Basak, B., Ph. D thesis, Plymouth Polytechnic (CNAA), 1973.

72. Newkirk, A. E., Anal. Chem., 1960, 32, 1558

73. Coats, A. W. & Redfern, J. P., Nature, 1964, 201, 68

74. Leco, Saint Joseph, Michigan, U. S. A.

75. Brunauer, S., & Deming, L. S., & Deming, W. S., & Teller, E., J. Amer. Chem. Soc., 1940, 62, 1723

76. Brunauer, S., & Emmett, P. H., & Teller, E., J. Amer. Chem. Soc., 1938, 60, 309

77. C. I. Electronics Limited, Churchfields, Salisbury, Wiltshire.

78. Glasson, D. R., J. Chem. Soc., 1956, 1506

79. Glasson, D. R. & Linstead-Smith, Diana E. B., "Progress in Vacuum Microbalance Techniques", 1973, Vol2, 209, (London: Heyden).

80. Peiser, H. S., "X-ray Diffraction by Polycrystalline Materials", 1960, London (Chapman and Hill)

81. Scherrer, "Zsigmondy Kolloidchemie", 3rd. edn. 1920, 387

82. Bragg, "Crystalline State", 1933, 1, 189

83. Seljakow, Z. Phys., 1925, 31, 439

84. Jones, F. W., Proc. R. Soc. (A), 1938, 166, 16-42

85. Basak, B., Glasson, D. R., & Jayaweera, S. A. A., "Particle Growth in Suspension". Soc. chem. Ind., 1973, Monogr. No. 38, 143-151 (London: The Society)

86. Rodwell, G. F., J. Chem. Soc., 1863, 16, 42

87. Lucas, M., Bull. Soc. Chim., 1909, 3, 15

88. Muck, F., Zeit. Chem., 1868, 2(4), 241

89. Krivobok, V. I. & Nakhodnova, A. P., (Donets, Gos. Univ. USSR) 1967

90. Natta, G., IX Cong. intern. quim. pura. applicada., 1934, 2, 177-190

91. Komarova, T. N., Zhiteneva G. M., Rumyantseva, Y. V., Isv. fiz-khim., 1966, 7(1), 23-25

92. Nixon, J. C., & Hayton, J. D. & Lawrie, D. C. & Tynan, A. E., Nature, 1961, 192, 516-518

93. Glasson, D. R., J. appl. Chem., Lond., 1960, 10, 38

94. Vogel, A. I., "Text book of Qualitative Inorganic Analysis", 3rd edn. p. 806 (Longmans)

95. Glasson, D. R., Johnson, J. S., & Sheppard, M. A., J. appl. Chem. Lond., 1969, 19, 46

96. Reuter, B., & Stein, R., Z. Elektrochem., 1957, 61, 444-449

98. James, K. V., Plymouth Polytechnic report, 1976

99. Gregg, S. J. & Sing, K. S. W., "Adsorption, Surface Area and Porosity", 1967, 143-146 (Academic Press, London and New York)

101. Kubaschewski, O., & Hopkins, B. E., "Oxidation of Metals and Alloys", 2nd edn., 1962, London (Butterworths)

102. Glasson, D. R. & Jayaweera, S. A. A., J. appl. Chem., Lond., 1968, 18, 65

103. Gulbransen, E. A., & Andrew, K. F., J. electrochem. Soc., 1951, 98, 241

104. Richards, A. W., ISP Research Dept., Avonmouth, Report 73/1, 1973

105. Glasson, D. R., & Harper, R. A., Plymouth Polytechnic report, 1975

106. Glasson, D. R., & O'Neill, P., 1st European Symposium on Thermal Analysis, Salford, 1976

107. Mondage-Dufy, H., Ann. Chim., 1960, 5, 1

108. Glasson, D.R., J.Appl.Chem., 1961, 11, 28

109. Gammage, R.B., Ph.D thesis, Exeter Univ., 1964

110. Gammage, R.B. & Glasson, D.R., Chem y. Ind., 1963, 1466 and J. Coll. Interface Sci., 1976, 55, 396

111. ISP 1975 Conference, private communication.

A computer programme written in Fortran IV for use with
the ICL 1905 for the calculation of particle size distribution from
the data obtained from the Coulter Counter Model Industrial D.

```
      COULTER COUNTER COMPUTATIONS
      MASTER PROGRAMME                                          1
      DIMENSION TH(20),CUR(20),AT(20),NAV(20),NBAC(20),CNAV(20),V(20),G(  2
     *20),DN(20),VAV(20),VPS(20),SDV(20),CUM(20)                 3
C     READ IN NUMBER OF RESULTS,NRES                            4
    3 READ(2,2)ITEST                                            3A
    2 FORMAT(I2)                                                3B
      IF(ITEST)200,6,6                                          3C
    6 READ(2,1)NRES                                             4
    1 FORMAT(I5)                                                6
      SDV(1)=0.0                                                7
C     WRITE OUT TITLES                                          8
      WRITE(3,90)                                               8A
   90 FORMAT(1H1)                                               8B
      WRITE(3,99)                                               9
   99 FORMAT(1H1,29HCOULTER COUNTER COMPUTATIONS )             10
      WRITE(3,98)                                               11
   98 FORMAT(/12HTTHRESHOLD  ,7HCURRENT,3X,5HATTEN,2X,5HBACKG,3X,7HAVERA 12
     *GE,3X,11HCTD.AVERAGE,3X,8HPT.DIAM.,3X,3HPT.FREQ.,3X,8HVOL.PART,3X, 13
     *11HTOT.VOL.PT.,3X,5HWT.PC.)                               14
C     CALCULATE AVERAGE,PART,VOLUME,PART,DIAMETER.              15
      READ(2,100)COF,CONS                                       16
  100 FORMAT(2F6.2)                                             17
      DO 10 I=1,NRES                                            18
      READ(2,101)TH(I),CUR(I),AT(I),NAV(I),NBAC(I)             19
  101 FORMAT(F5.1,F6.4,F3.1,I6,I5)                              20
      C=COF*(IAV(I)/1000.0)**2                                  21
      CNAV(I)=NAV(I)+C-NBAC(I)                                  22
      V(I)=TH(I)*CUR(I)*AT(I)                                   23
      G(I)=CONS*(ABS(V(I))**(4.0/3.0)/V(I))                     24
   10 CONTINUE                                                  25
C     CALCULATE PARTICLE FREQ.                                  26
      DO 11 J=1,(NRES-1)                                        27
      IF(CNAV(J+1)-CNAV(J))7,8,8                                27A
    8 DN(J)=(CNAV(J+1)-CNAV(J))                                 28
      GO TO 11                                                  28B
    7 DN(J)=(CNAV(J)-CNAV(J+1))                                 28C
   11 CONTINUE                                                  29
      DO 12 K=1,(NRES-1)                                        30
      VAV(K)=(V(K)+V(K+1))/2                                    31
   12 CONTINUE                                                  32
C     SUMMING PARTICLES                                         33
      DO 13 L=1,NRES                                            34
      VPS(L)=DN(L)*VAV(L)                                       35
      SDV(L)=SDV(L)+VPS(L)                                      36
      SDV(L+1)=SDV(L)                                           36B
C     CALCULATE PERCENTAGE WEIGHT                               37
   13 CONTINUE                                                  38
      SD=SDV(NRES)-SDV(NRES-1)                                  39
      SUM=SDV(NRES)+SD/2                                        40
      DO 14 M=1,NRES                                            41
      CUM(M)=(SDV(M)/SUM)*100                                   43
      WRITE(3,97)TH(M),CUR(M),AT(M),NBAC(M),NAV(M),CNAV(M),G(M),DN(M),VA 45
     *V(M),VPS(M),CUM(M)                                        46
   97 FORMAT(/2X,F5.1,5X,F6.4,5X,F3.1,3X,I5,4X,I6,3X,F8.1,6X,F5.2,//1X,F 47
     *6.1,7X,F7.3,4X,F7.1,5X,F6.2)                              48
   14 CONTINUE                                                  44
      GO TO 3                                                   48B
  200 STOP                                                      49
      END                                                       50
```

APPENDIX II

A computer programme written in Fortran IV for use with the IBM 1300 to represent the particle size distribution (see Appendix I) in graphical form.

```
GRAPH PLOT OF PARTICLE SIZE DISTRIBUTION.
        DIMENSION CUM(30),G(30)
C       RAISED PEN, PLOTTED POSITION 0.0,0.0
        CALL FPLOT(1,0.0,-11.0)
C       DETERMINATION OF SCALE
        CALL SCALE(0.10,0.25,0.0,0.0)
C       MAKE UP GRID IN X DIRECTION
        CALL FGRID(0.0,0.0,5.0,20)
C       MAKE UP GRID IN Y DIRECTION
        CALL FGRID(1,0.0,0.0,2.0,20)
        CALL FPLOT(2,0.0,0.0)
        X=5.0
        Y=0.0
        DO 20 I=1,20
        CALL FCHAR(X,0.5,0.1,0.1,0)
        WRITE(7,3)X
    3   FORMAT(F4.0)
        X=X+5.0
   20   CONTINUE
        DO 30 J=1,21
        CALL FCHAR(-5.0,Y,0.1,0.1,0)
        WRITE(7,4)Y
    4   FORMAT(F4.1)
        Y=Y+2.0
   30   CONTINUE
        CALL FCHAR(30.0,2.0,0.1,0.1,0)
        WRITE(7,5)
    5   FORMAT(' WEIGHT PERCENT')
        CALL FCHAR(-8.0,8.0,0.1,0.1,1.57)
        WRITE(7,6)
    6   FORMAT(' PARTICLE SIZE IN MICRONS')
        READ(2,100)NRES
  100   FORMAT(I2)
        CALL FPLOT(-2,0.0,0.0)
        DO 10 I=1,NRES
        READ(2,101)CUM(I),G(I)
  101   FORMAT(F5.0,F5.2)
C       PLOT POINTS
        CALL FPLOT(0,CUM(I),G(I))
   10   CONTINUE
        CALL FCHAR(20.0,35.0,0.2,0.2,0.0)
        WRITE(7,1)
    1   FORMAT(' PARTICLE SIZE DISTRIBUTION')
        CALL EXIT
        END
```

APPENDIX III

CALCULATION OF SINTER MIXES

The calculation of sinter mixes to give a target analysis is achieved by using the "effective analyses" of the individual constituents. The target analysis for the research carried out to study the effect of bentonite, moisture and pelletization on a poor sintering mix was 45% zinc, with 15% of the new zinc coming from Waelz oxide, 20% lead, 7.5% iron and 5% sulphur as fuel. The "effective analyses" of the components is given in Table 6.2b.

To balance the zinc, lead and iron a set of simultaneous equations were derived:-

$$\text{Let} \quad \text{Broken Hill Zinc ore} = x_1$$
$$\text{Broken Hill Lead ore} = x_2$$
$$\text{Blue Powder} = x_3$$
$$\text{Waelz oxide} = x_4$$

The zinc balance:-

$$0.6426x_1 + 0.052x_2 + 0.2965x_3 + 0.438x_4 = 0.45 \qquad (1)$$

The lead balance:-

$$0.0121x_1 + 0.752x_2 + 0.25x_3 + 0.083x_4 = 0.20 \qquad (2)$$

The iron balance:-

$$0.0981x_1 + 0.0297x_2 + 0.0411x_3 + 0.0474x_4 = 0.075 \qquad (3)$$

Since 15% of zinc is to come from Waelz oxide

$$0.15(0.6426x_1 + 0.052x_2 + 0.2965x_3 + 0.438x_4) = 0.438x_4$$

thus $\quad x_4 = 0.2586x_1 + 0.771x_2 + 0.120x_3 \qquad (4)$

By substitution for x_4 in equations (1), (2) and (3) we get the three following equations:-

$$0.7558x_1 + 0.086x_2 + 0.349x_3 = 0.45$$

$$0.0335x_1 + 0.57x_2 + 0.26x_3 = 0.20$$

$$0.1104x_1 + 0.056x_2 + 0.0468x_3 = 0.075$$

Solving the simultaneous equations yields:-

$$x_1 = 0.4865; \quad x_2 = 0.2353; \quad x_3 = 0.2529$$

By back substitution of x_1, x_2 and x_3 in equation (4) $\quad x_4 = 0.1743$

Checking shows that with these ratios of x_1, x_2, x_3 and x_4 the overall analysis is Zn = 44.3%, Pb = 18.8%, Fe = 6.8%, S = 23.1%. Since the sulphur requirement is 5%, sinter returns (which has a similar analysis to that of the target analysis, see Table 6.2b) must make up a substantial part of the final mix.

Thus, to give 5% sulphur, the final mix must contain 78.3% sinter returns and 21.7% fresh material. This modifies the overall analysis to Zn = 44.6%, Pb = 19.4%, Fe = 7.8%, S = 5%.

The gangue content was then calculated and additional sand and limestone added to give the target analysis of 3.5% silica and 5% lime.

After allowing for the moisture content of the materials, the final weights of each component were calculated (given in Table 6.2c) to give a total mix weight of 22 kg.

APPENDIX IV

Extended abstract of paper being presented at the 1st European

Symposium on Thermal Analysis, Salford, September 1976

TG AND DTA STUDIES OF THE OXIDATION OF

LEAD SULPHIDE

By S.A.A. Jayaweera and P. Sleeman

John Graymore Chemistry Laboratories,

Plymouth Polytechnic, Plymouth PL4 8AA,

England.

The oxidation of lead sulphide has been investigated using TG and DTA in conjunction with X-ray, microscopic and general analytical techniques.

Results indicate that the oxidation of lead sulphide proceeds via lead sulphate and basic lead sulphates before lead oxide is finally obtained. For basic studies, precipitated lead sulphides have been oxidized in static air, air flowing and oxygen atmospheres on a massflow balance at various temperatures.

The lead sulphide samples were widely different in surface area ($2-10m^2g^{-1}$) and crystallinity, (average crystallite size 400-80nm). Nevertheless they behaved similarly in that they all were converted to lead sulphate at lower temperatures (200°C in some cases) and to the basic sulphates at higher temperatures ($400-600^\circ$C to $PbSO_4.PbO$, $800-900^\circ$C to $PbSO_4.2PbO$, $900-950^\circ$C to $PbSO_4.4PbO$) varying with sample, before being completely desulphurized to lead oxide.

Pure lead sulphate is perfectly stable at temperatures up to 900°C, but above 400°C will react with lead oxide.

The thermal stability and oxidizability of lead sulphite at similar temperatures suggest that it might be a common intermediate in the earlier stages of oxidation. ($4PbSO_3 \longrightarrow PbS + 3PbSO_4$), cf, alkaline earth metal sulphites. Thus, lead sulphite tends to decompose more readily in vacuo and disproportionate in nitrogen.

Figures 1 and 2 show typical thermogravimetric curves from 400 to 950°C for the 1h isothermal oxidations of lead sulphide, sample J80 with a surface area of $3.0m^2g^{-1}$ and an average crystallite size of 265nm.

In the slow oxidation at 400°C, the only phases identified by X-ray diffraction are $PbSO_4$ and the initial PbS, the 4.3% weight gain after 1h corresponds to a conversion of 16.1% PbS to $PbSO_4$. The lead sulphate formation reaches a maximum at 500°C with an overall weight gain of

15%; analysis shows the presence of the basic sulphate $PbSO_4.PbO$, as well as $PbSO_4$ and a small amount of PbS remaining. From 550 to 750°C the overall weight gain after 1h decreases from 13.6% to 4.2%; accordingly the X-ray analysis shows the formation of $PbSO_4.PbO$ at the expense of $PbSO_4$. At 800°C there is an inflextion in the curve at 10 min., ascribed to the formation of lead oxide, and later a further gain due to the reaction of PbO and SO_2 giving $PbSO_4$. At 850°C there is a small (1%) weight gain at 6 min representing sulphation, preceeding a maximum weight loss of 2% (12min) due to PbO formation and then a further slow weight gain, as it reacts with any SO_2 produced. At 900 and 950°C there is no initial weight gain, but greater weight losses of 5.8% (7min) and 8.8% (5min) respectively. After the weight loss maxima there are small weight gains and then a steady weight loss due to vapourization of PbO up to 1h; X-ray analysis shows the presence of $PbSO_4.4PbO$ and PbO.

FIGURE 1.

SAMPLE J80 ISOTHERMALLY OXIDIZED IN STATIC AIR

FIGURE 3.

SAMPLE Q24   OXIDIZED IN STATIC AIR   5°C MIN⁻¹

SAMPLE Q24   OXIDIZED IN AIR FLOWING AT 500 ml min⁻¹   5°C MIN⁻¹

SAMPLE Q24   OXIDIZED IN OXYGEN FLOWING AT 500 ml MIN⁻¹   5°C MIN⁻¹